Dipl.-Phys. Matthias Schlögl

Spatio-Temporal Image Reconstruction for Accelerating Dynamic MRI Applications using Variational Priors

DISSERTATION

zur Erlangung des akademischen Grades
Doktor der Naturwissenschaften (Dr. rer. nat.)

eingereicht an der
Technischen Universität Graz

Betreuer
Univ.-Prof. Dipl-Ing. Dr.techn. Rudolf Stollberger

Institut für Medizintechnik

Fakultät für Informatik und Biomedizinische Technik

Graz, September 2018

EIDESSTATTLICHE ERKLÄRUNG

Ich erkläre an Eides statt, dass ich die vorliegende Arbeit selbstständig verfasst, andere als die angegebenen Quellen/Hilfsmittel nicht benutzt, und die den benutzten Quellen wörtlich und inhaltlich entnommenen Stellen als solche kenntlich gemacht habe. Das in TUGRAZonline hochgeladene Textdokument ist mit der vorliegenden Dissertation identisch.

Graz, am _____ _____

Datum Unterschrift

Acknowledgements

In the course of conducting this thesis I had the luck and pleasure to work together with many talented and interesting people. Without the help, guidance and support of many it would have been impossible to successfully complete this formative chapter in my life.
First of all I would like to thank my supervisor Prof. Rudolf Stollberger for his support and scientific guidance in the incredibly spacious world of Magnetic Resonance Imaging and its numerous applications. From the Institute of Mathematics and Scientific Computing is a pleasure the express my gratitude to Prof. Kristian Bredies and Martin Holler who both contributed a great deal to shape my scientific education in a mathematically rigorous and cordially manner.
To establish the necessary understanding of these both worlds, first, MRI technology/physics and it applications potential and second the power of mathematical imaging with the corresponding optimization, is central to this thesis and many more conducted in the realm of the SFB research center *Mathematical Optimization and Applications in Biomedical Sciences*.
Furthermore I would like to thank all the colleagues and cooperation partners from the Institute of Medical Engineering, the Department of Neurology, the Medical University of Graz, the Department of Mathematics and Scientific Computing, the Ludwig Boltzman Institute for Clinical Forensic Imaging, the Institute of Computer Graphics and Vision, the Center for Advanced Imaging and Research at New York School of Medicine and the Academic Medical Center in Amsterdam. A special thanks goes to Oliver Maier and Kerstin Hammernik for reviewing my thesis. Thank you all for a very enjoyable time inside and outside the office and during the conferences.
Finally, I am deeply grateful for all my good friends and family, for their continuing unconditional support and love and for being a constant source of joy in my life. This is especially true for my beloved Lena and our daughter Antonia. I dedicate this thesis to you.

Abstract

Magnetic Resonance Imaging (MRI) emerged during the second half of the last century to one of the most important clinical device for non-invasive imaging of the human body. By now it is not only possible to achieve incredible image quality with very high resolutions and different soft-tissue contrast but also to extract a wide range of more complex information such as diffusion, perfusion, flow, brain activation, or even metabolic information. MRI became the leading technology for diagnostic imaging of many diseases such as tumor, stroke, or cardiovascular diseases with the advantage of not using ionizing radiation as in computer tomography.
For many of the more complex information made accessible with MRI, it is necessary to encode *dynamic* processes, such as imaging of the beating heart, capturing the temporal course of an injected contrast agent with high temporal resolution or inferring on quantitative information from a characteristic signal evolution. In order to reach and improve necessary conditions of spatio-temporal resolution and spatial coverage the encoding process needs to be very fast.
Today, sequence design for rapid imaging already reached limitations defined by hardware and energy deposition constrains, such that further progress is only achievable by leaving out acquisitions steps. This, however, comes at the cost of increasing the *ill-posedness* of the corresponding reconstruction problem that would conventionally lead to severe artifacts and noise corruption. From a mathematical view-point it is therefore necessary to employ the concept of *regularisation*, where strong improvements require the regularisation to be tailored specifically to the dynamic MRI reconstruction problem.
The core of this thesis is the analysis and application of modern dynamic regularization strategies to different dynamic MRI (dMRI) modalities. Covered examples include functional cardiac imaging and cardiac perfusion imaging, dynamic contrast enhanced MRI, time-resolved angiography, and accelerated MR parameter mapping.

Kurzfassung

Die Magnetresonanztomographie (MRT) trat im Laufe der zweiten Hälfte des letzten Jahrhunderts als eines der wichtigsten klinischen Techniken für die nicht-invasive Bildgebung des menschlichen Körpers hervor. Inzwischen ist es nicht nur möglich mit sehr hohen Auflösungen und vielfältigem Weichteilkontrast eine unglaubliche Bildqualität zu erzielen, sondern auch eine Vielzahl komplexerer Informationen wie Diffusion, Perfusion, Fluss, Gehirnaktivierung oder sogar metabolische Informationen zu extrahieren. Die MRT wurde zur führenden Technologie für die diagnostische Bildgebung vieler Krankheiten wie Tumor-, Schlaganfall- oder Herz-Kreislauf-Erkrankungen mit dem Vorteil, keine ionisierende Strahlung wie in der Computertomographie zu verwenden.
Für viele der komplexeren Informationen, die mit der MRT zugänglich gemacht werden, ist es notwendig, *dynamische* Prozesse zu kodieren. Prominente Beispiele sind die Darstellung des schlagenden Herzens, den zeitlichen Verlauf eines injizierten Kontrastmittels mit hoher zeitlicher Auflösung zu erfassen oder aus einer charakteristischen Signalentwicklung auf quantitative Informationen zu schließen. Um notwendige Bedingungen für die räumlich-zeitliche Auflösung und räumliche Abdeckung zu erreichen und zu verbessern, ist es notwendig den Prozess der Signalkodierung zu beschleunigen.
Da inzwischen die Möglichkeiten der schnellen Bildgebungs-Stratgien bereits an technische und gesundheitliche Grenzen stoßen, ist eine weitergehende Beschleunigung nur noch durch Reduzierung von Akquisitionsschritten erreichbar. Dies führt jedoch zu einer Zunahme der *Schlechtgestelltheit* des Rekonstruktionsproblems, was herkömmlicherweise zu starken Bildartefakten führt. Aus mathematischer Sicht ist es daher notwendig, das Konzept der Regularisierung zu verwenden, welche speziell auf das Problem der Rekonstruktion dynamischer MRT-Bilder zugeschnitten werden muss, um eine Verbesserung der Bildqualität zu erreichen. Der Kern dieser Arbeit ist die Analyse und Anwendung moderner dynamischer Regularisierungs-Strategien für verschiedene dynamische MRT-Verfahren. Die in dieser Arbeit behandelten Anwendungen umfassen funktionelle Herzbildgebung und kardiale Perfusionsbildgebung, dynamische kontrastverstärkte MRT, zeitaufgelöste Angiographie sowie beschleunigte MR-Parameterkartierung.

Contents

List of Figures

1 Introduction

The fascinating technique of Magnetic Resonance Imaging (MRI) emerged during the second half of the last century to one of the most important clinical device for non-invasive imaging of the human body. Already forty years have passed after the fundamental physical theory of nuclear magnetic resonance was investigated before the first scanners were constructed in the late 1970s. By now it is not only possible to achieve incredible image quality with very high resolutions and different soft-tissue contrast but also to extract a wide range of more complex information such as diffusion, perfusion, flow, brain activation, or even metabolic information. MRI became the leading technology for diagnostic imaging of many diseases such as tumor, stroke, or cardiovascular diseases with the advantage of not using ionizing radiation as in computer tomography. A huge society of researchers is dedicated to continuously advance technical possibilities and enable new clinical, biological, and psychological insights in the understanding, imaging, and treatment of diseases and about the human being in general.
For many of the more complex information made accessible with MRI, it is necessary to encode *dynamic* processes, such as imaging of the beating heart or inference of quantitative information from a characteristic signal evolution. This, however, poses more difficulties for the design of the imaging and encoding process and requires fast imaging strategies. Since the later already reached limitations defined by hardware and energy deposition constrains, further progress is only achievable on the encoding side, by leaving out acquisitions but comes at the cost of increasing *ill-posedness* of the reconstruction problem. Suitable *regularization*, tailored to dynamic MRI reconstruction and the demonstration of applicability to different dynamic MRI (dMRI) modalities, is the core of this thesis.

1.1 Overview of the Thesis

The thesis is organized as follows. In Chapter 2 the basics of MRI is briefly outlined and the principal characteristic signal equation is derived. Furthermore, an overview about encoding strategies for different dMRI applications is provided. The following Chapter 3 is concerned with the analysis of the MR reconstruction problem for dynamic data under the condition of noise, discretization and undersampling. State-of-the-art reconstruction methods for *parallel imaging* and *compressed sensing* are reviewed and a newly proposed regularization functional, termed *infimal convolution of total generalized variation functionals*, is put in the context of ongoing research. Furthermore, the numerical solution, methods and the principal problem of evaluation is described before practical aspects are summarized. With this basis laid out, the next three chapters are concerned with specific applications. Chapter 4 describes the application to accelerated functional cardiac and cardiac perfusion imaging. This chapter provides the major discussion of the proposed regularization strategy and the comparison to other state-of-the-art methods. Chapter 5 deals with the application to perfusion MRI with two examples of dynamic contrast-enhanced MRI and dynamic MR angiography. In Chapter 6 the reconstruction of quantitative information from undersampled spatio-parametric data is discussed. This also includes the proposal and evaluation of a fitting algorithm that utilizes regularization on multiple parameter-maps. Finally, a conclusion and outlook is provided in Chapter 7.

2 Principles of Magnetic Resonance Imaging

2.1 Physics of Magnetic Resonance Imaging

The following chapter, oriented on the books by Levitt [1] and Brown et al. [2], provides a brief summary of the fundamental physics, necessary to understand MRI. For the basic notation used in quantum mechanics the reader is also referred to part three in **Levit2007**. A general introduction to imaging of dynamic information in MRI is provided in the second part.

2.1.1 Nuclear Spin

The physical basis for magnetic resonance imaging is the nuclear paramagnetism and the existence of the quantum mechanical *spin* property for atomic nuclei, denoted as $\hat{S}$.Many atomic nuclei posses a non-zero spin which results in a *magnetic moment* $\vec{\mu}$ with the fundamental linear relationship given by

$$\hat{\mu} = \gamma \hat{S}, \tag{2.1}$$

where γ denotes the *gyro-magnetic ratio*. In MRI the major nuclei used for imaging is the spin-$\frac{1}{2}$ system hydrogen ^1H, because of its big occurrence within the human body. For this particular case the gyro-magnetic ratio equals $\gamma = 2\pi \cdot 42.5775 \, \frac{\mathrm{MHz}}{\mathrm{T}}$ and the spin-operator $\hat{S} = \frac{\hbar}{2}(\sigma_x, \sigma_y, \sigma_z)$ can be described with the *pauli matrices* $\sigma_{x,y,z} = \frac{\hbar}{2}\mathcal{I}_{x,y,z}$ with

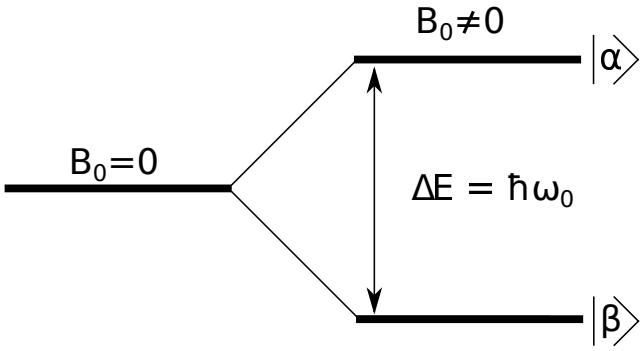

Figure 2.1: Illustration of Zeeman Splitting of a Spin-$\frac{1}{2}$ system in an external static magnetic field B_0.

$$\mathcal{I}_x = \begin{pmatrix} 0 & 1 \\ 1 & 0 \end{pmatrix}, \mathcal{I}_y = \begin{pmatrix} 0 & -i \\ i & 0 \end{pmatrix}, \mathcal{I}_z = \begin{pmatrix} 1 & 0 \\ 0 & -1 \end{pmatrix}. \tag{2.2}$$

2.1.2 Zeeman States

Exposing this single spin-$\frac{1}{2}$ system to a static magnetic field along the z-axis with magnitude B_0, i.e. $\vec{B} = B_0\vec{e}_z$, lifts the degeneracy of energetically equal spin states into *Zeeman states* $|\alpha\rangle$ and $|\beta\rangle$ as first observed by Zeeman in 1897 [3].

$$|\alpha\rangle = \left|n, l, +\frac{1}{2}\right\rangle = \left|+\frac{1}{2}\right\rangle \quad \text{and} \quad |\beta\rangle = \left|n, l, -\frac{1}{2}\right\rangle = \left|-\frac{1}{2}\right\rangle. \tag{2.3}$$

For this short notation the principal quantum number $n = 1$ (assumed to be in ground-state) as well as the orbital quantum number $l = \frac{1}{2}$ are omitted. Also, the coupling of electron and nuclear magnetic momentum for weak external magnetic fields is not taken into account.

The defined states $|\alpha\rangle$ and $|\beta\rangle$ are eigen-states to the spin Hamiltonian $\mathcal{H}_0$ defined as

$$\mathcal{H}_0 = -\hat{\mu} \cdot \vec{B} = -\omega_0 \mathcal{I}_z \tag{2.4}$$

with eigen-values of $\pm\omega_0$, where $\omega_0 = -\gamma B_0$ is called the *Larmor frequency*. As illustrated in Figure 2.1 the difference in energy between the two states is $\Delta E = \hbar\omega_0$. It is important to note that each single-spin system can not be considered to be either in state $|\alpha\rangle$ or $|\beta\rangle$ but always as a super-position

$$|\psi\rangle = c_\alpha |\alpha\rangle + c_\beta |\beta\rangle \tag{2.5}$$

and $(|\alpha\rangle, |\beta\rangle)$ form an orthonormal basis with mixing coefficients c_α and c_β $(c_\alpha + c_\beta = 1)$. Generally, the time-dependent evolution of the spin-state is determined by the time-dependent Schrödinger equation:

$$i\hbar \frac{\partial}{\partial t} |\psi(t)\rangle = \mathcal{H}_0 |\psi(t)\rangle \tag{2.6}$$

2.1.3 Spin Ensembles

Since always the contribution of a number of spins $N_s \sim 10^{19}$ per mm^3 of human tissue (average) is measured instead of a single spin, it is necessary to find a description of *spin systems*, which can be given by a density operator

$$\hat{\rho} = \overline{|\psi\rangle \langle\psi|} = {N_s}^{-1} \sum_{i=0}^{N} |\psi_i\rangle \langle\psi_i| \tag{2.7}$$

and writes as follows using the representation in 2.5:

$$\hat{\rho} = \begin{bmatrix} \overline{c_\alpha c_\alpha^\star} & \overline{c_\alpha c_\beta^\star} \\ \overline{c_\beta c_\alpha^\star} & \overline{c_\beta c_\beta^\star} \end{bmatrix} = \begin{bmatrix} \rho_{\alpha\alpha} & \rho_{\alpha\beta} \\ \rho_{\beta\alpha} & \rho_{\beta\beta} \end{bmatrix} \tag{2.8}$$

This representation already leads us to the more intuitive and macroscopic picture of net-*longitudinal* or *transversal* magnetization, calling $\rho_{\alpha\alpha}$ and $\rho_{\beta\beta}$ average *populations* of state $|\alpha\rangle$ and $|\beta\rangle$ respectively and $\rho_{\alpha\beta}$ and $\rho_{\beta\alpha}$ average *coherences*. For the real and positive populations it holds that $\rho_{\alpha\alpha} + \rho_{\beta\beta} = 1$, which means that, if in average both populations are unequal, a net-magnetization either parallel or anti-parallel to the direction of the external

magnetic field is built up. The coherences, on the other hand, are complex and represent a directional transverse magnetization, perpendicular to the external magnetic field.
In order to describe the temporal behavior of the coherences and populations one needs to use the *Liouville-van-Neumann equations*, that can be derived from the time-dependent Schrödinger equation (2.6):

$$i\hbar\frac{d}{dt}\hat{\rho}(t) = [\mathcal{H}, \hat{\rho}(t)] = \Big(\mathcal{H}\,\hat{\rho}(t) - \hat{\rho}(t)\,\mathcal{H}\Big) \tag{2.9}$$

2.1.4 Thermal Equilibrium

Considering an undisturbed spin-system, i.e. neglecting the exchange with the molecular surrounding, the statistical occupation of a spin-populations $\xi \in (\alpha, \beta)$ will follow the *Boltzmann distribution*

$$p(\xi) = \frac{\exp\left\{-\frac{E_\xi}{k_B T}\right\}}{\sum\limits_{\xi\in(\alpha,\beta)} \exp\left\{-\frac{E_\xi}{k_B T}\right\}} \tag{2.10}$$

leading to a higher occupation of the lower energy level of the order of 10^{-5} for room temperature and fields of the order of 1 T. $k_B = 1.380\,66 \times 10^{-23}\,\mathrm{J/K}$ denotes Boltzmann's constant. The population difference in the high-temperature approximation ($\Delta E << k_B T$) is $\Delta N = N_s(p(\alpha) - p(\beta)) \approx \frac{N_s}{2}\,\mathbf{B}$, where

$$\mathbf{B} = \frac{\hbar\gamma B_0}{k_B T} \tag{2.11}$$

denotes the *Boltzmann Factor*. Considering the sum over all magnetic moments $\vec{\mu}_i$, this leads to a longitudinal equilibrium magnetization of

$$M_{||,\mathrm{eq}} = N_s\frac{\gamma^2\hbar^2 B_0}{4k_B T} \tag{2.12}$$

parallel to the static B_0 field as mentioned earlier in Subsection 2.1.3. The number of spins N_s in a typical imaging volume of $1\,\mathrm{mm}^3$ is around 6×10^{19}, and thus compensates for the considerable small difference in occupation, which establishes the basis for a reasonable MRI signal for hydrogen. For other spin-$\frac{1}{2}$ systems this is markedly harder to achieve. The coherences between all states are zero, thus no transversal net-magnetization will be present in the equilibrium state.

2.1.5 Free Precession and Excitation

With the static Hamiltonian $\mathcal{H}_0 = \omega_0 \hat{I}_z$, and using the definitions in Equ. 2.7 and Equ. 2.8 for the spin-ensembles, a time-dependent solution for the Liouville equations 2.9 can be given as

$$\hat{\rho}(t) = \hat{R}_z(\omega_0 t)\hat{\rho}(t=0)\hat{R}_z(-\omega_0 t) \quad \text{where } \hat{R}_z(\alpha) = \begin{bmatrix} e^{-i\alpha} & 0 \\ 0 & e^{i\alpha} \end{bmatrix} \tag{2.13}$$

This means that the populations $\rho_{\alpha\alpha}$ and $\rho_{\beta\beta}$ are stationary while the coherences $\rho_{\alpha\beta}$ and $\rho_{\beta\alpha}$ are rotating with the Larmor frequency ω_0, which is commonly called *free precession*.
Even without considering differences in magnetization due to tissue relaxation properties, the spin density $\frac{N_s}{V}$ will generate a first imaging contrast. Since only rotating transversal magnetization can be detected it is necessary to translate the equilibrium longitudinal magnetization to *excitation of coherences*. This can be achieved via RF pulses in resonance with the Larmor frequency ω_0. A description of the new time-dependent Hamiltonian $\mathcal{H}(t) = \mathcal{H}_0 + \mathcal{H}_{\mathrm{rf}}(t)$ can be given with the time-dependent RF-Hamiltonian $\mathcal{H}_{\mathrm{rf}}(t)$ with phase Φ_p and rf-frequency ω_{rf}.

$$\mathcal{H}_{\mathrm{rf}}(t) = -\hbar\gamma B_1 \left(\cos\left(\omega_{\mathrm{rf}} t + \Phi_p\right)\hat{I}_x \sin\left(\omega_{\mathrm{rf}} t + \Phi_p\right)\hat{I}_y\right) \tag{2.14}$$

Simplifying the situation to "on-resonance pulses", i.e. when $\omega_{\mathrm{rf}} = \omega_0$, and removing the time-dependence by switching the coordinate system to the "rotating frame", i.e. into a coordinate system rotating with the Larmor frequency, the evolution of the density operator can be computed as

$$\hat{\rho}(t) = \hat{R}_{\Phi_p}(\theta)\hat{\rho}(t=0)\hat{R}_{\Phi_p}(-\theta) \tag{2.15}$$

where $\theta = |\hbar\gamma B_1|\tau_p$ is the *nutation angle* for a hard RF-pulse with amplitude $|B_1|$ and *pulse duration* τ_p and $\hat{R}_{\Phi_p}(\theta)$ is called the *general rotation operator*

$$\hat{R}_{\Phi_p}(\theta) = \hat{R}_z(\Phi_p)\hat{R}_x(\theta)\hat{R}_z(-\Phi_p), \quad \hat{R}_x(\alpha) = \begin{bmatrix} \cos\left(\frac{\alpha}{2}\right) & -i\sin\left(\frac{\alpha}{2}\right) \\ -i\sin\left(\frac{\alpha}{2}\right) & \cos\left(\frac{\alpha}{2}\right) \end{bmatrix}. \tag{2.16}$$

Using this results one can compute two important experiments.

90 deg **hard RF pulse**

In this case the general rotation operator reduces to $\hat{R}_x(\frac{\pi}{2})$. The initial state $\hat{\rho}(0) = \frac{1}{2}\mathbb{1} + \frac{\mathbf{B}}{2}\hat{I}_z$, i.e. only unequal populations and no coherences resulting in a net-longitudinal magnetization vector, is transformed to $\hat{\rho}(\tau_p) = \frac{1}{2}\mathbb{1} - \hat{I}_y$. This state exhibits *equalized populations* with the *differences transferred to coherences*. The corresponding "classical" picture is that of tilting the longitudinal magnetization $M_{||} = M_z$ pointing in z-direction into the transversal plane, creating *transversal magnetization* $M_\perp = (M_x, My)$.

180 deg **hard RF inversion pulse**

Here the general rotation operator writes as $\hat{R}_x(\pi)$. Performing the calculation on the initial state $\hat{\rho}(0)$ as above, this translates into $\hat{\rho}(\tau_p) = \frac{1}{2}\mathbb{1} - \frac{\mathbf{B}}{2}\hat{I}_z$, i.e. the sign of the populations switched, effectively creating an *inversion* of the populations, while the zero coherences are preserved.
It is important to note the connection to the concept of *absorption* and *stimulated emission*. Transferring energy via *on-resonant* RF-pulses to the spin system causes a transition between the two spin-states and annihilates the difference in population while creating coherences. Further energy deposition even inverts the equilibrium state with further absorption, reaching a maximum in system-energy. However, continued energy deposition again

reduces the system-energy by *stimulated emission* back to the initial equilibrium. The flip-angle θ can be generalized to arbitrary RF-pulse shapes by computing

$$\theta = \int_0^{\tau_p} \gamma B_1(\tau) d\tau. \tag{2.17}$$

2.1.6 Relaxation

In the ideal situation of *non-interacting* spin-systems with the molecular surroundings, an arbitrary RF-Pulse would produce a specific amount of shift in populations, while producing coherences that would undergo *free precession* forever. Of course, this situation is not encountered in real experiments and natural decays of both, populations back to the thermal equilibrium state, as well as vanishing coherences can be observed. This tissue-dependent process is called *relaxation* and is the basis for generating basic MRI contrasts. There exist two types of relaxation, firstly *spin-lattice relaxation*, that describes the relaxation of populations and secondly *spin-spin relaxation*, describing the relaxation of coherences. Phenomenologically, these can be expressed in a macroscopic model with the *Bloch equations*, that describe the time-dependency of the magnetization vector $\vec{M} = (M_x, M_y, M_z)$.

$$\frac{d\vec{m}}{dt} = \gamma \vec{m}(t) \times \vec{B}(t) - \frac{1}{T_1} \begin{pmatrix} 0 \\ 0 \\ M_z - M_z^{\text{eq}} \end{pmatrix} - \frac{1}{T_2} \begin{pmatrix} m_x(t) \\ m_y(t) \\ m_z(t) - M_z^{\text{eq}} \end{pmatrix}. \tag{2.18}$$

The Bloch equations give a phenomenological description in the macroscopic limit, but can also be derived from quantum-mechanical viewpoint based on the *Redfield theory*. Spin-lattice relaxation attributes to the thermal exchange of excited protons with the surrounding tissue, leading to an exponential return to the thermal equilibrium, while spin-spin relaxation corresponds to the interaction of magnetic moments and a loss of coherence and, therefore, transverse magnetization. Spin-spin relaxation occurs faster, such that $T_2 \leq$

T_1. In practice the transverse magnetization vanishes much faster, due to B_0 inhomogeneities, with time constant $T_2^\star$.

2.1.7 Signal Detection

As indicated before, only the net transversal magnetization can be detected. Since it rotates with the Larmor frequency and thus generates a time dependent magnetic flux $\Phi(t)$. According to Faraday law of induction, this produces a proportional voltage $U(t)$, that also corresponds to the measured signal, within a receive coil of area A, i.e.

$$U(t) \propto -\frac{d\Phi(t)}{dt} = \int_A \frac{\partial \vec{B}}{\partial t} dA.$$

With the *principle of reciprocity*, which means that the role of magnetization and coil can be reversed, this leads to

$$U(t) \propto \int_V \vec{M}(\vec{r'}, t) \underbrace{\frac{\mu_0}{4\pi} \oint_{wire} \frac{dl \times (\vec{r} - \vec{r'})}{\|\vec{r} - \vec{r'}\|^3} d^3r'}_{B(\vec{r'}):\textbf{Biot-Savart's law}} \tag{2.19}$$

Here it is useful to write the transverse magnetization in complex notation as $M_\perp(\vec{r}, 0) = M_x(\vec{r}, 0) + iM_y(\vec{r}, 0)$. Neglecting relaxation processes, the time dependent magnetization rotates with spatially independent Larmor frequency,

$$M_\perp(\vec{r}, t) = M_\perp(\vec{r}, 0)e^{i\omega_0 t}$$

and yields, making use of Eq. 2.19, the MR signal equation with complex coil sensitivity $\vec{B}(\vec{r}) = B_x(\vec{r}) + iB_y(\vec{r})$, i.e.

$$s \propto \int_V \vec{M}_\perp(\vec{r}, 0)\vec{B}(\vec{r})e^{i\omega_0} d\vec{r} \tag{2.20}$$

It is important to note that in reality the principle of reciprocity might be violated, especially at high fields, such that there is a difference between the two circularly polarized components of $\vec{B}(\vec{r})$, where the *transmit field* is usually denoted as B^+ and the *receive field*, i.e. the coil sensitivities, are denoted as B^- [4], [5].

2.2 Spatial Encoding

2.2.1 Fourier Imaging

So far the theory for *nuclear magnetic resonance* of protons was described. In 1973 the later Nobel prize laureate Lauterbur came up with the idea to use spatially varying gradient fields overlayed onto the principal static magnetic field to *spatially encode* the magnetization [6]. These gradient fields are generated with a coil system embedded on the inside of the main magnet. The fast switching of the gradient system and the emerging Lorentz forces are responsible for the characteristic and often deafening sound of MR systems. Generation of a linearly varying field $\vec{G}(t)$ alters the Larmor frequency, such that

$$\omega(\vec{r},t) = \omega_0 - \gamma\vec{G}(t)\vec{r}$$

translates Eq. 2.20 after *demodulation* as outlined in Haacke [2], i.e. removing the constantly rotating part (ω_0),

$$s(t) \propto \int_V \vec{M}_\perp(\vec{r},0)\vec{B}^-(\vec{r})e^{-i\vec{k}(t)\vec{r}}d\vec{r}. \tag{2.21}$$

The set of discrete signal samples $s(t_i)$ at times t_i is called *k-space* with *k-space coordinates* $\vec{k}(t_i)$

$$\vec{k}(t) = \gamma\int_0^t \vec{G}(t')\vec{r}dt'. \tag{2.22}$$

If all time dependencies but the magnetic gradients are neglected, one can see that these are constructed to generate *Fourier coefficients* of localized transverse magnetization, such that the MR image can be reconstructed afterwards under the limitations of sampling theory - discussed in the next chapter - via Fourier transformation. Here, the concept of Fourier encoding is described for 3D encoding (2D Fourier encoding is commonly used in practise) after *slice-selective encoding*, also introduced by Mansfield [7]. Slice-selective encoding refers to excitation of spin-systems within a defined slice. This can be achieved with a linear gradient in slice direction together with an adequate RF pulse, tailored to excite a defined frequency bandwidth.
For both 2D or 3D encoding, the transverse magnetization is not static but decays very rapidly with time-constant $T_2^\star$, which was termed the *free-induction decay* (FID). The need to generate sufficient signal within hardware constraints, lead to the development of a rich variety of MR *pulse sequences* to generate usable signal or *echoes* at specific time points. Since the signal is not only dependent on the proton density but also on the signal *history*, this also forms the basis of one of the major strengths of MRI, namely the ability to generate different contrasts dependent on sequence parameters and tissue specific relaxation properties. These sequences for echo generation can roughly divided into *gradient-echo* (GE) and *spin-echo* (SE) sequences.

2.2.2 Pulse Sequences

For gradient-echo imaging, also referred to as gradient recalled imaging, a *dephasing* gradient is administered after the excitation pulse, that causes the magnetization to decay even more rapidly than the FID. Afterwards a gradient of opposite polarity is switched on that causes the spins to partially re-phase (see Fig. 2.2). A loss of coherence due to field inhomogeneities can not be reversed, such that the signal intensity at *echo time* (TE) is proportional to $e^{-TE/T_2^\star}$. Fast repetitions of excitation pulses lead to a influence of longitudinal relaxation, since there is insufficient time for complete recovery. After a series of initial pulses this results in a defined *steady-state* signal that is used for imaging.
Also, a train of RF pulses always causes spin and *stimulated echoes*. A very popular sequence, termed *fast low-angle shot* FLASH [8], that is also used

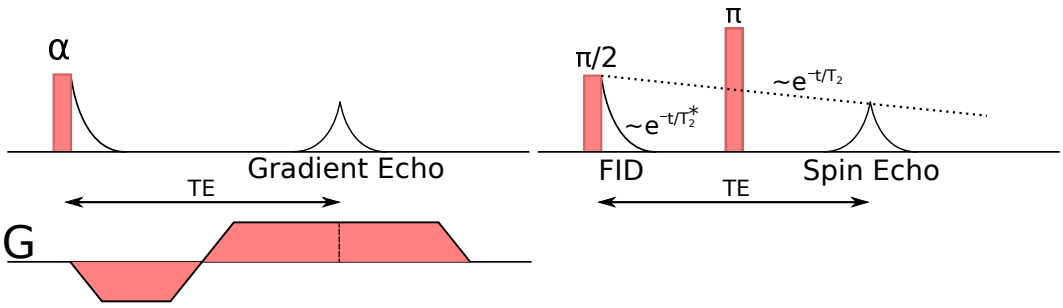

Figure 2.2: Schematic mechanism to produce gradient (left) and spin (right) echoes.

in this thesis, combines low flip angle RF pulses with additional *spoiler* gradients and RF spoiling to destroy residual transverse magnetization and suppress the influence of spin and stimulated echoes.
A technique that makes use of all available signal components without spoiling is called *Steady state free precession* (SSFP). To achieve such a situation it is necessary to rephase all signal before the next excitation and employ higher flip-angles to enhance the spin and stimulated echo amplitudes. This technique is often used in cardiac imaging due to favorable contrast between blood and myocardium.
Spin echoes firstly described by Hahn [9] on the other hand use a second *refocusing* 180 deg RF pulse for echo generation. The RF pulse administered at the half of the echo time, inverts the dephasing transversal magnetization, such that the coherences are restored and form the spin echo (see Fig. 2.2). This technique is very robust to field inhomogeneities but deposits more RF energy due to the second pulse and is also not as time efficient as GE based sequences. Because of that, spin echo sequences are rarely used in clinical practice in contrast to fast derivations like *fast spin echo* (FSE) or *half-fourier acquisition single-shot turbo spin echo* (HASTE).

2.2.3 K-space Trajectories

The basic pulse sequence block need to be repeated to gather a sufficient number of echoes that correspond to the desired image contrast and fill the *k-space*. To this end, the spatial encoding gradients need to be adapted for every repetition. Classically, this is divided into *frequency* and *phase*

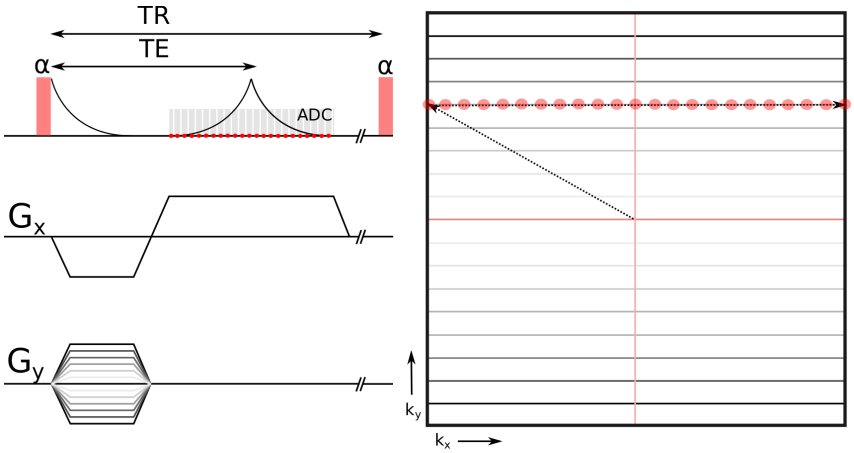

Figure 2.3: Cartesian sampling

encoding, a terminology that corresponds to *Cartesian* k-space sampling as depicted in Fig. 2.3. Originally Lauterbur proposed a *radial* sampling as illustrated in Fig. 2.4. Radial sampling is also used extensively throughout this thesis, due to many advantages for dynamic applications and image reconstruction discussed later. Back then, it turned out that the hardware requirements were not capable to achieve these k-space trajectories with sufficient accuracy, such that Cartesian imaging became, and still remain, a standard for most applications.

2.3 Imaging of Spatio-temporal or -Parametric Information

Dynamic MRI is a generic term that includes a manifold of applications with change of intensity information within an additional dimension. This needs to be discriminated more thoroughly, dependent on the dynamic information that is of interest. The applications investigated within this thesis can be divided into firstly *(1) imaging of physiological movements*, i.e. spatial displacements, where cardiac functional imaging is investigated. Secondly, *(2) imaging of temporal processes*, namely the continuous alterations of signal evolution due to the passing contrast agent in perfusion MRI and lastly

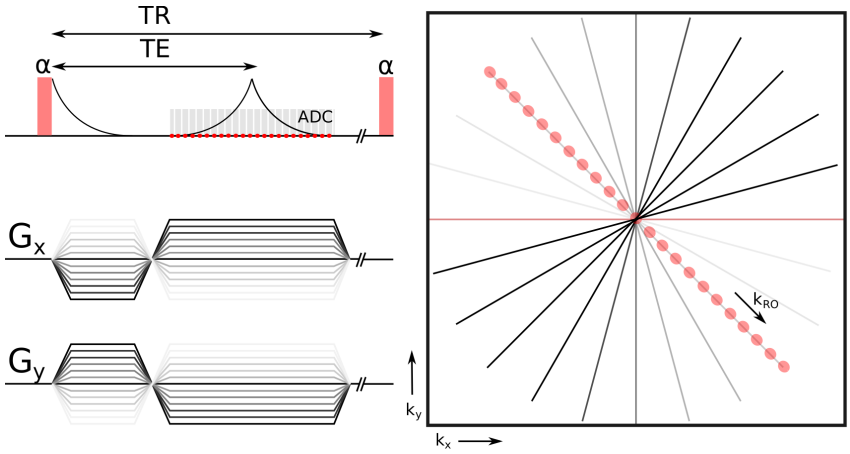

Figure 2.4: Radial sampling

(3) imaging of parametrically changing information, based on sequence modifications to encode quantitative information. In practice these categories can be mixed, e.g. one can be interested to encode parametric information for cardiac imaging. This section is dedicated to give an overview of dedicated *encoding strategies* for the described categories and describe the major assumptions, and limitations.

2.3.1 Encoding of Spatial Displacements

Cardiac and respiratory motions are the major movements of the human body. They can be described as *pseudo-periodic*, since the need for repetition can be perturbed by e.g. cardiac arrhythmia. While respiratory motion is, in general, no information of interest, it is a major source for artifacts. Imaging of the cardiac function, on the other hand, with cardio-vascular diseases being among the major causes for mortality, is a very important tool in MRI that allows for detection, therapy planing, and monitoring of cardiac dysfunctions.
The pseudo-continuous nature of the cardiac movement allows the employment of *cardiac triggering*, i.e. the synchronization of the MR signal acquisition with, most-importantly, the electrocardiogram (ECG), gained with externally placed ECG-electrodes or other *navigator signals*. This technique

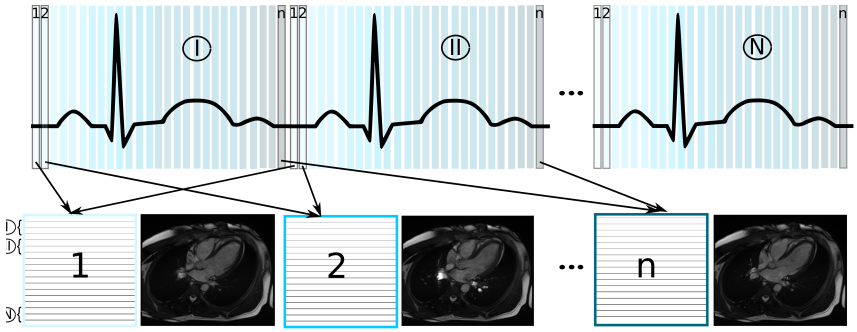

Figure 2.5: Illustration of the principle of CINE cardiac imaging using the ECG signal. The cardiac cycle is divided in n phases that are acquired in N segments and therefore N heartbeats.

is commonly termed CINE because of its "cinematographic" appearance. CINE imaging can usually be performed in two fashions, namely *retrospectively* and *prospectively*, i.e. sorting the acquired data after acquisition or define an acquisition window beforehand. Although, fast imaging sequences have been developed, the acquisition time is still very limited in comparison to the time-scale of physiological motion, such that only a small amount of data can be acquired during one heartbeat. Under conventional sampling limits, several heartbeats, depending on the image resolution, are required to gain a sufficient amount of data per imaged slice as displayed in Fig. 2.5. It is also necessary that the intervals of the cardiac cycle are defined, such that the assumption of motion consistency within one time-frame is valid, which is bounded by the fastest motion phase during heart contraction in systolic phase. A general rule of thumb is that the temporal resolution should be below 50 ms to ensure this constraint. Furthermore, all scans have to be performed under breath-held condition for about 15 to 20 seconds, which can be problematic to achieve for sick patients. The most promising solution to image patients with arrhythmia or breath-held incapabilities is *real-time imaging*, i.e. acquiring all necessary data for one slice in one heartbeat, which conventionally requires to drastically reduce the spatial resolution and employ parallel imaging strategies, subject to the next chapter.
Currently most of the clinical routine cardiac protocols consist in slice-per-slice imaging for different cardiac orientations with conventional Cartesian sampling using FLASH or SSFP based signal encoding, where the later

provides a better contrast between blood and myocardium. Mayor progress has been achieved by employing non-Cartesian trajectories, in particular radial readouts.
Radial sampling can be used as surrogate to Cartesian sampling in CINE based ECG-triggered cardiac imaging, real-time imaging [10] or as self-gated version, where the navigator signal can be extracted from the data since every spoke samples the DC component of k-space [11]. Very recently, this lead to the development of 3D whole-heart imaging approaches, that can be acquired in a *stack-of-stars* sampling or a full 3D *spiral phylotaxis pattern*. Both approaches offer the possibility to extract, both, a cardiac and respiratory signal directly from the data and use this information for retrospective *binning* into cardiac and respiratory phases of the whole 3D volume. This is commonly termed *self navigation*. A necessary condition to guarantee a certain degree of k-space coverage for each motion-bin is a modification of the conventional linear sampling scheme to the sampling with *golden-angles* [12] in the 2D stack case and the *spiral phylotaxis* [13], [14] for full 3D acquisition. Binning for respiratory states can be effectively used to correct for breathing motion [15] but was also found to provide additional information in cardiac MRI [16]. The *golden-angle radial stack-of-stars* or *RAdial Volumetric Encoding* (RAVE) is also a suitable basis for encoding of temporal processes.

2.3.2 Encoding of Temporal Processes

Perfusion imaging tries to capture the temporal dynamic of an injected contrast agent. The modalities investigated in this thesis are, firstly, cardiac perfusion imaging and, secondly, dynamic contrast-enhanced MRI in body imaging and MR angiography (MRA). For cardiac perfusion imaging, breathing and heart motion need to be suppressed while imaging the contrast agent in consecutive heartbeats for a larger heart-volume. This is achieved with gating the signal acquisition to a diastolic window during breath-hold as illustrated in Fig. 2.6. For conventional acquisition only limited spatial coverage with low in-plane resolution is possible. As outlined in Chap. 5, it is important to capture the contrast dynamic with high temporal frame-rate in a larger volume. Here the aforementioned golden-angle RAVE approach is very suitable, since each measurement provides complementary

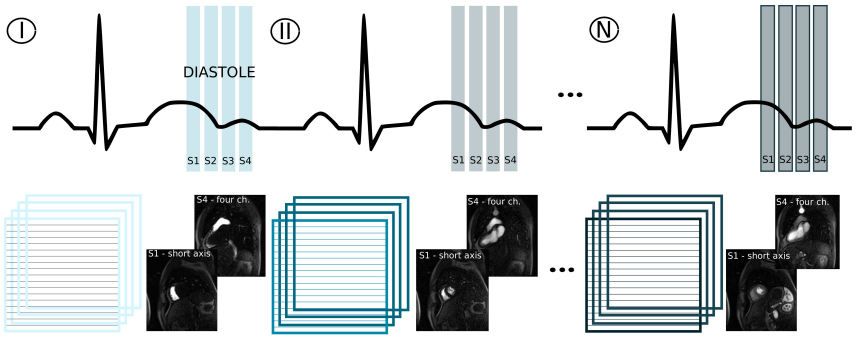

Figure 2.6: Illustration of the principle of cardiac perfusion imaging. K-space data from several slices (usually three short-axis and one four-chamber view) is acquired with the corresponding distribution of the contrast agent within the cardiac volume and tissue in each of N heartbeats in breath-hold.

information and allows a retrospective selection of temporal resolution by grouping together a different fibonacci-number of consecutive measurements into one temporal frame. It is important to choose a Fibonacci number, i.e. $f_n = f_{n-1} + f_{n-2}, n \geq 2, f_0 = 0, f_1 = 1$, to yield a uniform distribution of data in each k-space time-frame. The in-plane golden-angle radial sampling is combined with Cartesian encoding in slice direction. As described in [11] this "hybrid scheme provides better performance for fat saturation, reduced sensitivity to eddy-currents and k-space discontinuities and data acquisitions with flexible slice resolution". Also it allows for entangling the 3D encoding with 1D Fourier transformation in slice direction which is useful to reduce the computational burden. Fig. 2.7 illustrates this principle.

2.3.3 Parametric Encoding for Quantitative Parameter Estimation

Parametric encoding, as described more in detail in chapter 6, is more easy to achieve, in comparison to the aforementioned encodings, since the signal is altered directly with sequence parameter choices rather than physiological motion. However, this degree of freedom needs to be chosen such that sampling efficiency and parameter sensitivity is high. Again 3D stack-of-stars sampling, e.g. for T_1 encoding based on the FLASH signal

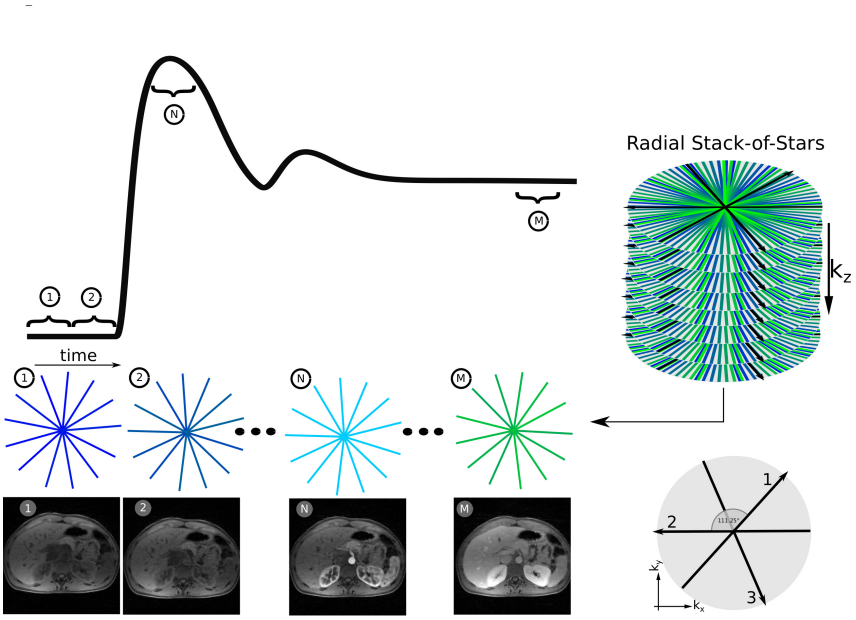

Figure 2.7: Illustration of the principle of radial stack-of-stars imaging. One stack of spokes is measured with the same angle and corresponding angles are acquired with multiples of the golden angle. Figure adapted from [17].

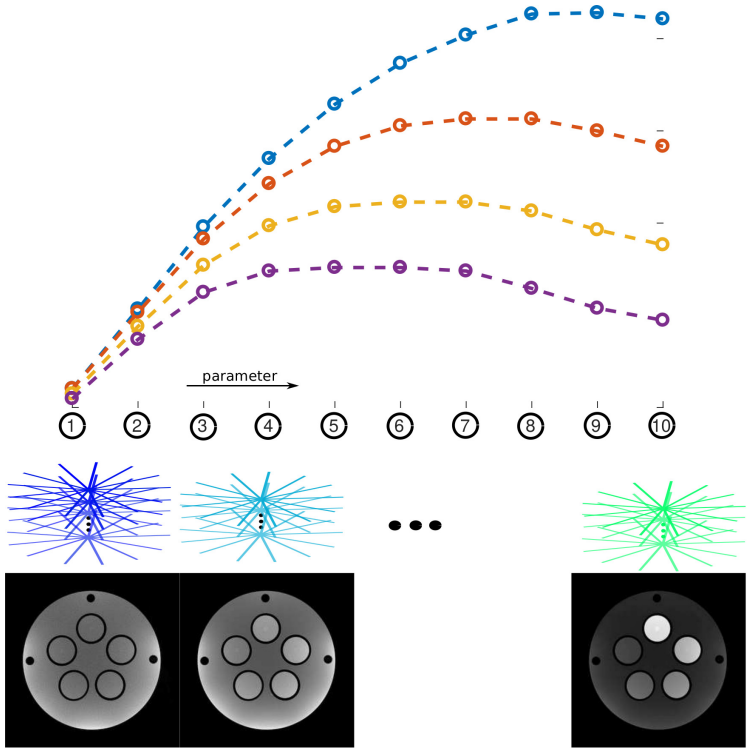

Figure 2.8: Illustration of the principle of parametric encoding with radial stack-of-stars imaging.

equation, is an efficient strategy because of the benign pronunciation of undersampling artifacts as basis for advanced reconstruction methods, as illustrated in Fig. 2.8

3 Principles of dynamic MR Image Reconstruction from undersampled Data

With the theoretical basics of the MR experiment described in chap. 2 this chapter is now concerned with the analysis of the corresponding *MR image reconstruction* problem. More specifically the analysis is given by taking into account the process of discretization, noise influence and more importantly reducing the number of acquisitions, commonly termed "undersampling". To stabilize the inversion under these conditions the concept of regularization and compressed sensing is introduced and generalized to the situation of dMRI applications.

3.1 The MRI inverse problem

Starting again with the principal MR signal equation for a stationary magnetization, a Fredholm integral of first order,

$$s_j(\vec{k}) = \int_{\Omega} d\vec{r}\, \mathrm{m}_{\perp}(\vec{r}) c_j(\vec{r}) e^{-i<\vec{k},\vec{r}>}, \tag{3.1}$$

the corresponding *inverse problem* is to compute the transverse magnetization $\mathrm{m}_{\perp}(\vec{r})$ on its support $\Omega \subset \mathbb{R}^D$, $D \in \{2,3\}$, from observed signals $s_j(\vec{k})$ given the known encoding function for the j-th receiver coil $c_j(\vec{r})$, i.e. $E_j(\vec{k},\vec{r}) = c_j(\vec{r})e^{-i<\vec{k},\vec{r}>}$. This task is also commonly termed *MR reconstruction*.

Inverse problems are said to be *ill-posed* if one or more of the following properties stated by Hadamard in 1902 [18] are violated.

1. **Existence**: A solution exists
2. **Uniqueness**: The solution is unique
3. **Stability**: The solution depends continuously on the data

3.1.1 Discretization

For simplicity we first consider the single-coil reconstruction problem, i.e. $c_1(\vec{r}) = 1$ for the one-dimensional case ($\mathrm{m}_\perp(\vec{r}) = \mathrm{m}_\perp(x)$). The signal must be acquired discretely and with a finite number of samples, such that an infinite number of continuous solutions for $\mathrm{m}_\perp(\vec{r})$ exist. The problem of reconstructing a continuous function from its noiseless, discretely sampled Fourier coefficients is described in seminal works on sampling theory, most notably by Whittaker, Nyquist, Kotel'nikov and Shannon (e.g. [19], [20]). Assuming that the magnetization has a finite support, i.e. $\mathrm{m}_\perp(x) = 0$ for $|x| < \frac{\mathrm{FOV}}{2}$, commonly termed the *Field-of-View* FOV, it can be shown that the MR image can be perfectly reconstructed from an *infinite* number of its discrete Fourier coefficients as follows

$$\mathrm{m}_\perp(x) = \Delta k \sum_{n=-\infty}^{\infty} s(n\Delta k) e^{2\pi i (n\Delta k)x}, \quad |x| < \frac{1}{2\Delta k}, \tag{3.2}$$

with sampling intervals Δk, such that the *Nyquist limit* can be defined as

$$\mathrm{FOV} < \frac{1}{\Delta k}. \tag{3.3}$$

Sampling below the Nyquist limit results in aliasing artifacts within the reconstructed image.Furthermore, only a *finite* number of samples can be acquired, i.e. $n \in \{-\frac{N}{2}, \cdots, \frac{N}{2}\}$. Thus a continuous approximation of the magnetization can only be calculated using a minimum-norm constrain on the missing Fourier coefficients, effectively setting these to zero. This leads to the description of the reconstruction problem with the *discrete Fourier transform* ($\mathcal{DFT}$) for an image evaluation on the m-th discrete pixel:

$$\begin{aligned} \mathrm{m}_{\perp}(m\Delta x) &= \Delta k \sum_{n=-\frac{N}{2}}^{\frac{N}{2}-1} s(n\Delta k) e^{2\pi i (n\Delta k)(m\Delta x)} \\ &= \Delta k \sum_{n=-\frac{N}{2}}^{\frac{N}{2}-1} s(n\Delta k) e^{2\pi i n m/N}. \end{aligned} \tag{3.4}$$

Here,

$$\Delta x \leq \frac{1}{N\Delta k}, \tag{3.5}$$

is called the *pixel resolution*. A low number of acquisitions and therefore low spatial resolution leads to more pronounced *Gibbs Ringing* and *partial-volume effects*. It can be shown that a therefore desirable higher *spatial resolution* can only be achieved by acquiring a higher number of samples at the cost of increased acquisition time and reduced SNR. Zero-filled reconstruction of such a low amount of acquired k-space effectively leads to an image interpolation but does not add additional information. For a more exhaustive description concerning the pixel resolution the reader is referred to [21]. Since the numerical computation itself relies on a discretized model, this will from now on be indicated by switching the notation for Eq. 3.1, by defining the discrete MR forward model $\mathcal{K}$,

$$\begin{aligned} &\mathcal{K} : \mathcal{U} \mapsto \mathcal{V} \\ &\mathcal{K} : u \mapsto \left(\mathcal{DFT}\{\hat{\mathcal{C}}_c u\}\right)_{c=1}^{N_c} := d, \end{aligned} \tag{3.6}$$

that maps the discretized magnetization $u \in \mathcal{U} = \mathbb{C}^{N_x \times N_y}$, with N_x and N_y being the number of image-pixels in x- and y-direction respectively, to k-space data $d \in \mathcal{V} = \mathbb{C}^{N_r \times N_e \times N_c}$, where N_r and N_e denotes the number of samples in readout and phase-encoding direction, and N_c the number of receiver coils. N_r and N_e are also used for notation of Non-Cartsian trajectories, where N_r always denotes the number of samples acquired during one ADC readout and N_e the number of encodings for successive echoes, e.g. the number of radial spokes. $\hat{\mathcal{C}}_j$ describes the linear operation of point-wise multiplication of the j-th receiver coil sensitivity with the magnetization.

3.1.2 Noise

Concerning the stability of computing the inverse solution *noise* is a major issue. Dependent on the corresponding forward model the uncertainty in the data can be augmented tremendously in the solution.Noise is always present in the MRI experiment, with thermal noise from the imaging object being the primarily source apart from thermal fluctuation of charges with the individual receiver coil-elements. As described by Nyquist and Johnson [22], [23] the thermal noise generates stationary, additive and normally distributed noise with zero mean and variance σ^2 for both imaginary and real component with the following proportionality:

$$\sigma^2 \propto 4Rk_b\mathrm{BW}T \tag{3.7}$$

Here R denotes the *coils effective resistance*, BW the *readout bandwidth*, k_b the *Boltzmann constant*, and T the *temperature* in Kelvin, yielding noisy, discrete data $\tilde{d}_{n,c}$ for the n-th sample in the c-th coil.

$$\tilde{d}_{n,c} = d_{n,c} + n_{n,c}, \quad n_{n,c} \propto \mathcal{N}(0, \sigma_c^2) \tag{3.8}$$

For array coils there exist individual variances σ_c^2 and noise correlations between the receiver coils due to electromagnetic coupling that can be described by a *noise covariance matrix* Σ. Having access to $N_{samp} \sim 10^5$ noise-only-samples η_c for each coil, that are mostly contained in measurement files or can be acquired with zero-flip-angle acquisition, the elements of Σ can be computed as follows:

$$\Sigma_{n,m} = \frac{1}{N_{samp}} < \eta_n, \eta_m > \quad n, m = 1, \cdots, N_c \tag{3.9}$$

The noise covariance matrix (see Fig. 3.1) can be employed to improve the reconstruction quality by computing the weighted least-squares solution (see 3.7.4). For fully sampled data the noise variance in data-space σ_d translates directly to globally equal noise in image space σ_i due to the linearity of the Fourier transform, such that

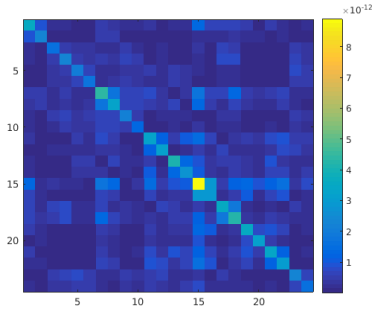

Figure 3.1: Example for noise covariance matrix for measurement with a 32-channel head-coil

$$\sigma_i^2 = \frac{\sigma_d^2}{N} \tag{3.10}$$

for an image matrix of $N = N_x N_y$ pixels. The SNR in this case can be defined on a pixel basis as:

$$\mathrm{SNR}(u_n) = \frac{|u_n|}{\sigma_i}. \tag{3.11}$$

3.1.3 Undersampling and Parallel Imaging

As outlined before, the requirement for consecutive measurements leads to time-consuming acquisition times, which states a fundamental drawback for MRI. Acquiring a lower amount of data, with respect to the theoretical limits stated by Nyquist and Shannon, reduces the scanning time. This is commonly termed *sub-Nyquist* sampling or just *undersampling*. If the reconstruction is carried out by applying the inverse Fourier transformation to the incomplete MR data, the reconstructed image will be corrupted by intense aliasing artifacts that are characteristic for the employed sampling trajectory (see Fig. 3.2).

The loss in encoding information can be compensated to a certain extend by employing the spatial information of the localization with multiple receiver

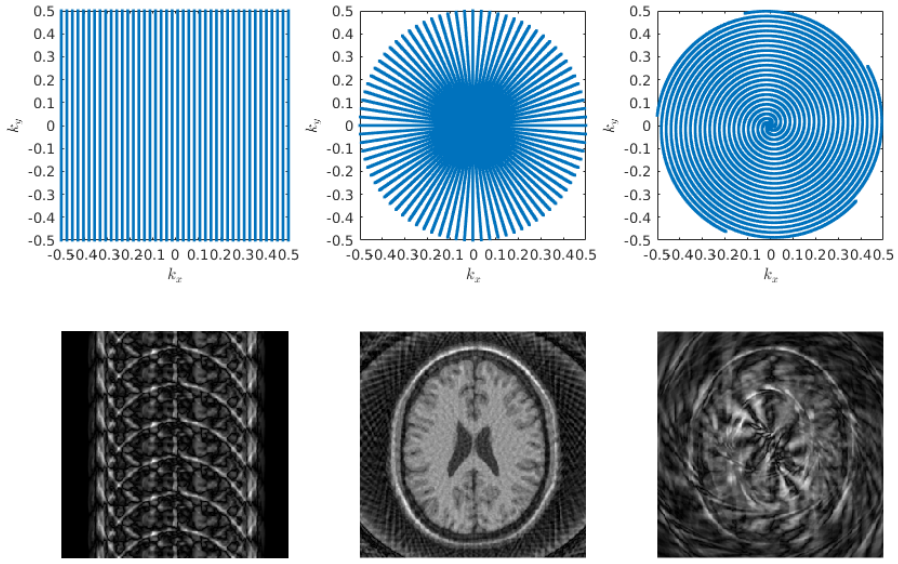

Figure 3.2: Effect of sub-Nyquist sampling for Cartesian (left), radial (middle) and spiral (right) acquisition.

coils. After early investigations by Carlson et al. [24], Sodickson et al. [25] found a formalism to describe missing k-space coefficients by *simultaneous acquisition of spatial-harmonics* SMASH constructed from the coil sensitivities. This laid the basis for a very important development in MRI known as *parallel imaging* (PI), that is nowadays used routinely to accelerate MR acquisition.
It is out of scope to give a complete overview of PI methods in this thesis, however some important works should be mentioned. PI is roughly divided in *k-space based* and *image based* methods. K-space based PI refers to estimation of correlations from multi-coil *autocalibration-lines* ACL, acquired within the Nyquist limit. Missing data points are then interpolated according to these correlations and their proximal acquired data points. In that way, the *coil sensitivity* information that is captured in the low-frequency information, is used inherently. Among, k-space based methods, *generalized autocalibrating partially parallel acquisitions* GRAPPA by Griswold et al. [26] and *Iterative Self-consistent Parallel Imaging Reconstruction From Arbitrary k-Space* SPIRiT are the most robust and clinically applied method based on SMASH.
In contrast, image-space based methods require an *explicit* estimation of the coil sensitivities in image space. After early works by [27] the first robust in-vivo implementation for undersampled Cartesian data with *Sensitivity Encoding* SENSE was achieved by Pruessmann et al [28]. There, the regular aliasing was entangled by computing the *least-squares solution* on a voxel-per-voxel basis given the coil sensitivities. However, this is a specific setting to which a general solution for arbitrary k-space trajectories was described two years later again by Pruessmann et al. [29].
The employment of arbitrary trajectories and the advantage of easier integration of image priors makes image-space methods the preferable choice. However, the explicit estimation of coil sensitivities was problematic such that more robust but less accurate k-space based methods are favored in clinics.
Recently, Uecker et al. [30] nicely described the connection between the two approaches which yields a more complete and robust method to explicitly estimate an extended set of coil sensitivities and combine the advantages from both proposals. With the coil sensitivities included in the forward mapping as defined in Eq. 3.6 the image space PI problem as also described in [29] reads as follows:

$$u^\star = \arg\min_u \frac{1}{2}\|Ku - d\|_2^2 \tag{3.12}$$

and leads to the solution

$$u^\star = (K^H K)^{-1} K^H d \tag{3.13}$$

where $K^\dagger = (K^H K)^{-1} K^H$ is called the *pseudo inverse*. Since the direct computation of the pseudo inverse is computationally tedious and requires a lot of memory an efficient solution needs to be computed *iteratively*. In [29] the *conjugate gradient* (CG) algorithm is used, giving rise to the terminology CG-SENSE. The CG algorithm is an optimal first order algorithm for convex and differentiable problems. However, the adjoint K^H of the forward problem is needed for which a derivation can be found in the Appendix (see App. 8.3.3).
However, a stable inversion of $(K^H K)$ is in general not possible, which is the crucial point for ill-posed linear inverse problems. This is where the important concept of *regularization* arises, that will be outlined in the statistical context. Furthermore, even if the inversion is stabilized with regularization, this will lead to a spatially dependent variation of SNR dependent on the receiver coil orientation and undersampling pattern, known as *geometry factor* or *g-factor* also described in [28].

3.1.4 Bayesian Point of View

From an Bayesian point of view the image reconstruction problem leaves us with a statistical uncertainty of finding the discrete MRI image u given discrete observations (measured data) d. Thus, we need to treat u as a random variable, that is governed by some probability distribution dependent on the observation. This probability density function or *posterior probability* $p(u|d)$ can be expressed with Bayes rule as

$$p(u|d) = \frac{p(d|u)p(u)}{p(d)}, \tag{3.14}$$

where $p(u)$ is the prior probability, $p(d)$ is called the *evidence* - that can be treated as a constant scaling factor - and $p(d|u)$ is the *likelihood*. The likelihood loosely states how well the observed data is described by a possible solution. Given independent and identically distributed (iid) samples, which holds for the MR measurement process, the likelihood can be expressed with a multi-variate Gaussian distribution:

$$p(d|u) \propto \exp\Big\{-(Ku-d)\Sigma^{-1}(Ku-d)\Big\}. \tag{3.15}$$

The more difficult question now is the design of a suitable prior probability $p(u)$. The seminal works of Phillips [31] and Tikhonov [32] proposed a *stabilizing functional* that yields a prior distribution of the form

$$p(u) \propto e^{-\alpha\|\Gamma u\|_2^2}. \tag{3.16}$$

The statistical interpretation therefore assumes that u should be drawn from a multi-variate Gaussian distribution with zero means.Substituting the now given likelihood and prior probability into Eq. 3.14, assuming for simplicity $\Sigma = Id$, yields:

$$p(u|d) \propto e^{\underbrace{-\|Ku-d\|_2^2 - \frac{\alpha}{2}\|\Gamma u\|_2^2}_{:=-E(u)}} \tag{3.17}$$

Given this posterior distribution, the *maximum-a-posteriori* (MAP) estimator is defined as:

$$\mathrm{u}^\star = \arg\max_u p(u|d). \tag{3.18}$$

This is equivalent to compute the minimum of $E(u)$, that is often termed *free energy* due to the connection to Gibbs free energy in statistical thermodynamics, and leads to the *variational problem*

$$\mathrm{u}^\star = \arg\min_u \underbrace{\frac{1}{2}\|Ku-d\|_2^2}_{\mathcal{D}(u,d)} + \underbrace{\frac{\alpha}{2}\|\Gamma u\|_2^2}_{\mathcal{R}(u)}. \tag{3.19}$$

This yields the Phillips-Tikhonov regularized solution of Eq. 3.13 for a given *data fidelity* $\mathcal{D}(u,d)$ and regularization functional $\mathcal{R}(u)$ with the solution

$$u^\star = (K^H K + \alpha \Gamma^H \Gamma)^{-1} K^H d. \tag{3.20}$$

It can be shown that $(K^H K + \alpha \Gamma^H \Gamma)$ is invertible and its inverse is bounded, i.e.

$$\|(K^H K + \alpha \Gamma^H \Gamma)^{-1}\|_2 \leq \frac{1}{\sqrt{\alpha}}, \tag{3.21}$$

yielding the desired stabilization. It is also worth to note that when the solution is computed iteratively with gradient-based methods, as for CG-SENSE, the regularization is realized in an implicit way (Landweber regularization). To sum up the previous section, the MR reconstruction problem of discrete data is ill-posed due to noise corruption and furthermore due to the desired goal of accelerating the acquisition process by sub-Nyquist sampling. It was outlined that a *data fidelity* term $\mathcal{D}(u,d)$ can be defined on a statistical basis and that the computation of a solution to the PI problem requires stabilization on the basis of a-priori information contained in a suitable regularization functional $\mathcal{R}(u)$, such that the generic problem can always described as

$$\mathrm{u}^\star = \arg\min_u \mathcal{D}(u,d) + \mathcal{R}(u) \tag{3.22}$$

The next sections are now concerned with the specification of these two "ingredients". First, the description of data fidelity is extended to the problem of undersampled *dynamic* MRI, addressing specific sampling strategies. Second, and more importantly, advanced regularization strategies for stable reconstruction of image series will be described.

3.2 The dynamic MRI Forward Problem

First we introduce a time-dependent magnetization $m_\perp(\vec{r},t)$ into the signal equation as follows

$$s_j(t) = \int_\Omega d\vec{r}\; m_\perp(\vec{r},t)c_j(\vec{r})e^{-i<\vec{k}(t),\vec{r}>}. \tag{3.23}$$

Usually, time-independent static receiver coils can be assumed, that holds true for static head-coils but might be violated for abdominal applications during free-breathing. There the receiver coil is flexible attached to the body. The MR operator for the discrete dynamic setting is then redefined as

$$\begin{aligned} &\mathcal{K} : \mathcal{U} \mapsto \mathcal{V} \\ &\mathcal{K} : u \mapsto \left(\mathcal{DFT}_t\{\hat{\mathcal{C}}_j u_t\}\right)_{c=1,\cdots,N_c}^{t=1,\cdots,N_t} := d, \end{aligned} \tag{3.24}$$

where $\mathcal{U} = \mathbb{C}^{N_x \times N_y \times N_t}$ with N_t being the number of time-frames and d is now the measured data in *k-t-space* [33], i.e. $d \in \mathcal{V} = \mathbb{C}^{N_r \times N_e \times N_c \times N_t}$. The time-dependence in $\mathcal{DFT}_t$ indicates the possibility of variable sampling in k-t-space. It is important to note that for dynamic imaging the data points sampled in one time-frame must be considered *motion-consistent*, i.e. it can be controlled or assumed that no *inter-frame* motion occurs. This would lead to artifacts due to k-space inconsistencies. Correction of intra-frame motion is adverse to imaging inter-frame movement, since it aims to correct for application-specific motion-related artifacts, such as involuntary head movement (see e.g.[34]), instead of imaging diagnostically valuable dynamic information. However, mixing of the two situations occurs frequently, such as breathing-artifact correction for cardiac MRI [35], [36].
For dynamic MRI we can define a *temporal resolution* Δt, i.e. the time between adjacent time-frames that must always been interpreted in the context of the application.
Since a common issue of all dMRI applications is the ultimate trade-off between temporal and spatial resolution and/or coverage, these benefited also strongly from PI techniques. Here, the additional degree of freedom of how to vary the temporal sampling pattern arouse and triggered a manifold

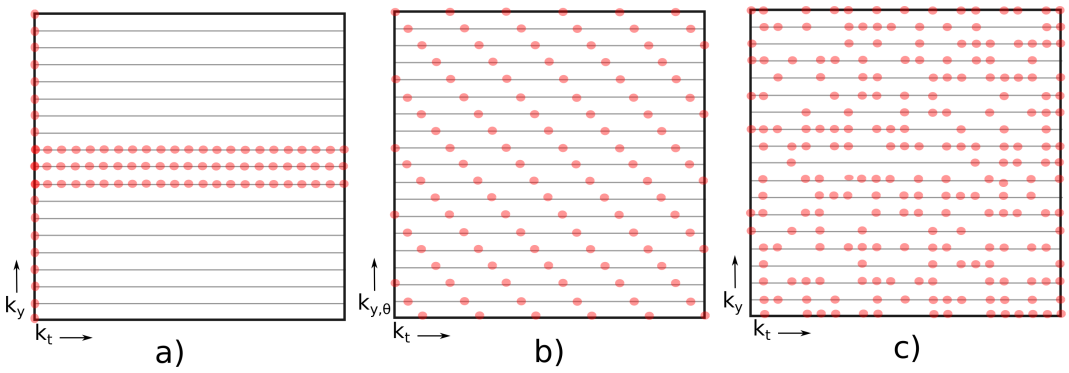

Figure 3.3: Overview of different k-t-sampling methods for view-sharing (a), uniform (b) and variable (c) sampling density. Adapted from [44]

of different methods. A very early work termed *MR fluoroscopy* [37] falls under the class of *keyhole* imaging, where only low frequency information is updated after acquisition of a fully sampled first scan. Other techniques like TRICKS [38] or TWIST [39] update different parts of k-space at randomly at different times. Other methods that explicitly employ PI reconstruction are TSENSE [40], TGRAPPA [41], k-t-SENSE [42] and k-t-GRAPPA [43] among many others. General classes of sampling approaches are illustrated in Fig. 3.3 adapted from [44], where a very complete and extensive review about acceleration of temporal techniques is given. This review also gives an overview compressed sensing techniques in the spatio-temporal context that is also covered in the next section.

3.3 Variational Models and Compressed Sensing for dynamic MRI

Adding a-priori information to the reconstruction problem in the form of advanced regularization strategies enables improved suppression of artifacts and noise, with stabilization of the corresponding inverse problem. As outlined before, the Tikhonov type regularization for image denoising was proposed as the L^2 norm of the differential of the image function on its support $\Omega \subset \mathbb{C}$, i.e.

$$R(u) = \int_{\Omega} |Du|^2 d\Omega, \tag{3.25}$$

where D denotes the differential operator. $R(u)$ has a low value for images with low gradient and thus low noise but leads to over-smoothing of edge structures.A key feature for visual perception in natural images are *jump discontinuities*. The space of *functions of bounded variation* (BV) defined as

$$\mathrm{BV}(\Omega) = \left\{ u \in L^1(\Omega) \mid \int_{\Omega} |Du| d\Omega < \infty \right\} \tag{3.26}$$

contains image functions that are said to have finite *total variation* (TV). Total variation is a very famous and extensively studied functional used for denoising of images with preservation of edges introduced by Rudin, Osher and Fatemi in 1992 [45], thus often termed the ROF model, that enforces the mentioned requirement of preserving jump discontinuities by enforcing *piecewise constancy* [46]. TV is essentially the L^1-norm of the image gradient and is defined in the continuous setting for a image function u as

$$\mathrm{TV}(u) = \sup_{v} \left\{ \int_{\Omega} u \operatorname{div} v \, d\Omega \mid v \in C_c^1(\Omega, \mathbb{C}^2), \|v\|_\infty \leq 1 \right\}. \tag{3.27}$$

For u being differentiable this can also be written as

$$\mathrm{TV}(u) = \int_{\Omega} |Du| \, d\Omega. \tag{3.28}$$

Using the discretized gradient

$$(\nabla u)_{i,j} = \begin{pmatrix} \delta_x^+ u_{i,j} \\ \delta_y^+ u_{i,j} \end{pmatrix}, \tag{3.29}$$

with the discrete forward differences $\delta_{x,y}^+$ as defined in the Appendix (see App. 8.2) this yields the discretized TV. The norm of the x- and y-derivative

can be varied to yield either the isotropic or anisotropic formulation of TV, i.e.

$$\mathrm{TV}_{\mathrm{iso}}(u) = \sum_{i,j} \sqrt{|\delta_x^+ u_{i,j}|^2 + |\delta_y^+ u_{i,j}|^2} \tag{3.30}$$

or

$$\mathrm{TV}_{\mathrm{aniso}}(u) = \sum_{i,j} |\delta_x^+ u_{i,j}| + |\delta_y^+ u_{i,j}|. \tag{3.31}$$

However, it is known that the anisotropic definition of TV yields poor results as it favors horizontal or vertical structures. The numerical definition of TV in reference to different choices for combining gradient directions is still an ongoing research topic (e.g. [47]).

Compressed Sensing

While the principal motivation of investigating suitable image regularizers is to find an abstract description for a general image model this has a strong connection to the concept of *Compressed Sensing* (CS). Compressed sensing was investigated independently by Donoho [48] and Candés [49] around 2004 and states a theory to enable the recovery of signals with sparse representation from incoherent measurements. Interestingly the first numerical and puzzling demonstration was the recovery of a Shepp-Logan from its radially undersampled Fourier-data using TV as sparsifying transform[50] (not mentioning MRI). The principal CS problem for an under-determined system in the MRI reconstruction context, i.e. K is the single-coil Fourier-Operator with the number of randomly sampled Fourier coefficients below the Nyquist limit, writes as

$$\mathrm{u}^\star = \arg\min_u \|\Phi u\|_0, \quad s.t. \ \|Ku - d\|_2^2 \leq \epsilon. \tag{3.32}$$

Here Φ is a suitable sparsifying transform that maps the image u to a representative space that can be described with few coefficients. Popular choices are the Wavelet transformation, trained dictionary patches or the

sparse image gradients (see Fig. 3.4). The "sparsest" solution is measured with the L^0-norm, i.e. the number of non-zero elements, which is an NP-hard problem. This lead to the use of L^1-norm as closest convex surrogate to the L^0 norm, and thus enables an efficient computation of a solution. The unconstrained CS problem with regularization parameter α is then defined as

$$\mathrm{u}^\star = \arg\min_u \frac{1}{2}\|\mathcal{K}u - d\|_2^2 + \alpha\|\Phi u\|_1 \tag{3.33}$$

In order to give any recovery guarantee, the sampling has to fulfill the so-called *restricted-isometry-property* (RIP), that is the sensing matrix K needs to satisfy

$$(1-\delta_k)\|s\|_2^2 \leq \|\mathcal{K}s\|_2^2 \leq (1+\delta_k)\|s\|_2^2 \tag{3.34}$$

where $0 < \delta_k < 1$ is the isometry constant for a k-sparse vector $s = \Phi u, u \in \mathbb{C}^N$, i.e. u can be described with $k << N$ coefficients in the transform domain. Descriptively, this means that a conventional reconstruction of the sparsely sampled signal should result in incoherent noise-like artifacts, which holds for randomly or radially sampled MR data (see Fig. 3.2).
While the construction of image prior models is driven by considerations about penalizing unnatural image features, such as highly disorganized and non-smooth images while conserving jumps at image borders, the theory of CS describes the recovery of image signals under the condition of *sparsity*, *incoherence* through *non-linear reconstruction*. Since both approaches are concerned with equal problems, their basic ideas are strongly connected. In e.g. [51] CS is discussed in the context of image processing, where the "sparse and redundant representation modeling" is described as "a way of synthesizing signals according to a prior defined on the coefficients of this [sparse] representation". It is also worth to note that in many image processing tasks such as denoising, incoherence is implicitly given, while in MRI reconstruction this condition depends on the way the k-space trajectory is designed.
In the further discussion of reconstruction methods in dynamic MRI both view points are taken into account, while in the MRI community the CS

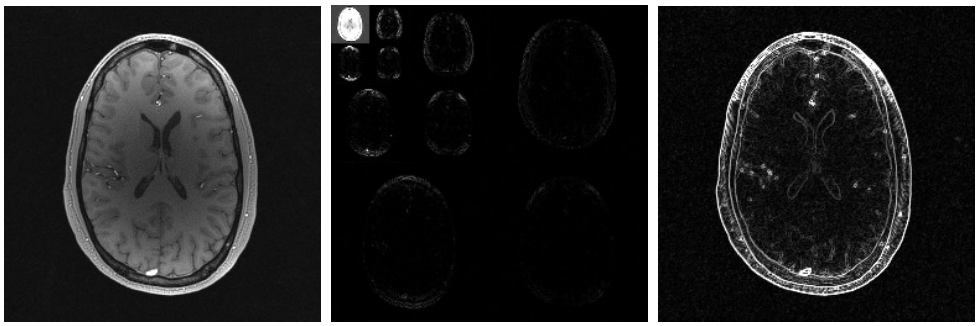

Figure 3.4: Examples for sparse transformations with Wavelets (middle) and spatial gradients (right) of a T_1-weighted MR head image (left).

argumentation prevails. This must be amounted to historical reasons, since the first applications to MRI reconstruction by Block [52] using TV and Lustig [53] using Wavelets were implemented shortly after the establishment of CS theory by Candés and Donoho and the close geographical relation between Donoho and Lustig at Standford University.

3.3.1 Total Generalized Variation

Although the classical choice of TV as image regularization functional enforces piecewise constancy while having a simple convex structurethis leads to the well known *staircasing effect* (e.g. [54]). To overcome this limitation Bredies et al. [55] introduced the concept of *total generalized variation* (TGV) that enables the incorporation of higher-order derivatives up to a certain order and enforces *piecewise smoothness*. This assumption proved to yield enhanced reconstruction quality for natural images in different image processing tasks [56], [57]. A denoising example is provided in Fig. 3.5. In MRI this situation is met for low SNR scenarios but more importantly also for pathological structures embedded in homogeneous tissue.
The definition of the TGV functional of order k with positive weights $\{\alpha_i\}_{i=0,\cdots,k-1}$ is defined in the dual formulation as

$$\mathrm{TGV}_{\alpha}^{k}(u) = \sup\left\{ \int_{\Omega} u \operatorname{div}^{k} v \, dx \mid v \in \mathcal{C}_{c}^{k}(\Omega, \mathrm{Sym}^{k}(U)), \right. \\ \left. \|\operatorname{div}^{l} v\|_{\infty} \leq \alpha_{l}, l = 0, \cdots, k-1 \right\}. \tag{3.35}$$

Here $\mathrm{Sym}^{k}(U)$ is the space of *symmetric tensors* on U and $\mathcal{C}_{c}^{k}(\Omega, \mathrm{Sym}^{k}(U))$ with $\Omega \subset U = \mathbb{C}^{N_x \times N_y}$ the space of compactly supported symmetric tensor fields [58]. $\mathrm{TGV}_{\alpha}^{k}$ defines a convex semi-norm favoring piecewise k-polynomial intensity variations. This definition generalizes TV as $\mathrm{TGV}_{\alpha}^{1}(u) = \alpha \, \mathrm{TV}(u)$. A popular and computationally traceable version, that is also used throughout this work is the *second order* TGV^{2}

$$\mathrm{TGV}_{\alpha}^{2}(u) = \sup\left\{ \int_{\Omega} u \operatorname{div}^{2} v \, dx \mid v \in \mathcal{C}_{c}^{2}(\Omega, \mathrm{Sym}^{2}(U)), \right. \\ \left. \|v\|_{\infty} \leq \alpha_{0}, \|\operatorname{div} v\|_{\infty} \leq \alpha_{1} \right\}. \tag{3.36}$$

In the minimum and discretized representation (see [59]) this writes as

$$\mathrm{TGV}_{\alpha}^{2}(u) = \min_{v} \alpha_{1} \|\nabla u - v\|_{1} + \alpha_{0} \|\mathcal{E} v\|_{1}, \tag{3.37}$$

with $\mathcal{E}$ defining the symmetrized gradient $\mathcal{E}$ on $v = (v_x, v_y) \in U^2$ as $\mathcal{E} v = \frac{1}{2}(\nabla v + (\nabla v)^{T})$

$$(\mathcal{E} v)_{i,j} = \begin{pmatrix} (\delta_{x}^{-} v_{x})_{i,j} & \frac{1}{2}\left[(\delta_{x}^{-} v_{y})_{i,j} + (\delta_{y}^{-} v_{x})_{i,j}\right] \\ \frac{1}{2}\left[(\delta_{x}^{-} v_{y})_{i,j} + (\delta_{y}^{-} v_{x})_{i,j}\right] & (\delta_{y}^{-} v_{y})_{i,j} \end{pmatrix} \tag{3.38}$$

where the numerical *backward differences* are again defined in the Appendix (see App. 8.2).

It is out of the scope of this thesis to provide mathematical rigorous descriptions and definitions for TGV and such that the interested reader is referred to [55]. TGV^2-regularized MRI reconstruction for static images was applied for the first time by Knoll et al. [60] and consecutively to different other MR applications such as non-linear PI reconstruction [61], Diffusion-Tensor imaging [62], PatLoc imaging [63], susceptibility mapping [64], [65], and ASL denoising [66] among others. The following section is now concerned with the concepts for regularization of spatio-temporal data.

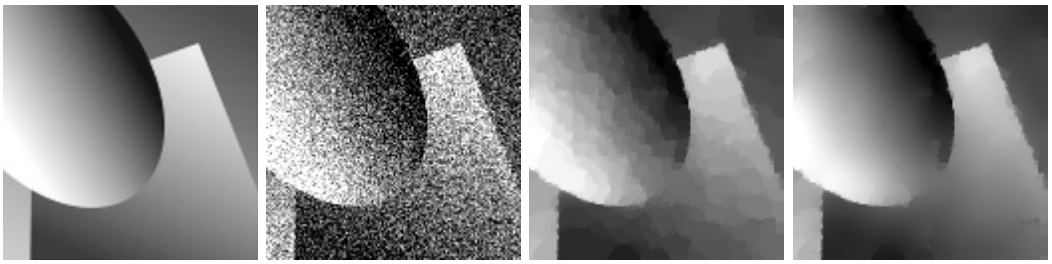

Figure 3.5: Comparison of TV and TGV^2_α models for variational image denoising with L^2-discrepancy from [67]. The TV-denoised image clearly exhibits stair-casing artifacts.

3.3.2 Regularization for spatio-temporal data

Given the definition of spatial TV and TGV it is straightforward to define their spatio-temporal versions by adding the temporal dimension and spatial and temporal weights $\beta = (\mu_x, \mu_y, \mu_t)$ to the gradient and symmetrized gradient in the discretized spatio-temporal domain $\mathcal{U} = \mathbb{C}^{N_x \times N_y \times N_t}$, such that

$$\begin{aligned} \nabla_\beta &: \mathcal{U} \mapsto \mathcal{U}^3 \\ (\nabla_\beta u)_{i,j,t} &= \begin{pmatrix} \mu_x(\delta_x^+ u)_{i,j,t} \\ \mu_y(\delta_y^+ u)_{i,j,t} \\ \mu_t(\delta_t^+ u)_{i,j,t} \end{pmatrix} \end{aligned} \tag{3.39}$$

$$\mathcal{E}_\beta : v = (v_x, v_y, v_t) \in \mathcal{U}^3 \mapsto \mathcal{U}^6$$
$$(\mathcal{E}_\beta v)_{i,j} = \begin{pmatrix} \mu_s(\delta_x^- v_x)_{i,j,t} \\ \mu_s(\delta_y^- v_y)_{i,j,t} \\ \mu_t(\delta_t^- v_t)_{i,j,t} \\ \frac{1}{2}\left[\mu_y(\delta_y^- v_x)_{i,j,t} + \mu_x(\delta_x^- v_y)_{i,j,t}\right] \\ \frac{1}{2}\left[\mu_t(\delta_t^- v_x)_{i,j,t} + \mu_x(\delta_x^- v_t)_{i,j,t}\right] \\ \frac{1}{2}\left[\mu_t(\delta_t^- v_y)_{i,j,t} + \mu_y(\delta_y^- v_t)_{i,j,t}\right] \end{pmatrix} \tag{3.40}$$

Note that in the definition of $\mathcal{E}_\beta$ the dimension was reduced since the symmetric elements are counted only once in order to reduce the computational burden which has to be accounted for the corresponding norms. By applying the resulting TV_β or TGV^2_β regularization functionals to spatio-temporal data it can expected to obtain good results for image sequences that are piecewise constant, resp. piecewise smooth in space and time. However, it is not clear how to choose the temporal weighting μ_t since it depends on the local temporal evolution of a pixel in time in correspondence with the spatial weighting. For the later it is clear since the discretized voxel-sizes are given trough the defined measurement matrix. Furthermore, in [68] it is pointed out that the "human eye is for example very sensitive to brightness variations in time on a stable background", which is an indication that for image sequences different considerations as for static images must be taken into account, which is also an open topic within the image processing community. Especially the extension of TV to the temporal domain was not found suitable to not provide such a realistic model for dynamic data [69]. In [70] an approach is presented by regularizing only the static background of an image sequence after separation into foreground and background.
This already aimed in the direction of dynamic image separation with *low-rank and sparse* decomposition based approaches, that also became very popular for MRI reconstruction. Prior to low-rank and sparse decomposition, many different regularization approaches for dynamic MRI applications were used based on CS. Due to the quasi-periodic nature in cardiac imaging the *temporal Fourier transform* was used as sparsifying transform in the *k-t-FOCUSS* [71] and *k-t-SPARSE-SENSE* [72] method. Wavelet based spatio-temporal regularization [73], spatio-temporal finite differences [74]

or combinations of these, e.g. *k-t-SPARSE* [75] or [76], have also been successfully applied for this application.
Even though the temporal Fourier transformation turned out to be a suitable choice for periodic applications, such as cardiac cine imaging, limitations were reported for the non-periodic setting, such as dynamic contrast-enhanced (DCE) applications. In [77], Liang proposed to reconstruct undersampled dynamic data by exploiting a representation with a low number of temporal basis functions trained with singular value decomposition from fully sampled low resolution data. This method was the basis for following work as described in [78], [79], employing principal component analysis (PCA), and more recently, in [80], to efficiently reconstruct dynamic data. Using PCA as sparsifying transform was also discussed in [76], [81].
The exploration of data driven sparsifying transforms, as with PCA, assumes that the dynamic data lies in a low dimensional subspace, i.e., that an appropriate matrix representation of the image sequence is of low rank. Mathematical foundations of low-rank matrix recovery from undersampled data were studied in [82], where the nuclear norm is used as convex relaxation of the non-convex low-rank constraint. The image series is organized in a matrix with $N = N_x \times N_y$ rows with the spatial information and $M = N_t$ columns with the temporal frames. The nuclear norm is defined for $u \in \mathbb{C}^{N\times M}$ as

$$\|u\|_\star = \sum_{n}^{\min(M,N)} \sigma_n \tag{3.41}$$

where σ_n are the singular values of the singular-value decomposition of u. Recovery guarantees can again be stated under restricted isometry properties. One of the first applications of such a regularization to dMRI reconstruction was reported in [83], where the connection to the earlier work of [77] was pointed out.
In consequence to former findings of using sparsity constraints for dMRI reconstructions, a joint combination of sparsity and low-rank constraints on dMRI data was developed in [84]–[86]. In [84], non-convex Schatten p-quasi-norms were suggested as improvement to the nuclear norm, which, due to non-convexity, impose more difficulties to computing a robust numerical solution.

In [87], [88] a decomposition into low-rank and sparse component (L+S) was proposed which is also referred to as *robust PCA*. This was applied in [89], [90] and [91] (*k-t-RPCA*) to dMRI reconstruction, explicitly in combination with PI in [90]. The corresponding reconstruction problem with weights for the low-rank component λ_L and sparse component λ_S reads as follows:

$$\mathrm{u}^\star = \arg\min_{L,S} \frac{1}{2}\|\mathcal{K}u - d\|_2^2 + \lambda_L\|L\|_\star + \lambda_s\|\Phi S\|_1 \quad s.t. \quad u = L + S. \tag{3.42}$$

In [90], the authors argue that L+S is a natural choice for dynamic data as it models innovations on top of a highly correlated background and is therefore applicable for all kind of dMRI applications. Actually, these models require a global and explicit separation of dynamic data and background. Such a separation is, however, not generally applicable and recent works employ a patch-based decomposition to locally improve reconstruction quality [92]–[94] with increased computational complexity. In [94] for instance, patches are generated from an initial dynamic CS reconstruction via motion tracking, followed by a patch-based low-rank reconstruction, yielding further improvements in image quality. In contrast to that Holler et al. [95] addressed the problem of extending the concept of total variation type functionals to the dynamic setting.

3.3.3 Infimal Convolution of Total Generalized Variation

To illustrate the concept of *Infimal Convolution of Total Generalized Variation* (ICTGV) we first consider again the spatio-temporal TV_β functional defined as

$$TV_\beta(u) = \sum_{i,j,t} \sqrt{|\mu_s \delta_x^+ u_{i,j,t}|^2 + |\mu_s \delta_y^+ u_{i,j,t}|^2 + |\mu_t \delta_t^+ u_{i,j,t}|^2} \tag{3.43}$$

and $\beta = (\mu_s, \mu_t)$, the ratio $\frac{\mu_t}{\mu_s}$ fixes the space-time scaling and leads to a temporal regularization proportional to this ratio. As this ratio cannot be defined in advance, it must be tuned to adapt to the specific regularization

properties. For typical dMRI datasets, however, a uniform choice is difficult due to locally contradicting requirements. Different parts of a dynamic data set may require either a stronger spatial *or* stronger temporal regularization depending on the dynamic properties of the investigated region. Defining $\beta_1 = (\mu_{1,s}, \mu_{1,t})$ and $\beta_2 = (\mu_{2,s}, \mu_{2,t})$ with either large or small space-time ratio, i.e. $\frac{\mu_{1,t}}{\mu_{1,s}} > 1$ and $\frac{\mu_{2,t}}{\mu_{2,s}} < 1$, Holler et al. proposes to employ the *infimal convolution* of the two differently spatio-temporally weighted functionals TV_{β_1} and TV_{β_2}, i.e.

$$\mathrm{ICTV}_{\beta,\gamma}(u) = \min_v \ \mathrm{TV}_{\beta_1}(u - v) + \mathrm{TV}_{\beta_2}(v). \tag{3.44}$$

Since TV_{β_1} emphasizes piecewise regularity in space and time, while allowing more deviation in time, TV_{β_2} acts the other way around. The combination of these two limiting cases via infimal convolution, yields an automatic separation into components $(u - v)$ and v, where either one of the requiring conditions is fulfilled.
To avoid the introduction of staircasing artifacts of TV regularization, balancing between two differently weighted second-order spatio-temporal TGV^2 functionals is employed, defining the second order ICTGV^2 functional with weighting parameters $\{\gamma_1, \beta_1, \gamma_2, \beta_2\}$ as

$$\mathrm{ICTGV}^2_{\beta_{1,2},\gamma_{1,2}}(u) = \min_v \ \gamma_1 \, \mathrm{TGV}^2_{\beta_1}(u - v) + \gamma_2 \, \mathrm{TGV}^2_{\beta_2}(v) \tag{3.45}$$

with the definition of TGV^2 as in Eq. 3.37 and the definition of the weighted gradient and symmetrized gradient as in Eq. 3.39 and 3.40.
It was shown in [68] that ICTGV^2 yields an analytically well defined convex regularization functional that, in the setting of differently weighting temporal and spatial derivatives, is invariant with respect to translations and rotations in space. Numerically, the solution of ICTGV^2 regularized inverse problems can be carried out with the same techniques as for TV regularization, only the number of variables increases. Particularly for convex data fidelity term - such as the one resulting from MR modeling - state of the art duality based optimization algorithms can be applied and the approximation of globally optimal solutions can be assured. With the established definitions of the dynamic MR data fidelity and regularization functionals

it is now possible to put these ingredients together and describe the main reconstruction problem of this thesis.

3.3.4 Spatio-Temporal Variational Regularization for Dynamic MRI Reconstruction

The application of $\mathrm{ICTGV}^2_{\gamma,\beta}$, TGV^2_{β} and TV_{β} regularization for reconstruction of accelerated dynamic MRI with the defined dMRI forward operator $\mathcal{K}$ in Eq. 3.24 amounts to solve the following minimization problems:

$$\mathrm{u}^\star \in \arg\min_u \frac{\lambda}{2}\|\mathcal{K}u - d\|_2^2 + \mathrm{TV}_{\beta}, \tag{3.46}$$

$$\mathrm{u}^\star \in \arg\min_u \frac{\lambda}{2}\|\mathcal{K}u - d\|_2^2 + \mathrm{TGV}_{\beta}, \tag{3.47}$$

$$\mathrm{u}^\star \in \arg\min_u \frac{\lambda}{2}\|\mathcal{K}u - d\|_2^2 + \mathrm{ICTGV}^2_{\gamma,\beta}\,. \tag{3.48}$$

These minimization problems are non-smooth but convex and can be solved by a first-order duality based method that is outlined in the section 3.5 after the description of model parameter normalization.

3.3.5 Model and regularization parameters

Variational methods use a *regularization parameter*, denoted by λ in Equ. 3.48, that weights data fidelity versus regularization and should be chosen according to the expected noise level. In addition to that, the proposed regularization functional encompasses several weighting parameters $\{\alpha_0, \alpha_1, \gamma_1, \beta_1, \gamma_2, \beta_2\}$ that define a model of the expected image structure (*model parameters*).

Regularization parameter: Given a fixed set of model parameters only the choice of one regularization parameter remains. This choice should depend

on the SNR, the number of voxels, time frames and, the subsampling rate of the MR data. Concerning the later, the cost of the data fidelity term decreases linearly with the subsampling ratio, since the forward operator maps only to sampled data. Based on this observation the regularization parameter is defined as a linear function of the *subsampling or reduction factor* r, i.e., $\lambda(r) = ar + b$, and hence need to fix the slope a and intercept b. A further adaption to the noise level and image dimension is possible but omitted for the sake of simplicity.

Model parameters: The parametrization of the regularization functional is performed in a way that a variation of the model parameter does not influence the overall trade-off between regularization and data fidelity. Hence, the model parameters must be chosen only once for an expected image structure, e.g. CINE cardiac imaging, and remain unaffected from the noise level and subsampling ratio of subsequent measurements.
The first parameter that is inherent to TGV^2 regularization is the ratio $\frac{\alpha_1}{\alpha_0}$ that defines the weighting of the different orders of differentiation. Previous TGV^2 imaging applications and studies found that fixing this ratio to $\frac{1}{\sqrt{2}}$ yields a robust choice [56], [96], which is used throughout this work.

Concerning the weighing parameters $\{\gamma_1, \beta_1, \gamma_2, \beta_2\}$ in Eq. 3.45 the ICTGV^2 functional can be rewritten as

$$\text{ICTGV}^2_{s,t_1,t_2}(u) = \min_v \gamma_1(s)\,\text{TGV}^2_{\beta(t_1)}(u-v) + \gamma_2(s)\,\text{TGV}^2_{\beta(t_2)}(v). \quad (3.49)$$

Thus, only three parameters remain to be fixed: $s \in [0,1]$ defines the weights $\gamma_i(s)$ of the first and the second TGV^2 functional and $t_i \in (0,\infty)$ define two different weightings $\beta(t_1)$, $\beta(t_2)$ of the temporal versus the spatial derivative. The functions $\gamma_i(\cdot)$ are chosen with the intention of not influencing the trade-off between data fidelity and regularization as follows:

$$\gamma_1(s) := \frac{s}{\min(s, 1-s)}, \quad \gamma_2(s) := \frac{1-s}{\min(s, 1-s)}\,.$$

In contrast to a straightforward convex combination, i.e. s and $(1-s)$, this ensures that the overall cost of the functional does not reduce to zero as s

comes close to zero or one. The smaller of the two factors $\gamma_1(s)$ and $\gamma_2(s)$ always equals one and hence s allows to balance between the $\mathrm{TGV}^2_{\beta(t_i)}$ functionals without reducing or increasing the overall cost of $\mathrm{ICTGV}^2_{s,t_1,t_2}$.
In order to normalize the weighting between spatial and temporal regularization we pursue the following approach: Given again weights μ_s and μ_t of the spatial and temporal derivative, respectively, we require that integrating the resulting vector norm on the gradient over all possible directions gives the same results as the standard Euclidean norm. This amounts to fix

$$1 = \frac{1}{2\pi} \int_0^{\pi} \int_0^{2\pi} \sqrt{(\mu_s \sin\theta \cos\varphi)^2 + (\mu_s \sin\theta \sin\varphi)^2 + (\mu_t \cos\theta)^2}\, \mathrm{d}\varphi\, \mathrm{d}\theta$$

and provides the spatial and temporal weights as function of their ratio, i.e. $(\mu_s, \mu_t) = \beta(t)$, with a given ratio $t = \frac{\mu_t}{\mu_s} \in (0, \infty)$. The thus defined model parameters $\{s, t_1, t_2\}$ define a unique *decomposition* into two components $(u - v)$ and v as defined in Equ. 3.49.

3.4 Decomposition into components

The definition of the ICTGV^2 model parameters yields a new approach for a decomposition into two components that reflect *locally* different requirements for stronger or weaker temporal regularity, between the two extremes defined with $\beta(t_1)$ and $\beta(t_2)$. Additionally, it is possible to weight the two spatio-temporal regularization functionals with $\gamma(s)$. It is intuitively clear that a set of model parameters will depend on the type of dynamic modality, e.g. cardiac functional or dynamic contrast enhanced MRI. However, within the application model parameterers are fixed and thus represent an general selection strategy for a given modality, reflecting generic spatio-temporal behavior.
Fixation of the model parameters is realized by grid-search for a defined parameter range and evaluation against constructed ground-truths (see Sec. 3.6), either from numerical phantoms or fully-sampled measurements. Training was performed over heuristic ranges for $t_1 \in \{1, 2, \cdots, 9\}$, $t_2 \in \{0.25, 0.5, 1, 2, 3\}$ and $s \in \{0.2, 0.3577, 0.5, 0.6423, 0.8\}$. Figure 3.6 exemplary shows the "energy", i.e. the sum over all pixel intensities, of the

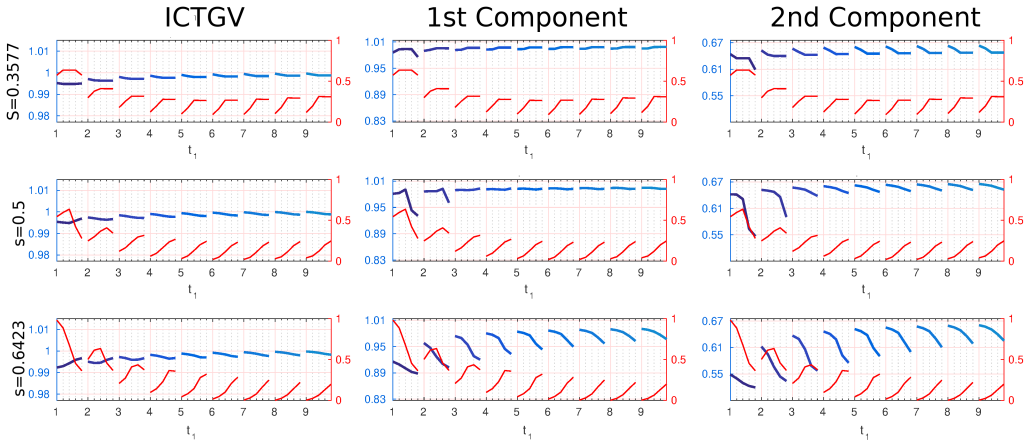

Figure 3.6: Energy (blue) and normalized RMSE (red) of ICTGV (first column) reconstruction, component 1 $(u - v)$ (second column) and component 2 (v) (third column)for different model parameter choices ($s \in \{0.3577, 0.5, 0.6423\}$, $t_1 \in \{1, 2, \cdots, 9\}$ and $t_2 \in \{0.25, 0.5, 1, 2, 3\}$) computed from undersampled reconstruction of numerical DCE phantom data ([97]).

components together with the reconstruction error in terms of root-mean-squared-error (RMSE) for a numerical DCE phantom. Although "optimal" parameters can be derived in terms of lowest RMSE, it is apparent that actually a set of optimal parameters with minor deviations in error norm can be given. Thus, it is possible to achieve similar overall reconstruction results, with the possibility to alter the information content in the two different components.

In Fig. 3.7 an optimal choice for model parameterers is given for the application to perfusion MRI as treated in Chap. 5 in comparison to a L+S decomposition. Similar to L+S, a decomposition in tracer kinetic and structural information is achieved but with higher differentiation into faster and slower tracer characteristics. The investigation of potentially diagnostic information from varying decompositions is subject to future research. It is also notable that ICTGV can be extended to yield a decomposition into an arbitrary number of components, with the drawback of increased computational complexity. Also, ICTGV model parameters can be tuned to yield a L+S like decomposition.

3.5 Numerical Solution

As pointed out, the numerical optimization problem that needs to be solved is convex yet non-smooth. Convex optimization became increasingly important with the growing number of optimization problems and computational power. While the convex and smooth PI problems are most efficiently solved with the *conjugate gradient* (CG) method, most of the CS problems like k-t-SPARSE-SENSE or L+S can be solved with the *fast iterative soft-thresholding algorithm* (FISTA) introduced by Beck and Teboulle [98]. It is essentially a proximal gradient method that uses the unitary of the sparsifying transform which holds for Fourier and Wavelet transformation. The derivative operation is not unitary such that often a ϵ-smoothed version of TV is employed that reduces the problem from convex but non-smooth to convex and smooth. Luckily the watershed in optimization is between non-convex and convex optimization, where for the later it is possible to derive convergence guarantees and rates.
A working horse to solve the dMRI ICTGV problem is the primal-dual splitting algorithm investigated by Chambolle and Pock [99]. With this algorithm it is possible to compute solutions for a generic problem description that reads as

$$\min_x F(Hx) + G(x), \tag{3.50}$$

and corresponds to the *saddle-point problem* that is formulated with the use of *convex conjugate* (definition see App. 8.1) as follows

$$\min_x \max_y \; < Hx, y > - F^\star(y) + G(x). \tag{3.51}$$

Here $G : \mathbb{C}^n \mapsto \mathbb{R}^+$ and $F : \mathbb{C}^n \mapsto \mathbb{R}^+$ are convex functions with its convex conjugate $F^\star$ and H is a continuous linear operator. In [99] the authors define the following iterative update rules with dual and resp. primal step-sizes σ and τ:

$$\begin{aligned} &\tau\sigma\|H\|_2 < 1, \theta \in [0,1]\,, \text{update } x^n, y^n, \bar{x}^n : \\ &\begin{cases} y^{n+1} &= (Id + \sigma\partial F^\star)^{-1}(y^n + \sigma H\bar{x}^n) \\ x^{n+1} &= (Id + \tau\partial G)^{-1}(x^n - \tau H^H y^{n+1}) \\ \bar{x}^{n+1} &= x^{n+1} + \theta(x^{n+1} - x^n). \end{cases} \end{aligned} \tag{3.52}$$

$(Id + \tau\partial G)^{-1}$ and $(Id + \tau\partial F^\star)^{-1}$ are the *proximal mapping* operators on $F^\star$, resp. G and H^H is the hermitian adjoint operator to H. The definitions of the convex conjugate and proximal mappings are given in the Appendix (see App. 8.1). It is now necessary to cast the optimization problems defined in Eq. 3.46, Eq. 3.47, and Eq. 3.48 in the form of Eq. 3.50, which is exemplary carried out for ICTGV^2. With the definitions of the 2d-time gradients and symmetrized gradients and corresponding norms that can be found in the Appendix (see App. 8.3) the full optimization problem writes as:

$$\begin{aligned} &\min_{u,w_1,v,w_2} \frac{\lambda}{2}\|\mathcal{K}u - d\|_2^2 \\ &+ \gamma_1(s)\left(\alpha_1\|\nabla_{\beta(t_1)}(u - v) - w_1\|_1 + \alpha_0\|\mathcal{E}_{\beta(t_1)}w_1\|_1\right) \\ &+ \gamma_2(s)\left(\alpha_1\|\nabla_{\beta(t_2)}v - w_2\|_1 + \alpha_0\|\mathcal{E}_{\beta(t_2)}w_2\|_1\right). \end{aligned} \tag{3.53}$$

It is our goal to obtain a saddle-point or primal-dual problem as in Eq. 3.50 that is equivalent to our original problem. To this aim, first note that ICTGV can be reformulated as

$$\text{ICTGV}^2_{\beta,\gamma}(u) = \min_{x=(u,w_1,v,w_2)} \|H_1 x\|_{1,\alpha,\gamma}$$

with

$$H_1 = \begin{pmatrix} \nabla_{\beta(t_1)} & -\text{Id} & -\nabla_{\beta(t_1)} & 0 \\ 0 & \mathcal{E}_{\beta(t_1)} & 0 & 0 \\ 0 & 0 & \nabla_{\beta(t_2)} & -\text{Id} \\ 0 & 0 & 0 & \mathcal{E}_{\beta(t_2)} \end{pmatrix}, \tag{3.54}$$

and

$$\|(p_1, q_1, p_2, q_2)\|_{1,\alpha,\gamma} = \gamma_1(s)\left(\alpha_1\|p_1\|_1 + \alpha_0\|q_1\|_1\right) + \gamma_2(s)\left(\alpha_1\|p_2\|_1 + \alpha_0\|q_2\|_1\right)$$

representing a weighted L^1 norm. Furthermore, the convex conjugates of $\|\cdot\|_{1,\alpha,\gamma}$ and $\frac{\lambda}{2}\|\cdot - d\|_2^2$ are required and are given for $z = (p_1, q_1, p_2, q_2)$ as

$$\|z\|_{1,\alpha,\gamma}^* := \sup_{z'} \; < z, z' > - \|z'\|_{1,\alpha,\gamma} = \mathcal{I}_{\{\|\cdot\|_{\infty,\alpha,\gamma}\leq 1\}}(z),$$

where

$$\mathcal{I}_{\{\|\cdot\|_{\infty,\alpha,\gamma}\leq 1\}}(z) = \begin{cases} 0 & \text{if } \max\{\gamma_1\alpha_1\|p_1\|_\infty, \gamma_1\alpha_0\|q_1\|_\infty, \gamma_2\alpha_1\|p_2\|_\infty, \gamma_2\alpha_0\|q_2\|_\infty\} \leq 1, \\ \infty & \text{else,} \end{cases}$$

and

$$(\frac{\lambda}{2}\|\cdot - d\|_2^2)^*(r) := \sup_{r'} \; < r', r > - \frac{\lambda}{2}\|r' - d\|_2^2 = \frac{1}{2\lambda}\|r\|_2^2 + < d, r > .$$

The expression $\mathcal{I}_{\{\|\cdot\|_{\infty,\nu}\leq 1\}}$ is an abbreviation for the convex indicator function of the set $\{q \in U \mid \|q\|_\infty \leq 1\}$. Then, a formulation equivalent with the minimization problem in 3.53 is obtained as

$$\begin{aligned}
&\min_u \frac{\lambda}{2}\|\mathcal{K}u - d\|_2^2 + \mathrm{ICTGV}^2_{s,t_1,t_2}(u) \\
\Leftrightarrow &\min_{x=(u,w_1,v,w_2)} \frac{\lambda}{2}\|Ku - d\|_2^2 + \|H_1 x\|_{1,\alpha,\gamma} \\
\Leftrightarrow &\min_{x=(u,w_1,v,w_2)} \max_{y=(z,r)} < \mathcal{K}u, r > - < d, r > - \frac{1}{2\lambda}\|r\|_2^2 + < H_1 x, z > - \mathcal{I}_{\{\|\cdot\|_{\infty,\alpha,\gamma}\leq 1\}}(z) \\
\Leftrightarrow &\min_{x=(u,w_1,v,w_2)} \max_{y=(z,r)} < Hx, y > - < d, r > - \frac{1}{2\lambda}\|r\|_2^2 - \mathcal{I}_{\{\|\cdot\|_{\infty,\alpha,\gamma}\leq 1\}}(z) \\
\Leftrightarrow &\min_{x=(u,w_1,v,w_2)} \max_{y=(z,r)} < Hx, y > - F^*(y).
\end{aligned}$$

with $H = \begin{pmatrix} H_1 \\ K_1 \end{pmatrix}$, $K_1 x = \mathcal{K}u$, $G \equiv 0$ and

$$F^*(y) = F^*(z, r) = < d, r > + \frac{1}{2\lambda}\|r\|_2^2 + \mathcal{I}_{\{\|\cdot\|_{\infty,\alpha,\gamma}\leq 1\}}(z),$$

the convex conjugate of $F(y) = F(z,r) = \frac{\lambda}{2}\|r-d\|_2^2 + \|z\|_{1,\gamma,\beta}$.

In the update-scheme of the primal-dual algorithm also the adjoint of H_1 and K are required. While the adjoint of K is given in the Appendix (see App.8.3.3) the adjoint of H_1 with the definitions of the divergences given in App. 8.3 reads as:

$$H_1^H = \begin{pmatrix} \operatorname{div}_{\beta_1}^1 & 0 & 0 & 0 \\ -\mathrm{Id} & \operatorname{div}_{\beta_1}^2 & 0 & 0 \\ -\operatorname{div}^1 \beta_1 & 0 & \operatorname{div}_{\beta_2}^1 & 0 \\ 0 & 0 & -\mathrm{Id} & \operatorname{div}_{\beta_2}^2 \end{pmatrix}. \tag{3.55}$$

For the case of TGV_β, TV_β or $ICTV_{s,t_1,t_2}$ the considerations can be carried out in the same manner such that only H_1 needs to be redefined as

$$H_1^{\mathrm{tv}} = \nabla_\beta, \tag{3.56}$$

$$H_1^{\mathrm{tgv}} = \begin{pmatrix} \nabla_\beta & -\mathrm{Id} \\ 0 & \mathcal{E}_\beta \end{pmatrix}, \tag{3.57}$$

$$H_1^{\mathrm{ictv}} = \begin{pmatrix} \nabla_{\beta_1} & -\nabla_{\beta_1} \\ 0 & \nabla_{\beta_2} \end{pmatrix}. \tag{3.58}$$

The final update schemes for the corresponding algorithms for TV_β (Alg. 3), TGV_β (Alg. 4), $\mathrm{ICTV}_{\beta,\gamma}$ (Alg. 5), and $\mathrm{ICTGV}^2_{\beta,\gamma}$ (Alg. 6), as well as the corresponding proximal mappings for F^* (App. 8.3.2) are described in the algorithm section of the Appendix 8.5.

3.5.1 A Primal-Dual Implementation of k-t-SPARSE-SENSE and L+S Reconstruction

It is also straight forward to restate the *k-t-SPARSE-SENSE* reconstruction method using temporal differences, i.e.

$$H_1^{\text{ktss}} = \partial_t, \tag{3.59}$$

in the same manner with only minor changes. It is also convenient to use the primal-dual algorithm for solving the L+S reconstruction problem with temporal differences as follows.

$$\begin{aligned} &\min_{L,S} \frac{1}{2}\|\mathcal{K}(L+S) - d\|_2^2 + \lambda_S \|\partial_t S\|_1 + \lambda_L \|L\|_\star \\ \Leftrightarrow &\min_{x=(L,S)} \max_{y=(z,r)} < Hx, y > -F^*(y) + G(x). \end{aligned} \tag{3.60}$$

with $H^{L+S} = \begin{pmatrix} \mathcal{K} & \mathcal{K} \\ 0 & \partial_t \end{pmatrix}$, $G = \lambda_L \|L\|_\star$ and

$$F^*(y) = F^*(z,r) =< d, r > + \frac{1}{2\lambda}\|r\|_2^2 + \mathcal{I}_{\{\|\cdot\|_{\infty,\lambda_S} \leq 1\}}(z).$$

Note, that with a change of variables $u = L + S$ it is also possible to write Eq. 3.60 in a infimal convolution type reconstruction problem, i.e.

$$\min_{u,L} \frac{1}{2}\|\mathcal{K}u - d\|_2^2 + \lambda_S \|\partial_t(u - L)\|_1 + \lambda_L \|L\|_\star. \tag{3.61}$$

The proximal mapping for $(Id + \tau\partial G)^{-1}$ has to be computed, which can be obtained as soft-thresholding on the singular values of the low-rank component L and is defined in the Appendix (8.3.2). Both corresponding algorithms were implemented for comparison purpose and are also given in the Appendix: Primal-Dual k-t-SPARSE-SENSE (Alg. 1) and Primal-Dual-Low-Rank-Sparse (Alg. 2).

3.5.2 Step Sizes

The algorithms described above converge with convergence order of $\mathcal{O}(1/k)$ as long as the primal and dual step-sizes σ and τ fulfill $\sigma\tau\|H\|_2 \leq 1$. However it is desirable to make as large steps as possible for fast convergence. The step-sizes can either be set constant after estimation of $\|H\|_2$, where the part given by the gradient and symmetrized gradient can be estimated as in [55] like $\|\nabla\|_2, \|\mathcal{E}\|_2 \leq \sqrt{8}, \sqrt{12}$ and the varying part of the MR-Operator can be accessed via power iterations. In the current implementation an adaptive step-size choice as described in [57] is employed. The adaptive choice still ensures convergence but potentially allows larger step-sizes and hence accelerates convergence. This is realized by the mapping $\mathcal{S}$, which for $\theta \in (0, 1)$ and

$$n = \frac{\|(\bar{x}) - x\|_2}{\|H(\bar{x} - x)\|_2}$$

is defined as

$$\mathcal{S}(\sigma\tau, \mathfrak{n}) = \begin{cases} \mathfrak{n} & \text{if } \sqrt{\theta\sigma\tau} \geq \mathfrak{n}, \\ \sqrt{\theta\sigma\tau} & \text{if } \sqrt{\sigma\tau} \geq \mathfrak{n} > \sqrt{\theta\sigma\tau}, \\ \sqrt{\sigma\tau} & \text{else.} \end{cases} \tag{3.62}$$

In [100] an adaption of the used primal-dual algorithm with line-search is proposed, that was also implemented but lead to the same convergence speed as the strategy with step-size adaption.

3.5.3 Primal-Dual Gap

The convergence proof of the general algorithm in [99] is based on the *primal-dual gap*. To monitor the rate of convergence a modified primal-dual gap is introduced as in [57], that in the case of ICTGV^2 reconstruction is given for $x = (u, v, w_1, w_2)$ and $y = (r, p_1, p_2, q_1, q_2)$ as:

$$\begin{aligned}\mathcal{G}(x_n, y_n) =& F(Hx_n) + < d, r > + \frac{1}{2\lambda}\|r\|_2^2 \\ &+ \sum_{i,j,t} |(-\operatorname{div}^1 p_1 - K^H r)_{i,j,t}| + \sum_{i,j,t} |(-p_1 - \operatorname{div}^2 q_1)_{i,j,t}| \\ &+ \sum_{i,j,t} |(-\operatorname{div}^1 p_1 - \operatorname{div}^1 p_2)_{i,j,t}| + \sum_{i,j,t} |(-p_1 - \operatorname{div}^2 q_2)_{i,j,t}|.\end{aligned} \tag{3.63}$$

3.5.4 GPU implementation

A major obstacle of advanced reconstruction methods are the prolonged computation times due to the algorithms complexity. A drawback of the employed primal-dual algorithm is the need to introduce dual variables that consume additional memory. In order to reduce reconstruction times the MATLAB prototype was translated to C++/CUDA enabling highly parallel GPU computations. As a consequence, the computational speed was improved drastically with up to 50-fold acceleration. Table 3.1 summarizes reconstruction times for typical data dimensions and a fixed number of iterations. According to the experience 500 iterations are sufficient for the primal-dual gap to indicate a voxel-wise error in the range of $[10^{-5}, 10^{-2}]$. The CUDA framework, termed AVIONIC[1] is able to perform all of the above described dynamic reconstructions as well as reconstruction for static 2D and 3D TGV^2 regularization.

3.6 Evaluation and validation

Evaluation of the reconstruction quality of MR images and validation of newly proposed reconstruction methods is a critical task for different reasons. However, it is complicated to establish a suitable ground-truth, i.e. a MRI scan of the investigated modality with high SNR and possibly no

[1] GNU GPLv3 license https://github.com/IMTtugraz/AVIONIC

Table 3.1: ICTGV reconstruction times in seconds (500 iterations), obtained with a MATLAB CPU implementation (Intel i5-2500K, 3.30GHz) and a CUDA GPU implementation (NVidia GeForce GTX 770), for different data-dimensions (3rd to 5th column) denoted as (N_x, N_y, N_t, N_c). The top rows depict the time in seconds to perform 500 iterations while the bottom rows show the total reconstruction time including coil sensitivity estimations.

Device		$(128, 128, 40, 12)$	$(416, 168, 25, 32)$	$(256, 216, 32, 30)$
CPU	Iterations	1325.38	5783.43	8919.39
	Total	1365.86	6238.18	9355.47
GPU	Iterations	34.54	134.34	199.33
	Total	39.73	176.61	244.61

measurement- or motion related artifacts. This is even more complicated for the dynamic MR applications due to the inherent temporal limitations, e.g. breath-hold for cardiac imaging. The construction MR phantoms for dynamic applications is also quite challenging. On the numerical side, many approaches exist to synthesize MR data on the sequence simulation basis like MRiLab [101] or JEMRIS [2]. However, these are limited to static MRI acquisition. For dynamic applications numerical phantoms were constructed in image space based on established scanning procedures, e.g. MRXCAT [97] for cardiovascular applications or for perfusion [102]. In that case one often faces so called *inverse crimes*, i.e. when the same discrete model is used for generating and reconstructing the data, from an actually infinite-dimensional quantity as outlined in Sec. 3.1.1. An approach to overcome this problem was presented in [103].
Secondly, the question remains what could be a suitable metric to rate medical images, where the end point is the diagnostic relevant information that could be of large or very tiny extend. Global measures like pixel-wise (RMSE) are not suitable to capture that information and furthermore do not take considerations about the human perception of images into account. The later problem triggered many attempts to investigate metrics based on the *human visual system* (HVS). Among these the structural-similarity index (SSIM) [104], [105] evolved to a sophisticated and accepted standard among

[2] http://www.jemris.org

image quality metrics [106].
However, emphmedical images, inherit far more complex information, as the general HVS is assuming, such that only skilled radiologists with many hours of training are capable of identifying pathological information[3]. This boils down to the problem of how advanced reconstruction methods need to be evaluated, since the prior knowledge introduced in form of regularization is constructed in a way to enforce *typical* image structures and not particularly *typical medical* image structures, which of course can not be specified easily. The eligible concern is that medical image information might be lost while achieving good reconstruction quality in terms of "nicely" looking images. On the other hand the difference in natural and medical images needs to be proven by carrying out extensive clinical studies. A selection of studies performed with CS methods can be found in [107].These observations and the still prolonged and/or computationally expensive reconstruction times are the major drawbacks of constrained reconstruction that impedes the clinical applicability.
Increased pressure for the technological transfer was built up for applications that strongly required acceleration to be applicable in the first place. Parallel imaging reconstruction was translated quite quickly to e.g. cardiac functional imaging to achieve acquisition times in breath-hold-duration. The supposed advantage of PI was that the reconstruction is still linear and translates the noise in well-behaved manner but results in a spatially variable noise enhancement, known as g-factor [28], that is effectively the main limitation for further acceleration. The g-factor that is accessible analytically can also provide a useful confidence measure. Advanced regularization is able to effectively suppress the noise enhancement an thus enables higher acceleration potential. As outlined in Sec. 3.1.4, the reconstruction as probability density would also provide such a confidence measure, but is hard to achieve. An alternative approach is the *pseudo-replica* approach [108] to access a reliability measure from non-linear filter responses and can also be used to gain MR reconstruction in SNR units as proposed by Kellman and Hansen et al. [109], [110].
The pseudo-replica approach roughly approximates the posterior distribution $p(u|d)$ by computing the reconstruction several times with varying

[3]Ehman, "What a radiologist sees" http://cds.ismrm.org/protected/DataSampling13/Program/talks/30800/

noise-inputs but equivalent noise standard deviation. Afterwards the SNR units are given by computing the mean $< u >$and standard-deviation σin each voxel, such that the real voxel-wise SNR can be defined by

$$\mathrm{SNR} = \frac{< u >}{\sigma}. \tag{3.64}$$

The g-facor map is then defined for an acceleration factor r as

$$g = \frac{\mathrm{SNR}_{\mathrm{unacc}}}{\sqrt{r}\,\mathrm{SNR}_{\mathrm{acc}}} \tag{3.65}$$

Fig. 3.8 exemplary shows g-factor maps and SNR unit reconstructions for linear (CG-SENSE) and ICTGV-regularized reconstructions for a numerical MRXCAT cine-cardiac dataset [97] with regualar undersampling pattern and different target SNR. The g-factor map indicates that a almost 100-fold suppression of noise is achieved with ICTGV, while leading to more uncertainty at morphological boundaries. For lower target SNR g-factor structures as visible for the linear reconstruction are again emphasized.

3.7 Practical Aspects for Reconstruction

After describing the principal reconstruction framework, this sections serves to briefly summarize important practical aspects useful for preprocessing of MR data. More specifically, aspects of Non-Cartesian reconstruction, sensitivity estimation, coil-compression, pre-whitening and general aspects of the MRI data-pipeline are discussed.

3.7.1 Non-Cartesian reconstruction

A great part of the reconstructions described in this work are computed from *Non-Cartesian*, more specifically golden-angle radial stack-of-stars MR data, with specific advantages over Cartesian imaging. One important aspect is the robustness to motion, since the k-space center is sampled every

repetition such that no aliasing like artifacts in phase-encoding direction can occur. Furthermore, there are no wrapping-artifacts for a smaller FOV since readout-oversampling can be performed for each spoke and undersampling artifacts appear more benign. Most importantly for dynamic applications, the golden angle sampling scheme [12] enables a retrospective selection of temporal resolution by grouping together a Fibonacci number of spokes to achieve an evenly coverage in each time-frame. However, several drawbacks also have to be compensated, like correction of gradient delays [111], or additional fat suppression to avoid blurring artifacts. In [112] an extensive summary is provided.
Concerning the reconstruction, Non-Cartesian data imposes additional difficulties. The data needs to be interpolated on a Cartesian grid, such that this type of reconstruction is also often termed *gridding*. Here, the choice of the gridding kernel is crucial, and most often Kaiser-Bessel windows are used. This convolution operation with a specific gridding-kernel has again to be corrected which is called *deapodization*. First implementations in MRI reconstruction were described in [113]. Today many tools exist to perform the non-uniform fast-fourier transform (NUFFT) with all necessary steps, like that Matlab implementation by Fessler et al. [114]. Since the computation is usually a bottleneck in iterative reconstruction, speed-up is very important, which can be achieved e.g. with the gpuNUFFT tool[4] [115] by Schwarzl et al. or the NFFT[5] [116].
Since for radial sampling, the density of sampling points for equidistant sampling on each spokes becomes higher this has to be compensated for and is known as *density compensation*. For radial data this has to be carried out in a linear way since the area around each sampling point increases linearly with the distance from the center, i.e. the density compensation dcf for the n-th sample ($n \in [-0.5, \cdots, 0.5]$) with N_r being the number of readout samples per spoke with two-fold oversampling and N_e the number of encoded spokes is given as

$$dcf(n) = N|n| = \frac{\pi N_e}{4N_r}|n|. \tag{3.66}$$

[4] http://www.opensourceimaging.org/project/gpunufft/
[5] https://www-user.tu-chemnitz.de/~potts/nfft/index.phppackage

The normalization factor N guarantees that the scaling between k-space and image is preserved independent on the number of spokes in one frame. For arbitrary trajectories density compensation can be computed with *voronoi* cells or e.g. with an iterative approach proposed by Pipe et al.[117]. Finally it is important to note, that for iterative reconstruction the data has to be scaled once with the square-root of the density compensation. Also, forward and backward gridding operations need also be performed with the square-root of the density compensation to ensure adjointness of the Non-Cartesian MR operator.

3.7.2 Coil Sensitivity Estimation

Proper estimation of coil sensitivity profiles for reconstruction of undersampled dynamic MR data is a crucial point, since the reconstruction quality is bounded by the degree of correct sensitivity estimation.The sensitivities need also to be estimated for every patient individually, even for fixed coil setups, since the coil loading changes. Usually it is sufficient to assess the information from a reference set of low-frequency k-space samples, which is intuitive, given that the image structure of the sensitives is spatially smooth. In the dynamic imaging setting however, one has the advantage that temporal sampling can be adapted to yield a fully sampled time-averaged k-space. Assuming that the receiver coils are fixed in time, the coil sensitivity estimation can be computed from the temporally averaged k-space.
It is out of scope to describe existing methods in detail. A frequently used approach is based on the work by Walsh et al. [118] (WALSH), where the actual concern was multi-coil image reconstruction with a matched filter approach. As mentioned, a recent approach by Uecker et al. termed ESPIRiT [30], provides a mathematical profound analysis about the connection between image-spaced and data-space based PI. There, it is described how not only the sensitivity maps are estimated from an eigenvalue problem but that it is also possible to derive an *extended* set, that includes additional information for limited FOV imaging. Image-based PI with the extended set is termed *soft-SENSE*, and can be applied in combination with other regularization strategies.
Another strategy also proposed by Uecker et al. is the *non-linear inversion*

algorithm (NLINV), that solves the MRI inverse problem in Eq. 3.1 by considering the coil sensitivity maps as unknowns. The corresponding non-linear problem is solved with an iteratively regularized Gauss-Newton algorithm, penalizing the sensitivities with a smoothness constrained [119]. Thus, both the magnetization and sensitivities are jointly reconstructed and the later is rather a side product. The framework also allows to regularize the magnetization, i.e. Tikhonov regularization as in the original paper, while TV and TGV constraints for improved noise suppression were also proposed in [61]. Throughout this work an image-space approach is employed that enforces smoothness assumptions on the sensitivities and TGV^2 constraint on the time-averaged magnetization in an iterative fashion over all receiver coils. The corresponding algorithm (VARCOIL) was presented in [120] and can also be found in the Appendix 8.4. It is also available online within the AVIONIC framework. For dynamic applications it was found that the VARCOIL algorithm yields equivalent reconstruction quality as ESPIRiT or NLINV sensitivities with superior quality compared to the WALSH approach. As mentioned this holds true for the assumption of static receiver coils and a "fully" sampled temporally averaged k-space. In the case of real-time imaging a motion robust approach again is the NLINV approach, where the coil sensitivities are estimated individually for each time frame [10]. Finally, the inherent normalization for the described methods, i.e.

$$\sqrt{\sum_{i=1}^{N_c} |c_i|^2} = 1,$$

effectively realizes a receive-sensitivity inhomogeneity correction as described in [26] and ensures adjointness of the MR operator.

3.7.3 Coil Compression

The development of array coils with many channels laid the basis for the developement of PI. However, the acceleration potential is not easy to determine since it depends on the number of *independent* receiver coils, which is lower than the number of physical channels due to the limited space of positional alignment. A high number of receive channels on the other side poses

an additional computational burden, especially for iterative reconstruction methods and increased demand of data storage. To this end, Buehrer et al. proposed a method for *coil compression* based on PCA [121].
The coil compression used in this work is based on [122], where a singular value decomposition is used on the data directly. In Fig. 3.9 displays an example of the information content given by the magnitude of the singular values for the converted channels for a 24-channel head array. A threshold defined usually to 10% to 15% of the largest singular value yields a compression of around 30% to 50%. For dynamic data, however, the strategy needs to be adapted since a different compression for each time-frame potentially yields different *virtual* receiver coils for every time-frame, that need to be estimated from the compressed data. Instead it is possible to compute a singular value decomposition from the time-averaged data, and apply the same transformation for every time-frame.

3.7.4 Pre-Whitening

As outlined in Sec. 3.1.2 the coil elements usually exhibit different noise levels and may be subject to inter-channel correlations due to cross-talk, which is undesirable. As already outlined in the CG-SENSE paper by Pruessman [29] it is possible to perform a *weighted* least-squares reconstruction, that takes the noise-correlation matrix into account, i.e. adapting Eq. 3.19 and solve

$$\mathrm{u}^{\star} = \arg\min_{u} \frac{1}{2}(Ku - d)^{H}\Sigma^{-1}(Ku - d) + \frac{\alpha}{2}\|u\|_2^2. \tag{3.67}$$

This requires the estimation of Σ as pre-processing step, which can be achieved with zero flip-angle acquisition but can also be contained within the measurement files. Instead of including the noise covariance matrix in the reconstruction iteratively the equivalent result is yielded by computing once *pre-whitened* data, i.e. de-correlating and normalizing the data in each channel, as

$$\tilde{d} = L^{-1}d, \qquad \Sigma = LL^{H}. \tag{3.68}$$

Here $\tilde{d}$ is the pre-whitened data with equal variance in each channel and L is a lower triangular matrix computed with Cholesky decomposition from Σ. However, pre-whitening is mainly necessary in the case of defective coil elements, where a suppression of artifacts is achieved. A numerical example is given in Fig. 3.10

3.7.5 Data Pipeline

To conclude this section, some relevant information about the MR data pipeline, specifically for Siemens systems, is given. MR rawdata is stored in a proprietary measurement data file format that can be exported from the scanner. It is also possible to enable a real time export in smaller data fragments during scanning in the DICOM standard. Rawdata from the measurement file can be extracted including meta-information with a Matlab based framework developed by the MR community (mapVBVD [6]). However, it can be tedious to pre-process the rawdata according to measurement parameters like partial-fourier or oversampling and apply necessary corrections, such as EPI phase-corrections. For different vendor platforms, commercially available software exists to handle such problems (like Gyrotools for Phillips), unfortunately not for Siemens. However, it is in principal possible to program reconstruction software in the Siemens MARS framework.
A promising community driven development is a new data standard for MRI data, termed *international society for magnetic resonance in medicine* (ISMRM) rawdata (ISMRMRD) [123], with available modules to convert the proprietary vendor measurement data for all major vendors to a generic HDF5 standard. Parallel to that, community driven reconstruction frameworks supporting this standard are being developed like Gadgetron [124] or the Berkely-Advanced-Reconstruction-Toolbox (BART) [125]. BART includes many pre-processing procedures like coil-compression and advanced reconstruction strategies. While Gadgetron can be run directly on the scanner console, many advanced reconstruction procedures require high computational power. For Siemens platforms, the Yarra framework[7] completes

[6] https://www.mr-idea.com/
[7] https://yarra.rocks/doc/concept/

to aforementioned developments, as it enables the automatic transfer of Siemens rawdata together with a reconstruction procedure to an external workstation, from which, after successful reconstruction, DICOM images can be re-imported again automatically into a picture-archiving system PACS.

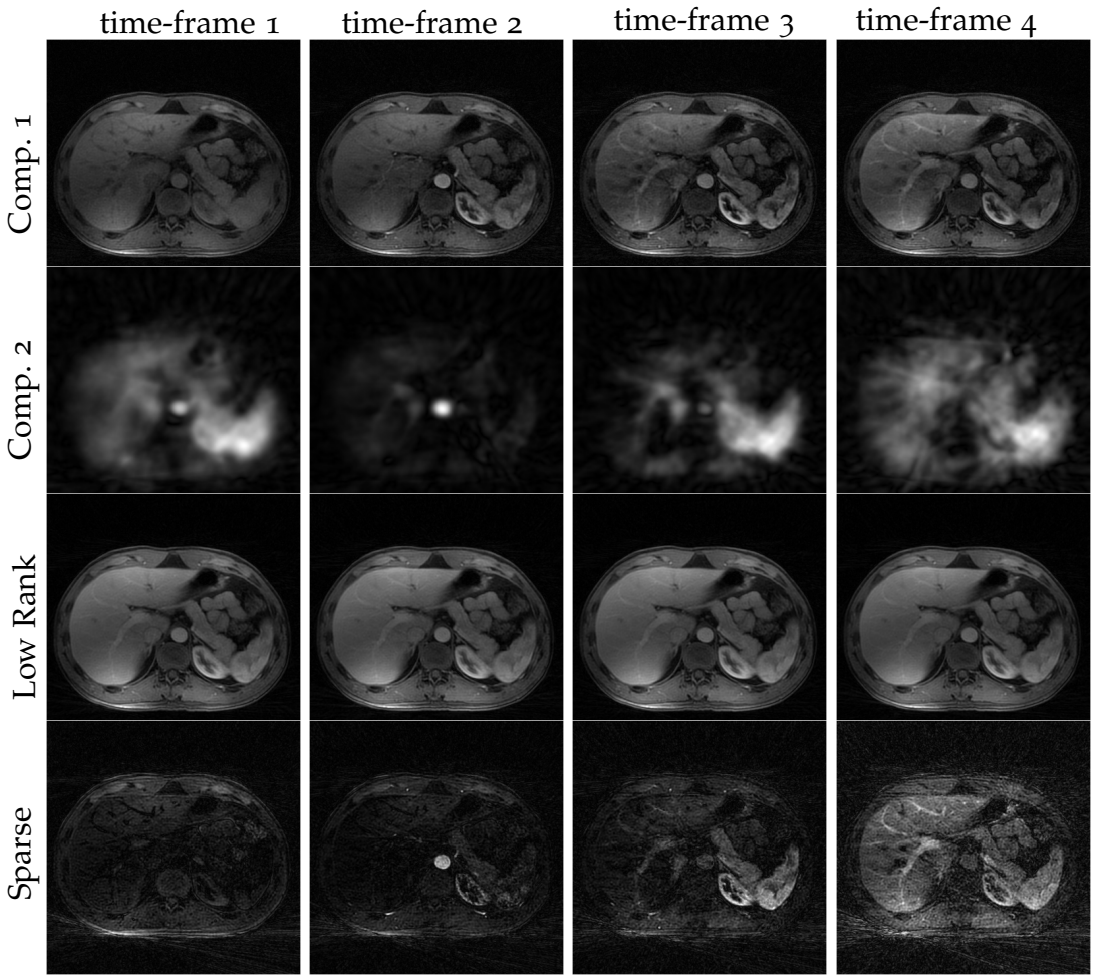

Figure 3.7: Comparison of decomposition into components for ICTGV based reconstruction (Comp.1 and Comp. 2) and L+S (low-rank and sparse component) for a DCE dataset.

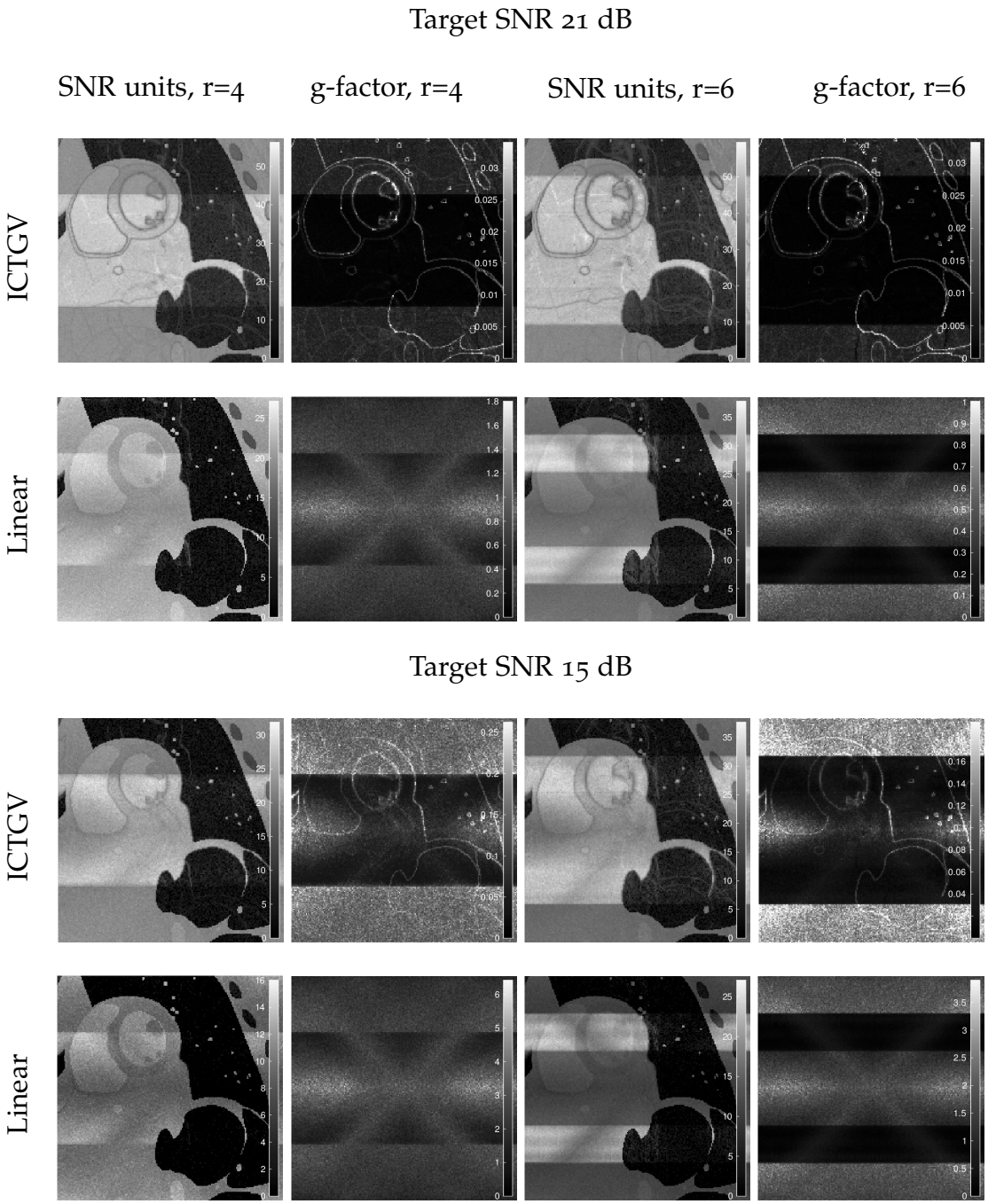

Figure 3.8: Comparison between ICTGV and Tikhonov regularized (linear) reconstruction in terms of SNR units and geometry-factor map gained from pseudo-replica experiments for target noise-levels of 21 and 15 dB and acceleration factors of 4 and 6 for a uniformly shifted undersampling pattern.

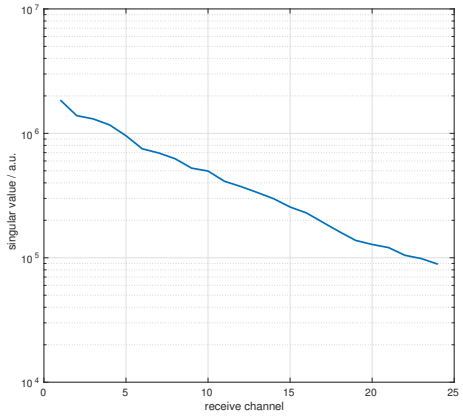

Figure 3.9: Sorted singular values from a singular-value decomposition of MR data acquired with 24 channels of a head-neck coil

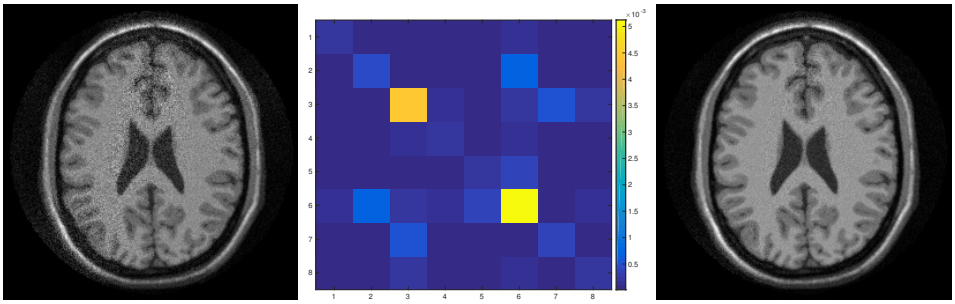

Figure 3.10: Numerical example to display the effect of accelerated Cartesian CG-SENSE reconstruction (r=4) without pre-whitening (left) and with pre-whitening (right). The noise covariance matrix of the broken eight coil receiver coil is displayed in the middle.

4 Cardiac Imaging

4.1 Introduction

Cardiac imaging is an important field of application in MRI. The sequence design for fast imaging and PI already enabled to study the heart function of the beating heart and myocardial perfusion, with CINE techniques based on ECG-triggering, within a single breath-hold [126].
For CINE cardiac imaging this requires the validity of a high degree of periodicity and the synchronization of the data acquisition with a navigator signal over several heartbeats, such that a slice may be acquired in around $10s$ for $1\,\mathrm{mm}^2$ isotropic resolution. In the case of arrhythmia, real-time imaging with decreased spatial resolution can be performed, which accounts to acquire a sufficiently filled k-space for each time-frame during one heartbeat. In order to avoid inter-frame motion artifacts an adequate temporal resolution ($< 50\,\mathrm{ms}$) needs to be adjusted, bounded by the phase of fasted heart contraction in systole, which typically yields around 20 time-frames. First breath-hold cinematographic cardiac MRI was based on multi-shot FLASH sequences [127], acquiring multiple phase-encoding lines for one time-segment during one heartbeat. However, spoiled GE delivers poorer contrast between blood and myocardium with short repetition times or slow blood flow, which lead to the use of SSFP based imaging with higher contrast-to-noise ratio, excellent blood-myocardial contrast and minimum TR. Although, a SSFP imaging is very sensitive to off-resonance effects, expressed as banding artifacts, and requires the use of frequency-scouts, it is now the dominant sequence for functional cardiac imaging in clinical routine. The mode for CINE acquisition is most commonly set to *retrospective* sorting, i.e. data is acquired continuously and sorted afterwards according to the ECG signal, in distinction to *prospective* triggering, where the acquisition window is defined at the beginning. Retrospective triggering enables

a maximum sampling efficiency of the cardiac cycle. Cardiac imaging is always performed in a specially defined orientation system, e.g. two, three and four-chamber or short-axis view [128].
Examining the myocardial viability was made feasible with gadolinium-based contrast-enhanced cardiac perfusion imaging and is now considered the standard methodology to characterize acute and chronic myocardial infarction. The contrast agent distributes itself during the first pass according to the extracellular fluid volume, that is larger for myocardial scars, and, in the case of acute infarction diffusion into the intracellular space is possible due to irregular cell-membrane permeability. In order to capture the single contrast injection dynamically with the requirement of highest possible spatial coverage, usually three slices in short-axis view (basal, mid and apical) together with a four-chamber view are acquired with low resolution during diastole. T_1-weighting is required and commonly achieved with inversion-recovery GE imaging [129].
Both CINE cardiac and cardiac perfusion imaging, already required the development of PI because the corresponding fast sequences operate on the SAR and nerve-stimulation limits. In order to acquire a sufficient amount of data within the constraints of breath-hold and spatial coverage undersampling strategies are required accounting for the ultimate trade-off between spatial resolution and/or coverage and temporal resolution. The development of CS is therefore a crucial development to further accelerate the MR acquisition to enable higher resolutions, reduced scan times or imaging of multiple slices in the case of CINE cardiac imaging, and increased spatial resolution and coverage for cardiac perfusion MRI.
These two applications also comprise two major classes of change in dynamic information, i.e. temporal change in morphology due to heart motion with conserved contrast and temporal change of contrast with fixed morphology due to the passing contrast agent. The sampling trajectory specific acceleration potential of the proposed regularization approach is therefore evaluated most extensively for these two applications. To this end, numerical simulations were performed and a comparison to state-of-the-art methods is given in this chapter according to previously published work [130].

4.2 Material and Methods

CINE cardiac MRI was evaluated with six datasets. Three fully sampled datasets were made available from the ISMRM reconstruction challenge 2013-2014[1] and a forth fully sampled dataset was a retrospectively gated balanced SSFP short-axis view of a health volunteer measured on a 3T scanner (Skyra, Siemens Healthcare, Erlangen, Germany) with the following scan parameters: FOV = 275 mm × 340 mm, matrix size = 208 × 168, 25 cardiac phases with a temporal resolution of 42.72 ms, TR/TE/FA = 3.56 ms/1.78 ms/40°, 6 mm slice-thickness, acquisition time (TA)=16 s. For reconstruction 30 channels from spine- and body-coil elements were automatically selected.
For evaluating the acceleration potential with the available sampling strategies on the 3T system two datasets were measured. Firstly a prospectively gated balanced SSFP dataset in short-axis view was acquired with regularly shifted Cartesian undersampling (TPAT) with acceleration factors of $r = \{4, 6, 8\}$ which corresponds to acquisition times of 3.55 s, 2.36 s and 1.27 s. The same orientation was measured with radial sampling with 108, 52 and 24 radial spokes per time-frame that corresponds to acquisition times of 9.37 s, 4.8 s and 1.22 s. The common imaging parameters were: 24 cardiac phases with temporal resolution 42.72 ms, TR/TE/FA = 3.56 ms/1.78 ms/40°, 6 mm slice-thickness, matrix size = 224 × 184 (Cart.) resp. 224 × 224 (rad.).
One dynamic perfusion dataset was made available from New York School of Medicine (NYU). It was acquired in a healthy adult volunteer with a modified Turbo-FLASH pulse sequence on a whole-body 3T scanner (Tim Trio, Siemens Healthcare, Erlangen, Germany) using a 12-element matrix coil array and was already used for evaluation purposes of undersampled dynamic MRI reconstruction in [90].
Different levels of acceleration from 4 to 16 were simulated from the fully-sampled multi-coil data with an optimized Cartesian sampling scheme for dynamic time-series as proposed in [131], which was found to be more efficient as variable density sampling. Multi-coil reconstructions from ICTGV, spatio-temporal TGV, TV and L+S [90] were evaluated quantitatively by means of SSIM and signal-to-error ratio (SER) as used in [84], [91] and

[1] http://challenge.ismrm.org/

defined in App. 8.1.0.12, against the sum-of-squares (SOS) reconstruction of the fully sampled data within a region of interest encompassing the heart. For additional evaluation of single-coil reconstructions with kt-RPCA [91], kt-SLR [84] and kt-FOCUSS [71] the coil-combined fully sampled references were transformed to data space. Artificial degrees of subsampling from 2 to 12 were computed again with the sampling pattern described in [131] with an additional block of 8 lines of low-resolution data around the k-space-center. This results in effective acceleration factors $r \in \{1.96, 3.6, 5.2, 6.5, 7.5\}$ for the CINE cardiac and $r \in \{1.9, 3.5, 4.8, 5.7, 6.5, 7.3\}$ for the cardiac perfusion dataset.

The image reconstruction pipeline for ICTGV^2, TGV^2 and TV was used as described in Sec. 3.5.4. For the L+S reconstruction, the implementation provided at `http://cai2r.net/resources/software` was used, where the proposed temporal Fourier transform was replaced by a temporal TV regularization, also provided by the authors, since this improved the results. For comparison to kt-RPCA, kt-SLR and kt-FOCUSS the reconstruction code provided online by the authors was used[2].

For ICTGV^2, a parameter tuning, as described in more detail below, was carried out a-priori and parameters where then fixed for CINE and perfusion imaging for all further experiments. A similar parameter tuning was also carried out for TGV and TV based reconstruction as depicted in Fig. 4.10. To ensure the best results, the parameters for L+S reconstruction were optimized separately for *each individual case and acceleration factor used in the evaluation*. Optimization was carried out on the parameter range as described in [90] and parameters were adapted for each case based on quantitative comparison to the (in practice unknown) ground truth.

The parameter choices for kt-RPCA, kt-SLR and kt-FOCUSS were also trained a-priori according to the parameter-ranges described in [91] for one acceleration factor of $r = 8$ (with additional k-space-center lines for kt-FOCUSS). As result, the parameters were fixed to $(\mu^{\text{perf}}, \rho^{\text{perf}}) = (200, 2)$, $(\mu^{\text{CINE}}, \rho^{\text{CINE}}) = (10, 2)$ for kt-RPCA, $(\alpha^{\text{perf}}, \beta^{\text{perf}}) = (\alpha^{\text{CINE}}, \beta^{\text{CINE}}) = (500, 10^{-3})$ for kt-SLR and $\lambda^{\text{perf}} = \lambda^{\text{CINE}} = 10^{-3}$ for kt-FOCUSS, respectively.

[2] kt-RPCA: `http://agsp.org/bt/ktrpca/`, kt-SLR: `http://user.engineering.uiowa.edu/~jcb/Software/ktslr_matlab/Software.html`, kt-FOCUSS: `http://bispl.weebly.com/k-t-focuss.html`.

The coil sensitivities for all multi-coil reconstructions were estimated with an iterative variational approach from the subsampled data as described in [120] (see App. 8.4).

Parameter Training

The three ICTGV^2 *model parameters* s, t_1, t_2 were fixed by evaluating a range of parameter sets with respect to SSIM and RMSE. For CINE cardiac imaging, two test cases from the ISMRM reconstruction challenge 2013-2014, different from the ones presented in the evaluation below, were used. The training was carried out for two acceleration factors ($r_1 = 5$, $r_2 = 10$), for which a ground truth and a good choice of regularization parameter was known. For cardiac perfusion imaging, the model parameter training was carried out with the MRXCAT perfusion phantom [97] with a selected slice in mid-ventricular short-axis view, standard settings and additional subsampling of $r = 6$, and the perfusion dataset from NYU. As a result, the model parameters were fixed as $(t_1, t_2, s) = (4, 0.5, 0.5)$ for CINE cardiac imaging and $(t_1, t_2, s) = (9, 1, 0.6423)$ for cardiac perfusion imaging.
The same test cases were also used for regularization parameter training. Based on the sampling-pattern described in [131], incomplete data was generated for different subsampling rates and the reconstructions for different parameter choices were compared against the ground truth. According to these experiments, final values the slope a and offset b, as described in Subsec. 3.3.5, were fixed to $(a, b) = (0.34, 4.57)$ for CINE cardiac and $(a, b) = (0.08, 1.56)$ for cardiac perfusion imaging. Single-coil reconstructions were carried out with the same parameters as for the multi-coil setting. An exemplary visualization of our results for parameter tuning is displayed in Fig. 4.1 and Fig. 4.2, respectively. A summary of all relevant parameter choices is given in Table 4.1. In order to remove a dependency of the regularization parameter from the signal range of the image data, a normalization to the median of the highest ten percent of the time-averaged reconstruction as preprocessing step was carried out.

Table 4.1: Regularization and model parameter choice

Symbol	Denomination	Chosen value		Testing range
Model parameter		CINE	Perf.	
α_0/α_1	Ratio of TGV weights	$1/\sqrt{2}$	$1/\sqrt{2}$	–
$t_1 \to \beta(t_1)$	Spatio-temporal weight 1st component	4	9	$[2, 4, 6.5, 9, 10]$
$t_2 \to \beta(t_2)$	Spatio-temporal weight 2nd component	0.5	1	$[0.2, 0.4, 0.5, 1, 2.5, 3]$
$s \to \gamma_{1,2}(s)$	Weighting between 1st and 2nd component	0.5	0.6423	$[0.3577, 0.5, 0.6423]$
Regularization parameter				
$\lambda(r) = ar + b$	Regularization parameter	$--$		$\lambda \in [0.5, \cdots, 27]$ $r \in [4, 8, 12, 16]$
a	Slope	0.34	0.08	$--$
b	Intercept	4.57	1.56	$--$

4.3 Results

Figure 4.3 shows ICTGV^2 reconstructions of a CINE cardiac dataset from the ISMRM challenge for different acceleration factors. The reconstructions exhibit a high degree of accordance to the fully-sampled reconstruction with improved noise-suppression in the background up to very high acceleration factors. Figure 4.4 shows down-sampling experiments for the measured short-axis dataset with an additional comparison to L+S reconstruction for acceleration factors of 12 and 16. Again the ICTGV^2 reconstruction reaches excellent quality up to $r = 12$ with slightly reduced fidelity for $r = 16$, while L+S based reconstructions exhibit corruption with residual undersampling and temporal blocking artifacts. Again, for L+S the parameters were trained

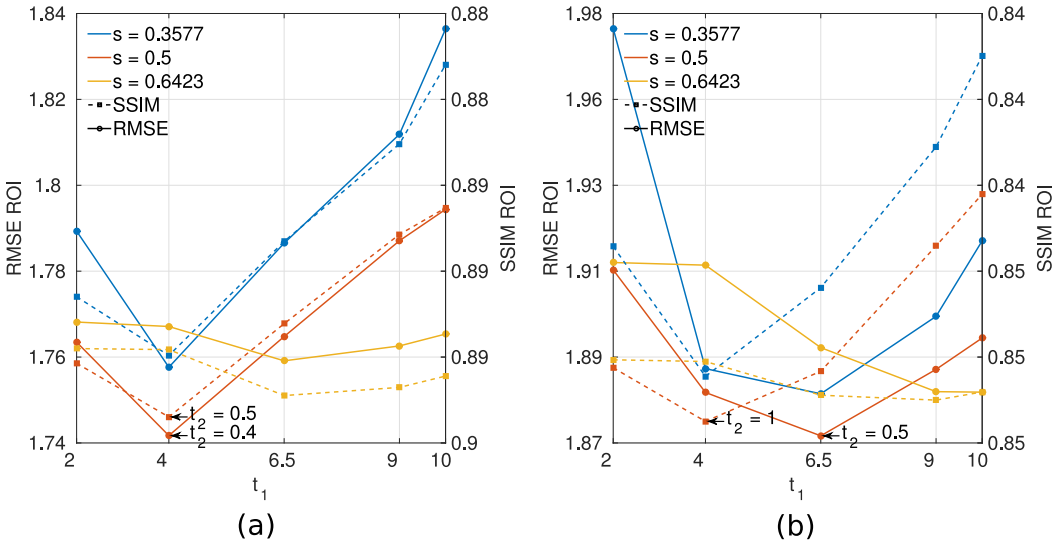

Figure 4.1: Evaluation of the model parameters s, t_1, t_2 by means of RMSE (solid lines) and SSIM (dashed lines) for a CINE cardiac test-case with acceleration factors $r = 5$ (a) and $r = 10$ (b). The colors indicate three different choices for s. The horizontal axis show different values for t_1 and the vertical axis the corresponding best RMSE and SSIM values achieved with $t_2 \in \{0.2, 0.4, 0.5, 1, 2.5, 3\}$, which are marked (arrow) with the corresponding best value for t_2.

for the same test case and each acceleration factor separately, while for ICTGV^2 parameters were fixed a-priori based on different data.

Figure 4.5 displays the results from a down-sampling experiment using perfusion data, where a good delineation of the myocardial wall and the papillary muscles was achieved up to $r = 16$. Reconstruction quality with L+S is slightly worse than with ICTGV^2, in particular a loss of spatial details is apparent.

A quantitative evaluation by means of SER and SSIM against the fully sampled reference as ground truth is summarized in Table 4.2. There, ICTGV^2 regularization is compared against spatio-temporal TGV$^2_\beta$ and TV$_\beta$ regularization and L+S reconstruction. Model and regularization parameter training was also carried out for both, TGV$^2_\beta$ and TV$_\beta$ reconstruction. For the L+S reconstruction parameter training was also carried out by means of SER and SSIM for each individual test case and acceleration factor of the evaluation. For CINE cardiac test cases, ICTGV^2 almost always scores best

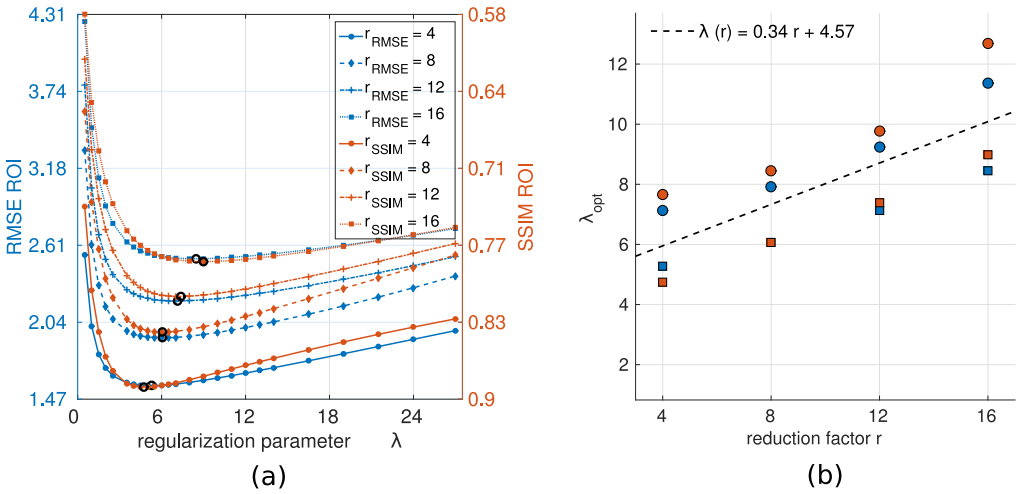

Figure 4.2: (a) RMSE (blue curves) and SSIM (red curves) evaluation exemplified for one CINE cardiac test case for different regularization parameters λ and acceleration factors $r = 4$ (solid line), $r = 8$ (dashed line), $r = 12$ (dashed-dotted line) and $r = 16$ (dotted line). The corresponding optimal values for λ are indicated with black circles and were calculated by spline-interpolation between the used sample-points. (b) Optimal values for λ according to RMSE (blue) and SSIM (red) for different acceleration factors and the test case displayed in (a) (squares) and the second test case (dots). The linear regression to both cases and metrics (black dashed line) yields the proposed parameter choice.

for both metrics with considerable improvement against L+S, in particular for higher acceleration factors. Compared to temporal TGV^2_β and TV_β, reconstruction quality improves slightly. In contrast to that, a substantial increase is observable when comparing ICTGV^2 reconstruction against temporal TGV^2_β and TV_β for the cardiac perfusion test case. Comparison to L+S for the perfusion case again shows a solid improvement with ICTGV^2.
Comparison of reconstruction quality between ICTGV^2 and TGV for multi-coil reconstruction of both, CINE cardiac imaging ($r = 16$) and cardiac perfusion ($r = 12$) reconstructions is displayed in Fig. 4.8. While the results for the CINE dataset are similar, the perfusion results show a loss of spatial details and a temporal blurring with spatio-temporal TGV. In particular, the ICTGV^2 reconstruction still allows to detect small image features that are lost with TGV.

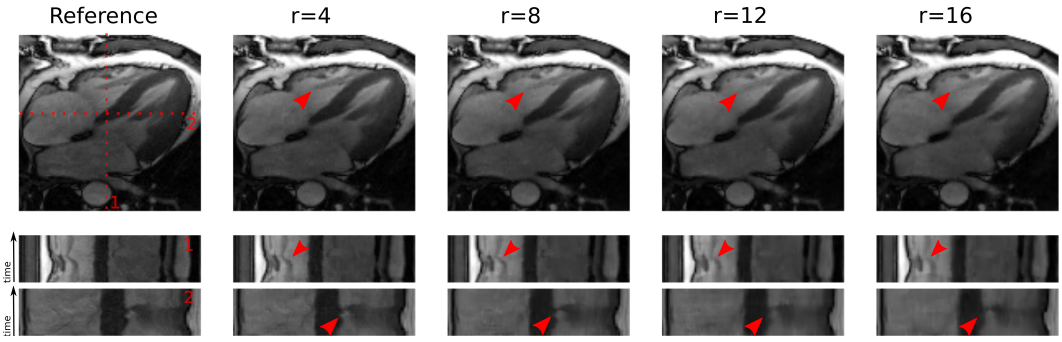

Figure 4.3: Magnitude images from simulated accelerations $r = (4, 8, 12, 16)$ for the four-chamber-view bSSFP dataset. The fully sampled sum-of-squares reconstruction is displayed in the 1st column and the therein indicated time-lines are shown in the 2nd and 3rd row.

Finally, reconstruction results for prospectively accelerated data acquisition procedures as available on current MR systems are displayed in Fig. 4.11 for regular Cartesian undersampling (termed TPAT in Siemens terminology) and radial undersampling in Fig. 4.12, together with PI reconstruction with the vendor implementation. For both sampling schemes a drastic gain in reconstruction quality is achieved.

Reconstruction results for single-coil data with ICTGV^2, kt-RPCA, kt-SLR and kt-FOCUSS from undersampled cardiac perfusion ($r = 7.3$) and CINE cardiac imaging ($r = 3.6$, $r = 7.5$) are displayed in Figure 4.6 and 4.7, respectively, together with the computed SER values in dB and indicated time courses (CINE) or the mean intensity within a ROI in the left ventricle (perfusion). A more detailed summary of quantitative evaluation results by means of SER and SSIM for acceleration factors is given in Table 4.3. The results show advantages of ICTGV^2 in terms of error measures, consistently for all acceleration factors. For the perfusion case, the ICTGV^2 signal time course is very close to the reference data set. The single time frames

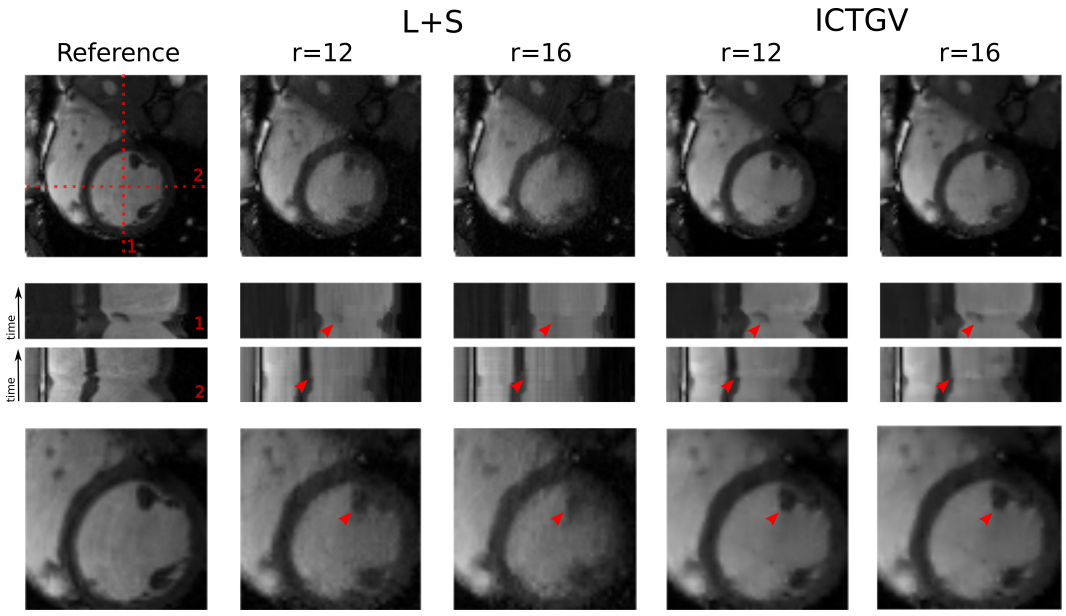

Figure 4.4: Comparison of magnitude images of fully sampled reference reconstruction (1st column), L+S (2nd and 3rd column) and ICTGV^2 reconstruction (4th and 5th column) for bSSFP CINE cardiac data acquired in short-axis-view and undersampling factors of $r = (12, 16)$. A late diastolic time-frame is displayed in the 1st row and indicated vertical and horizontal time-lines in the 2nd and 3rd row. A closeup of the heart region is displayed in the 4th row.

of ICTGV^2 and kt-SLR appear somewhat denoised, and some details, as highlighted by arrows, are best visible in the ICTGV^2 reconstruction. The individual images of all CINE reconstructions appear similar, however, the x-t plot exhibits some rippling for kt-FOCUSS and particular for kt-RPCA.

For the perfusion dataset the decomposition into ICTGV^2 components for $r = 8$ is shown in Fig. 4.9. Here, the static background, slower contrast dynamics with increased temporal blurring as well as morphologic changes are stored within the first component, while more rapid intensity changes (ventricles) are mapped in the second component. The separation is also displayed by the mean intensity change (magnitude) within the right ventricle (Fig. 4.9 b) and myocardium (Fig. 4.9 c), where a high agreement of the ICTGV^2 reconstruction to the fully sampled reference is observable.

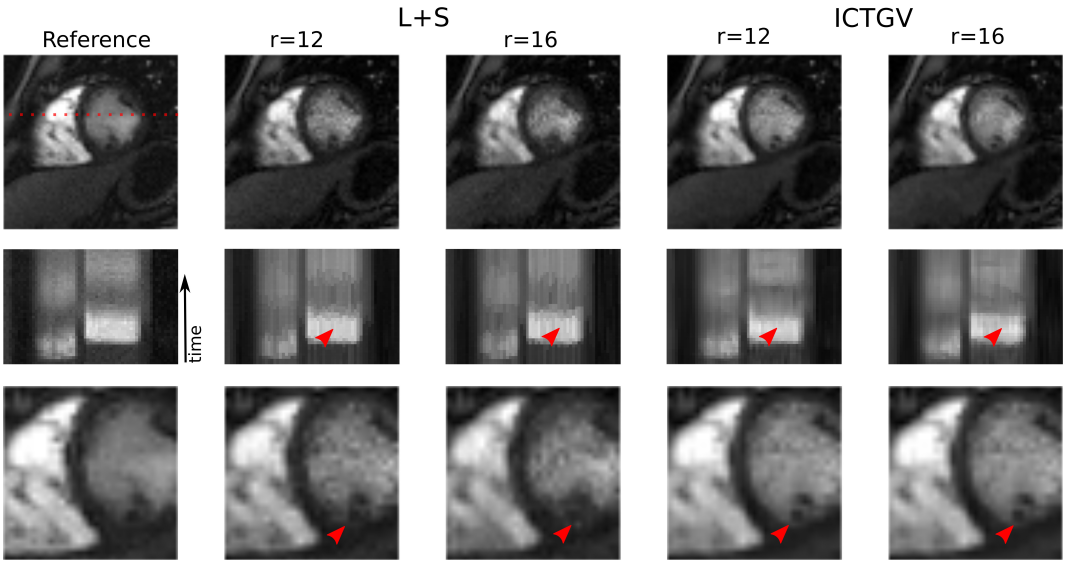

Figure 4.5: Comparison of magnitude images of fully sampled reference reconstruction (1st column), L+S (2nd and 3rd column) and ICTGV^2 reconstruction (4th and 5th column) for the cardiac perfusion dataset and undersampling factors of $r = (12, 16)$. A selected time-frame is displayed in the 1st row and the indicated time-line in the 2nd row. A close-up of the heart region is displayed in the 33rd row.

4.4 Discussion and Conclusion

The results presented in this work demonstrate the performance of ICTGV^2 as new spatio-temporal regularization approach for the reconstruction of undersampled dynamic multi-coil MRI data. Two exemplary application scenarios were considered: Cardiac CINE imaging with quasi-periodic morphological motion and cardiac perfusion imaging reflecting contrast changes to due alteration of tissue relaxation properties. The corresponding experiments show the capability of the proposed method to obtain artifact free results with high temporal fidelity and improved noise suppression for both applications up to high acceleration factors. This is confirmed both quantitatively, in terms of SER and SSIM, as well as qualitatively with selected frames and the visualization of time lines.
Furthermore, the proposed method was evaluated against state of the art reconstruction methods for single-coil and multi-coil reconstruction. In the

Table 4.2: Quantitative evaluation (best values underlined) of multi-coil reconstruction for ICTGV^2 against TGV$^2_\beta$, TV$_\beta$ and L+S reconstruction for CINE cardiac and cardiac perfusion cases by means of SER and SSIM against the fully sampled sum-of-squares reconstruction.

	ICTGV^2		TGV$^2_\beta$		TV$_\beta$		L+S	
	SER (dB)	SSIM	SER (dB)	SSIM	SER (dB)	SSIM	SER (dB)	SSIM
Short-axis view								
$r = 4$	25.79	0.9167	25.85	0.9164	25.60	0.9154	25.78	0.9154
$r = 8$	23.18	0.8738	23.13	0.8744	22.89	0.8690	21.75	0.8475
$r = 12$	21.45	0.8376	21.37	0.8374	21.21	0.8320	19.09	0.7802
$r = 16$	20.47	0.8160	20.41	0.8147	20.28	0.8107	17.31	0.7177
Four Chamber								
$r = 4$	20.32	0.8267	20.37	0.8216	20.26	0.8220	20.29	0.8109
$r = 8$	19.72	0.7787	19.72	0.7726	19.64	0.7718	19.54	0.7408
$r = 12$	19.17	0.7445	19.16	0.7399	19.11	0.7397	18.36	0.6853
$r = 16$	18.94	0.7211	18.92	0.7165	18.84	0.7154	17.43	0.6346
Cardiac Perfusion								
$r = 4$	21.30	0.8631	20.91	0.8554	19.91	0.8256	20.74	0.8564
$r = 8$	20.34	0.8347	19.77	0.8191	18.16	0.7554	19.58	0.8172
$r = 12$	18.71	0.8059	18.28	0.7817	16.57	0.6895	17.79	0.7855
$r = 16$	17.54	0.7813	17.28	0.7495	15.38	0.6407	17.01	0.7597

multi-coil setting, a comparison to the L+S approach shows improved performance both for CINE and perfusion imaging. This is quantified in SER and SSIM error metrics and can also be observed visually. Interestingly, also spatio-temporal TGV and TV regularization lead to comparable or improved results compared to L+S in terms of error metrics. One possible explanation for that is that L+S in fact does not make use of any regularity in space. Spatial regularity, however, is a strong source of redundancy which is exploited both by spatio-temporal TV/TGV and ICTGV^2. A second explanation might be the global nature of the low-rank prior, which is not able to adapt locally to contrast or morphological changes, a shortcoming which is overcome by

Table 4.3: Quantitative evaluation (best values underlined) of single-coil reconstruction for ICTGV^2 against kt-RPCA and kt-SLR and kt-FOCUSS reconstruction for CINE cardiac and cardiac perfusion cases by means of SER and SSIM against the fully sampled single-coil reconstruction.

	ICTGV^2		kt-RPCA		kt-SLR		kt-FOCUSS	
	SER (dB)	SSIM	SER (dB)	SSIM	SER (dB)	SSIM	SER (dB)	SSIM
Four Chamber View								
$r = 1.96$	29.24	0.9217	27.71	0.9214	28.86	0.9169	27.49	0.9052
$r = 3.6$	25.66	0.8524	21.63	0.8216	24.85	0.8295	24.56	0.8436
$r = 5.2$	23.42	0.8047	19.95	0.7674	22.52	0.7759	22.58	0.7955
$r = 6.5$	22.30	0.7680	18.70	0.7260	21.36	0.7335	20.87	0.7429
$r = 7.5$	20.98	0.7274	17.87	0.6879	20.29	0.6920	19.83	0.7058
Cardiac Perfusion								
$r = 1.9$	27.19	0.9429	25.99	0.9394	26.90	0.9421	26.63	0.9420
$r = 3.5$	24.73	0.9096	23.14	0.8980	23.94	0.8979	23.37	0.8946
$r = 4.8$	23.23	0.8847	21.41	0.8662	21.95	0.8562	21.59	0.8614
$r = 5.7$	22.16	0.8713	20.45	0.8505	20.76	0.8302	20.54	0.8415
$r = 6.5$	21.64	0.8614	19.93	0.8391	19.40	0.7780	20.14	0.8325
$r = 7.3$	20.62	0.8402	18.69	0.8118	18.50	0.7500	18.83	0.7988

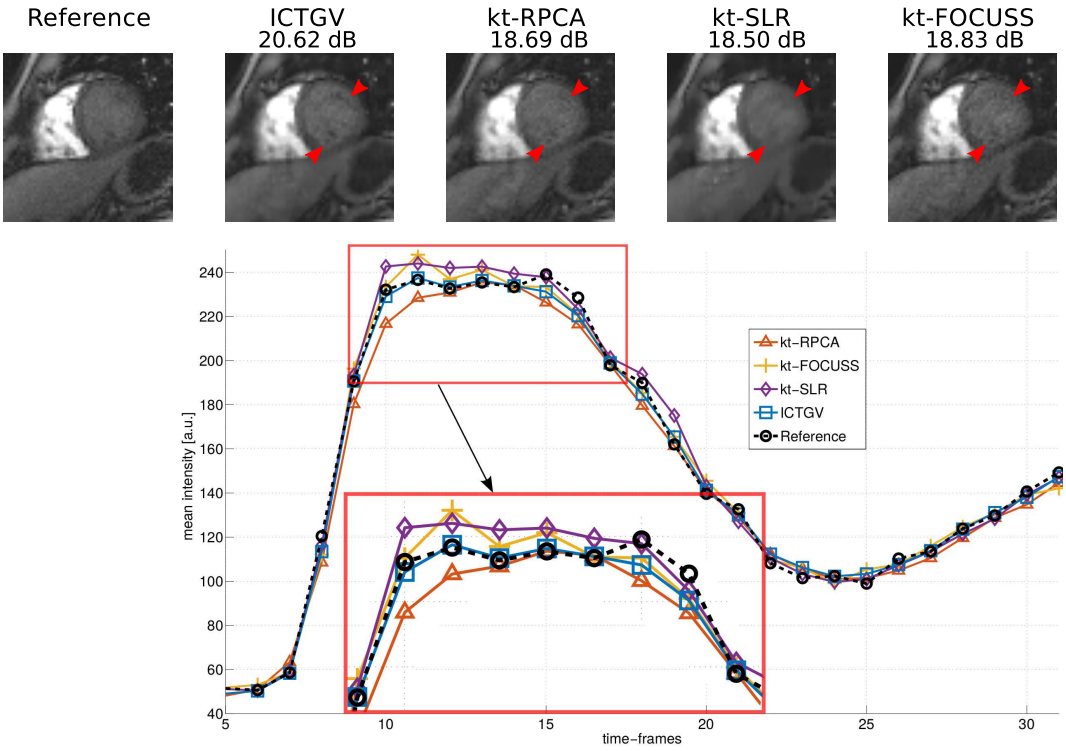

Figure 4.6: Coil-combined fully sampled reference (1st column), ICTGV^2 (2nd column), kt-RPCA (3rd column), kt-SLR (fourth column) and kt-FOCUSS (fifth column) single-coil reconstructions from undersampled Cartesian data ($r = 7.3$) for the cardiac perfusion dataset with computed SER values in dB. The mean time-course of an indicated 3×3 voxel region within the right ventricle is plotted for all methods under investigation with a closeup view of the peak-signal.

ICTGV^2 regularization. The kt-RPCA [91] method is, in principle, identical with L+S, yet, in contrast to the multi-coil reconstruction with L+S, temporal Fourier transform (tFT) is used instead of temporal TV. While L+S also proposed tFT as preferred choice, temporal TV gave improved results in our experiments and was hence used for comparison. The kt-SLR method on the other hand imposes sparsity constraints with spatio-temporal TV and non-convex low-rank constraints with Schatten p-quasi-norms (see App. 8.1) jointly, instead of the proposed decomposition approach. Using non-convex quasi-norms results in a challenging optimization problem, yet, with the parameters tuning as suggested in [91], reconstruction results remain very

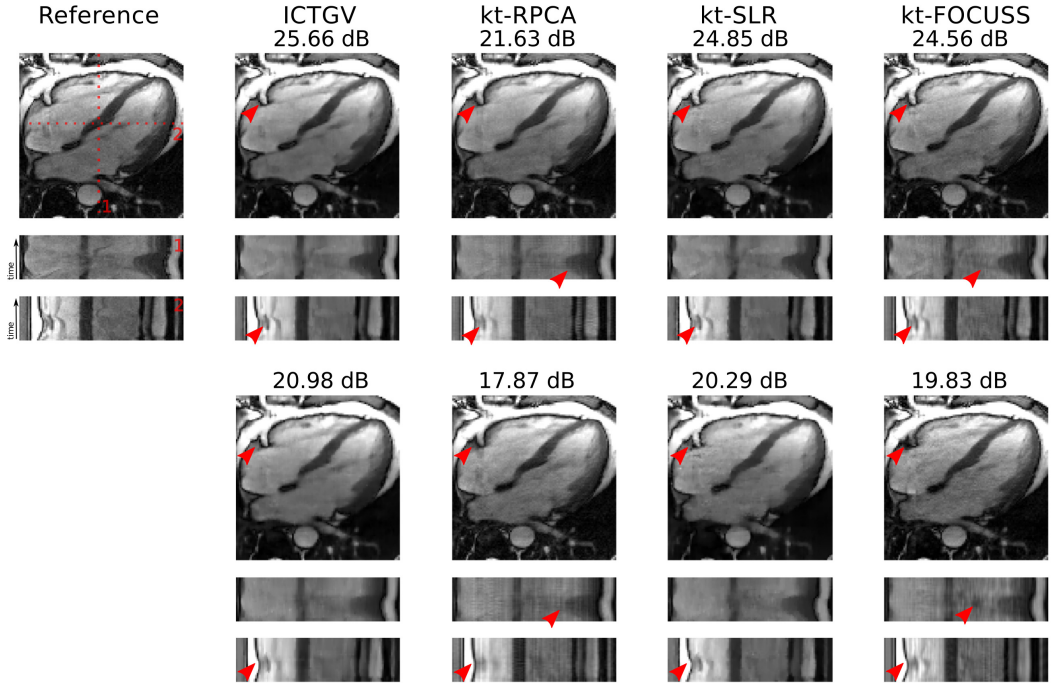

Figure 4.7: Coil-combined fully sampled reference (1st column), ICTGV^2 (2nd column), kt-RPCA (3rd column), kt-SLR (fourth column) and kt-FOCUSS (fifth column) single-coil reconstructions from undersampled Cartesian data with $r = 3.6$ (1st to 3rd row) and $r = 7.5$ (4th to 6th row) for the four chamber CINE cardiac dataset. Reconstructions are displayed with a selected time-frame and the indicated horizontal and vertical time-lines.

competitive to ICTGV^2. Computationally, however, ICTGV^2 reconstruction has the advantage of comprising the solution of a convex optimization problem, for which to proposed numerical algorithm guarantees global convergence. Also reconstructions gained with kt-FOCUSS, that conditionally requires low-resolution data, remain competitive for both applications yet with increased residual flickering in the temporal domain.
The evaluation against the vendor implementation clearly displays the drastic increase in reconstruction quality. However, due to restrictions on adjustable acceleration factors and not optimal sampling patterns on current systems it is not possible to exhaust the full potential of ICTGV^2 based reconstruction.
To assess the benefit of the proposed balancing between spatial and tem-

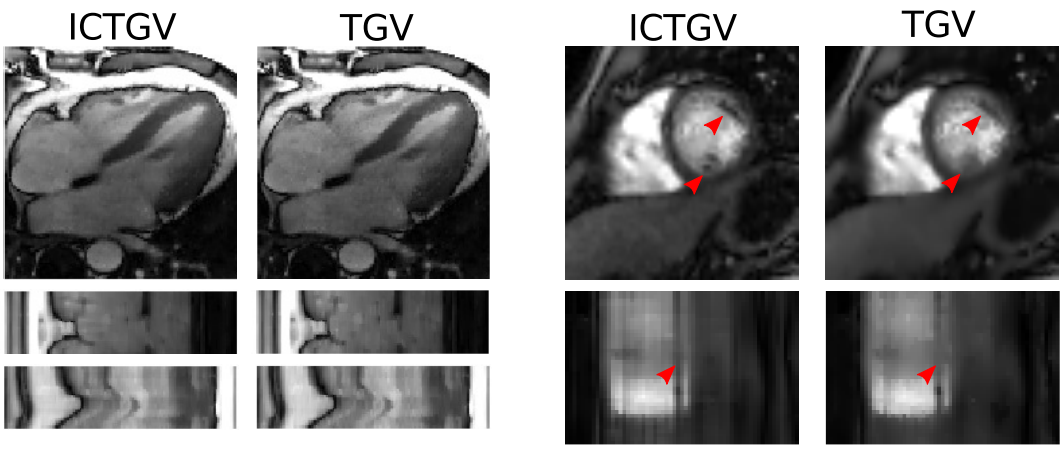

Figure 4.8: Comparison of ICTGV^2 vs TGV^2_β multi-coil reconstruction for CINE cardiac imaging (1st and 2nd column, $r = 16$) and cardiac perfusion imaging (3rd and 4th column, $r = 12$).

poral regularization, a comparison to spatio-temporal TGV$^2_\beta$ and TV$_\beta$ was carried out. A quantitative evaluation for different acceleration factors, test cases and error metrics shows the superiority of ICTGV^2, in particular for perfusion imaging (Table 4.2). The stronger improvement obtained with perfusion imaging can be explained by the observation that rapid intensity changes due to contrast inflow make a decomposition to different scales of temporal regularity even more beneficial. The comparison of Figure 4.8 further shows visual differences between ICTGV^2 and TGV reconstructions, which are apparent for the perfusion case, where small features are lost with TGV but still recovered with ICTGV^2. Overall, the experiments confirm that, even though the differences with CINE imaging might be subtle, ICTGV^2 is consistently superior to spatio-temporal TGV over different experimental setups.

In this context, it is also interesting to note that for spatio-temporal TV and TGV regularization, the parameter defining the ratio between temporal and spatial regularization, denoted by t, was optimized to achieve the best results. As can be seen in the plots provided in Fig. 4.10, the optimal value was found to be roughly in the interval [3,5] for both approaches, with a strong decrease of image quality for $t \to 0$ and $t \to \infty$. Hence a small

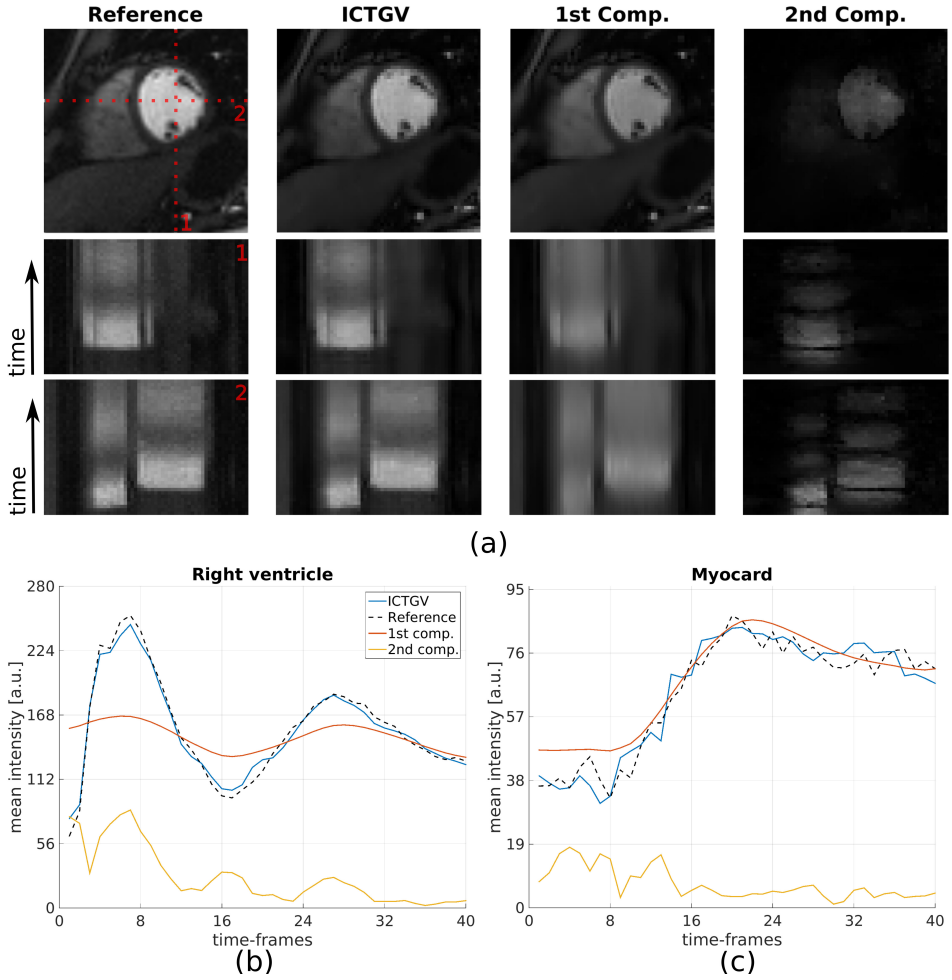

Figure 4.9: (a) Fully sampled reference (1st column), ICTGV^2 reconstruction (2nd column), 1st component (3rd column) and 2nd component (4th column) for a fixed reduction factor of $r = 8$ and a selected time-frame of a short axis perfusion dataset with the corresponding horizontal and vertical time-lines in the 2nd and 3rd row as indicated in the reference frame. Mean intensity change (magnitude) over time within the right ventricle (b) and the myocardium (c) due to the contrast agent for the reference (black-dotted line), ICTGV^2 reconstruction (blue solid line) and components (red and yellow solid line). The second component was rescaled for display purposes.

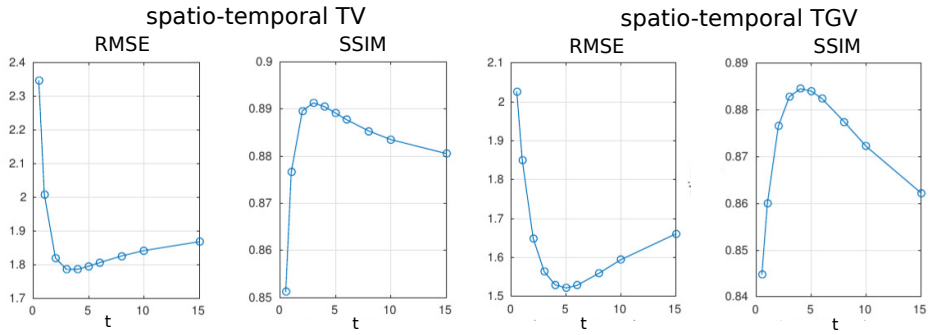

Figure 4.10: Quantitative evaluation of reconstruction results for different choices of the time-space-weighting t, for spatio-temporal TV (1st and 2nd column) and spatio-temporal TGV (3rd and 4th column), by means of RMSE and SSIM.

or large choice of t, which for spatio-temporal TV/TGV approximately yields pure spatial and pure temporal TV/TGV regularization, respectively, significantly worsens reconstruction quality. This indicates that both, pure spatial and pure temporal TV/TGV regularization are not sufficient to achieve state-of-the art results for undersampled dMRI reconstruction and a combined exploration of spatio-temporal redundancies is necessary.
An additional feature of the presented method is that a decomposition into two components is obtained. For cardiac perfusion imaging, slower portions of the intensity changes due to the passing contrast agent, e.g. in the myocardium, as well as changes in morphology are accumulated in the first component, while regions of fast intensity changes within the ventricles, liver and kidney are captured by the second component (see Fig. 4.9). This has similarities to a decomposition into a temporal component with correlated background (low-rank) and another with temporal changes (sparse). Yet our methods acts *locally*, while the low-rank assumption is inherently global. The local distribution of the image content to the two ICTGV^2 components depends on the model parameters, which were optimized for the overall reconstruction quality.

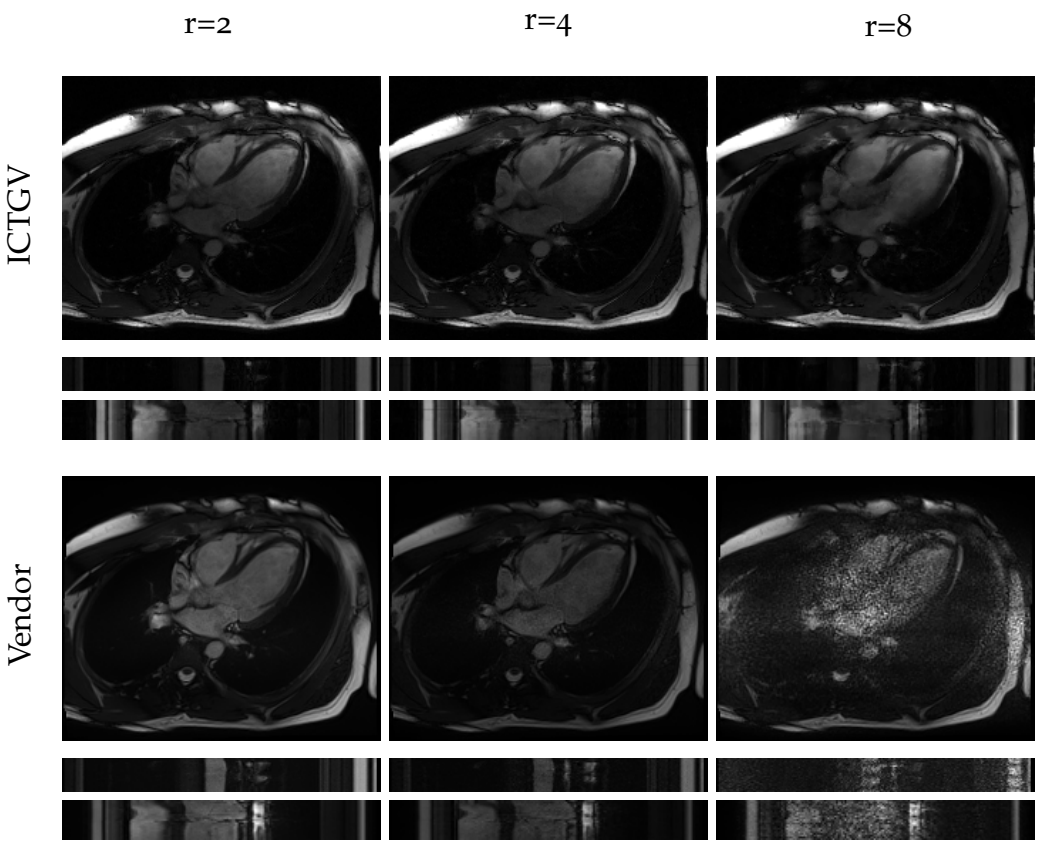

Figure 4.11: Reconstructions with ICTGV^2 (a-c) and Vendor implementation (d-f) for accelerated CINE cardiac imaging and T-PAT undersampling strategy ($r = 2, 4, 8$).

4.5 Conclusion

ICTGV^2 constitutes a powerful regularization functional for the investigated application to accelerated CINE cardiac and cardiac perfusion imaging. The experiments confirm a good visual representation of morphological details as well as contrast dynamics for acceleration factors of 12 and beyond. This enables CINE imaging in real-time without degrading spatial resolution or cardiac perfusion imaging with increased spatial resolution and coverage. A extensive comparison to existing state-of-art regularization strategies as well as spatio-temporal TGV and TV was carried out where

superior reconstruction quality was achieved especially for cardiac perfusion imaging. Since the two investigated modalities represent major classes for signal evolutions the general applicability of ICTGV^2 for dynamic MRI applications with yet application-specific model-parameters can be claimed. As an additional feature, the method allows a local separation of components beyond the paradigm of background and dynamic information and provides a model of different temporal scales of motion in MRI.

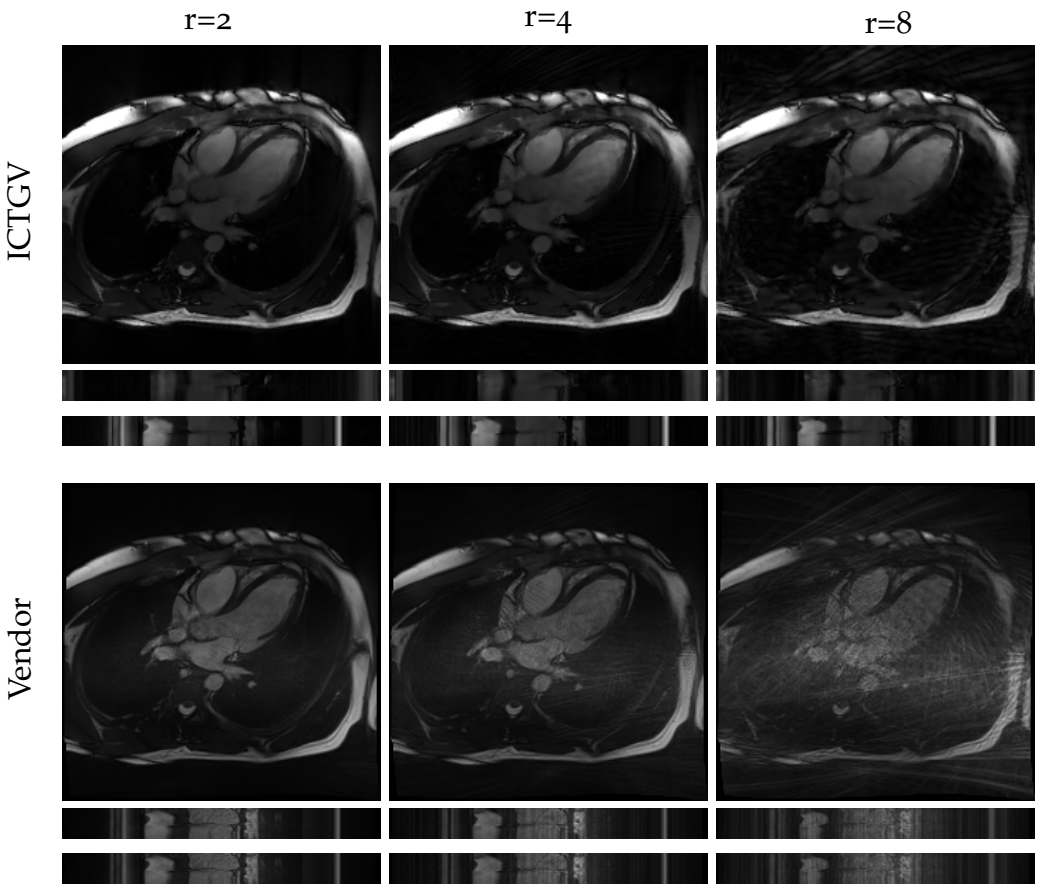

Figure 4.12: Reconstructions with ICTGV^2 and Vendor implementation for accelerated CINE cardiac imaging and radial undersampling strategy ($r = 2, 4, 8$).

5 Dynamic Perfusion Imaging

5.1 Introduction

Contrast-Enhanced CE MRI uses contrast agents (CA) with low molecular weight, based on gadolinium (Gd) compounds, to alter the signal contrast due to shortening T_1 and T_2 of blood and tissue. The CA is injected venously (suggested $0.1\,\mathrm{mmol\,kg^{-1}}$) with a short bolus ($\sim 3\,\mathrm{ml\,s^{-1}}$) followed by a saline flush. This bolus is then distributed in the vascular system and also diffusing into the *extra-vascular/ extra-cellular* (EES) or *leakage* space dependent on the permeability and surface area of the micro-vessels and the blood-flow. This generates a specific time-dependent signal change in dependence on blood flow and micro vessel permeability. Dynamic contrast-enhanced (DCE) MRI refers to T_1-weighted dynamic imaging of the CA distribution resulting in a bright depiction of the CA, in distinction to dynamic susceptibility contrast (DSC) MRI based on higher CA concentration and $T_2^\star$-weighted contrast, predominantly used in brain perfusion. In this chapter the proposed dynamic reconstruction framework is exemplarily applied to improve upon two important applications in dynamic contrast-enhanced MRI.

First, in the context of oncology where CE MRI is an important modality for diagnosing and characterization of tumors [132]. While in clinical routine a first qualitative analysis is based on acquiring only pre- and postcontrast images, i.e. before and after CA administration, to detect hyper- or hypointense tissue areas, a more meaningful analysis can be derived from the complete temporal course of the CA by means of semi-quantitative or quantitative analysis. Fully quantitative analysis can be achieved by fitting the signal intensity time-course to one of the recognized pharmacokinetic models (review of existing models given in [133]). The *extended Tofts model* [134]

assumes a two compartment model, i.e. blood plasma and the mentioned leakage space and is given as

$$c_{\text{tissue}}(t) = K_{\text{trans}} \int_0^t c_p(t) e^{\frac{K_{\text{trans}}(t-t')}{v_e}} dt' + v_p c_p(t), \tag{5.1}$$

where v_e and v_p denote the fractional volume of the CA in the leakage space and blood plasma, K_{trans} measured in $\text{ml}\,\text{min}^{-1}\,\text{kg}^{-1}$ a exchange rate constant between the two compartments and c_{tissue} and c_p the CA concentrations in $\text{mmol}\,\text{l}^{-1}$ at time-point t within the examined tissue and the blood plasma, resp. c_p is also often denoted as the *arterial-input-function* (AIF). Furthermore, the concentration is not linearly related to the measured T_1-weighted signal, such that additional T_1-mapping has to be performed, among other necessary correction such as B_1 inhomogeneity correction.
It was shown, that the quantitative maps, especially K_{trans} that is related to perfusion and tissue permeability, are valuable biomarkers for tumor characterization [135] with better repeatability than semi-quantitative methods [136]. However, the AIF should be sampled with a temporal resolution of less than 1 s [137] for accurate fitting , which is conventionally only achievable with decreased spatial coverage or spatial resolution at the increased risk to underestimate tumor "hot-spots" .
In this work a T_1-weighted 3D spoiled gradient-echo sequence with golden-angle stack-of-stars radial encoding, termed RAVE, is used [112] to continuously sample the CA uptake. This does not only allows for efficient timing of the acquisition with the CA administration but also for retrospective definition of the temporal resolution by grouping together the smallest possible Fibonacci number of spokes-per-time-frame. For conventional reconstruction, this, however, results in severe corruption with undersampling artifacts, that are eliminated with a ICTGV-based reconstruction.
The second investigated applications is dynamic contrast-enhanced MR angiography (CE-MRA), with the more specific and common target to image the rapid transit of the CA in arterial-venous malformations (AVM) [138]. An AVM is defined by the existence of a short-circuit between the arterial and venous system that bypassing the capillary bed and usually manifests itself in a complex network called *nidus*. This nidus can extend from a few millimeters to centimeters in diameter. The requirements for

accurate diagnosis, surgical planing, and monitoring is sufficient spatial and temporal resolution to correctly identify arterial feeder vessels, drainage patterns and vascular anomalies, e.g. aneurysms [139]. Clinically available state-of-art imaging methods rely on 3D encoded gradient echo imaging with view-sharing techniques and PI, such as *Time-resolved angiography With Interleaved Stochastic Trajectories* [140], [141] (TWIST), that enables temporal resolutions of $\sim 2\,\mathrm{s}$ for spatial resolutions of $\sim 1\,\mathrm{mm}^2$. The proposed approach to improve the temporal resolution is a combination of ICTGV reconstruction from golden-angle RAVE data, that enables temporal resolutions between 0.5 s to 0.8 s dependent on the number of spokes-per-frame used.
Before applying ICTGV based reconstruction on measured data, an evaluation based on numerical perfusion phantom simulations for training the regularization and model-parameters is given. Concurrently, a comparison to state-of-the-art methods, i.e. Golden-angle radial sparse parallel (GRASP) method [142], that is effectively the application of the k-t-SPARSE-SENSE [72] reconstruction to the described golden-angle radial data, and L+S reconstruction [90], was carried out. As for the measured data no ground-truth can be derived a comparison to conventional *gridding* reconstruction is given [142], [143]. Although these reconstructions are heavily corrupted with streaking artifacts, these appear noise-like and the temporal time-course is defined only by the data-fidelity.

5.2 Material and Methods

5.2.1 Numerical Simulations

Numerical simulations were carried out on the basis of a Sheep-Logan perfusion phantom used to evaluate GRASP reconstructions [102] for a specific kinetic parameter choice of $K_{\text{trans}} = (0.88, 0.63, 0.51, 0.26)/60\frac{1}{\text{min}}$ and $v_e = (1.43, 0.96, 0.76, 0.36)$ within four specific regions. As AIF a Parker model was used to compute data for 480 spokes in 60 s, resulting in a temporal resolution of $\Delta t = 0.125\,\mathrm{s}$ per spoke. This would be equivalent to sample 25 slices with TR of 5 ms. Additionally, data with the same temporal

resolution for 600 time-points was computed from a second abdominal phantom with different perfusion characteristics. For both phantoms 12-channel receiver coil sensitivities were simulated according to Biot-Savarts law to compute golden-angle data from each image time-point using the gpuNUFFT library [115]. Afterwards a realistic level of complex Gaussian noise was added to all channels with a target SNR of 30dB.
After parameter training reconstructions with ICTGV (optimal parameter $(s^{opt}, t_1^{opt}, t_2^{opt}) = (0.6423, 9, 1)$, GRASP and L+S were carried out for spf=$\{21, 13, 8\}$ equivalent to a temporal resolutions of $\Delta t = \{1\,\text{s}, 1.625\,\text{s}, 2.625\,\text{s}\}$. For the numerical simulations parameter evaluation for GRASP and L+S were carried out as follows:
$\lambda_L^{L+S} \in \{10^{-3}, 50^{-3}, 10^{-2}, 50^{-2}, 10^{-1}, 50^{-1}\}$, $\lambda_S^{L+S} \in \{50^{-3}, 10^{-2}, 50^{-1}, 10^{-3}\}$, $\lambda_{\text{GRASP}} \in \{0.1, 0.5, 1, 1.5, 2, 5, 10\}$ for each acceleration. For ICTGV the model parameter training was carried out as described in Sec. 3.4. The comparison as well as the parameter selection is given according to PSNR, that is well defined for the numerical phantom.

5.2.2 Abdominal dynamic T1w-Contrast-Enhanced MRI

Two dataset for abdominal T1w DCE MRI were evaluated. The first was made available together with GRASP reconstruction code from NYU[1]. As stated in [142], the HIPPA compliant data was acquired with the described RAVE sequence using a golden-angle acquisition scheme on a whole-body 3T scanner (Magnetom Verio, Siemens Healthcare, Erlangen, Germany) equipped with a 12-element receiver coil array and the following imaging parameter: 30 slices with 3mm slice-thickness, spatial resolution of $1 \times 1\text{mm}^2$, imaging matrix of 384×384, 600 spokes with 768 samples per spoke, TR/TE/FA=3.83ms/1.71ms/12°, resulting in a temporal resolution of Δt= 0.115s per stack-of-spokes and an acquisition time of TA= 69s.
The second RAVE dataset was made available at the courtesy of Tobias Block and was measured on a 1.5T scanner (Mangetom Avanto, Siemens Healthcare, Erlangen, Germany) with a 6-element body coil with the following imaging parameters: 38 Slices with 3mm slice-thickness, spatial resolution of $1.5 \times 1.5\text{mm}^2$, imaging matrix of 256×256, 2100 spokes with 512 samples

[1] http://cai2r.net/resources/software/grasp-matlab-code

per spoke, TR/TE/FA=4.27ms/1.88ms/12°, resulting in a temporal resolution of Δt= 0.162s per stack-of-spokes and an acquisition time of TA= 340s. For both datasets the CA injection was initiated intravenously with 10mL of gadopentate dimeglumine (Gd-DTPA) (Magnevist, Bayer Healthcare, Leverkusen) followed by a 20mL saline flush, both injected at a rate of $2\text{mL}\,\text{s}^{-1}$.

5.2.3 Time-resolved Magnetic Resonance Angiography

After obtaining informed consent, a scan of seven AVM patients was performed using both the TWIST and RAVE techniques on a 3T scanner with a 32-channelhead-neck coil, approved by the responsible ethics committee. First, one half dose ($0.1\text{ml}\,\text{kg}^{-1}$) equaling 8mL of Dotarem contrast media was injected with $3\text{mL}\,\text{s}^{-1}$ with a consecutive saline flush of 20mL at the same rate and TWIST imaging was performed with the following imaging parameters: 26 Slices with 3.5mm slice-thickness and 15.5% slice-oversampling, spatial resolution of $1.05 \times 1.05\text{mm}^2$, imaging matrix of 240×230, 75% phase-oversampling and iPAT-factor 4 (GRAPPA), BW= 650Hz/pixel, TR/TE/FA=3.01ms/1.1ms/23°, resulting in a temporal resolution of Δt= 2.1s per imaging volume.
Two hours later, the second half of the contrast agent was injected at $6\text{mL}\,\text{s}^{-1}$ with a consecutive saline flush of 30mL at the same rate, and the RAVE measurement was acquired with the following imaging parameters: 26 Slices with 3.5mm slice-thickness and 15.5% slice-oversampling, spatial resolution of $1.05 \times 1.05\text{mm}^2$, imaging matrix of 320×320, 700 spokes with 640 samples per spoke, TR/TE/FA=3.85ms/1.79ms/23deg, resulting in a temporal resolution of Δt= 0.115s per stack-of-spokes and an acquisition time of TA= 80s.

5.2.4 Reconstruction

For reconstruction the first DCE and the angiography dataset were compressed via SVD-based channel compression to 6 and 9 virtual channels. For the angiography dataset, data from receive channels with dominant

streaking artifacts in the time-averaged reconstructions were removed manually after visual inspection as described in [112] and K-space calibration was performed with the available correction data as described in [111]. The temporal coverage of the second DCE- and the angiography dataset was reduced to 600 measured spokes covering the essential part of the contrast dynamic. This can be selected easily by peak detection of the k-space-center energy over time, which corresponds to highest enhancement due to the CA.
ICTGV reconstruction was carried out with the GPU based AVIONIC framework with the regularization- and model parameters found optimal for reconstructing the numerical phantom data with similar noise-behavior as the measurement data. GRASP and L+S reconstructions were carried out for the same parameters found optimal in the numerical training. However, the reconstruction quality was checked individually for the same parameter ranges as used for the numerical phantoms. For GRASP and L+S reconstruction the algorithms in the primal-dual implementation as described in Sec. 3.5 were used due to unresolved scaling issues in the non-Cartesian implementation provided by the authors of the GRASP and L+S method. For ICTGV additional reconstructions were carried out with increased and decreased weighting on the regularization to study the effect on the temporal behavior in connection to the image quality in the spatial domain.
For the first DCE dataset, ICTGV, GRASP and L+S reconstructions were computed from 8 spokes-per-frame corresponding to a temporal resolution of $\Delta t = 0.92$s and for the second DCE dataset from 13 ($\Delta t = 2.1$s), 8 ($\Delta t = 1.3$s) and 5 ($\Delta t = 0.81$s) spokes-per-frame. For the angiography dataset reconstructions were computed from 8 ($\Delta t = 0.92$s) and 5 ($\Delta t = 0.58$s) spokes-per-frame. For the angiography dataset all acquired slices were reconstructed individually to compute a coronal dynamic maximum-intensity-projection (MIP) from the baseline-subtracted image sequences.
For all studied datasets an evaluation is given by comparing the mean signal intensity in characteristic regions (3×3 voxels) to the gridding reconstruction and displaying reconstructions for time-frames in baseline, arterial phase and venous phase. Selected characteristic regions were the aorta (AO) and portal vein (PV) to study the enhancement for the DCE datasets and apical and basal arteries, nidus and apical vein in a coronal slice containing the nidus for the angiography dataset.

5.3 Results

Fig. 5.1 and Fig. 5.2 display closeups of the simulation results for the numerical Sheep-Logan and abdominal DCE phantom.There, a selected arterial phase time-frame from reconstructions with ICTGV, GRASP and L+S from 21, 13 and 8 spokes-per-frame is compared to the noiseless ground-truth. Each phantom has four regions with AIF and characteristic tissue enhancement for which the temporal evolution for all methods and ROIs is displayed in Fig. 5.3 and Fig. 5.4 for two different temporal resolutions. Table 5.1 summarizes the evaluation of the reconstruction quality in terms of PSNR values according to Def. 8.1.0.14 and the noise-free numerical reference. All methods were trained to match the true time-course of the characteristic signal enhancement, where a higher temporal resolution leads to better fidelity of the temporal evolution. In the spatial domain however, ICTGV reconstruction yields almost perfect results, while GRASP and L+S still exhibit residual noise and undersampling artifacts which is also reflected by the quantitative evaluation with an increase of PSNR around 10dB for ICTGV. Fig. 5.5 displays the temporal evolution of the locally different decomposition into components (magnitude) for ICTGV based reconstruction for both numerical phantoms and all four regions.

Table 5.1: PSNR values in dB for both numerical DCE phantoms and ICTGV, GRASP and L+S reconstructions from 21, 13 and 8 spokes-per-frame. The PSNR values are computed with respect to the interpolated time-points in the noise-less ground-truth.

Phantom 1			
	ICTGV	GRASP	L+S
21 spf	52.98	45.88	44.85
13 spf	52.86	45.67	45.02
8 spf	51.77	45.26	44.36
Phantom 2			
21 spf	59.11	50.09	47.47
13 spf	57.70	49.14	47.17
8 spf	55.84	47.94	46.43

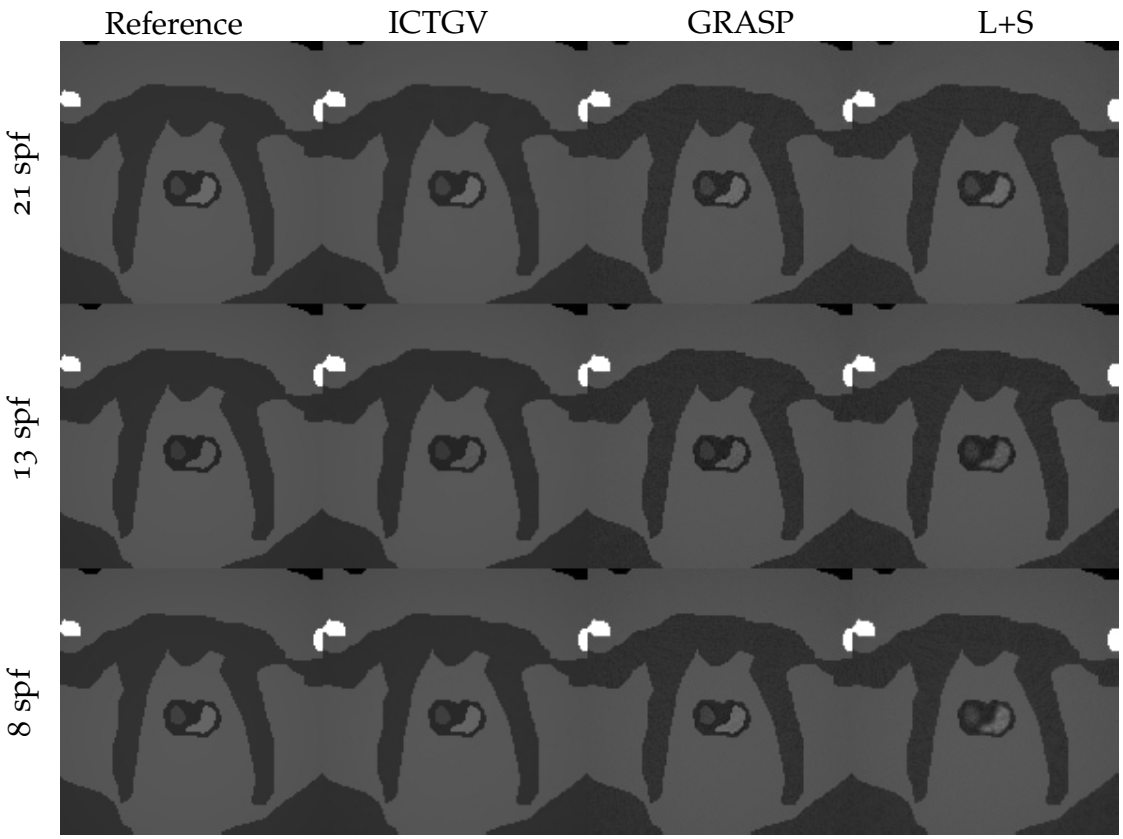

Figure 5.1: Close-up of simulation results from numerical perfusion phantom with simulated temporal resolutions of 8, 13 and 21 spokes-per-frame (spf). Comparison between ICTGV, L+S and GRASP reconstruction against the reference for a selected time-frame.

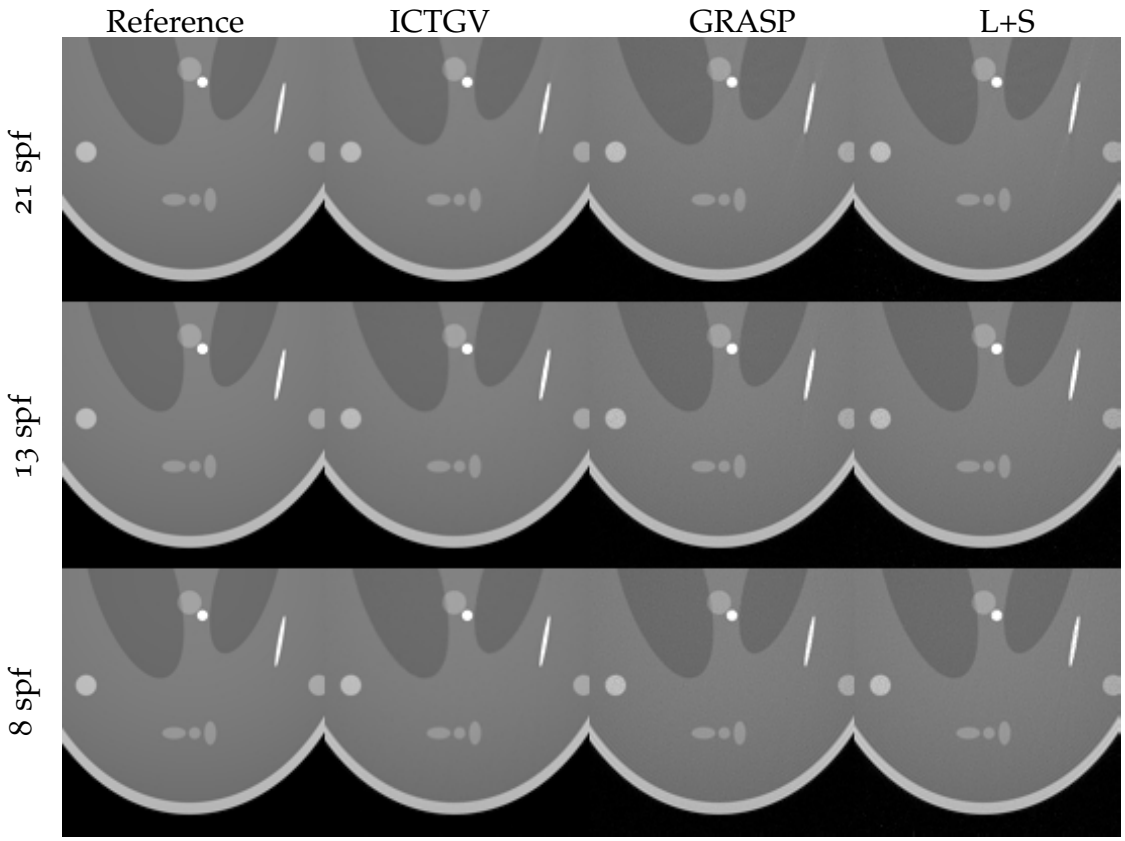

Figure 5.2: Close-up of simulation results from numerical perfusion phantom with simulated temporal resolutions of 8, 13 and 21 spokes-per-frame (spf). Comparison between ICTGV, L+S and GRASP reconstruction against the reference for a selected time-frame.

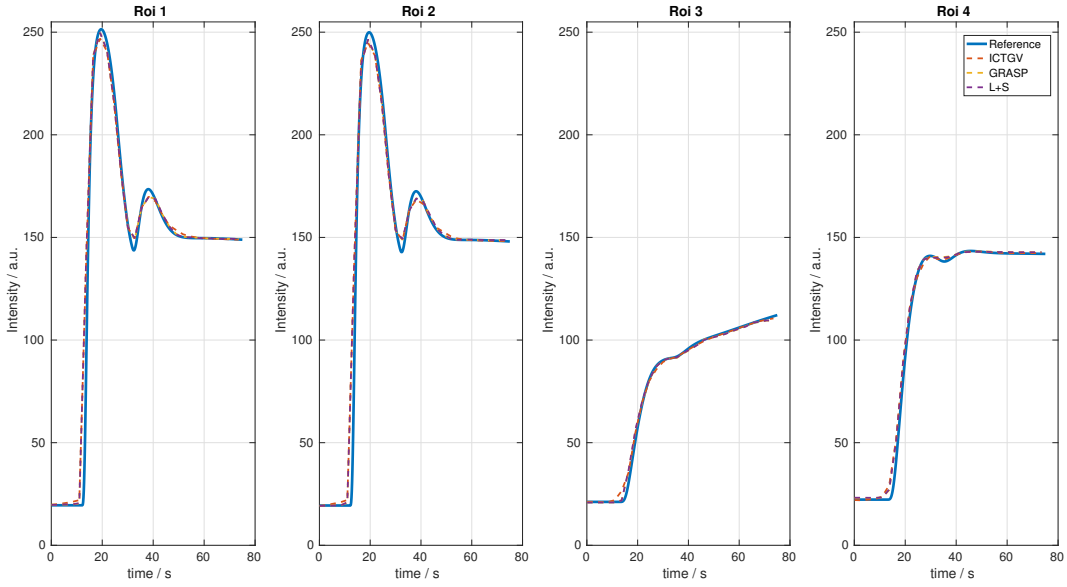

(a) 21 spokes-per-frame

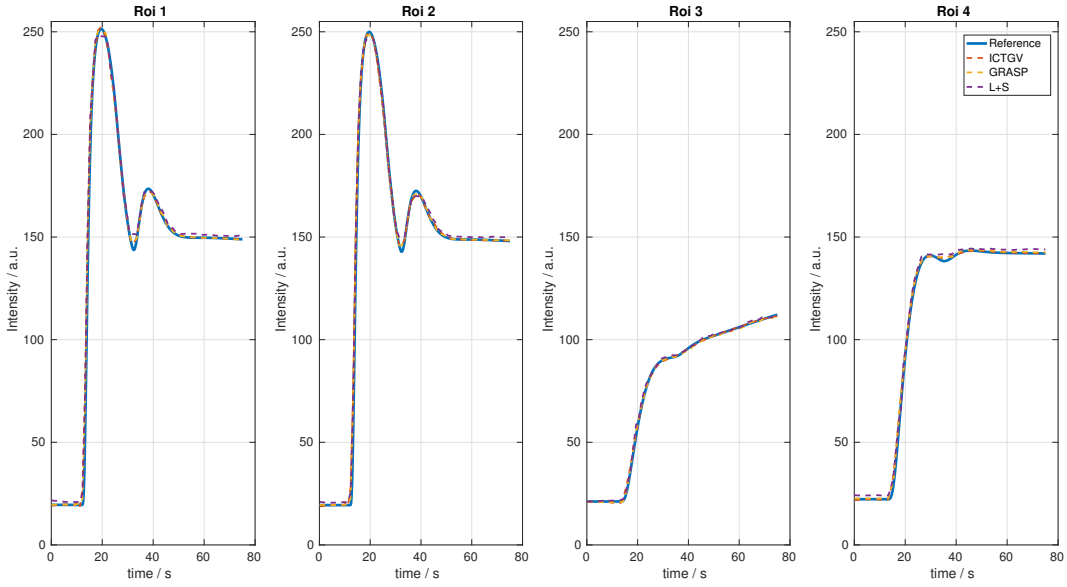

(b) 8 spokes-per-frame

Figure 5.3: Simulation results for the first numerical perfusion phantom with simulated temporal resolutions of 21 (a) and 8 (b) spokes-per-frame (spf). The plots compare the mean signal intensity variation within selected regions-of-interest between reference, ICTGV, GRASP and L+S reconstruction against the true reference.

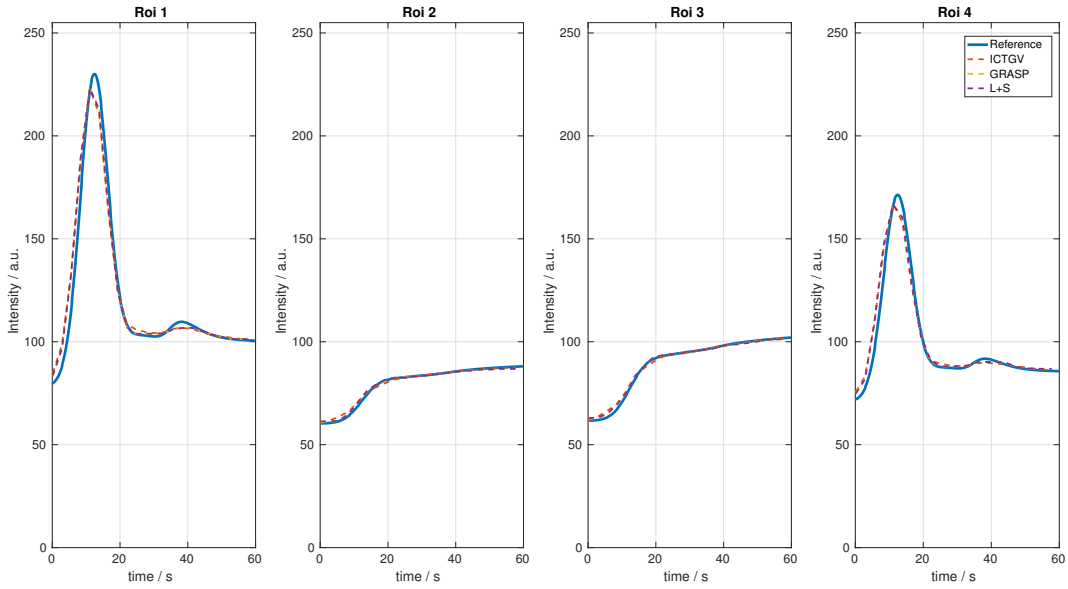

(a) 21 spokes-per-frame

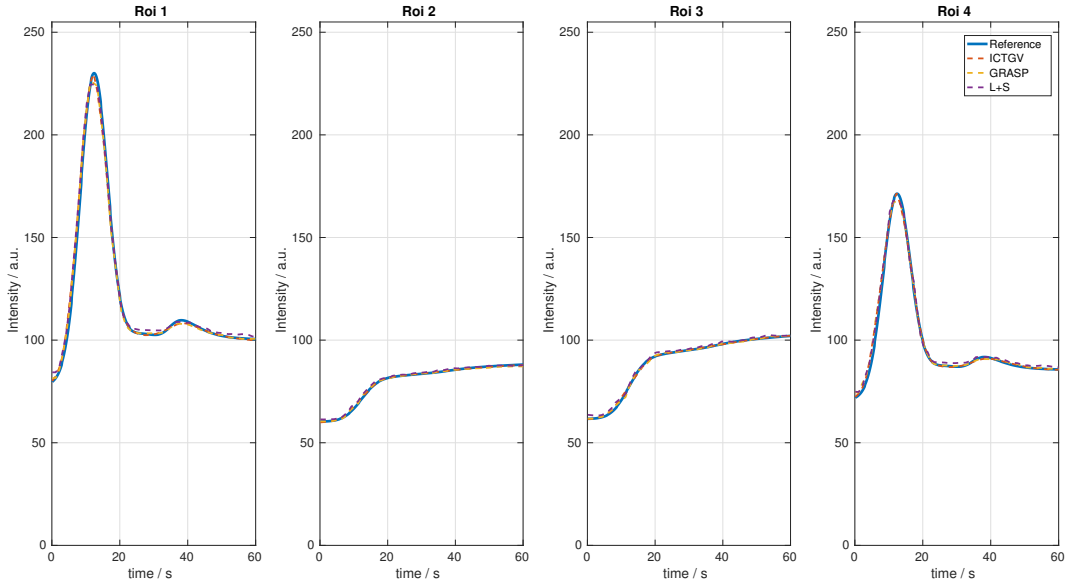

(b) 8 spokes-per-frame

Figure 5.4: Simulation results for the second numerical perfusion phantom with simulated temporal resolutions of 21 (a) and 8 (b) spokes-per-frame (spf). The plots compare the mean signal intensity variation within selected regions-of-interest between Reference, ICTGV, GRASP and L+S reconstruction against the true reference.

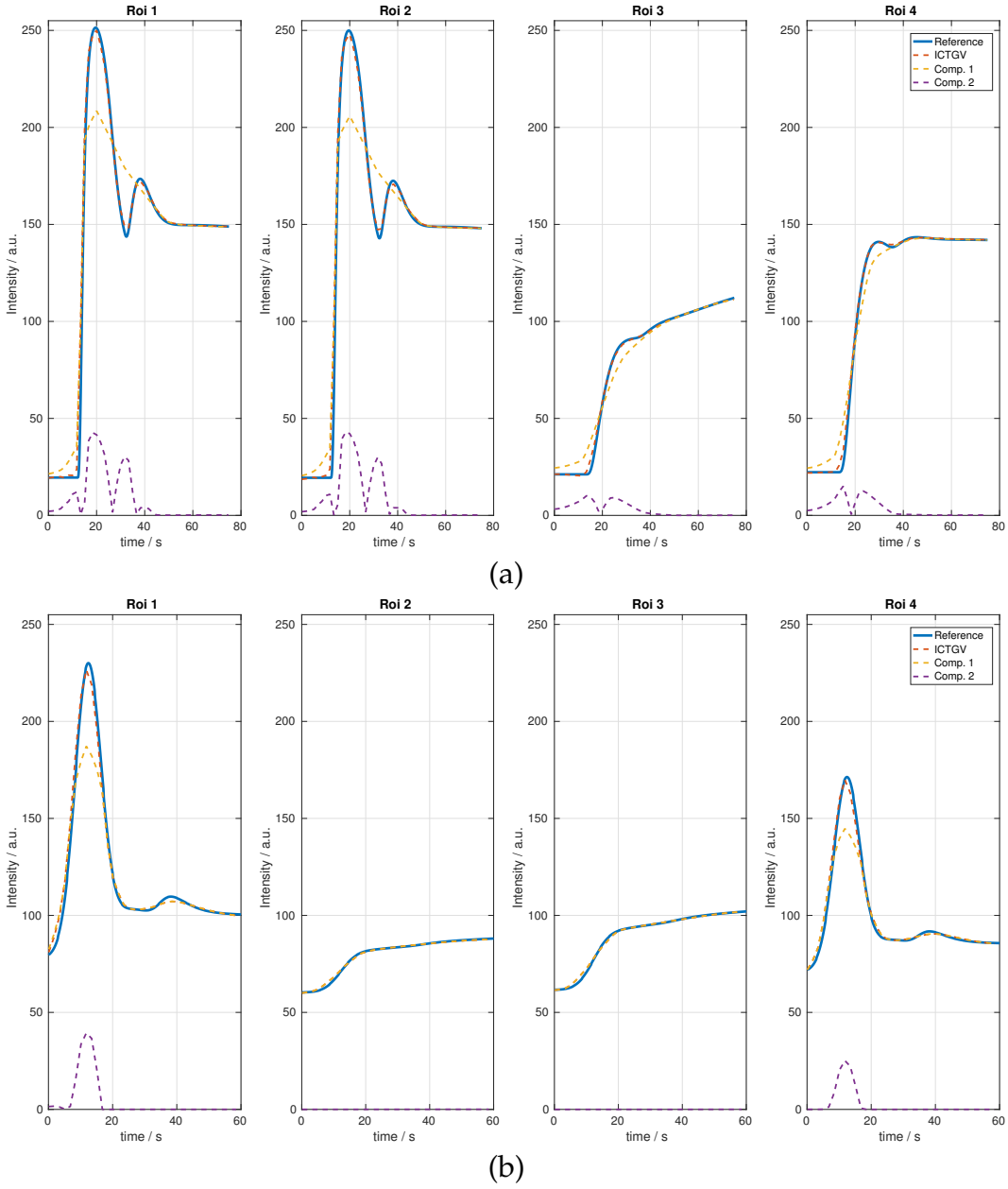

Figure 5.5: ICTGV based decomposition into components for regions with different temporal dynamics for the numerical prostate (a) and Sheep-Logan phantoms (b).

A comparison between ICTGV, GRASP and L+S reconstruction from 8 spokes-per-frame for the first DCE dataset is displayed in Fig. 5.6 for selected time-frames in baseline, arterial and venous phase with a closeup in Fig. 5.7. The corresponding temporal signal evolution within the AO and PV together with the gridding reconstructions are displayed in Fig. 5.8. As before, all reconstructions match the signal evolution corresponding to the gridding reconstruction with pronounced second pass. In comparison to ICTGV reconstruction GRASP and L+S reconstructions are disturbed in the spatial domain due to insufficient noise-suppression and residual streaking artifacts.
Fig. 5.9 shows the influence of ICTGV reconstruction with high, optimal and low weighting on the regularization on the image quality in the spatial domain in Fig. 5.10 and resp Fig. 5.11 the corresponding decomposition into components for the AO and PV. For high influence of the regularization no residual streaking artifacts are visible, while structures tend to blur. More importantly, the temporal evolution does not follow the gridding reconstruction anymore and peak values are diminished, which also influences the decomposition. For low influence of the regularization, noise is enhanced and streaking artifacts disturb the image quality while the temporal evolution matches to the gridding reconstruction. Optimal regularization fulfills both requirements of matching the temporal evolution while yielding sharp image structures with noise- and streaking-artifact suppression for a characteristic component decomposition. As visible in Fig. 5.10 and Fig. 5.11 the influence of streaking artifacts gets enhanced mainly in the second component for low influence in the regularization.

In Fig. 5.12 ICTGV reconstructions from the second DCE dataset are compared for different factors of 13, 8 and 5 spokes-per-frame again for baseline, arterial and venous phase together with the depiction of a temporal cross-section including the AO in Fig. 5.13 and the mean signal evolution in the AO and PV in Fig. 5.14. With the increase in temporal resolution residual streaking artifacts become more visible but still a high quality in terms of depiction of spatial details and fidelity of the temporal evolution can be preserved for temporal resolutions.

Reconstructions from a coronal slice containing the AVM with 5 spokes-per-frame are displayed for baseline, arterial and venous time-frames again for different weightings on the regularization in Fig. 5.15 and comparing

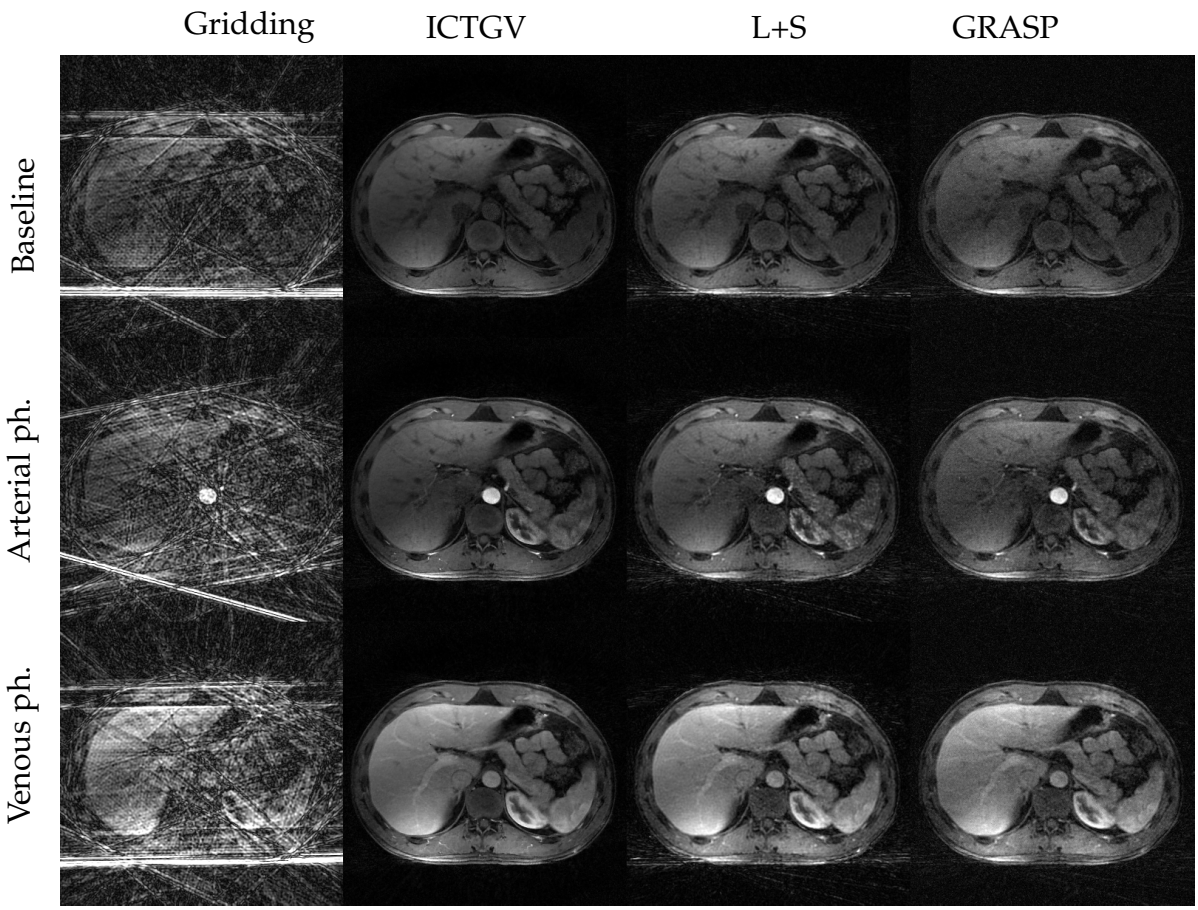

Figure 5.6: Comparison on gridding, ICTGV, L+S and GRASP reconstruction 8 spokes-per-frame for optimal reconstruction parameters for the first DCE dataset. Frames are displayed for three characteristic time-points (baseline, arterial phase, venous phase).

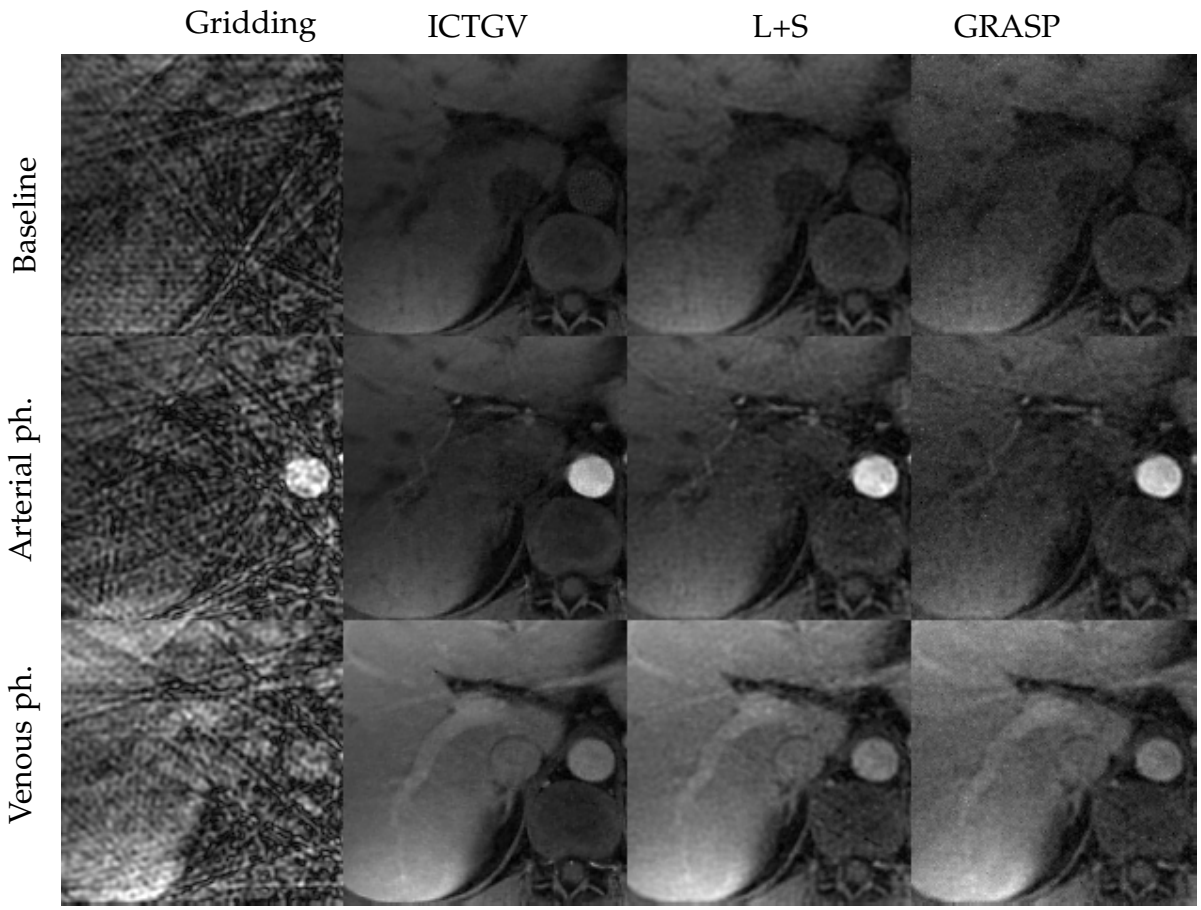

Figure 5.7: Closeup comparison of gridding, ICTGV, L+S and GRASP reconstruction from 8 spokes-per-frame for optimal reconstruction parameters for the first DCE dataset. Frames are displayed for three characteristic time-points (baseline, arterial phase, venous phase).

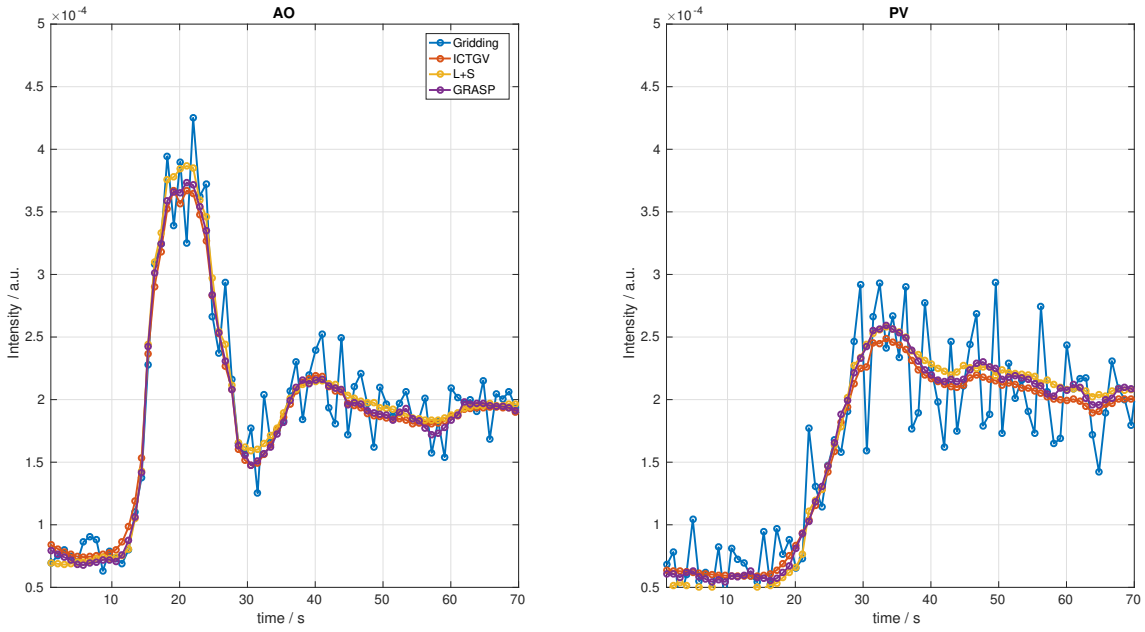

Figure 5.8: Comparison of the intensity time-course within the aorta (AO) and portal vein (PV) for gridding, ICTGV, L+S and GRASP reconstructions.

to GRASP and L+S reconstruction in Fig. 5.18. Corresponding temporal evolutions in four regions (apical and basal artery, nidus and apical vein) are shown in Fig. 5.16 for different weightings, decomposition into components in Fig. 5.17 and comparison to GRASP and L+S in Fig. 5.19. Similar to the observations for the abdominal DCE datasets, optimal weighting for ICTGV reconstruction yields results with high quality depiction of imaging structures with an acceptable level of residual noise and streaking while preserving the temporal fidelity. Reconstructions from GRASP and L+S are corrupted with higher levels of noise and residual streaking while still preserving the temporal fidelity.
Finally, selected time-frames of the dynamic MIP computed from all slices that show the contrast enhancement within the nidus with a temporal resolution of $\Delta t = 0.58$s are displayed in Fig. 5.20. Enhancement within the arteries is clearly distinguishable before enhancement within the nidus.

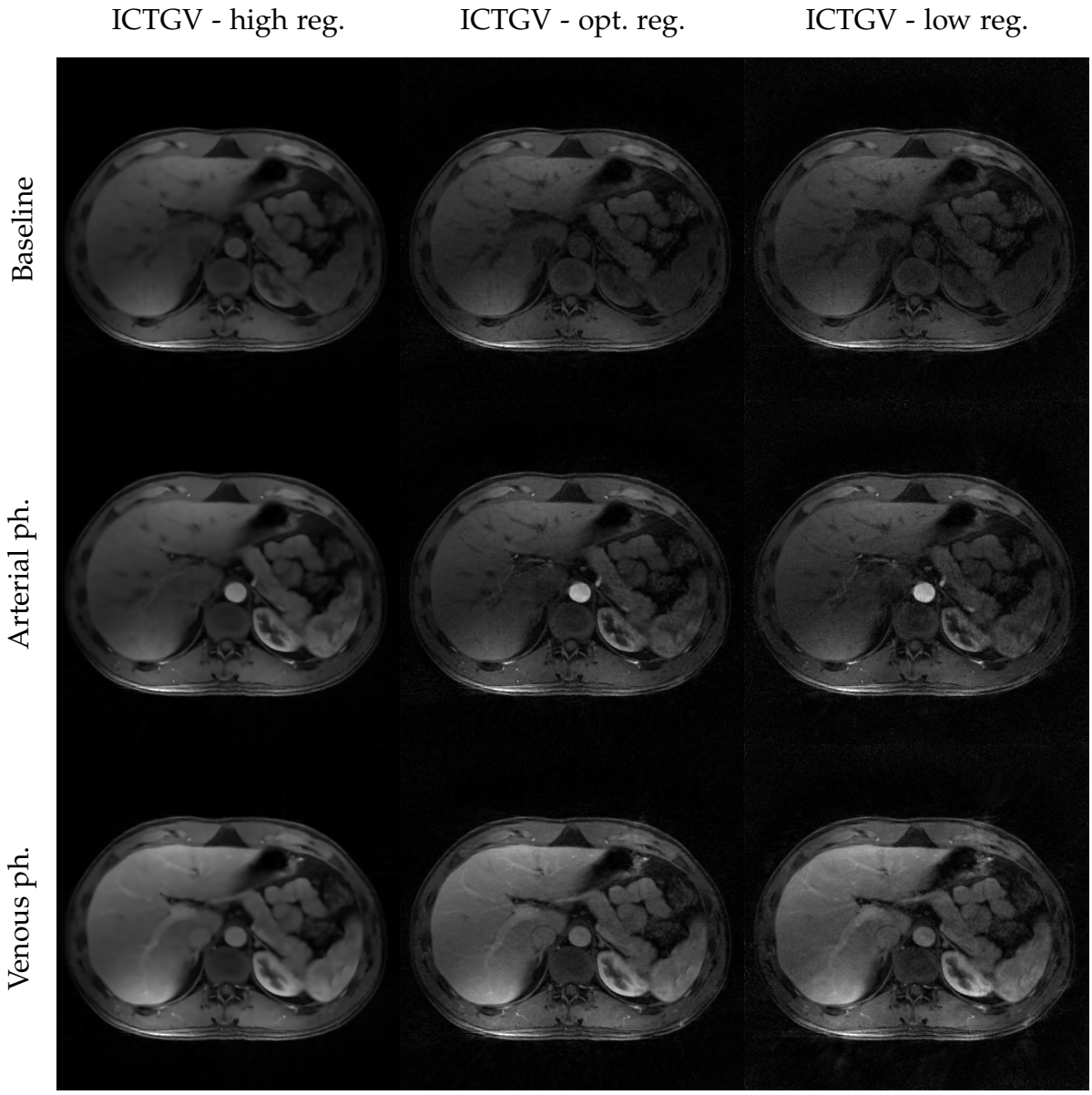

Figure 5.9: Comparison of ICTGV reconstructions for different data-fidelity weights.

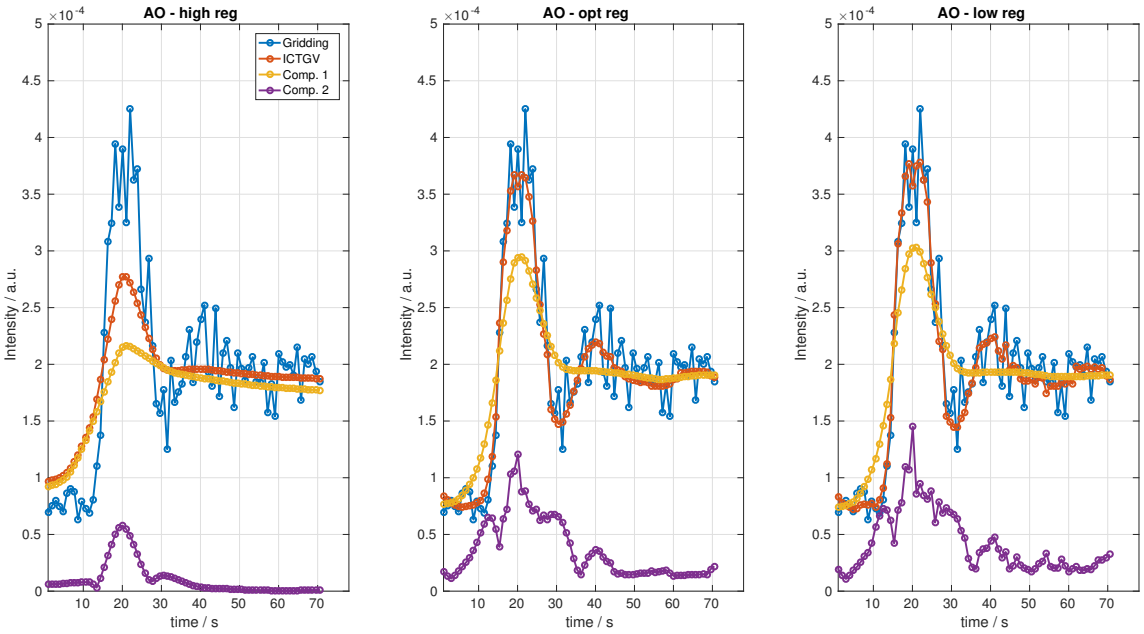

Figure 5.10: Comparison of the intensity time-course within the aorta (AO) for ICTGV reconstructions and different data-fidelity weights and corresponding decomposition.

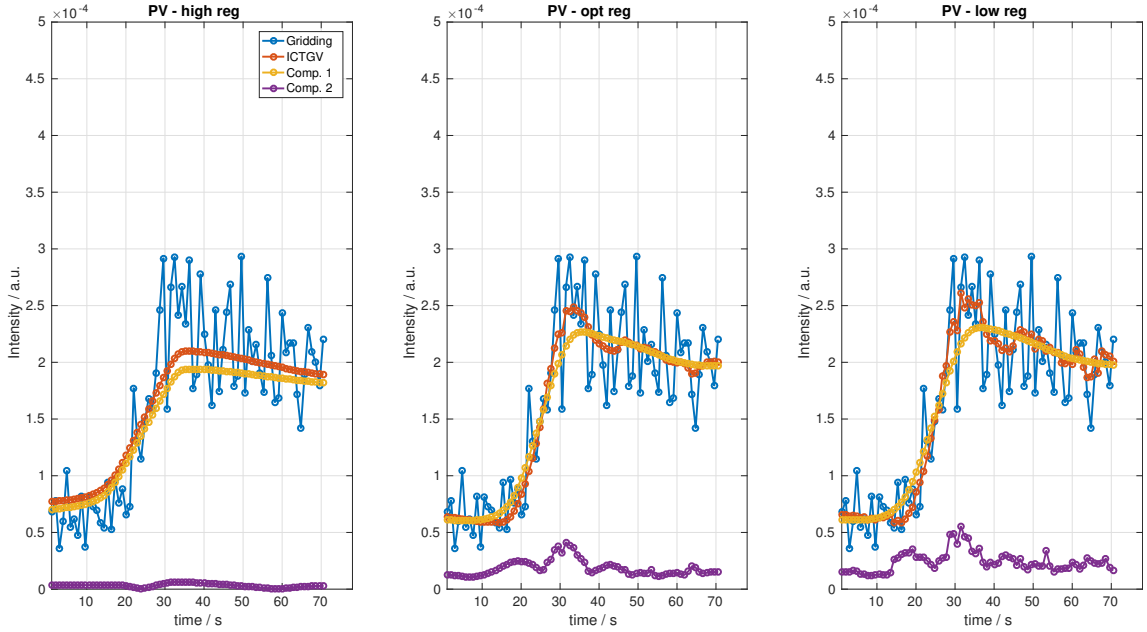

Figure 5.11: Comparison of the intensity time-course within the portal vein (PV) for ICTGV reconstructions and different data-fidelity weights and corresponding decomposition.

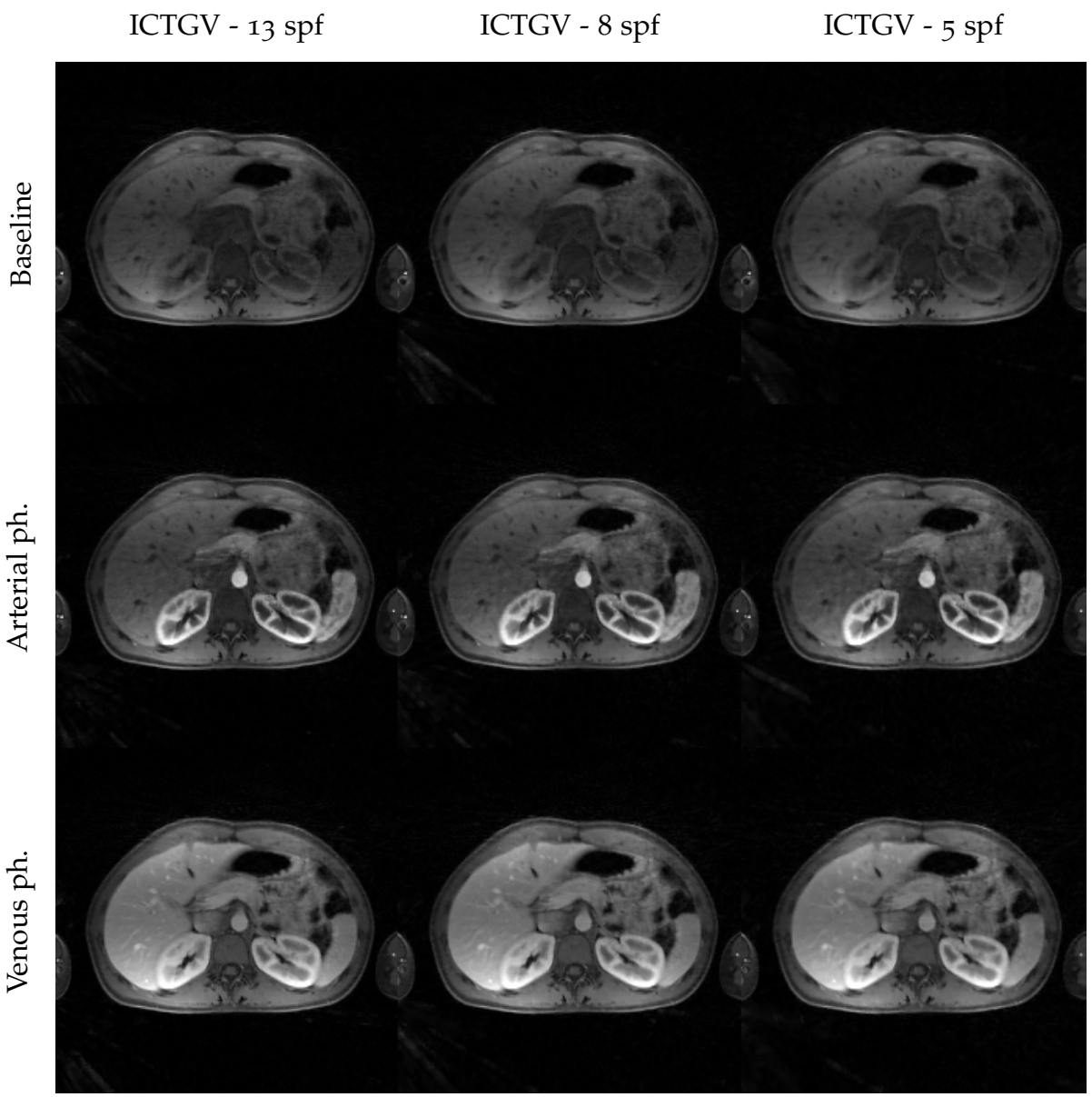

Figure 5.12: Comparison of ICTGV reconstructions for 13, 8 and 5 spokes-per-frame for three temporally aligned characteristic time-points (baseline, arterial phase, venous phase).

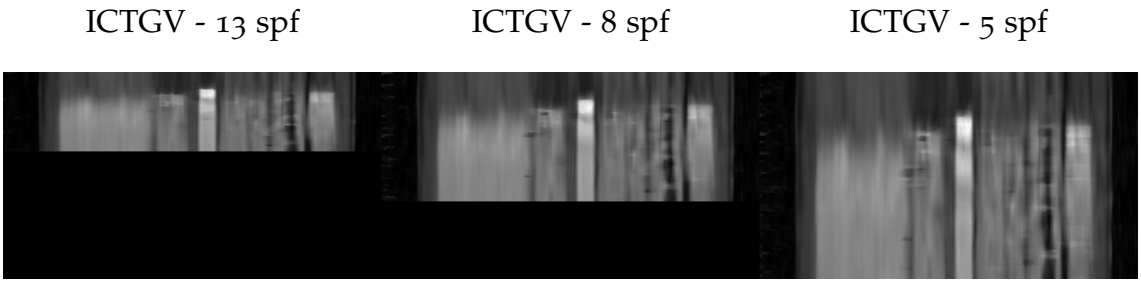

Figure 5.13: Comparison of ICTGV reconstructions for 13, 8 and 5 spokes-per-frame with a temporal cross section.

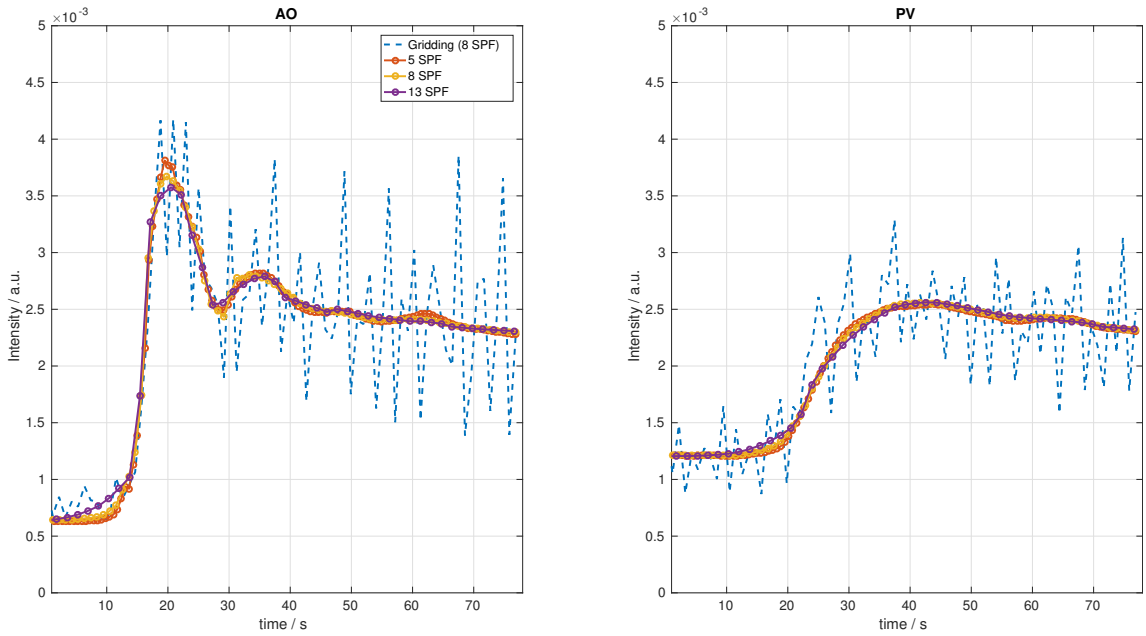

Figure 5.14: Comparison of the intensity time-course within the aorta (AO) and portal vein (PV) for ICTGV reconstruction from 13, 8 and 5 spokes-per-frame for the second DCE dataset to a gridding reconstruction from 8 spokes-per-frame.

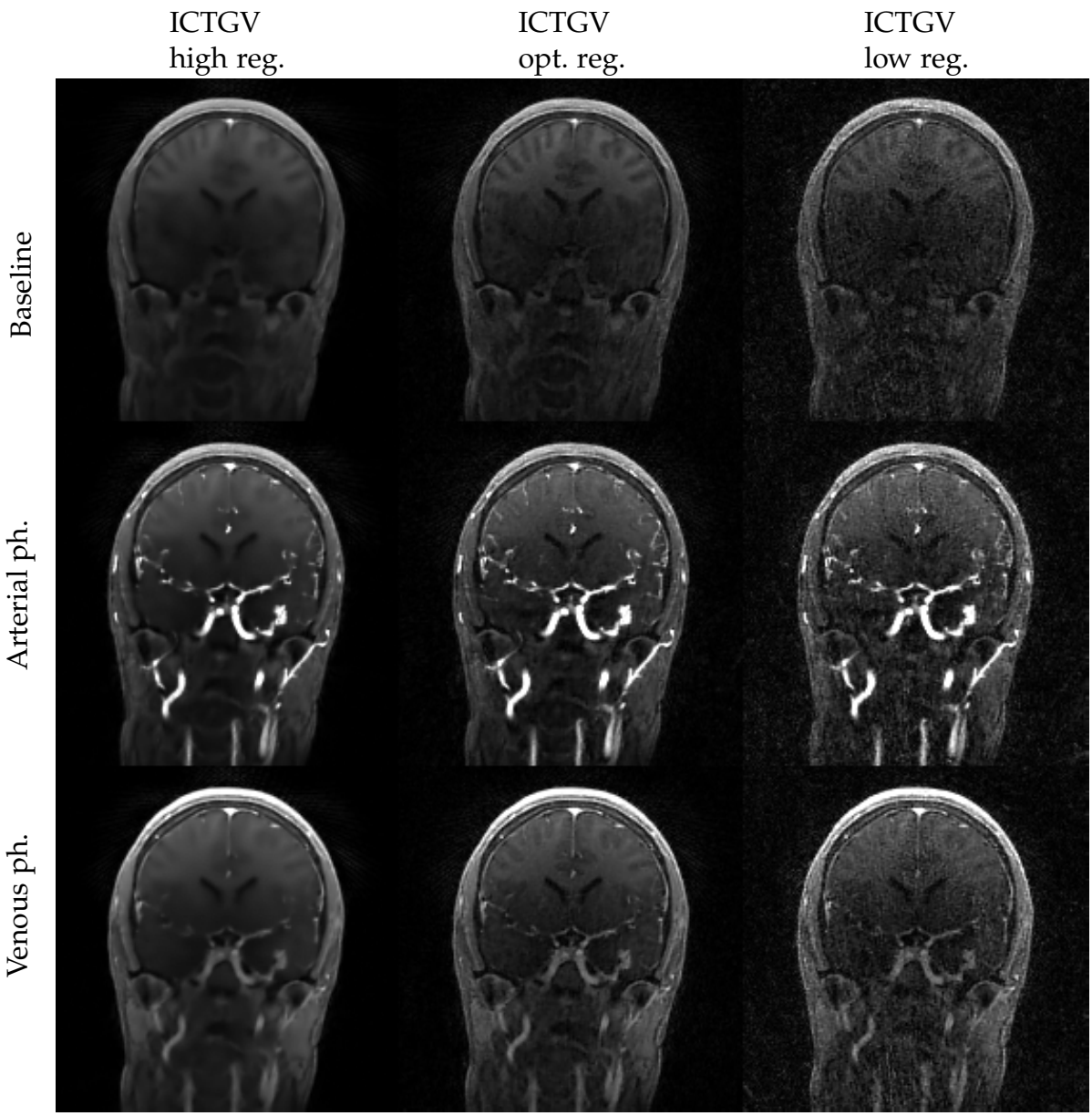

Figure 5.15: Comparison of ICTGV reconstructions for different data-fidelity weights and GRASP reconstruction from 5 spokes-per-frame for characteristic time-points.

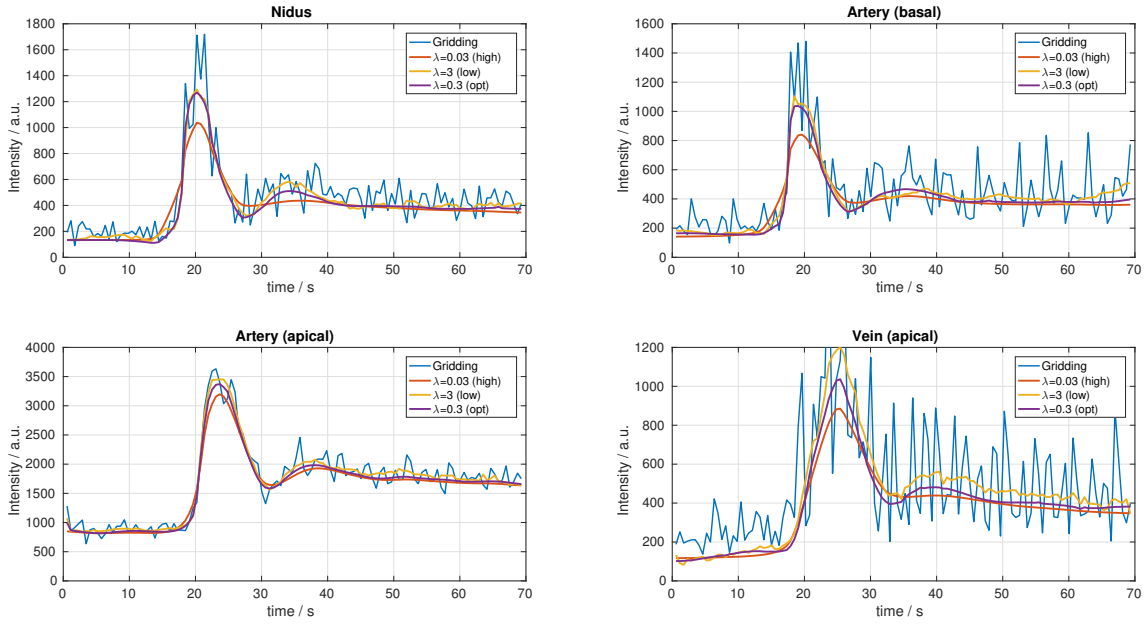

Figure 5.16: Comparison of the intensity time-course within different characteristic regions (nidus, basal and apical arteries and vein) for ICTGV reconstruction from 5 spokes-per-frame for the angiography dataset and different data-fidelity weights.

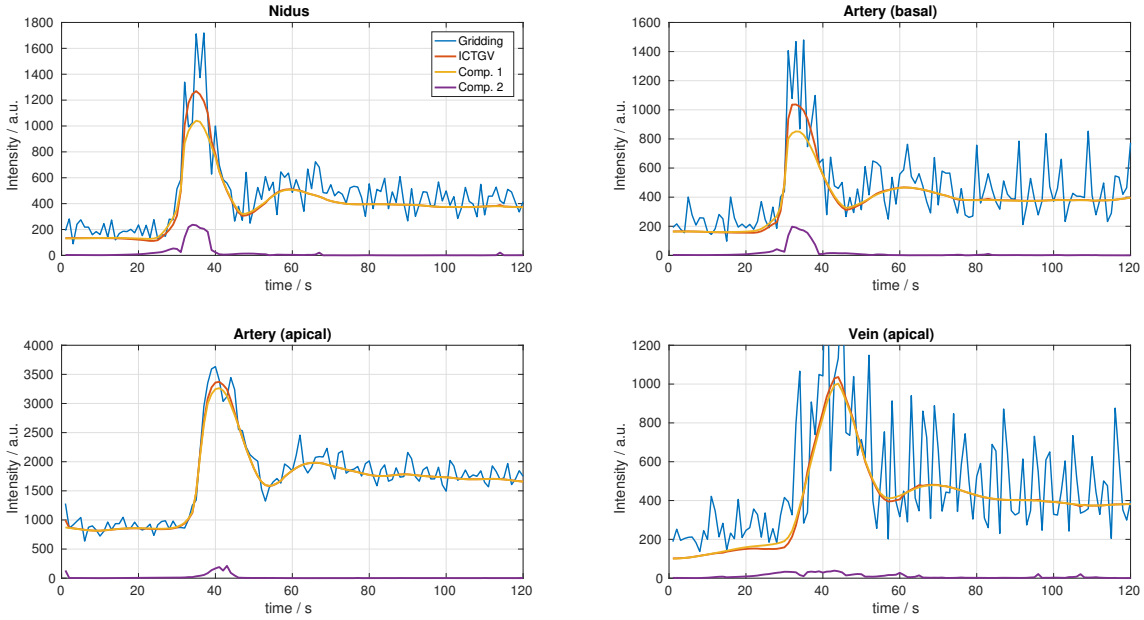

Figure 5.17: Display of the intensity time-course of ICTGV reconstruction and corresponding decomposition within different characteristic regions (nidus, basal and apical arteries and vein) from 5 spokes-per-frame for the angiography dataset.

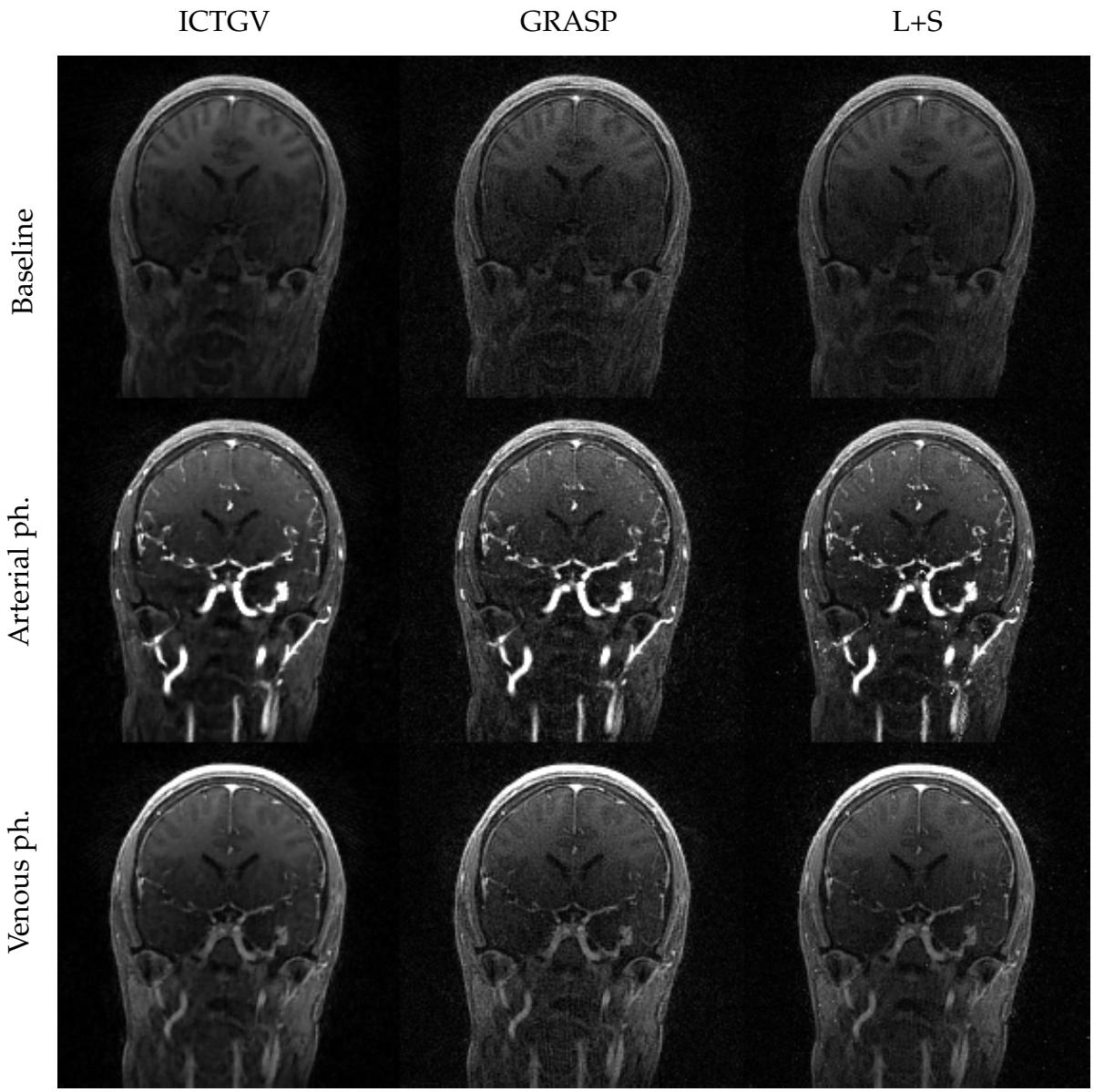

Figure 5.18: Comparison of ICTGV against GRASP and L+S reconstructions from 5 spokes-per-frame for characteristic time-points.

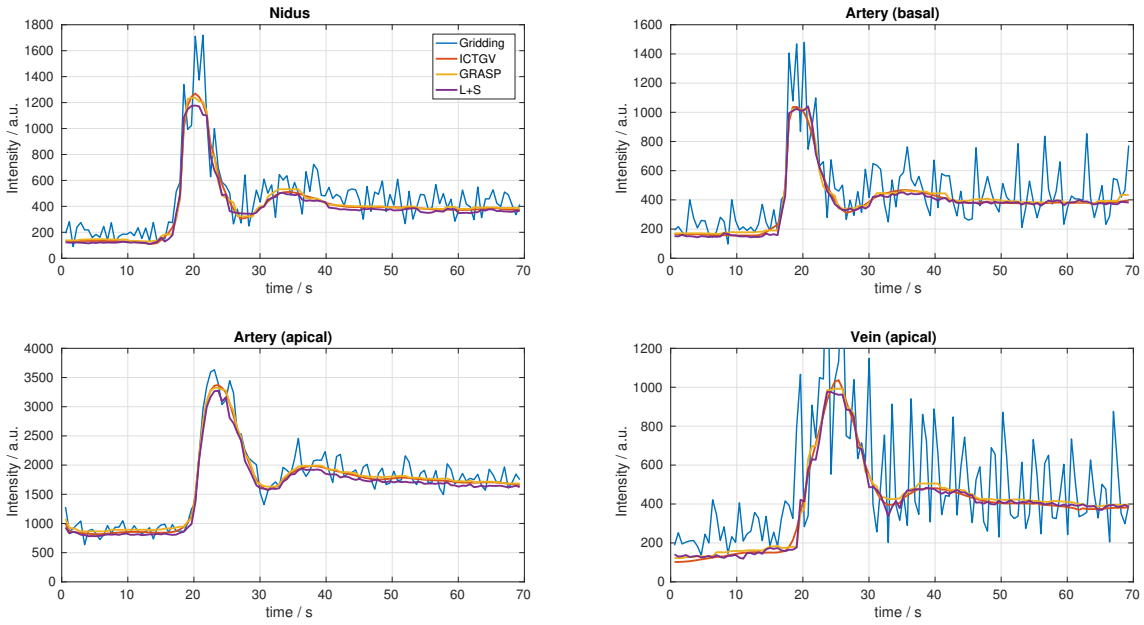

Figure 5.19: Display of the intensity time-course of ICTGV against gridding, GRASP and L+S reconstruction within different characteristic regions (nidus, basal and apical arteries and vein) from 5 spokes-per-frame for the angiography dataset.

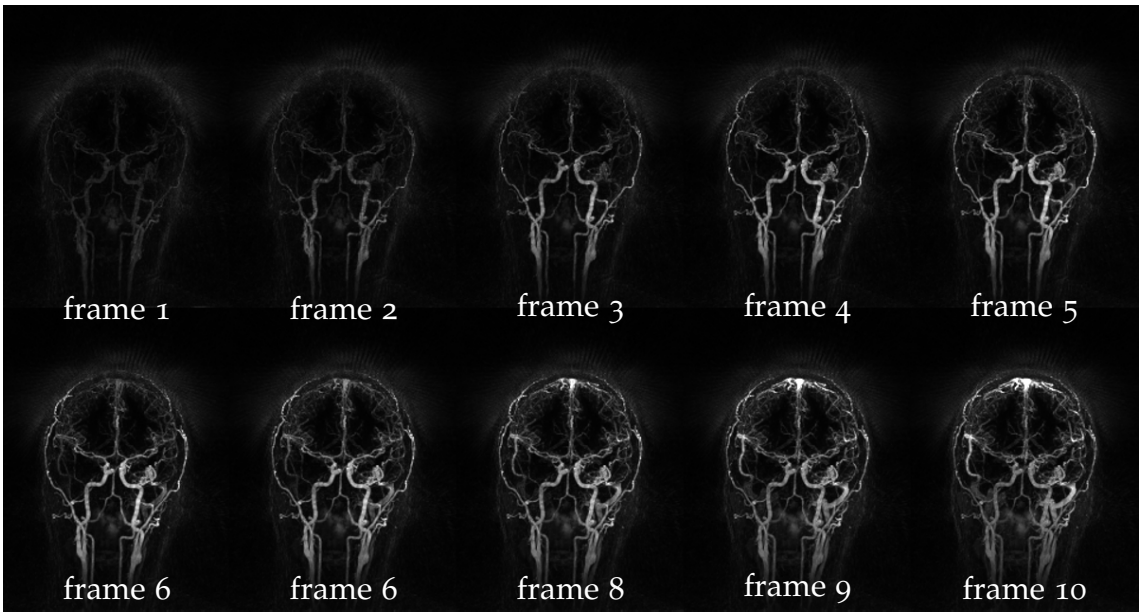

Figure 5.20: Dynamic maximum-intensity-projection (MIP) for ten selected time-frames displaying the enhancement within the nidus with 0.58s temporal resolution (5 spokes-per-frame) from all reconstructed slices after baseline subtraction.

5.4 Discussion and Conclusion

In literature high temporal resolution was found to be important for correct determination of the AIF [137] ($\Delta t \leq 1\,\mathrm{s}$), exact parameter mapping with complex models [144] or lesions with rapid enhancement [143] ($\Delta t \leq 2\,\mathrm{s}$). In the simulation as well as the measured data, this holds true for 8 spokes-per-frame corresponding to a temporal resolution of $\Delta t = 1\,\mathrm{s}$. A high temporal resolution, however, comes at the cost of increased excess of residual undersampling artifacts and noise-enhancement. For all methods under investigation it is possible to weight the data-fidelity strongly enough to preserve the correct temporal behavior at the cost of decreased suppression of noise and residual undersampling artifacts. When the regularization is too strongly weighted it is possible to almost completely eliminate noise and artifacts, while diverging from the temporal fidelity. It is therefore crucial to find an optimal balancing parameter λ to fulfill both requirements. For the numerical simulations it was found that for a given noise-level λ can be used for different acceleration factors due to the inherently scaling of the density compensation to a lower number of data per temporal frame as described in Sec. 3.7.1.
For ICTGV reconstruction the model-parameter training based on the numerical phantoms with fixed λ and noise-level yields a specific choice for DCE applications and therefore a characteristic decomposition into components reflecting locally varying requirements for spatio-temporal regularization. This enables for higher weighting on the regularization while still preserving locally different temporal evolutions with enhanced quality of the spatial depiction. For GRASP-based reconstruction no additional parameters for the temporal weighting is required since this methods omits spatial regularization that comes at the cost of the decreased ability to suppress noise and undersampling artifacts in the spatial domain. High regularization for GRASP still results in improved image quality with loss in temporal fidelity, since this effectively accounts for temporal averaging with improving the SNR. Interestingly, no mayor improvement of L+S decomposition over GRASP could be observed, which means that for a global decomposition no additional information could be exploited.
Reconstruction parameters for the numerical setting could be transferred to the in-vivo measurements that exhibit a similar noise-behavior. For these

datasets care has to be taken to correctly pre-process the data such as dismissing data from erroneous receive channels. This is most faithfully avoided by excluding receive-channels that are distant to the iso-center as described in [112].
The evaluation against the reference methods was evaluated under the condition that the temporal fidelity for each method matches either the gridding reconstruction or the true numerical reference. Under this condition ICTGV based reconstruction yields an improvement in image quality in the spatial domain with improved residual artifact- and noise suppression.
For abdominal DCE imaging this poses a basis for further improvement in quantitative evaluation according to pharmako-kinetic models. This however requires further considerations for additional pre-processing like B_1^+-, slice-profile and concentration corrections and is subject to future research.
In the case of time-resolved MRA an almost four-fold increase in temporal resolution as compared to state-of-the-art imaging with the TWIST technique with the same imaging geometry and spatial coverage is feasible with acceptable image quality and correct temporal behavior.For this application high temporal resolution is hypothesized to yield a diagnostic improvement by increased detectability of feeding arteries to the AVM, which is part of an ongoing patient-study.
Limitations to the proposed method are the complexity and consequently long reconstruction times in the order of 5 to 10 minutes per slice using coil-compression with optimized GPU code and sufficient primal-dual iterations. This point might be overcome by improved algorithmic design with better convergence behavior like [145] or learned reconstruction procedures [146]. Also the robustness of the weighting-parameter λ in the case of more drastically varying SNR scenarios is still an issue and requires further reasoning. Furthermore, long reconstruction times and extensive consumption of memory impedes the possible reconstruction of 3D-temporal volumes with a further expected improvement in image quality.

6 Quantitative MRI

6.1 Introduction

The defined goal of quantitative MRI (qMRI) is the extraction of tissue characteristic quantifiable information from a MRI scan. This requires the formulation of a model that connects the measured MRI signal with physical and physiological properties. It is then possible to use these quantities as *biomarkers*, given sufficient statistically significant difference between healthy and diseased tissue conditions. Biomarkers serve as a very valuable tool for monitoring the status, change, or chronic condition of a pathology independent on the used scanner platform. The following chapter is concerned with the imaging of longitudinal relaxation time T_1, based on the *Variable-Flip-Angle* VFA method with the focus on accelerated imaging and accurate, robust parameter quantification.
The T_1 time is intrinsically connected to the water content, the macromolecule concentration, water binding and water proton exchange. Thus, for brain imaging T_1 times for myelin in white matter (WM) are shorter than for gray matter (GM). Demyeliniation and increase in water content due to multiple sclerosis therefore increases T_1, where significant differences to normal controls were reported in [147]. Further applications for T_1 mapping include the assessment of myocardial infarction [148] and tissue remodeling [149], normalization of contrast agent concentration in DCE MRI among others. For an extensive review about important applications for T_1 mapping the reader is referred to [150].
Many approaches were developed to measure the longitudinal relaxation time. While the Inversion-Recovery IR method, based on the early work of Hahn [151] for NMR measurements with robust MRI in-vivo protocols ([152]), can be considered as ground-truth, measurement times are far beyond clinical feasibility. The *inversion-recovery Look-Locker* (IRLL method

[153] is based on the IR method but leads to decreased measurement times by applying a train of low flip angle pulses with defined spacing after an initial inversion pulse.
The investigated VFA method on the other hand uses 3D spoiled steady-state gradient echoes with constant TR, constant TE and different flip angles θ_p [154] and is also termed DESPOT (Driven-equilibrium single-pulse observation of T_1) [155]–[157]. For the described assumptions the well-known analytical expression of the signal-intensity S is dependent on M_0 and T_1 for a given flip-angle θ_p as follows:

$$S_p(u = (M_0, T_1)) = M_0 \frac{1 - e^{-\frac{T_R}{T_1}}}{1 - \cos\theta_p e^{-\frac{T_R}{T_1}}} \sin\theta_p \tag{6.1}$$

In theory the VFA approach requires only two "ideal" flip angles for most correct estimation of a specific T_1 value [158], however more measurements with varying flip angle are needed to improve the accuracy for a broader range of T_1 values. It was investigated that a larger set of flip angles increases the accuracy for the physiological range of T_1 [159], while it decreases the accuracy for a specific T_1 value gained from a two-angle-measurement. In [158] acquisition of up to 10 flip-angles in the context of neurological brain T_1 mapping are proposed based on a *genetic algorithm* approach, giving the basis for choosing a set of angles used in this work, i.e. $\theta = \{2, 3, 4, 5, 7, 9, 11, 14, 17, 22\}^\circ$ for both simulations and real data acquisitions. The non-linear signal model in Eq. 6.1 can be rearranged to facilitate the computation of M_0 and T_1 by a linear fitting routine, that is yet biased by noise [160] for low SNR regimes.
Sufficient SNR is also necessary to improve the well-posedness of the corresponding fitting problem, which can be achieved by additional averaging with increased scan time or larger slice-thickness with increased sensitivity to partial-volume effects. This problem is addressed by improved regularization of the inversion problem as described later.
Additionally, the VFA method assumes an exact flip-angle over the whole FOV, which is not the case with pronounced spatially-dependent deviations from the nominal flip-angle at field strengths of 3 T. To account for this issue the estimation of a B_1 map is necessary as preprocessing procedure. While the Double-Angle-Method DAM [161] describes an important and

robust approach for in-vivo estimation of the active B_1 field more recent approaches are less time-consuming. In this work the Bloch-Siegert Method (BSM) [162] with an highly accelerated extension [163] based on variational modeling is used.
Although, necessary corrections as described above are considered, it was found in a study [164] that T_1 values vary across sites and in-vivo measurements up to 30%, due to incomplete spoiling and inaccurate B_1 mapping for IR, IRLL and VFA, where the later tends to overestimate and IRLL to underestimate T_1. In [165] differences between measurements from different vendors, measurement methods, scanner type, sample positions and field strength measured with a standardized phantom were reported. These studies suggest individual calibration of the used methods against the inversion recovery reference method to improve the accuracy of T_1 mapping.
With the established method of VFA for T_1 mapping the requirement of imaging several 3D volumes with high resolution, SNR, and several flip-angles is time-consuming and therefore leads to higher error-proneness due to patient motion, such that acceleration of the measurement process is highly desirable. Furthermore, requirements for high resolutions with whole-brain coverage biases the parameter estimation due to increased noise levels. These two problems are addressed by firstly, sub-sampled data-acquisition and ICTGV-based dynamic reconstruction that exploits the information redundancy in the parametric dimension and secondly the point of robust parameter fitting under varying SNR conditions is addressed by proposing an image-space model-based reconstruction MBR framework. The later is based on the iteratively regularized Gauss-Newton algorithm with additional multi-spectral variational regularization. The proposed combination yields a two-step procedure addressing the goal of fast and robust biomarker imaging exemplified for T_1 estimation based on the VFA method.

6.2 Proposed Reconstruction from Accelerated Radial VIBE Data

In order to achieve a scan-time reduction, sub-sampling is performed in each of the parametric measurements. For T_1 estimation from VFA measurements the aim is to determine the acceptable acceleration potential in order to reduce the overall scan time. This is investigated on the basis of 3D golden-angle radial stack-of-stars RAVE acquisitions [112]. Compared to conventional Cartesian VIBE acquisition this has the advantage that sub-sampling can be performed for each slice by grouping different amounts of Fibonacci-numbers of spokes, instead of sub-sampling in the two phase-encoding dimensions, where for VIBE measurements the number of k_z-phase encodings is typically smaller.
The successive reconstruction of the parameter maps is carried out in a two-step procedure. First, a ICTGV reconstruction is performed on the under-sampled spatio-parametric datasets to remove aliasing artifacts and perform denoising. To this end the corresponding ICTGV model parameters (see Sec. 3.3.5), that are model-free in the sense that no *explicit* information about the VFA signal equation is used, are trained on numerical phantom data for this specific application with locally different smooth signal behavior in the parametric dimension. The smoothness assumption is not enforced particularly but is implicitly contained in the piece-wise smoothness assumption of the spatio-temporal TGV functionals. The reconstruction can be carried out in a convex setting. In the second step the parameter maps are estimated with a iteratively regularized Gauss-Newton IRGN framework employing additional multi-spectral regularization strategies to further stabilize the parameter estimation. This is adverse to MBR in k-space, where the model-specific equation is included in the MRI forward model and a solution is computed directly.
The present work can be integrated into the context of existing approaches for accelerated qMRI methods. ”Two step-procedures” include the seminal work by Doneva et. al [166], where regularization was trained from specific signal-models to mitigate under-sampling artifacts for IRLL and multi-echo spin-echo MESE measurements, that effectively laid the basis for the concept of MR fingerprinting [167]. In [168] a temporal-smoothness CS reconstruction is carried out for accelerated Cartesian VFA reconstructions

and in [169] low-rank or locally low-rank [170] and sparsity constraints are employed, usually followed by conventional parameter estimation on a voxel-by-voxel basis. Important works for k-space based MBR are, e.g. accelerated T_2 estimation from radial [171] and Cartesian [172], [173] fast-spin echo data, or T_1 mapping from single-shot IR-LL radial data [174], with additional estimation of the B_1 map in [175], [176]. The later works also employ the IRGN approach, that is used in this work for the image based MBR approach.

MBR in image space

The generic reconstruction problem for general qMRI problems, with N_p parametric maps $u = (q_i)_{i=1,\cdots,N_p}$, e.g. $u = (M_0, T_1)$ can be written as follows:

$$\mathrm{u}^\star = (q_i^\star)_{i=1,\cdots,N_p} = \arg\min_u \frac{\lambda}{2} \sum_p \|S_p(u) - I_p\|_2^2 \tag{6.2}$$

Here $S_p(u)$ denotes the signal in image space according to the model S as for VFA given in Eq. 6.1, for a given parameter p and I_p the reconstructed image for parameter p. Since $S_p(u)$ is in general non-linear, a solution is proposed according to the Gauss-Newton strategy. To this end $S_p(u)$ needs to be linearized at a given point u_k with a first order Taylor approximation, i.e.

$$S_p(u) \approx S_p(u_k) + DS_p|_{u=u_k}(u - u_k) \tag{6.3}$$

with $DS_p|_{u=u_k}$ being the differential operator of $S_p(u)$ evaluated at u_k. Eq. 6.2 can then be rewritten as

$$\mathrm{u}^\star{}_{k+1} = \arg\min_u \frac{\lambda}{2} \sum_p \|DS_p u - \tilde{I}_p\|_2^2, \quad \tilde{I}_p = I_p + DS_p u_k - S(u_k) \tag{6.4}$$

for the solution of the k-th Gauss-Newton step. In order to control the convergence an additional step size penalty and regularization on the parameter-maps is added, yielding the following reconstruction problem.

$$\mathrm{u}^\star{}_{k+1} = \arg\min_u \frac{\lambda}{2} \sum_p \|DS_p u - \tilde{I}_p\|_2^2 + \frac{\delta}{2}\|u - u_k\|_2^2 + \mathcal{R}(u) \tag{6.5}$$

As a choice for the regularization functional $\mathcal{R}(u)$ two versions are proposed. Firstly, TGV^2 regularization on each parameter map separately ($\mathrm{TGV}^2_{\mathrm{sep}}$)and secondly a coupling between the multiple parameter maps with multi-channel TGV^2 using a point-wise Frobenius norm ($\mathrm{TGV}^2_{\mathrm{frob}}$). The later promotes joint sparsity of the edge sets of both parameter maps that are considered to have structural similarity. The $\mathrm{TGV}^2_{\mathrm{frob}}$ norm has been employed for denoising of multi-channel images in [67] or for the joint reconstruction of PET and MR images in [177]. The corresponding regularization terms are defined as follows:

$$\mathrm{TGV}^2_{\mathrm{sep}}(u) = \sum_{i=1}^{N} \mathrm{TGV}^2_{\alpha}(q_i), \tag{6.6}$$

and

$$\mathrm{TGV}^2_{\mathrm{frob}}(u) = \arg\min_{w} \alpha_1 \| |\nabla u - w|_{\mathrm{frob}} \|_1 + \alpha_0 \| |\mathcal{E} w|_{\mathrm{frob}} \|_1. \tag{6.7}$$

It is worthy to note, that the reconstruction problems in each Gauss-Newton step are strongly convex due to the step size penalty and can be solved efficiently with the aforementioned primal-dual algorithm and with the Conjugate-Gradient algorithm for L^2-regularization using only the step size penalty. The algorithms for the numerical solution to the corresponding reconstruction problems can be found in the Appendix (see App. 8.5.7). These also require the evaluation of the forward and adjoint derivative operators DS_k and resp. DS_k^H for the k-th Gauss-Newton step and the given signal model. For the VFA approach these are defined as follows.

$$DS_k : u = (M_0, T_1) \mapsto \left(\frac{\partial S_{p_i}(u)}{\partial M_0}|_{u=u_k} M_0 + \frac{\partial S_{p_i}(u)}{\partial T_1}|_{u=u_k} T_1 \right)_{i=1,\cdots,N_p} \tag{6.8}$$

$$DS_k^H : y \mapsto \left(\sum_{i}^{N_p} \overline{\frac{\partial S_{p_i}(u)}{\partial M_0}}|_{u=u_k} y_i, \sum_{i}^{N_p} \overline{\frac{\partial S_{p_i}(u)}{\partial T_1}}|_{u=u_k} y_i \right) \tag{6.9}$$

6.3 Material and Methods

The first part of the evaluation of the proposed two-step reconstruction approach consists in numerical simulations for the VFA technique with the

model-based approach under different levels of SNR. To this end, a numerical brain phantom from MRiLab[1] [101] was used. Synthetic VFA contrasts with matrix size of 200×200 were generated in image space according to the signal equation 6.1 for $\theta = \{2, 3, 4, 5, 7, 9, 11, 14, 17, 22\}^\circ$ and TR$= 5$ ms assuming a perfect uniform spatial B_1 distribution. Different levels of noise were modulated to yield PSNR of $\{10, 15, 20, 25, 30\}$dB according to Def. 8.1.0.14 and normalized to the Ernst angle. Afterwards, the T_1 and M_0 maps were again estimated with the proposed IRGN method with the different regularization approaches from the noisy data. The statistical distribution of deviation from the true T_1 values for three characteristic brain-specific T_1 values of WM ($T_1^{wm} = 600$ ms, #voxels$\sim 10^4$), GM ($T_1^{gm} = 950$ ms, #voxels$\sim 10^4$) and cerebrospinal-fluid (CSF) ($T_1^{csf} = 2500$ ms, #voxels$\sim 10^4$) was computed.
Afterwards, synthetically accelerated golden-angle radial MRI data was generated for the same flip angle set and for Fibonnaci numbers of spf $= \{55, 34, 21, 13, 8\}$ spokes-per-frame with a target PSNR of 30dB, which roughly accords to in-vivo measurements described later for 1 mm^2 in-plane resolution and 3 mm slice-thickness. Acceleration factors to fully sampled reconstructions are calculated according to the theoretical Nyquist-limit for radial acquisitions, i.e. $\frac{N\pi}{2\text{spf}}$ spokes for matrix size of $N \times N$. Reconstruction parameters for ICTGV and concurrent MBR estimation were trained from these numerical examples for ICTGV parameter ranges as described in Section 3.4.
Fully sampled RAVE measurement data were obtained from a cylindric MR phantom that contains five compartments with different amounts of Gd doped water leading to T_1 ranges of 200 ms to 1600 ms with 3 mm^2 slice-thickness. As reference, a fully sampled IR scan with inversion times of $TI = \{80, 200, 400, 800, 1200, 2000\}$ms and a Cartesian VIBE scan with equal measurement parameters as with the RAVE dataset was carried out. A comparison is based on computing the T_1 times within ROIs of the five compartments for fully sampled IR, Cartesian VIBE and RAVE data and concurrently retrospectively sub-sampled RAVE data from 34, 21 and 13 spokes-per-frame for the central slice. Flip-angle correction was taken into account with BSM.
Fully sampled RAVE in-vivo head measurement data were acquired from

[1] https://leoliuf.github.io/MRiLab/

Table 6.1: Measurement and reconstruction parameters.

RAVE parameter	
FOV	$256 \times 256\text{mm}^2$
matrix	256×256
TR/TE	5 ms/2.2 ms
θ	$\{2, 3, 4, 5, 7, 9, 11, 14, 17, 22\}^\circ$
BW	510 Hz/pixel
ICTGV parameter	
λ	0.3
(t_1,t_2,s)	$(8, 1, 0.58)$
PD iterations	1000
$\frac{\alpha 0}{\alpha_1}$	$\frac{1}{\sqrt{2}}$
MBR parameter	
$(\lambda, \delta, \gamma)$	$(10^3, 10^2, 10)$
$(q_\lambda, q_\delta, q_\gamma)$	$(1, 0.95, 0.95)$
Gauss-Newton steps	30
PD iterations	500

three different healthy volunteers with slice-thicknesses/number of partitions of 5 mm/30, 3 mm/40 and 1 mm/30 with the described set of flip-angles. Reconstructions from retrospectively selected under-sampled data with 34,21 and 13 spokes-per-frame were computed with the described two-step procedure from the central slice only after 1D Fourier-transformation along the k_z direction. Corresponding imaging and reconstruction parameters are summarized in Tab. 6.1. The evaluation was carried out by computing the mean and standard-deviation within four characteristic regions: frontal and apical WM (#voxels$\sim$ 200), cortical GM (#voxels$\sim$ 50) and putamen ,#voxels$\sim$ 50. Flip-angle correction was again taken into account with the BSM.

6.4 Results

Fig. 6.1 displays the results of T_1 estimation with the proposed fitting routines L^2, $\text{TGV}^2_{\text{sep}}$ and $\text{TGV}^2_{\text{frob}}$ compared to the standard linearized solution (DESPOT) from simulated VFA image data with different target SNR noise levels. The corresponding mean T_1 values with standard deviation are summarized in Tab. 6.2 and the convergence of the corresponding algorithms is displayed in Fig. 6.2. For low SNR situations (15dB) the DESPOT method exhibits substantial noise-bias as known from literature, while fitting the non-linear model with step size penalty (L^2) preserves the mean T_1 time with diminished variance. Outliers that are still visible in L^2 based estimation are erased with $\text{TGV}^2_{\text{sep}}$ and $\text{TGV}^2_{\text{frob}}$ regularization. Employing the separate TGV regularization on M_0 and T_1 lead, however, to incorrect T_1 estimation in low-and high signal areas which is overcome with $\text{TGV}^2_{\text{frob}}$ regularization. The later however tends to degrade T_1 values in high signal areas (CSF), which becomes more drastic with lower SNR. Results for T_1 estimation from under-sampled numerically simulated measurement data according to the golden-angle RAVE acquisition with fixed noise level after ICTGV reconstruction are displayed in Fig. 6.3 for $\text{TGV}^2_{\text{frob}}$ and L^2 only. Again, a summary of the corresponding mean T_1 values and standard-deviation is given in Tab. 6.3 and the convergence of the corresponding algorithms in Fig. 6.4. Results gained with $\text{TGV}^2_{\text{sep}}$ are not displayed since these exhibit the same behavior as in Fig. 6.1. Again, L^2-T_1 estimation yields correct mean T_1 estimates with residual outliers that are suppressed for estimation with $\text{TGV}^2_{\text{frob}}$ regularization. The later also improves robustness of the estimation which is reflected by decreased standard-deviation for all ROIs of about 50% to 25%. For simulated WM and GM T_1-values a good accordance to the ground-truth could be achieved, while for high T_1 values (CSF) again a reduced bias is apparent for all estimation methods.
Fig. 6.5 displays reconstruction results from retrospectively under-sampled RAVE MR phantom data from 34, 21 and 13 spokes-per-frame compared to standard fully-sampled gridding reconstruction with L^2-fit. For the MR phantom evaluation fully sampled IR data and standard Cartesian VIBE data with the same measurement parameters as the RAVE scan was acquired for comparison purpose. Fig. 6.6 displays the corresponding results, comparing firstly fully sampled RAVE and Cartesian VIBE measurements to the

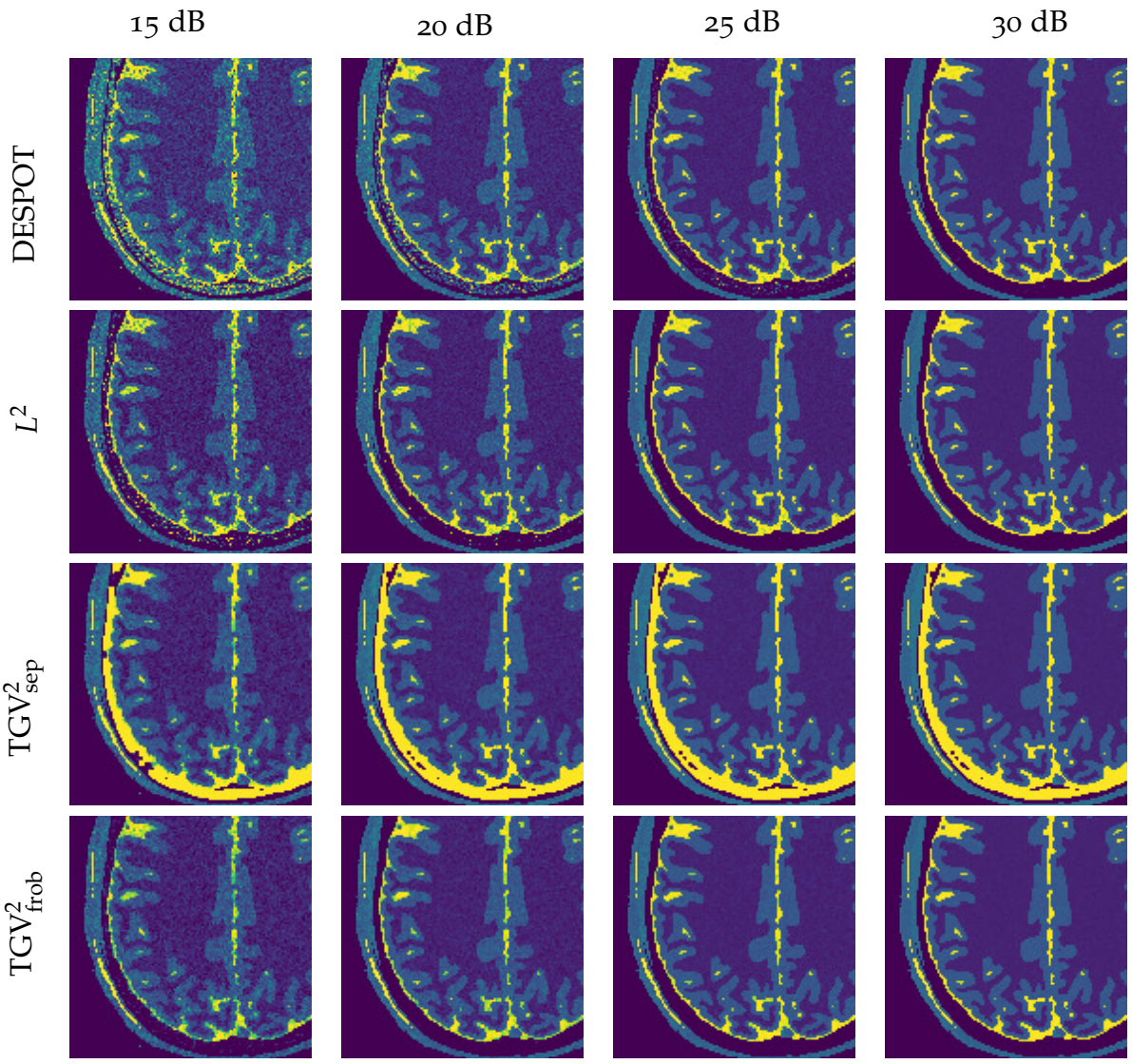

Figure 6.1: Results of T_1 estimation with the proposed fitting routines from a 10-angle VFA simulation with different SNR (normalized to the Ernst angle).

Table 6.2: Mean T_1 times with standard-deviation for the different parameter estimation methods and SNR levels under investigation for three ROIs of the numerical brain phantom.

	DESPOT	L^2	$\text{TGV}^2_{\text{sep}}$	$\text{TGV}^2_{\text{frob}}$
	White Matter - 600 ms			
15 dB	691 ± 139	611 ± 117	614 ± 90	608 ± 96
20 dB	628 ± 73	603 ± 65	612 ± 51	603 ± 53
25 dB	609 ± 40	601 ± 37	611 ± 29	602 ± 30
30 dB	603 ± 22	601 ± 20	609 ± 16	601 ± 17
	Gray Matter 950 ms			
15 dB	1060 ± 224	961 ± 188	965 ± 136	947 ± 143
20 dB	987 ± 117	956 ± 106	977 ± 81	951 ± 82
25 dB	961 ± 64	952 ± 59	978 ± 46	949 ± 46
30 dB	953 ± 36	950 ± 33	973 ± 26	949 ± 26
	CSF 2500 ms			
15 dB	2542 ± 956	2497 ± 768	2488 ± 534	2365 ± 222
20 dB	2608 ± 542	2499 ± 416	3234 ± 694	2450 ± 131
25 dB	2547 ± 294	2508 ± 239	3646 ± 313	2446 ± 56
30 dB	2512 ± 161	2498 ± 132	3666 ± 209	2478 ± 39

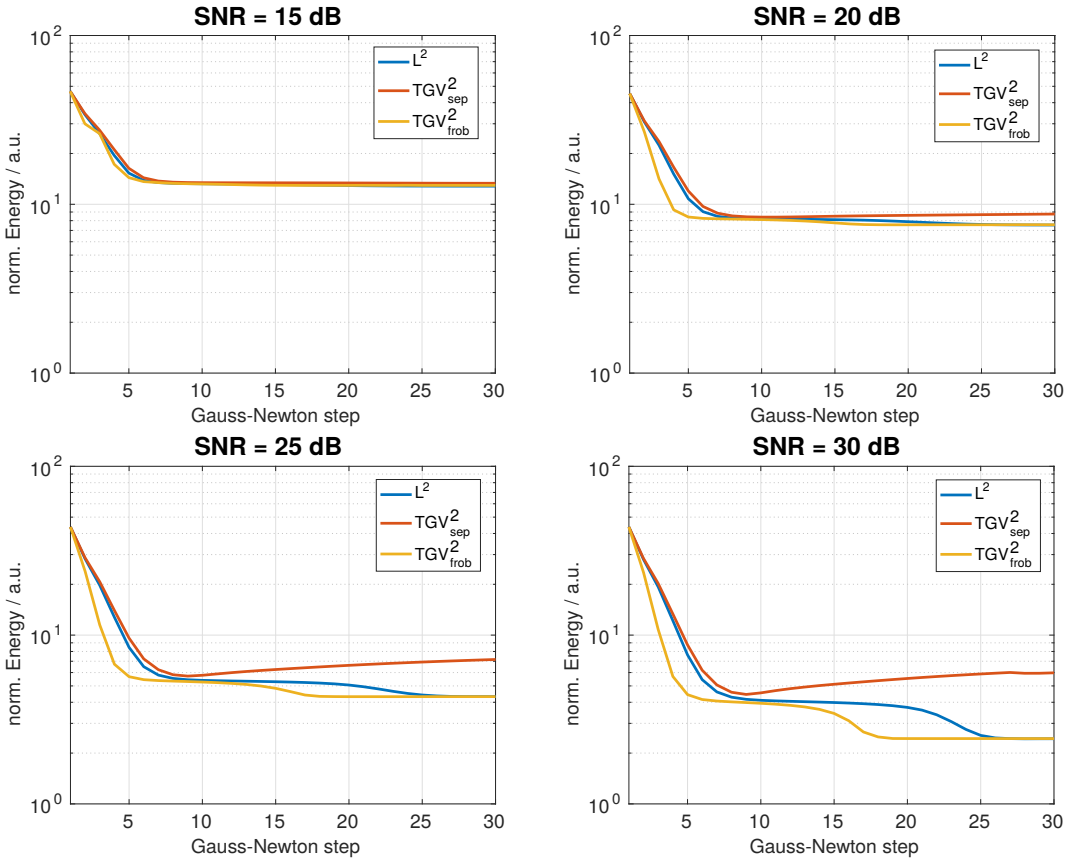

Figure 6.2: Evaluation of the convergence for L^2, $\mathrm{TGV}^2_{\mathrm{sep}}$ and $\mathrm{TGV}^2_{\mathrm{frob}}$ based T_1-estimation from numerically simulated VFA data with different SNR by computing the residuum for each Gauss-Newton step.

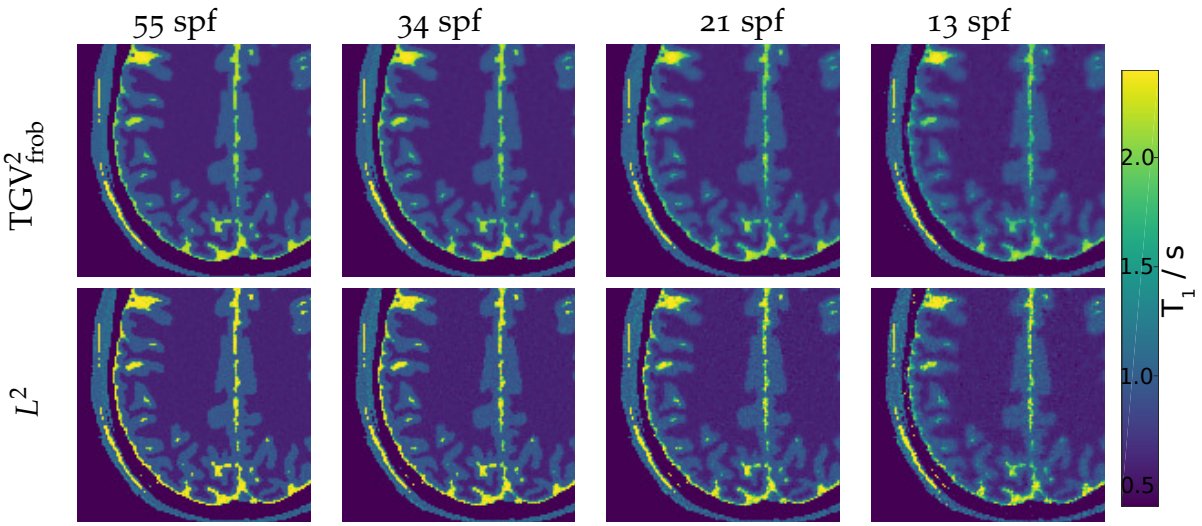

Figure 6.3: T_1 maps estimated with L^2 and TGV$^2_{frob}$ regularized IRGN method from a 10-angle under-sampled (55, 34, 21 and 13 spokes-per-frame) numerical VFA phantom data series reconstructed with ICTGV

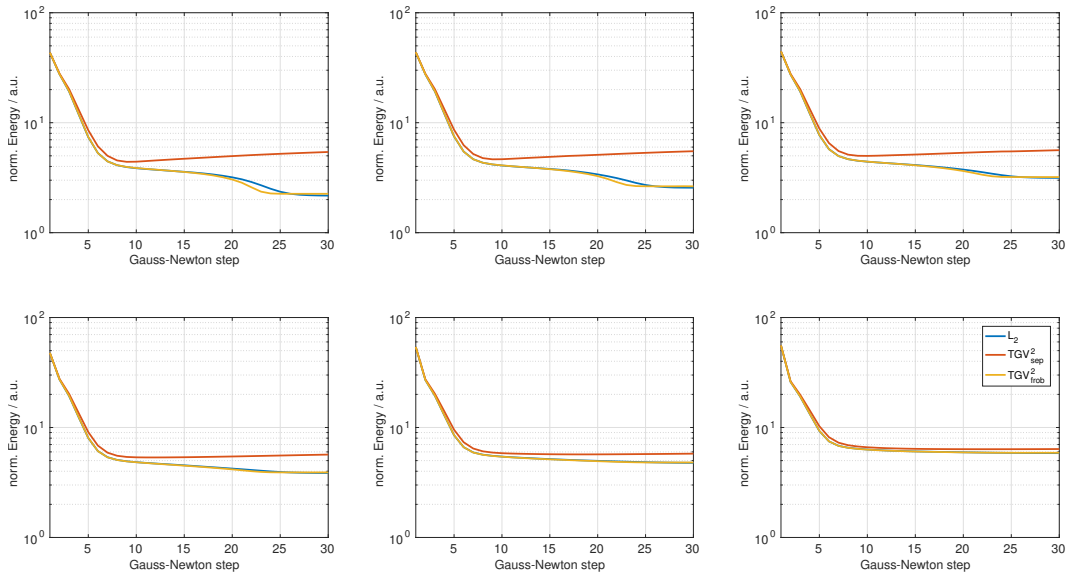

Figure 6.4: Evaluation of the convergence for L^2,TGV$^2_{sep}$ and TGV$^2_{frob}$ based T_1-estimation from numerically simulated VFA data with different under-sampling factors by computing the residuum for each Gauss-Newton step.

Table 6.3: Mean T_1 times with standard-deviation for the different parameter estimation methods and acceleration factors under investigation for three ROIs of the numerical brain phantom.

	DESPOT	L^2	$\text{TGV}^2_{\text{sep}}$	$\text{TGV}^2_{\text{frob}}$
	600 ms - White Matter			
55 spf	602 ± 23	600 ± 20	609 ± 11	600 ± 11
34 spf	603 ± 28	600 ± 25	609 ± 15	600 ± 15
21 spf	606 ± 35	602 ± 31	606 ± 53	601 ± 22
13 spf	610 ± 42	607 ± 38	614 ± 30	607 ± 30
	950 ms - Gray Matter			
55 spf	953 ± 46	952 ± 41	973 ± 24	948 ± 20
34 spf	952 ± 53	951 ± 47	972 ± 31	948 ± 28
21 spf	953 ± 66	951 ± 59	964 ± 112	948 ± 41
13 spf	950 ± 80	946 ± 72	968 ± 61	948 ± 58
	2500 ms - CSF			
55 spf	2616 ± 324	2489 ± 180	3523 ± 180	2383 ± 60
34 spf	2585 ± 365	2493 ± 182	3490 ± 438	2371 ± 66
21 spf	2520 ± 443	2483 ± 282	2640 ± 1009	2337 ± 98
s 13 spf	2510 ± 541	2471 ± 291	3289 ± 540	2310 ± 131

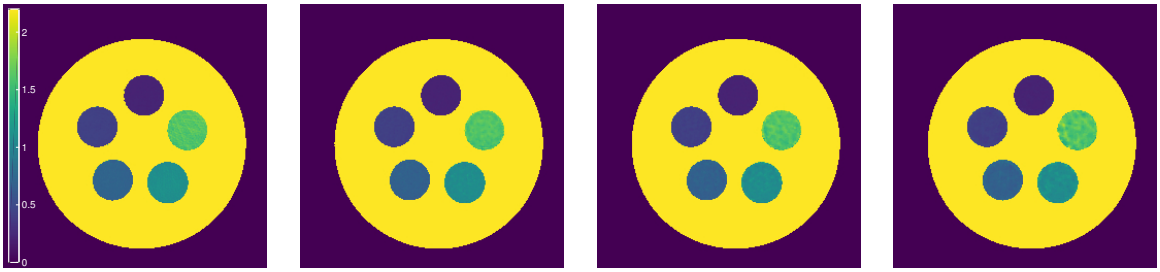

(a) Reference (b) 34 spf (c) 21 spf (d) 13 spf

Figure 6.5: Reference T_1 map from fully sampled 10 flip-angle RAVE data (400 spokes-per-frame) and L^2-estimation compared to accelerated subsets with 34, 21 and 13 spokes-per-frame reconstructed with ICTGV and fitted with $\text{TGV}^2_{\text{frob}}$ regularized IRGN method.

IR gold standard, where in both cases BSM mapping was performed, and secondly an comparison between reconstructions from unaccelerated and accelerated RAVE measurements for the five doped phantom compartments, where also a forward computation of the VFA-model for each compartment and all measured flip-angles is provided. Both, fully sampled RAVE and Cartesian VIBE based T_1-estimations are in good accordance with the IR measurements. Also, the mean T_1 values computed from accelerated measurement are in excellent accordance to the unaccelerated reconstructions with L^2-based T_1-estimation. This is also reflected by comparing the forward signal-model $S_\theta(M_0, T_1)$ for each flip-angle according to the estimated T_1 and M_0 estimates to the fully-sampled measurement for each compartment. Close-ups for all in-vivo T_1 reference datasets, computed with L^2 regularization from fully-sampled gridding reconstruction with different SNR are displayed in Fig. 6.7. The corresponding T_1-estimates with the linearized voxel-wise computation (DESPOT) from ICTGV reconstructions of accelerated subsets (34, 21 and 13 spokes-per-frame) are displayed in Fig. 6.8. Similarly, T_1-estimates gained with L^2-based estimation are displayed in Fig. 6.9, while results computed with $\text{TGV}^2_{\text{frob}}$ regularization are displayed in Fig. 6.10. The corresponding mean T_1-estimates based on L^2 and $\text{TGV}^2_{\text{frob}}$ regularization from four characteristic regions are summarized in Tab. 6.4 for the data-set with 1 mm slice-thickness, for 3 mm in Tab. 6.5, and Tab. 6.6 for 5 mm.
For all cases ICTGV reconstruction enables a removal of under-sampling

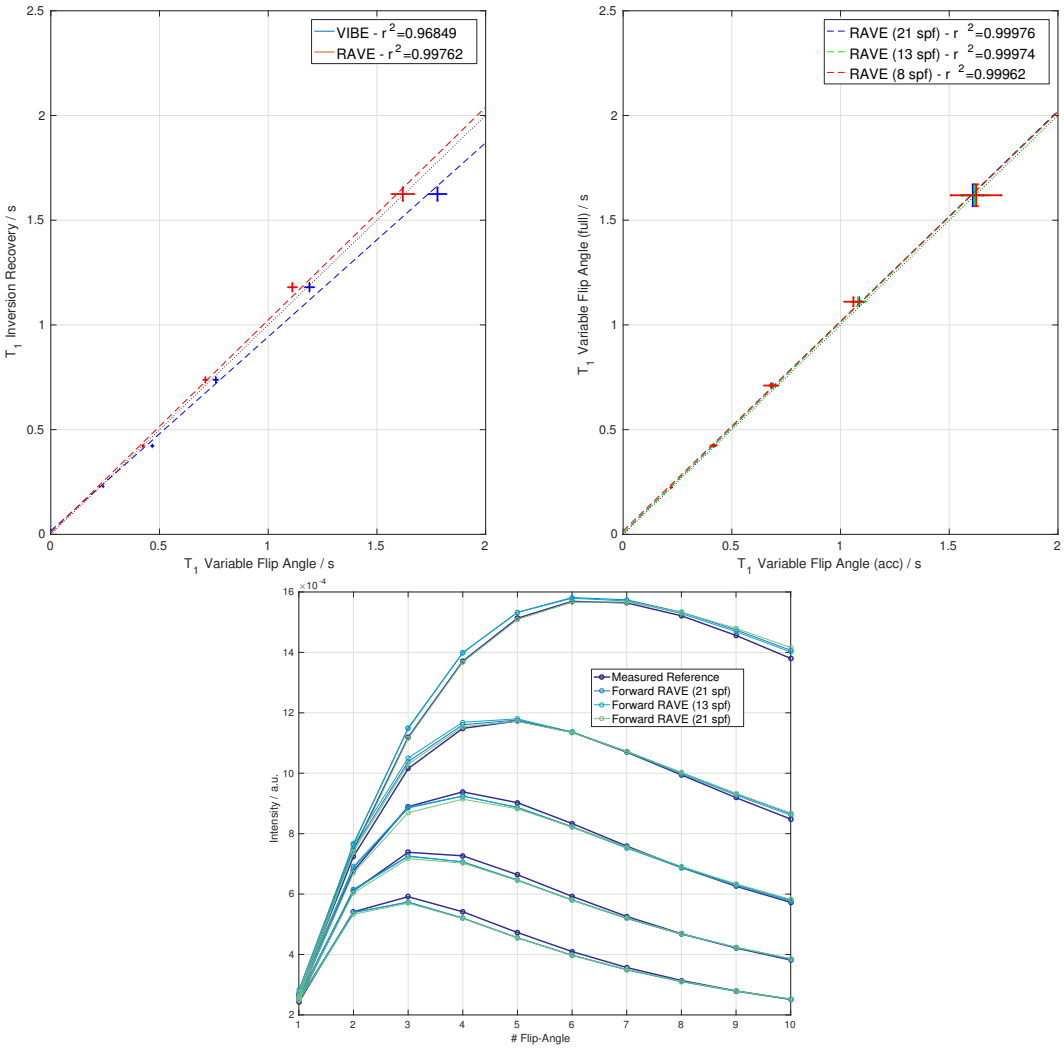

Figure 6.6: (a) Comparison of IR fit for the five compartments of the MR phantom against T_1 estimates with L^2-IRGN estimation from fully sampled VFA RAVE and Cartesian VIBE data. (b) Comparison of T_1 estimates with L^2-IRGN method from fully sampled RAVE data against T_1 estimates from ICTGV reconstructed subsampled RAVE data with $\mathrm{TGV}^2_{\mathrm{frob}}$ estimation. (c) Comparison of the forward computation according to the VFA signal model with M_0 and T_1 maps from accelerated measurements against fully sampled reconstructions for each flip-angle

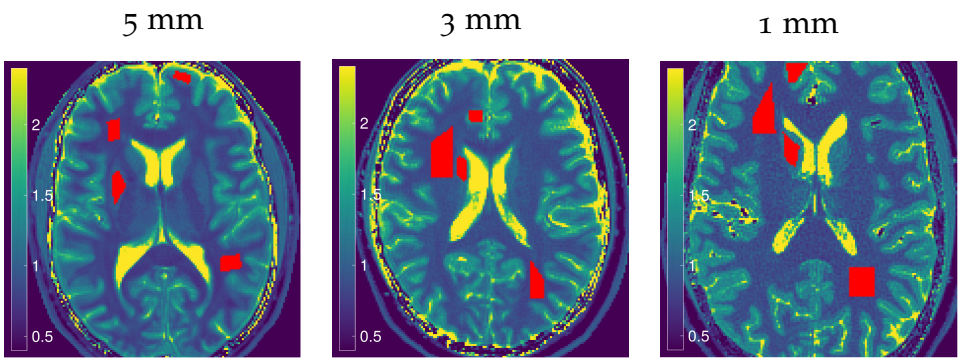

Figure 6.7: T_1 maps estimated with L^2-IRGN method from fully sampled VFA-RAVE data (10 measurements) with 5 mm, 3 mm and 1 mm slice-thickness with indicated ROIs (frontal and apical WM, cortical GM and putamen).

artifacts with high image fidelity for accelerations up to 13 spokes-per-frame ($\sim$ 30-fold acceleration). For the dataset with higher base SNR (3 mm and 5 mm) the standard-deviation for both L^2 and $\text{TGV}^2_{\text{frob}}$ reconstructions is almost equal. With increasing acceleration the error at tissue boundaries increases for all estimation methods. For the low SNR dataset (1 mm slice-thickness), DESPOT and L^2 based T_1 estimation leads to increased uncertainty within homogeneous tissue regions and a higher number of outliers, which is improved substantially by employing $\text{TGV}^2_{\text{frob}}$ regularization. For this dataset a bias towards increased mean T_1 estimates with higher acceleration is apparent.

6.5 Discussion and Conclusion

The analysis of the proposed MBR methods with different regularization strategies shows that a substantial improvement in terms of accuracy and robustness is achievable compared to state-of-the-art voxel-wise estimation with a linearized model (DESPOT) when insufficient SNR is present. The proposed algorithms based on the IRGN method solves the non-linear signal model and are able to remove a noise-bias towards increased T_1 values proportional to the SNR. L^2 regularization on both M_0 and T_1 already regu-

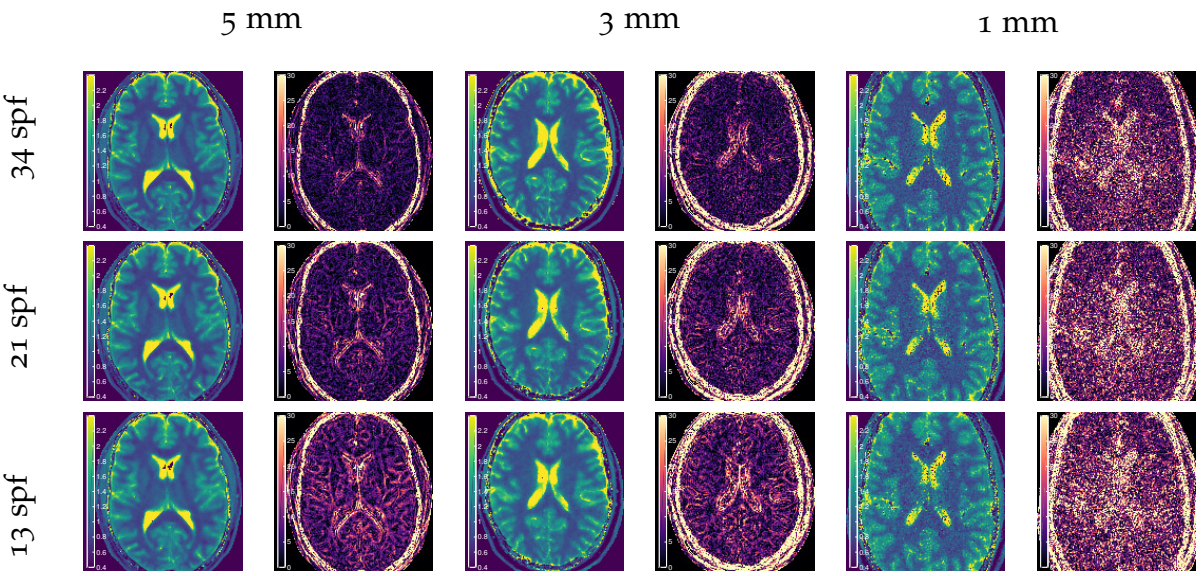

Figure 6.8: T_1 maps estimated with the DESPOT method from accelerated ICTGV reconstructed 10 flip-angle RAVE datasets with 5mm, 3mm and 1mm slice-thickness and corresponding error-maps (% deviation) to the fully sampled references (see Fig. 6.7)

Table 6.4: Mean T_1 times with standard-deviation for L^2- and $\text{TGV}^2_{\text{frob}}$-IRGN based parameter estimation within four characteristic ROIs from the RAVE invivo-dataset with 1mm slice-thickness

	WM frontal	WM apical	GM cortical	Putamen
Reference (L^2)	858 ± 52	885 ± 55	1406 ± 74	1170 ± 88
55 spf - TGV_{frob}	858 ± 48	884 ± 52	1404 ± 62	1200 ± 86
L^2	860 ± 69	889 ± 87	1402 ± 99	1213 ± 158
34 spf -TGV_{frob}	869 ± 54	886 ± 73	1387 ± 65	1181 ± 77
L^2	872 ± 78	893 ± 108	1385 ± 101	1197 ± 156
21 spf -TGV_{frob}	852 ± 75	899 ± 77	1436 ± 74	1190 ± 110
L^2	856 ± 96	905 ± 109	1434 ± 95	1190 ± 168
13 spf -TGV_{frob}	872 ± 72	895 ± 66	1388 ± 65	1202 ± 211
L^2	876 ± 93	900 ± 102	1387 ± 99	1235 ± 309

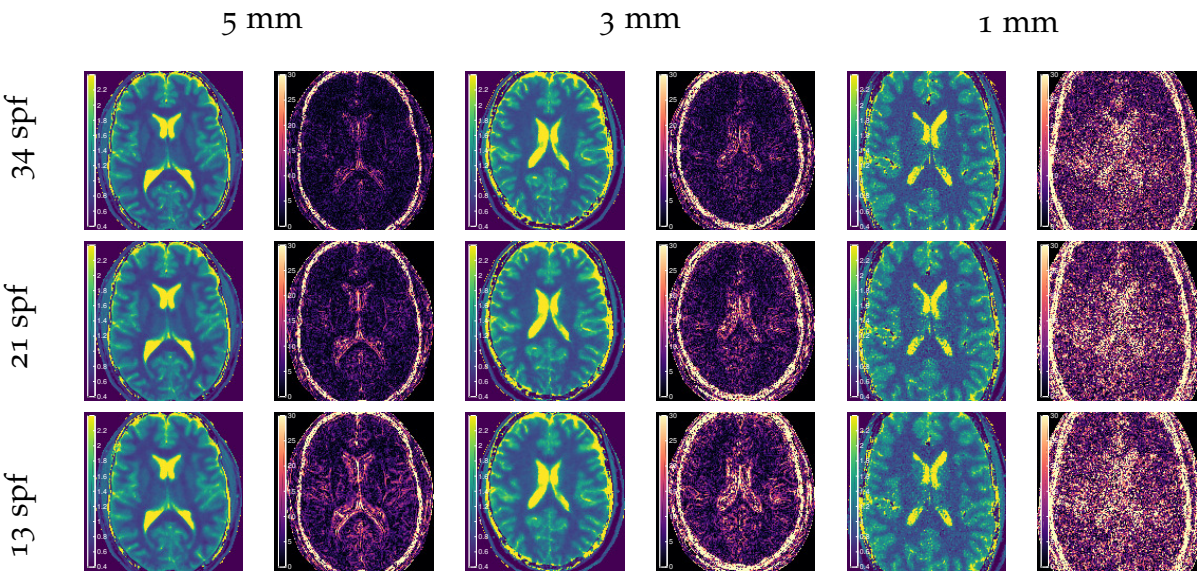

Figure 6.9: T_1 maps estimated with the L^2-IRGN method from accelerated ICTGV reconstructed 10 flip-angle RAVE datasets with 5mm, 3mm and 1mm slice-thickness and corresponding error-maps (% deviation) to the fully sampled references (see Fig. 6.7)

Table 6.5: Mean T_1 times with standard-deviation for L^2- and $\text{TGV}^2_{\text{frob}}$-IRGN based parameter estimation within four characteristic ROIs from the RAVE invivo-dataset with 3mm slice-thickness

	WM frontal	WM apical	GM cortical	Putamen
Reference (L^2)	870 ± 31	838 ± 38	1513 ± 62	1123 ± 34
55 spf - TGV_{frob}	874 ± 26	837 ± 37	1524 ± 61	1126 ± 39
L^2	874 ± 26	837 ± 37	1524 ± 62	1126 ± 39
34 spf -TGV_{frob}	880 ± 27	846 ± 43	1522 ± 62	1122 ± 47
L^2	880 ± 27	846 ± 43	1522 ± 63	1122 ± 47
21 spf -TGV_{frob}	881 ± 33	846 ± 32	1508 ± 68	1143 ± 39
L^2	881 ± 34	846 ± 32	1508 ± 68	1143 ± 39
13 spf -TGV_{frob}	886 ± 27	856 ± 41	1523 ± 70	1161 ± 66
L^2	886 ± 27	856 ± 41	1523 ± 70	1161 ± 66

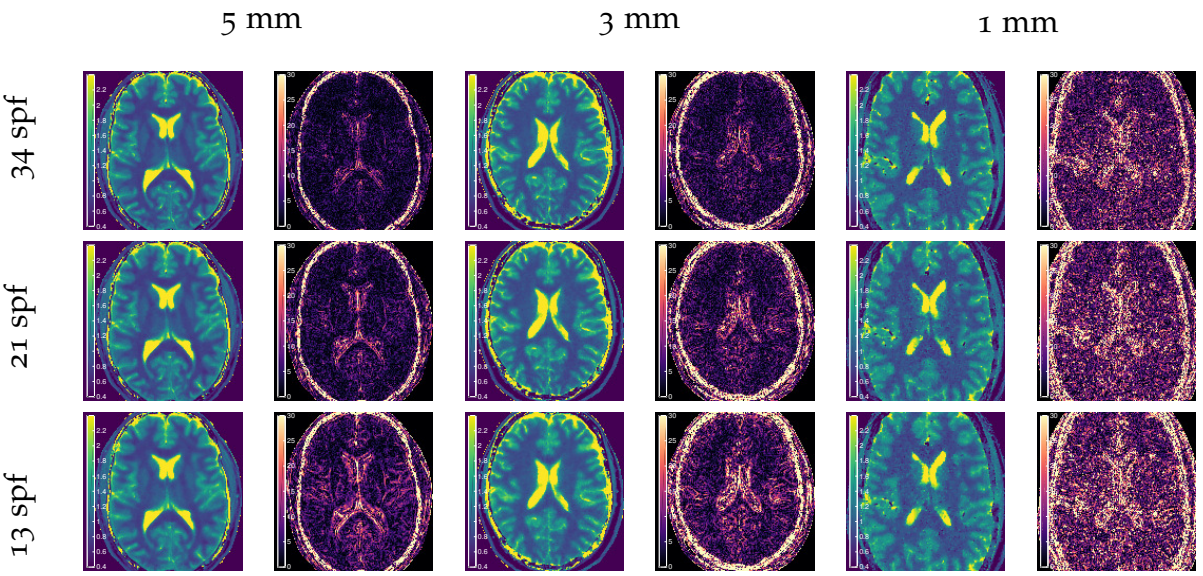

Figure 6.10: T_1 maps estimated with the TGV^2_{frob}-IRGN method from accelerated ICTGV reconstructed 10 flip-angle RAVE datasets with 5 mm, 3 mm and 1 mm slice-thickness and corresponding error-maps (% deviation) to the fully sampled references (see Fig. 6.7)

Table 6.6: Mean T_1 times with standard-deviation for L^2- and TGV^2_{frob}-IRGN based parameter estimation within four characteristic ROIs from the RAVE invivo-dataset with 5mm slice-thickness

	WM frontal	WM apical	GM cortical	Putamen
Reference (L^2)	782 ± 31	788 ± 31	1258 ± 68	999 ± 36
55 spf - TGV_{frob}	785 ± 30	794 ± 25	1259 ± 67	995 ± 32
L^2	785 ± 30	794 ± 25	1259 ± 67	995 ± 32
34 spf -TGV_{frob}	787 ± 26	794 ± 25	1265 ± 68	1000 ± 33
L^2	787 ± 26	794 ± 26	1265 ± 68	1000 ± 34
21 spf -TGV_{frob}	785 ± 24	801 ± 27	1282 ± 79	1011 ± 39
L^2	785 ± 24	801 ± 27	1282 ± 79	1011 ± 39
13 spf -TGV_{frob}	791 ± 24	809 ± 29	1295 ± 98	1020 ± 33
L^2	791 ± 24	809 ± 30	1295 ± 98	1020 ± 34

larizes jointly on both parameters and leads to a stable estimation without exploiting similar spatial structures. Regularizing with TGV^2 constraints *separately* lead, however, to convergence problems and ambiguities in specific regions due to the non-convexity optimization problem. It could be shown that a further improvement can be achieved by treating the parameter maps as multiple channels and employing TGV^2_{frob} type regularization as in [67]. This regularization strategy stabilizes deviations from target T_1 values by enforcing spatial smoothness properties while allowing for jump discontinuous at tissue borders on all parameter-maps jointly. However, it was found that at discontinuities with greater difference in magnitude sharp transitions may be blurred and thus bias mean T_1-estimates within these homogeneous ROIs towards lowered values. Employing nuclear-TGV^2 as e.g. in [177] might lead to further improvement for this situation.
The performance of developed algorithms was exemplarily evaluated in the context of T_1 estimation from noisy VFA data but can be adapted to other parameter mapping situations with multiple parametric dimensions and spatial structure, such as e.g. fitting pharmaco-kinetic parameter from DCE MRI data as described in Chap. 5.
A validation of the signal model was evaluated by using an MRI phantom that contains five water compartments with differently high fractions of Gd doping. A T_1 ground-truth was established with a standard IR experiment. The correspondence of T_1 values computed from the IR experiment were in good accordance to both fully-sampled spoiled-gradient echo non-Cartesian RAVE and Cartesian VIBE measurements as long as flip-angle deviations are taken into account. The goal of accelerated T_1 estimation was achieved by acquiring golden-angle radial RAVE data below the Nyquist limit. In this situation off-set angles have to be determined for the following scan with different flip-angle according to the fibonacci-number of spokes chosen for acceleration. For better comparison purpose to a gold-standard 550 spokes were measured for each volume and accelerated subsets with correct offsets were drawn from the fully-sampled datasets. ICTGV regularization was employed to achieve a stable reconstruction while removing undersampling artifacts. A differentiation to other reconstruction methods was omitted due already performed extensive comparisons in Chap. 4 and 5.
The established two-step procedure, i.e. ICTGV reconstruction followed by MBR, was evaluated for numerical and MR phantoms as well as for

in-vivo head measurements in different SNR situations. For all situations reconstruction parameters were trained on the numerical datasets. Adequate data-normalization to the median of the highest ten percent of the gridding reconstruction of the averaged data over all parametric encodings guaranteed the usability of trained reconstruction parameters for reconstruction of MR measurement data.
It was found that a sufficient SNR level does not increase the quality of T_1 estimation by image MBR with better priors, since an sufficient amount of denoising can already be achieved during the ICTGV reconstruction. For low SNR scenarios, it turned out, however, that a bounded weight on the data-fidelity in ICTGV regularized reconstruction better preserves the signal evolution in the parametric domain, while residual noise-enhancement remains. In concurrent MBR a further improvement with $\mathrm{TGV}^2_{\mathrm{frob}}$-regularization can then be realized. Stronger ICTGV regularization in the first place would lead to improved denoising at the ost of deviations from the true, characteristic signal evolution which then leads in incorrect T_1 estimation in MBR. Again, a proper selection of the regularization parameter plays a crucial role.
Concerning the chosen signal model, the application of ICTGV on VFA data requires a high number of measurements in the parametric domain which was set to ten according to literature suggestions that target the correct estimation of a broader range of T_1 values. Determination of optimal sequence parameter adjustments for VFA based T_1 estimation dependent on SNR and sensitivity to T_1 remains an ongoing research area (e.g. [178]), and the relation to specific acceleration strategies based on incomplete data requires additional considerations that are out of scope of this work. Measuring radial stack-of-stars data instead of Cartesian VIBE data gives the freedom to use favorable radial undersampling patterns in isotropic slices over randomly Cartesian undersampling in two phase-encoding directions. To reduce the computational burden the inherently 3D RAVE measurements can be entangled in slice encoding direction but ideally the reconstruction should take place on the 3D-temporal volume which is limited by available GPU memory.
Finally, it needs to be argued that ICTGV enforces characteristic properties on image sequences in general and no further information about the signal model is provided. This is adverse to acceleration strategies in MR parameter estimation based on the works of Doneva et al [166] or Velikina et al [168], where model-specific information is used during the iterative recon-

struction as regularization information followed by voxel-wise estimation of the parameter-maps. Another counterpart is to use MBR directly in k-space as originally proposed by [171] or [172] by incorporating the signal model directly in the data-fidelity that, however, imposes more complexity on the convergence properties. Additional regularization in that case has to be applied directly to the parametric maps, where a $\mathrm{TGV}^2_{\mathrm{frob}}$ type regularization is used in [179]. It is hard to determine which strategy is superior to another since all have specific strengths and limitations. A possible improvement on the currently proposed two-step procedure would be to project on the image-space MBR estimates already several times during the ICTGV regularized reconstruction. Still, it was shown that a huge acceleration potential of $r = 20\ (21\mathrm{spf}), \cdots, 30\ (13\mathrm{spf})$ for high quality and accurate T_1 estimation from RAVE-VFA data is possible within measurement times of 0.65 s (13 spf) to 1 s (21 spf) per slice. Current fingerprinting protocols report measurement times from 48 s per slice [180] to 4 s per slice [181] for joint estimation of M_0, T_1 and T_2 maps.

7 Conclusions and Outlook

The goal of this thesis was the analysis of regularization strategies in the context of different characteristic dynamic MRI applications with varying goals. For cardiac imaging based on Cartesian encoding it was shown that 12 to 16-fold acceleration of data acquisition is feasible with the potential to achieve equivalent spatial resolutions for real-time imaging as under breath-hold conditions or increase spatial resolution and coverage drastically for cardiac perfusion imaging. For DCE MRI based on golden-angle radial stack-of-stars encoding the proposed reconstruction framework is able to provide high image quality with temporal resolutions below one second while preserving a high spatial coverage and spatial-resolution. This reflects a standard that was recently only achievable with computer-tomography and lays the basis for improving the analysis of DCE MRI. For dynamic MRA the increase in temporal resolution is sought to increase the detectability of AVM feeder vessels but requires further evaluation. Finally, the same sequence design was also exploited to accelerate the mapping of longitudinal relaxation rates and enables measurement times of around one second per slice with $1\,\mathrm{mm}^2$ resolution. In conjunction a general variational framework in image-space was presented to improve multi-parameter estimation from non-linear signal models in low SNR situations.
The ICTGV^2 regularization functional, consisting of two second order TGV^2 functionals, proved to state a powerful a-priori model for stabilizing the reconstruction of MR image sequences under the condition of incomplete dynamic MR data with different k-space sampling trajectories and under varying noise levels with different temporal/parametric signal evolutions. The concept enables the automatic decomposition into two components with locally different requirements on spatio-temporal regularization. Corresponding training of reconstruction and model-parameters and evaluations against constructed ground-truths indeed revealed that this leads to improved reconstruction quality and therefore supports the theoretical

reasoning behind the decomposition approach. It can be argued that for specific situations where the signal evolution is less complex, e.g. similarly smooth in time for different image patches, similar reconstruction quality can be achieved with less model-complexity and computational burden. However, specific cases are inherently contained in the more complex model such that an increased robustness can be expected for unforeseen situations within the same modality.
Consecutively, the ICTGV^2 concept was put in the context of state-of-the-art image sequence regularizers and parallel-imaging/compressed-sensing reconstruction models applied in MRI, and was shown to yield superior image quality while preserving the temporal fidelity. However, it might be possible to further increase reconstruction quality by selecting a higher number of components. The analytical framework described in [68] as well as the numerical implementation in principle allow the inclusion of an arbitrary number of TGV or other functionals. This could be interesting to resolve different types or scales of motion, e.g. for free-breathing DCE application, but again comes at the cost of increased model-parameter complexity and computational burden.
The presented method clearly distinguishes between model and regularization parameters. The assumption that the former influence the image model but are independent of the overall trade-off between regularization and data fidelity has been confirmed by experiments showing that the optimal choice of model parameters is robust along different subsampling rates and yields different optimal choices for different dynamic MRI applications.
The choice of the regularization parameter remains a crucial task. A low emphasis on the data-fidelity alters the true temporal or parametric signal evolution while giving he illusion of high image quality in the spatial domain.The later observation also holds for all investigated regularization strategies such that a meaningful comparison can only be given under the condition of preserved temporal fidelity.For Cartesian imaging the proposed linear adaptation of the regularization parameter constitutes a heuristic to compensate for alteration of the data-fidelity-cost due to subsampling which was confirmed by experimental results that also showed a robustness against deviations from the optimal weighing of roughly 10%. In general, the regularization parameter needs to be tuned according to the noise level and matrix size. For applications where a similar noise behavior and

imaging parameters are expected, the implemented data normalization procedure guarantees the re-usability of the regularization weighting. In this work it has been omitted that the noise level may also vary along the temporal/parametric dimension which actually would require a set of regularization weights as described in [182].
In this work suitable regularization- and model-parameters were computed by grid-search on reasonable parameter-ranges according to constructed ground-truths. For cases like CINE cardiac imaging or quantitative MRI a ground-truth can be established with long scanning times. In DCE MRI this is not possible due to temporal restrictions of the passing contrast-agent dynamics such that parameter tuning was carried out with artificial numerical ground-truths. A further improvement in selecting better reconstruction parameters will be found in the emerging field of *learning* these within a deep variational network as described e.g. in [183], [184] not yet applied for dynamic data or using a learned version of the primal-dual algorithm as described in [146]. With these approaches it should be possible to drastically reduce the reconstruction times that are still beyond clinical demands even for GPU optimized computation. Concurrently this will also enable the fast computation of 3D-temporal/parametric volumes with extended regularization possibilities in 4D.

8 Appendix

8.1 Definitions

Definition 8.1.0.1. Proximal mapping
The proximal mapping with respect to a convex function f is defined as

$$x^\star = (Id + \nu f)^{-1}(\xi) = P_\nu(\xi) = \arg\min_x \frac{\|x - \xi\|_2^2}{2} + \nu f(x) \tag{8.1}$$

Definition 8.1.0.2. Convex Conjugate
Let $F : \mathbb{C}^N \mapsto \mathbb{R}$, then the convex conjugate (or Fenchel dual) is defined as

$$F^\star(y) = \sup_x < x, y > -F(x) \tag{8.2}$$

For $x \in \mathbb{C}^N$ the following norms are defined:

Definition 8.1.0.3. L^p norm

$$\|x\|_p = \left(\sum_{n=1}^{N} |x_n|^p \right)^{\frac{1}{p}} \tag{8.3}$$

Definition 8.1.0.4. L^2 norm

$$\|x\|_2 = \sqrt{\sum_{n=1}^{N} |x_n|^2} \tag{8.4}$$

Definition 8.1.0.5. L^∞ or Chebyshev norm

$$\|x\|_\infty = \lim_{p \to \infty} \|x\|_p = \max\{|x_i| \mid i = 1, \cdots, N\} \tag{8.5}$$

Definition 8.1.0.6. L^0 norm (no real norm)

$$\|x\|_0 = \lim_{p\to 0} \|x\|_p^p = \text{card}\{i \leq N \mid x_i \neq 0\} \tag{8.6}$$

Definition 8.1.0.7. Frobenius norm
For $x \in \mathbb{C}^{N\times M}$ the Frobenius norm is defined as

$$\|x\|_{\text{frob}} = \sqrt{\sum_{m=1}^{M}\sum_{n=1}^{N} |x_{m,n}|^2} \tag{8.7}$$

Definition 8.1.0.8. Nuclear norm
For $x \in \mathbb{C}^{N\times M}$ and σ_n being the singular values of x the Nuclear norm is defined as

$$\|x\|_\star = \sum_{n=1}^{\min(M,N)} \sigma_n \tag{8.8}$$

Definition 8.1.0.9. Schatten p-norm
For $x \in \mathbb{C}^{N\times M}$ and σ_n being the sorted singular values of x, i.e. $\sigma_i \geq \sigma_i + 1$, the Schatten p-norm is defined as

$$\|x\|_p = \left(\sum_{n=1}^{\min(M,N)} \sigma_n^p\right)^{\frac{1}{p}} \tag{8.9}$$

Definition 8.1.0.10. Scalar product for functions on $\mathcal{L}^2(\Omega)$
$f, g \in \mathcal{L}^2(\Omega), \Omega = \mathbb{C}$

$$< f, g >= \int_\Omega dx\ f(x)\overline{g(x)} < \infty$$

Definition 8.1.0.11. Adjoint operator
The adjoint or hermitean-conjugate K^H of a linear operator $K \in \mathcal{L}(\mathcal{X}, \mathcal{Y})$ is defined as

$$< K^H y, x >=< y, Kx > \quad \forall x \in \mathcal{X}\ , y \in \mathcal{Y}$$

Definition 8.1.0.12. Signal-to-Error-Ratio
The signal-to-error-ratio SER in dB between a reference vector x and y, $x, y \in \mathbb{C}^N$ is defined as

$$\text{SER}(x, y) = -10 \log_{10} \frac{\|x - y\|_2^2}{\|x\|_2^2}$$

Definition 8.1.0.13. Root-Mean-Squared-Error
The Root-Mean-Squared-Error RMSE between a two vectors x and y, $x, y \in \mathbb{C}^N$ is defined as

$$\mathrm{RMSE}(x,y) = \frac{\|x-y\|_2}{\sqrt{N}}$$

Definition 8.1.0.14. Peak-Signal-to-Noise-Ratio
The Peak-Signal-to-Noise-Ratio PSNR in dB for the noisy approximation y of a noise-free vector x, $x, y \in \mathbb{C}^N$ is defined as

$$\mathrm{PSNR}(x,y) = -10\log_{10}\frac{\max(x)^2}{\|x-y\|_2^2}$$

8.2 Discrete 2d-time forward and backward differences

Definition 8.2.0.1. Discrete Forward-Differences
The discrete forward differences $U = \mathbb{C}^{N_x \times N_y \times N_t}$, $\delta_x^+, \delta_y^+, \delta_t^+ : U \mapsto U$ with Dirchlet boundary conditions are defined as

$$\begin{aligned}
\delta_x^+ u_{i,j,t} &= \begin{cases} u_{i+1,j,t} - u_{i,j,t} & \text{if} \quad 0 \le i < N_x - 1, \\ 0 & \text{if} \quad i = N_x - 1, \end{cases} \\
\delta_y^+ u_{i,j,t} &= \begin{cases} u_{i,j+1,t} - u_{i,j,t} & \text{if} \quad 0 \le j < N_y - 1, \\ 0 & \text{if} \quad j = N_y - 1, \end{cases} \\
\delta_t^+ u_{i,j,t} &= \begin{cases} u_{i,j,t+1} - u_{i,j,t} & \text{if} \quad 0 \le t < N_t - 1, \\ 0 & \text{if} \quad t = N_t - 1, \end{cases}
\end{aligned} \tag{8.10}$$

Definition 8.2.0.2. Discrete Backward-Differences
The discrete backward differences on $U = \mathbb{C}^{N_x \times N_y \times N_t}$, $\delta_x^-, \delta_y^-, \delta_t^- : U \mapsto U$

with Dirchlet boundary conditions are defined as

$$\begin{aligned}
\delta_x^- u_{i,j,t} &= \begin{cases} u_{i,j,t} - u_{i-1,j,t} & \text{if} \quad 0 < i \leq N_x - 1, \\ 0 & \text{if} \quad i = 0, \end{cases} \\
\delta_y^- u_{i,j,t} &= \begin{cases} u_{i,j,t} - u_{i,j-1,t} & \text{if} \quad 0 < j \leq N_y - 1, \\ 0 & \text{if} \quad j = 0, \end{cases} \\
\delta_t^- u_{i,j,t} &= \begin{cases} u_{i,j,t} - u_{i,j,t-1} & \text{if} \quad 0 < t \leq N_t - 1, \\ 0 & \text{if} \quad t = 0, \end{cases}
\end{aligned} \tag{8.11}$$

Definition 8.2.0.3. Adjoint of discrete Forward-Differences
The adjoint of discrete forward differences $U = \mathbb{C}^{N_x \times N_y \times N_t}$, $\delta_x^{*+}, \delta_y^{*+}, \delta_t^{*+} : U \mapsto U$ with Dirchlet boundary conditions are defined as

$$\begin{aligned}
\delta_x^{*+} u_{i,j,t} &= \begin{cases} u_{2,j,t} & \text{if} \quad i = 1 \\ u_{i+1,j,t} - u_{i,j,t} & \text{if} \quad 0 < i < N_x, \\ -u_{N_x,j,t} & \text{if} \quad i = N_x, \end{cases} \\
\delta_y^{*+} u_{i,j,t} &= \begin{cases} u_{i,2,t} & \text{if} \quad j = 1 \\ u_{i,j+1,t} - u_{i,j,t} & \text{if} \quad 0 < j < N_y, \\ -u_{i,N_y,t} & \text{if} \quad j = N_y, \end{cases} \\
\delta_t^{*+} u_{i,j,t} &= \begin{cases} u_{i,j,2} & \text{if} \quad t = 1 \\ u_{i,j,t+1} - u_{i,j,t} & \text{if} \quad 0 < t < N_t, \\ -u_{i,j,N_t} & \text{if} \quad t = N_t, \end{cases}
\end{aligned} \tag{8.12}$$

Definition 8.2.0.4. Adjoint of discrete Backward-Differences
The discrete backward differences on $U = \mathbb{C}^{N_x \times N_y \times N_t}$, $\delta_x^{*-}, \delta_y^{*-}, \delta_t^{*-} : U \mapsto$

U with Dirchlet boundary conditions are defined as

$$\delta_x^{*-} u_{i,j,t} = \begin{cases} u_{1,j,t} & \text{if} \quad i = 1 \\ u_{i,j,t} - u_{i-1,j,t} & \text{if} \quad 0 < i < N_x, \\ -u_{N-1,j,t} & \text{if} \quad i = N_x, \end{cases}$$
$$\delta_y^{*-} u_{i,j,t} = \begin{cases} u_{i,1,t} & \text{if} \quad j = 1 \\ u_{i,j,t} - u_{i,j-1,t} & \text{if} \quad 0 < j < N_y, \\ -u_{i,M-1,t} & \text{if} \quad j = N_y, \end{cases} \tag{8.13}$$
$$\delta_t^{*-} u_{i,j,t} = \begin{cases} u_{i,j,1} & \text{if} \quad t = 1 \\ u_{i,j,t} - u_{i,j,t-1} & \text{if} \quad 0 < t < N_t, \\ -u_{i,j,N_t-1} & \text{if} \quad t = N_t, \end{cases}$$

8.3 Discrete 2d-time operations

We denote by N_x and N_y the image space dimensions, by N_t the number of time-frames, by $U = \mathbb{C}^{N_x \times N_y \times N_t}$ the space of image sequences and by C the number of coils. Spatio-temporal weights are denoted as $\beta = (\mu_x, \mu_y, \mu_t)$.

Definition 8.3.0.1. Gradient
The gradient is defined as

$$\nabla_\beta : \mathcal{U} \mapsto \mathcal{U}^3$$
$$(\nabla_\beta u)_{i,j,t} = \begin{pmatrix} \mu_x (\delta_x^+ u)_{i,j,t} \\ \mu_y (\delta_y^+ u)_{i,j,t} \\ \mu_t (\delta_t^+ u)_{i,j,t} \end{pmatrix} = \begin{pmatrix} v^1 \\ v^2 \\ v^3 \end{pmatrix} \tag{8.14}$$

Definition 8.3.0.2. Divergence
The divergence is defined as the adjoint operation to the gradient, i.e. $\nabla_\beta^* = -\operatorname{div}_\beta^1$

$$\operatorname{div}_\beta^1 : \mathcal{U}^3 \mapsto \mathcal{U}$$
$$(\operatorname{div}_\beta^1 v)_{i,j,t} = \left(\mu_x (\delta_x^{*-} v^1)_{i,j,t} + \mu_y (\delta_y^{*-} v^2)_{i,j,t} + \mu_t (\delta_t^{*-} v^3)_{i,j,t} \right) \tag{8.15}$$

Definition 8.3.0.3. Symmetrized Gradient
The symmetrized gradient is defined as

$$\mathcal{E}_\beta : v = (v^1, v^2, v^3) \in \mathcal{U}^3 \mapsto \mathcal{U}^6$$

$$(\mathcal{E}_\beta v)_{i,j,t} = \begin{pmatrix} \mu_x(\delta_x^- v^1)_{i,j,t} \\ \mu_y(\delta_y^- v^2)_{i,j,t} \\ \mu_t(\delta_t^- v^3)_{i,j,t} \\ \frac{1}{2}\left(\mu_y(\delta_y^- v^1)_{i,j,t} + \mu_x(\delta_x^- v^2)_{i,j,t}\right) \\ \frac{1}{2}\left(\mu_t(\delta_t^- v^1)_{i,j,t} + \mu_x(\delta_x^- v^3)_{i,j,t}\right) \\ \frac{1}{2}\left(\mu_t(\delta_t^- v^2)_{i,j,t} + \mu_y(\delta_y^- v^3)_{i,j,t}\right) \end{pmatrix} = \begin{pmatrix} w^1 \\ w^2 \\ w^3 \\ w^4 \\ w^5 \\ w^6 \end{pmatrix} \tag{8.16}$$

Definition 8.3.0.4. Symmetrized Divergence
The symmetrized divergence is defined as the adjoint operation to the gradient, i.e. $\mathcal{E}_\beta^* = -\operatorname{div}_\beta^2$

$$\operatorname{div}_\beta^2 : w = (w^1, w^2, w^3, w^4, w^5, w^6) \in \mathcal{U}^6 \mapsto \mathcal{U}^3$$

$$(\operatorname{div}_\beta^2 v)_{i,j,t} = \begin{pmatrix} \mu_x(\delta_x^{*+} w^1)_{i,j,t} + \mu_y(\delta_y^{*+} w^4)_{i,j,t} + \mu_t(\delta_t^{*+} w^5)_{i,j,t} \\ \mu_x(\delta_x^{*+} w^4)_{i,j,t} + \mu_y(\delta_y^{*+} w^2)_{i,j,t} + \mu_t(\delta_t^{*+} w^6)_{i,j,t} \\ \mu_x(\delta_x^{*+} w^5)_{i,j,t} + \mu_y(\delta_y^{*+} w^6)_{i,j,t} + \mu_t(\delta_t^{*+} w^3)_{i,j,t} \end{pmatrix} \tag{8.17}$$

8.3.1 Norms

We denote by N_x and N_y the image space dimensions, by N_t the number of time-frames, by $U = \mathbb{C}^{N_x \times N_y \times N_t}$ the space of image sequences and by N_c the number of coils.

The L^2 norm is defined for $d \in \mathbb{C}^{N_x \times N_y \times N_t \times N_c}$ as

$$\|d\|_2^2 = \sum_{i,j,t,c} |d_{i,j,t,c}|^2$$

The L^1 norm $\|\cdot\|_1$ is defined - abusing notation for $v = (v^1, v^2, v^3) \in U^3$ - as

$$\|v\|_1 = \sum_{i,j,t} \sqrt{|v^1_{i,j,t}|^2 + |v^2_{i,j,t}|^2 + |v^3_{i,j,t}|^2}$$

and for $w = (w^1, w^2, w^3, w^4, w^5, w^6) \in U^6$ as

$$\|w\|_1 = \sum_{i,j,t} \sqrt{|w^1_{i,j,t}|^2 + |w^2_{i,j,t}|^2 + |w^3_{i,j,t}|^2 + 2|w^4_{i,j,t}|^2 + 2|w^5_{i,j,t}|^2 + 2|w^6_{i,j,t}|^2},$$

where the factor 2 in front of w_4, w_5, w_6 compensates for the symmetrization of the Jacobian in the definition of $\mathcal{E}_\beta$.

8.3.2 Proximal mappings

The relevant proximal mappings (Definition 8.1) in this work are computed as

- $F^*(y) = \mathcal{I}_{\{\|\cdot\|_{\infty,\eta} \leq 1\}}(y)$

$$P_{\sigma F^*}(\xi) = P_\eta(\xi) = \arg\min_y \frac{\|y - \xi\|_2^2}{2} + \mathcal{I}_{\{\|\cdot\|_{\infty,\eta} \leq 1\}}(y),$$

which is the point-wise projection on the L^∞ unit ball for each voxel $\xi_{i,j,t}$

$$P_\eta(\xi)_{i,j,t} = \frac{\xi_{i,j,t}}{\max\left(1, \frac{|\xi_{i,j,f}|}{\eta}\right)}$$

- $F^*(y) = \frac{1}{2\lambda}\|y\|_2^2 + < d, y >$

$$P_{\sigma F^*}(\xi) = P_{L^2}(\xi) = \frac{\xi - \sigma d}{1 + \frac{\sigma}{\lambda}}$$

- $G(x) = \lambda_L \|x\|_* = \lambda_L \|\Sigma_L\|_1$,

$$\begin{aligned} x &= U\Sigma_L V^H, \quad \Sigma = \operatorname{diag}(\sigma_i) \\ \hat{\sigma}_i = P_{*,\eta}(\sigma_i) &= \operatorname{sign}(\sigma_i)\max(0, |\sigma_i| - \eta) \\ \hat{L} &= U\hat{\Sigma}V^H \end{aligned}$$

8.3.3 MR Adjoint

Using the definition the scalar product 8.1.0.10 and adjointness 8.1.0.11 the adjoint of the MR signal equation 3.1 can be computed as follows

$$< y, Kx > = \sum_{j=1}^{N_c} \int d\vec{k}\; s(\vec{k}) \overline{\underbrace{\int d^3r\, \mathrm{m}_\perp(\vec{r}) c_j(\vec{r}) e^{i<\vec{k},\vec{r}>}}_{K\ x}} =$$

$$\int d^3r \overline{\mathrm{m}_\perp(\vec{r})} \underbrace{\sum_{j=1}^{N_c} \overline{c_j(\vec{r})} \int d\vec{k}\; s(\vec{k}) e^{-i<\vec{k},\vec{r}>}}_{K^H y} =< K^H\, y, x >$$

8.4 Variational Approach for Coil-Sensitivity Estimation

Variational approach to estimate coil sensitivities from temporal averaged dynamic MRI data as described in [120].

1. Compute time-averaged, coil-wise reconstructions (c_j) for the j-th coil, and u_0 with masks M_t

$$\begin{aligned} c_j &= \arg\min_v \sum_{t=1}^{T} \frac{1}{2} \| d_{j,t} - M_t \mathcal{F}(v) \|_2^2 \\ \Rightarrow c_j &= \mathcal{F}^{-1} \left(\frac{1}{\overline{M}} \sum_{t=1}^{T} d_{j,t} \right) \\ \text{where } \overline{M} &= \sum_{t=1}^{T} M_t \\ u_0 &= \sqrt{\sum_{j=1}^{N_c} |c_j|} \cdot \exp\{ i \sum_{j=1}^{N_c} \angle(c_j) \} \end{aligned} \tag{8.18}$$

2. Get absolute value of coil-sensitivities b_j with H1-regularization, $\mu = 10^{-5}$

$$\begin{aligned} |b_j| &= \arg\min_b \frac{\mu}{2}\|bu_0 - |c_j|\|_2^2 + \frac{1}{2}\|\nabla b\|_2^2 \\ \Rightarrow |b_j| &= (\mu u_0^H u_0 + \Delta)^{-1}(\mu u_0 - |c_j|) \\ \text{normalize } b_j : |b_j| &= \frac{|b_j|}{\sum_{i=1}^{N_c} |b_i|^2} \end{aligned} \tag{8.19}$$

3. Choose j_0, such that $|c_{j_0}|$ is maximal, w: weights for area of already explored coil-sensitivities

$$\begin{aligned} & b_{j_0} = |b_{j_0}| \rightarrow \text{ initialize with zero-phase} \\ & u_{j_0} = \arg\min_u \ \nu\mathrm{TGV}(u) + \frac{1}{2}\|b_{j_0}u - c_{j_0}\|_2^2 \\ & \text{for } k = 2, \cdots, N_c \\ & \quad \text{weights } w = \sum_{l=1}^{k} |u_{j_l}| \\ & \quad j_k = \max_{j_k} |b_{j_k} \cdot c_{j_{k-1}}| : \text{most overlap with } c_{j_{k-1}} \\ & \quad \angle(b_{j_k}) = \arg\min_v \frac{\mu}{2}\|\nabla v\|_2^2 + \frac{1}{2}\|w\left(vu_{j_{k-1}}|b_{j_k}| - c_{j_k}\right)\|_2^2 \\ & \quad b_{j_k} = |b_{j_k}| \cdot \exp\left(i\angle b_{j_k}\right) \\ & \quad u_{j_k} = \arg\min_u \ \nu\mathrm{TGV}(u) + \sum_{i=0}^{k-1} \frac{1}{2}\|b_{j_i}u - c_{0_k}\|_2^2 \\ & \text{end} \end{aligned} \tag{8.20}$$

4. Post-process

$$b_j = \arg\min_b \frac{\mu}{2} \sum_j \left(\|b\|_2^2 + \frac{1}{2}\|ub - c_j\|_2^2 \right) \tag{8.21}$$

8.5 Algorithms

8.5.1 k-t SPARSE SENSE reconstruction - primal dual

Algorithm 1: Primal-dual algorithm for solving k-t-SPARSE-SENSE [72] regularized dynamic MR reconstruction

Initialize: $u, \bar{u}, p, \sigma, \tau > 0$
Iterate:

Dual Update:
$p \leftarrow P_{\lambda_S}\left(p + \sigma \partial_t \bar{u}\right)$
$r \leftarrow P_{L^2}\left(r + \sigma K \bar{u}\right)$

Primal Update:
$u^+ \leftarrow u - \tau\left(-\operatorname{div}_t p^+ + K^H r^+\right)$

Stepsize Update (Definition of $\mathcal{S}$ and H see Section 3.5):
$\sigma_+ \leftarrow \mathcal{S}\left(\sigma\tau, \frac{\|(u^+)-u\|}{\|H(u^+)-u\|}\right)$
$\tau_+ \leftarrow \sigma_+$

Extrapolation and update:
$\bar{u} \leftarrow 2u^+ - u$
$u \leftarrow u^+$

8.5.2 Low-rank plus Sparse reconstruction - primal dual

Algorithm 2: Primal-dual algorithm for solving L+S [90] regularized dynamic MR reconstruction

Initialize: L, $\bar{L}$, S, $\bar{S}$, p, $\sigma, \tau = \frac{1}{\sqrt{12+2\|K\|}}$

Iterate:

Dual Update:

$p \leftarrow P_{\lambda_S}\left(p + \sigma \partial_t \bar{S}\right)$

$r \leftarrow P_{L^2}\left(r + \sigma K(\bar{L} + \bar{S})\right)$

Primal Update:

$L^+ \leftarrow P_{*,\tau\lambda_L}\left(L - \tau K^H r^+\right)$

$S^+ \leftarrow S - \tau\left(K^H r^+ - \mathrm{div}_t\, p^+\right)$

Extrapolation and update:

$\bar{L} \leftarrow 2L^+ - L$

$L \leftarrow L^+$

$\bar{S} \leftarrow 2S^+ - S$

$S \leftarrow S^+$

8.5.3 spatio-temporal TV reconstruction - primal dual

Algorithm 3: Primal-dual algorithm for solving TGV regularized dynamic MR reconstruction

Initialize: $u, \bar{u}, p, \sigma, \tau > 0$
Iterate:

Dual Update:
$p \leftarrow P_{\alpha_1}\left(p + \sigma \nabla_\beta \bar{u}\right)$
$r \leftarrow P_{L^2}\left(r + \sigma K \bar{u}\right)$

Primal Update:
$u^+ \leftarrow u - \tau\left(-\operatorname{div}_\beta^1 p^+ + K^H r^+\right)$

Stepsize Update (Definition of $\mathcal{S}$ and H see Section 3.5):
$\sigma_+ \leftarrow \mathcal{S}\left(\sigma\tau, \frac{\|(u^+)-u\|}{\|H^{tv}(u^+)-u\|}\right)$
$\tau_+ \leftarrow \sigma_+$

Extrapolation and update:
$\bar{u} \leftarrow 2u^+ - u$
$u \leftarrow u^+$

8.5.4 spatio-temporal TGV^2 reconstruction - primal dual

Algorithm 4: Primal-dual algorithm for solving TGV regularized dynamic MR reconstruction

Initialize: (u, w), $(\bar{u}, \bar{w})$, (p, q), $\sigma, \tau > 0$
Iterate:

Dual Update:
$p \leftarrow P_{\alpha_1}\left(p + \sigma \nabla_\beta \bar{u} - \bar{w}\right)$
$q \leftarrow P_{\alpha_0}\left(q + \sigma \mathcal{E}_\beta \bar{w}\right)$
$r \leftarrow P_{L^2}\left(r + \sigma K \bar{u}\right)$

Primal Update:
$u^+ \leftarrow u - \tau\left(-\operatorname{div}_\beta^1 p^+ + K^H r^+\right)$
$w^+ \leftarrow w - \tau\left(-p^+ - \operatorname{div}_\beta^2 q_1^+\right)$

Stepsize Update:
$\sigma_+ \leftarrow \mathcal{S}\left(\sigma\tau, \frac{\|(u^+, w^+) - (u, w)\|}{\|H((u^+, w^+) - (u, w))\|}\right)$
$\tau_+ \leftarrow \sigma_+$

Extrapolation and update:
$(\bar{u}, \bar{w}) \leftarrow 2(u^+, w^+) - (u, w)$
$(u, w) \leftarrow (u^+, w^+)$

8.5.5 spatio-temporal ICTV reconstruction - primal dual

Algorithm 5: Primal-dual algorithm for solving ICTV regularized dynamic MR reconstruction

Initialize: (u, v), $(\bar{u}, \bar{v},)$, (p_1, p_2), $\sigma, \tau > 0$
Iterate:

Dual Update:
$p_1 \leftarrow P_{\gamma_1 \alpha_1} \left(p_1 + \sigma \nabla_{\beta_1} (\bar{u} - \bar{v}) \right)$
$p_2 \leftarrow P_{\gamma_2 \alpha_1} \left(p_2 + \sigma \nabla_{\beta_2} \bar{v} \right)$
$r \leftarrow P_{L^2} \left(r + \sigma K \bar{u} \right)$

Primal Update:
$u^+ \leftarrow u - \tau \left(- \operatorname{div}^1_{\beta_1} p_1^+ + K^H r^+ \right)$
$v^+ \leftarrow v - \tau \left(- \operatorname{div}^1_{\beta_1} p_1^+ - \operatorname{div}^1_{\beta_2} p_2^+ \right)$

Stepsize Update (Definition of $\mathcal{S}$ and H see Section 3.5):
$\sigma_+ \leftarrow \mathcal{S} \left(\sigma\tau, \frac{\|(u^+, v^+) - (u,v)\|}{\|H((u^+, v^+) - (u,v))\|} \right)$
$\tau_+ \leftarrow \sigma_+$

Extrapolation and update:
$(\bar{u}, \bar{v} \leftarrow 2(u^+, v^+) - (u, v)$
$(u, v) \leftarrow (u^+, v^+)$

8.5.6 spatio-temporal ICTGV^2 reconstruction - primal dual

Algorithm 6: Primal-dual algorithm for solving ICTGV regularized dynamic MR reconstruction

Initialize: (u, v, w_1, w_2), $(\bar{u}, \bar{v}, \bar{w}_1, \bar{w}_2)$, (p_1, q_1, p_2, q_2), $\sigma, \tau > 0$
Iterate:

Dual Update:

$$p_1 \leftarrow P_{\gamma_1 \alpha_1}\left(p_1 + \sigma \nabla_{\beta_1}(\bar{u} - \bar{v}) - \bar{w}_1\right)$$
$$q_1 \leftarrow P_{\gamma_1 \alpha_0}\left(q_1 + \sigma \mathcal{E}_{\beta_1} \bar{w}_1\right)$$
$$p_2 \leftarrow P_{\gamma_2 \alpha_1}\left(p_2 + \sigma \nabla_{\beta_2} \bar{v} - \bar{w}_2\right)$$
$$q_2 \leftarrow P_{\gamma_2 \alpha_0}\left(q_2 + \sigma \mathcal{E}_{\beta_2} \bar{w}_2\right)$$
$$r \leftarrow P_{L^2}\left(r + \sigma K \bar{u}\right)$$

Primal Update:

$$u^+ \leftarrow u - \tau\left(-\operatorname{div}^1_{\beta_1} p_1^+ + K^H r^+\right)$$
$$w_1^+ \leftarrow w_1 - \tau\left(-p_1^+ - \operatorname{div}^2_{\beta_1} q_1^+\right)$$
$$v^+ \leftarrow v - \tau\left(-\operatorname{div}^1_{\beta_1} p_1^+ - \operatorname{div}^1_{\beta_2} p_2^+\right)$$
$$w_2^+ \leftarrow w_2 - \tau\left(-p_2^+ - \operatorname{div}^2_{\beta_2} q_2^+\right)$$

Stepsize Update (Definition of $\mathcal{S}$ and H see Section 3.5):

$$\sigma_+ \leftarrow \mathcal{S}\left(\sigma\tau, \frac{\|(u^+, v^+, w_1^+, w_2^+) - (u, v, w_1, w_2)\|}{\|H((u^+, v^+, w_1^+, w_2^+) - (u, v, w_1, w_2))\|}\right)$$
$$\tau_+ \leftarrow \sigma_+$$

Extrapolation and update:

$$(\bar{u}, \bar{v}, \bar{w}_1, \bar{w}_2) \leftarrow 2(u^+, v^+, w_1^+, w_2^+) - (u, v, w_1, w_2)$$
$$(u, v, w_1, w_2) \leftarrow (u^+, v^+, w_1^+, w_2^+)$$

8.5.7 Iteratively-regularized Gauss-Newton Algorithm for qMRI

Algorithm 7: Iteratively regularized Gauss-Newton algorithm regularization for qMRI

Initialize:
$k = 0$, $u_k = (q_1, \cdots, q_{N_q}) = 0$, $\lambda, \delta, \gamma, q_\delta, q_\gamma$
while $k < N_{max}$ **do**
  Initialize $DS|_{u=u_k}$, $DS^H|_{u=u_k}$
  Compute $\tilde{I}_p = I_p + DS_p u_k - S_p(u_k), p = 1, \cdots, N_p$
  Choose regularization strategy:
  if $\mathcal{R}_{L^2}(u)$ **then**
    Compute u_{k+1} with algorithm 8
  end
  if $\mathcal{R}(u) = \mathrm{TGV}^2_{sep}(u)$ **then**
    Compute u_{k+1} with algorithm 9
  end
  if $\mathcal{R}(u) = \mathrm{TGV}^2_{frob}(u)$ **then**
    Compute u_{k+1} with algorithm 10
  end
  $\delta \leftarrow \delta q_\delta$
  $\gamma \leftarrow \delta q_\delta$
end

Algorithm 8: Conjugate gradient method for L^2 regularized sub-problem of Alg. 8.5.7 for qMRI

Definitions:
$U = \mathbb{C}^{N_x \times N_y}$, Initialize:

$u \in U^P$, $M = \lambda D S^H D S + \delta Id$, $r = \lambda D S^H \tilde{I} + \delta u_k$

Solve with Conjugate-Gradient Method
$r_0 = r - M x_0$, $p_0 = r_0$
while $k < N_{max}$ **do**

$\alpha_k = \frac{<r_k, r_k>}{<p_k, M p_k>}$
$u^+ \leftarrow u_k + \alpha_k p_k$
$r^+ \leftarrow r_k + \alpha_k M p_k$

$\beta_k = \frac{<r^+, r^+>}{<r, r>}$
$p^+ = r^+ + \beta_k p_k$
end

Algorithm 9: Primal-Dual method for $\mathrm{TGV}^2_{\mathrm{sep}}$ regularized subproblem of Alg. 8.5.7 for qMRI

Definitions:
$U = \mathbb{C}^{N_x \times N_y}$,
$\nabla : U \to U^2$, $\mathcal{E} : U^2 \to U^3$

Initialize:
$\sigma, \tau = \frac{1}{\sqrt{12}}$ $u_i, \bar{u}_i \in U$, $v_i, \bar{v}_i \in U^2$, $p_i \in U^2$, $q_i \in U^3$,$i = 1, \cdots, P$,
$M = \lambda DS^H DS + (\frac{1}{\tau} + \delta) Id$, $r_{\mathrm{part}} = \lambda DS^H \tilde{I} + \delta u_k$

while $k < N_{max}$ **do**

Dual Update:
$p_i \leftarrow P_\gamma \left(p_i + \sigma(\nabla \bar{u}_i - \bar{v}_i)\right)$
$q_i \leftarrow P_{2\gamma} \left(q_i + \sigma \mathcal{E} \bar{v}_i\right)$

Primal Update:
$u_i^+ \leftarrow P_{L^2}(u_i + \tau \operatorname{div}^1 p_i^+)$
$v_i^+ \leftarrow v - \tau(-p_i^+ - \operatorname{div}^2 q_i^+)$

Extrapolation and Update:
$(\bar{u}_i, \bar{v}_i) \leftarrow 2(u_i^+, v_i^+) - (u_i, v_i)$
$(u_i, v_i) \leftarrow (u_i^+, v_i^+)$

end

$$P_\eta(\xi)_{j,l} = \frac{\xi_{j,l}}{\max\left(1, \frac{|\xi_{j,l}|}{\eta}\right)} \quad \text{and} \quad P_{L^2}(\xi) = M^{-1}\left(r_{\mathrm{part}} + \frac{\xi}{\tau}\right)$$

Algorithm 10: Primal-Dual method for $\mathrm{TGV}^2_{\mathrm{frob}}$ regularized subproblem of Alg. 8.5.7 for qMRI

Definitions:
$U = \mathbb{C}^N, N = N_x N_y$, space of vectorized 2d parameter images,
$\nabla : U^P \to U^{P\times 2}$, $\mathcal{E} : U^{P\times 2} \to U^{P\times 3}$

Initialize:
$\sigma, \tau = \frac{1}{\sqrt{12}}$, $u, \bar{u} \in U^P$, $v, \bar{v} \in U^{P\times 2}$, $p \in U^{P\times 2}$, $q \in U^{P\times 3}$,
$M = \lambda D S^H D S + (\frac{1}{\tau} + \delta) Id$, $r_{\mathrm{part}} = \lambda D S^H \tilde{I} + \delta u_k$

while $k < N_{max}$ **do**

Dual Update:
$p \leftarrow P_\gamma\left(p + \sigma(\nabla \bar{u} - \bar{v})\right)$
$q \leftarrow P_{2\gamma}\left(q + \sigma \mathcal{E} \bar{v}\right)$

Primal Update:
$u^+ \leftarrow P_{L^2}(u + \tau \operatorname{div}^1 p^+)$
$v^+ \leftarrow v - \tau(-p^+ - \operatorname{div}^2 q^+)$

Extrapolation and Update:
$(\bar{u}, \bar{v}) \leftarrow 2(u^+, v^+) - (u, v)$
$(u, v) \leftarrow (u^+, v^+)$

end

$$P_\eta(\xi)_{i,p} = \frac{\xi_{i,p}}{\max\left(1, \frac{|\xi|_{\mathrm{frob}}}{\eta}\right)} \quad \text{and} \quad P_{L^2}(\xi) = M^{-1}\left(r_{\mathrm{part}} + \frac{\xi}{\tau}\right)$$

Bibliography

[1] M. H. Levitt, *Spin dynamics: basics of nuclear magnetic resonance*, 2nd ed. Chichester, England ; Hoboken, NJ, 2007, p. 714 (cit. on p. 3).

[2] R. W. Brown, Y.-C. N. Cheng, E. M. Haacke, M. R. Thompson, and R. Venkatesan, Eds., *Magnetic Resonance Imaging*. Chichester, UK, 2014. DOI: 10.1002/9781118633953 (cit. on pp. 3, 11).

[3] P. Zeeman, "The effect of magnetisation on the nature of light emitted by a substance", *Nature*, vol. 55, no. 1424, pp. 347–347, 1897. DOI: 10.1038/055347a0 (cit. on p. 4).

[4] M. Cercignani, N. G. Dowell, and P. S. Tofts, *Quantitative MRI of the Brain : Principles of Physical Measurement*, 2nd editio. 2018 (cit. on p. 11).

[5] D. I. Hoult, "The principle of reciprocity in signal strength calculations - a mathematical guide", *Concepts in Magnetic Resonance*, vol. 12, no. 4, pp. 173–187, 2000. DOI: 10.1002/1099-0534(2000)12:4<173::AID-CMR1>3.0.CO;2-Q (cit. on p. 11).

[6] P. Lauterbur, "Image formation by induced local interactions: Examples employing nuclear magnetic resonance", *Nature*, vol. 242, no. 5394, pp. 190–191, 1973. DOI: 10.1038/242190a0 (cit. on p. 11).

[7] P. Mansfield and P. K. Grannell, "Nmr 'diffraction' in solids?", *Journal of Physics C: Solid State Physics*, vol. 6, no. 22, pp. 422–426, 1973. DOI: 10.1088/0022-3719/6/22/007 (cit. on p. 12).

[8] A. Haase, J. Frahm, D. Matthaei, W. Haenicke, and K. Merboldt, "Flash imaging: Rapid nmr imaging using low flip angles pulses", *Journal of Magnetic Resononance*, vol. 67, no. 2, pp. 258–266, 1986. DOI: 10.1016/J.JMR.2011.09.021 (cit. on p. 12).

[9] E. L. Hahn, "Spin echoes", *Physical Review*, vol. 80, no. 4, pp. 580–594, 1950. DOI: 10.1103/PhysRev.80.580 (cit. on p. 13).

[10] M. Uecker, S. Zhang, D. Voit, A. Karaus, K. D. Merboldt, and J. Frahm, "Real-time mri at a resolution of 20 ms", *NMR in Biomedicine*, vol. 23, no. 8, pp. 986–994, 2010. DOI: 10.1002/nbm.1585 (cit. on pp. 17, 59).

[11] L. Feng, T. Benkert, K. T. Block, D. K. Sodickson, R. Otazo, and H. Chandarana, "Compressed sensing for body mri", *Journal of Magnetic Resonance Imaging*, vol. 45, no. 4, pp. 966–987, 2017. DOI: 10.1002/jmri.25547 (cit. on pp. 17, 18).

[12] S. Winkelmann, T. Schaeffter, T. Koehler, H. Eggers, and O. Doessel, "An optimal radial profile order based on the golden ratio for time-resolved mri", *IEEE Transactions on Medical Imaging*, vol. 26, no. 1, pp. 68–76, 2007. DOI: 10.1109/TMI.2006.885337 (cit. on pp. 17, 57).

[13] D. Piccini, A. Littmann, S. Nielles-Vallespin, and M. O. Zenge, "Spiral phyllotaxis: The natural way to construct a 3d radial trajectory in mri", *Magnetic Resonance in Medicine*, vol. 66, no. 4, pp. 1049–1056, 2011. DOI: 10.1002/mrm.22898 (cit. on p. 17).

[14] G. Bonanno, D. Piccini, M. Benedicte, M. O. Zenge, and M. Stuber, "A new binning approach for 3d motion corrected self-navigation whole-heart coronary mra using independent component analysis of individual coils", in *Proc. Intl. Soc. Mag. Reson. Med. 22 (2014) 0936.*, vol. 22, 2014, p. 5689 (cit. on p. 17).

[15] L. Feng, D. K. Sodickson, and R. Otazo, "A robust and automatic cardiac and respiratory motion detection framework for self-navigated radial mri", in *Proc. Intl. Soc. Mag. Reson. Med. 22*, vol. 61, 2014, p. 4360 (cit. on p. 17).

[16] L. Feng, S. Coppo, D. Piccini, J. Yerly, R. P. Lim, P. G. Masci, M. Stuber, D. K. Sodickson, and R. Otazo, "5d whole-heart sparse mri", *Magnetic Resonance in Medicine*, vol. 79, no. 2, pp. 826–838, 2018. DOI: 10.1002/mrm.26745 (cit. on p. 17).

[17] K. T. Block, H. Chandarana, G. Fatterpekar, M. Hagiwara, S. Milla, T. Mulholland, M. Bruno, C. Geppert, and D. K. Sodickson, "Improving the robustness of clinical t1-weighted mri using radial vibe", *MAGNETOM Flash, Siemens*, vol. 5, pp. 6–11, 2013 (cit. on p. 19).

[18] J. Hadamard, "Sur les problèmes aux dérivées partielles et leur signification physique.", *Princeton University Bulletin*, vol. 13, pp. 49–52, 1902 (cit. on p. 22).

[19] C. E. Shannon, "A mathematical theory of communication", *Bell System Technical Journal*, vol. 27, no. 3, pp. 379–423, 1948. DOI: 10.1002/j.1538-7305.1948.tb01338.x (cit. on p. 22).

[20] C. Shannon, "Communication in the presence of noise.", *Proceedings of the IRE*, vol. 37, pp. 10–21, 1949 (cit. on p. 22).

[21] Z.-P. Liang and P. C. Lauterbur, *Principles of Magnetic Resonance Imaging: A Signal Processing Perspective*. 1999. DOI: 10.1109/MSP.2002.1012356 (cit. on p. 23).

[22] H. Nyquist, "Thermal agitation of electric charge in conductors", *Physical Review*, vol. 32, no. 1, pp. 110–113, 1928. DOI: 10.1103/PhysRev.32.110 (cit. on p. 24).

[23] J. B. Johnson, "Thermal agitation of electricity in conductors", *Physical Review*, vol. 32, no. 1, pp. 97–109, 1928. DOI: 10.1103/PhysRev.32.97 (cit. on p. 24).

[24] J. W. Carlson and T. Minemura, "Imaging time reduction through multiple receiver coil data acquisition and image reconstruction", *Magnetic Resonance in Medicine*, vol. 29, no. 5, pp. 681–687, 1993. DOI: 10.1002/mrm.1910290516 (cit. on p. 27).

[25] D. K. Sodickson and W. J. Manning, "Simultaneous acquisition of spatial harmonics (smash): Fast imaging with radiofrequency coil arrays", *Magnetic Resonance in Medicine*, vol. 38, no. 4, pp. 591–603, 1997. DOI: 10.1002/mrm.1910380414 (cit. on p. 27).

[26] M. Griswold, D. Walsh, R. M. Heidemann, A. Haase, and P. Jakob, "The use of an adaptive reconstruction for array coil sensitivity mapping and intensity normalization", *Proc. Intl. Soc. Mag. Reson. Med. 10*, vol. 43, no. 5, p. 2410, 2002 (cit. on pp. 27, 59).

[27] J. B. Ra and C. Y. Rim, "Fast imaging using subencoding data sets from multiple detectors", *Magnetic Resonance in Medicine*, vol. 30, no. 1, pp. 142–145, 1993. DOI: 10.1002/mrm.1910300123 (cit. on p. 27).

[28] K. P. Pruessmann, M. Weiger, M. Scheidegger, and P. Boesiger, "Sense: Sensitivity encoding for fast mri", *Magnetic Resonance in Medicine*, vol. 42, no. 5, pp. 952–962, 1999. DOI: 10.1002/(SICI)1522-2594(199911)42:5<952::AID-MRM16>3.0.CO;2-S (cit. on pp. 27, 28, 55).

[29] K. P. Pruessmann, M. Weiger, P. Börnert, and P. Boesiger, "Advances in sensitivity encoding with arbitrary k-space trajectories", *Magnetic Resonance in Medicine*, vol. 46, no. 4, pp. 638–651, 2001. DOI: 10.1002/mrm.1241 (cit. on pp. 27, 28, 60).

[30] M. Uecker, P. Lai, M. J. Murphy, P. Virtue, M. Elad, J. M. Pauly, S. S. Vasanawala, and M. Lustig, "Espirit-an eigenvalue approach to autocalibrating parallel mri: Where sense meets grappa", *Magnetic Resonance in Medicine*, vol. 71, no. 3, pp. 990–1001, 2014. DOI: 10.1002/mrm.24751 (cit. on pp. 27, 58).

[31] D. L. Phillips, "A technique for the numerical solution of certain integral equations of the first kind", *Journal of the ACM*, vol. 9, no. 1, pp. 84–97, 1962. DOI: 10.1145/321105.321114 (cit. on p. 29).

[32] A. N. Tikhonov, "Solution of incorrectly formulated problems and the regularisation method.pdf", *Soviet Mathematics Doklady*, vol. 4, no. 4, pp. 1035–1038, 1963. DOI: 10.1111/J.1365-246X.2012.05699.X (cit. on p. 29).

[33] Q. Xiang and R. M. Henkelman, "K-space description for mr imaging of dynamic objects", *Magnetic Resonance in Medicine*, vol. 29, no. 3, pp. 422–428, 1993. DOI: 10.1002/mrm.1910290324 (cit. on p. 31).

[34] J. Maclaren, M. Herbst, O. Speck, and M. Zaitsev, "Prospective motion correction in brain imaging: A review", *Magnetic Resonance in Medicine*, vol. 69, no. 3, pp. 621–636, 2013. DOI: 10.1002/mrm.24314 (cit. on p. 31).

[35] M. Usman, D. Atkinson, F. Odille, C. Kolbitsch, G. Vaillant, T. Schaeffter, P. G. Batchelor, and C. Prieto, "Motion corrected compressed sensing for free-breathing dynamic cardiac mri", *Magnetic Resonance in Medicine*, vol. 70, no. 2, pp. 504–516, 2012. DOI: 10.1002/mrm.24463 (cit. on p. 31).

[36] C. Prieto, M. Doneva, M. Usman, M. Henningsson, G. Greil, T. Schaeffter, and R. M. Botnar, "Highly efficient respiratory motion compensated free-breathing coronary mra using golden-step cartesian acquisition", *Journal of Magnetic Resonance Imaging*, vol. 41, no. 3, pp. 738–746, 2015. DOI: 10.1002/jmri.24602 (cit. on p. 31).

[37] S. J. Riederer, T. Tasciyan, F. Farzaneh, J. N. Lee, R. C. Wright, and R. J. Herfkens, "Mr fluoroscopy: Technical feasibility", *Magnetic Resonance in Medicine*, vol. 8, no. 1, pp. 1–15, 1988. DOI: 10.1002/mrm.1910080102 (cit. on p. 32).

[38] F. R. Korosec, R. Frayne, T. M. Grist, and C. A. Mistretta, "Time-resolved contrast-enhanced 3d mr angiography", *Magnetic Resonance in Medicine*, vol. 36, no. 3, pp. 345–351, 1996. DOI: 10.1002/mrm.1910360304 (cit. on p. 32).

[39] R. P. Lim, M. Shapiro, E. Y. Wang, M. Law, J. S. Babb, L. E. Rueff, J. S. Jacob, S. Kim, R. H. Carson, T. P. Mulholland, G. Laub, and E. M. Hecht, "3d time-resolved mr angiography (mra) of the carotid arteries with time-resolved imaging with stochastic trajectories: Comparison with 3d contrast-enhanced bolus-chase mra and 3d time-of-flight mra", *American Journal of Neuroradiology*, vol. 29, no. 10, pp. 1847–1854, 2008. DOI: 10.3174/ajnr.A1252 (cit. on p. 32).

[40] P. Kellman, F. H. Epstein, and E. R. McVeigh, "Adaptive sensitivity encoding incorporating temporal filtering (tsense).", *Magnetic resonance in medicine*, vol. 45, no. 5, pp. 846–52, 2001 (cit. on p. 32).

[41] F. A. Breuer, P. Kellman, M. A. Griswold, and P. M. Jakob, "Dynamic autocalibrated parallel imaging using temporal grappa (tgrappa).", *Magnetic resonance in medicine*, vol. 53, no. 4, pp. 981–5, 2005. DOI: 10.1002/mrm.20430 (cit. on p. 32).

[42] J. Tsao, P. Boesiger, and K. P. Pruessmann, "K-t blast and k-t sense: Dynamic mri with high frame rate exploiting spatiotemporal correlations", *Magnetic Resonance in Medicine*, vol. 50, no. 5, pp. 1031–1042, 2003. DOI: 10.1002/mrm.10611 (cit. on p. 32).

[43] F. Huang, J. Akao, S. Vijayakumar, G. R. Duensing, and M. Limkeman, "K-t grappa: A k-space implementation for dynamic mri with high reduction factor.", *Magnetic Resonance in Medicine*, vol. 54, no. 5, pp. 1172–1184, 2005. DOI: 10.1002/mrm.20641 (cit. on p. 32).

[44] J. Tsao and S. Kozerke, "Mri temporal acceleration techniques", *Journal of Magnetic Resonance Imaging*, vol. 36, no. 3, pp. 543–560, 2012. DOI: 10.1002/jmri.23640 (cit. on p. 32).

[45] L. I. Rudin, S. Osher, and E. Fatemi, "Nonlinear total variation based noise removal algorithms", *Physica D: Nonlinear Phenomena*, vol. 60, no. 1-4, pp. 259–268, 1992. DOI: 10.1016/0167-2789(92)90242-F (cit. on p. 33).

[46] A. Chambolle, V. Caselles, D. Cremers, M. Novaga, and T. Pock, "An introduction to total variation for image analysis", *Theoretical foundations and numerical methods for sparse recovery*, vol. 9, pp. 263–340, 2010. DOI: 10.1515/9783110226157.263 (cit. on p. 33).

[47] L. Condat, "Discrete total variation: New definition and minimization", *SIAM Journal on Imaging Sciences*, vol. 10, no. 3, pp. 1258–1290, 2017. DOI: 10.1137/16M1075247 (cit. on p. 34).

[48] D. L. Donoho, "Compressed sensing", *IEEE Transactions on Information Theory*, vol. 52, no. 4, pp. 1289–1306, 2006. DOI: 10.1109/TIT.2006.871582 (cit. on p. 34).

[49] E. J. Candès, J. K. Romberg, and T. Tao, "Stable signal recovery from incomplete and inaccurate measurements", *Communications on Pure and Applied Mathematics*, vol. 59, no. 8, pp. 1207–1223, 2006. DOI: 10.1002/cpa.20124 (cit. on p. 34).

[50] E. J. Candès, J. K. Romberg, and T. Tao, "Robust uncertainty principles: Exact signal reconstruction from highly incomplete frequency information", *IEEE Transactions on Information Theory*, vol. 52, no. 2, pp. 489–509, 2006. DOI: 10.1109/TIT.2005.862083 (cit. on p. 34).

[51] M. Elad, M. A. Figueiredo, and Y. Ma, "On the role of sparse and redundant representations in image processing", *Proceedings of the IEEE*, vol. 98, no. 6, pp. 972–982, 2010. DOI: 10.1109/JPROC.2009.2037655 (cit. on p. 35).

[52] K. T. Block, M. Uecker, and J. Frahm, "Undersampled radial mri with multiple coils. iterative image reconstruction using a total variation constraint", *Magnetic Resonance in Medicine*, vol. 57, no. 6, pp. 1086–1098, 2007. DOI: 10.1002/mrm.21236 (cit. on p. 36).

[53] M. Lustig, D. Donoho, and J. M. Pauly, "Sparse mri: The application of compressed sensing for rapid mr imaging", *Magnetic Resonance in Medicine*, vol. 58, no. 6, pp. 1182–1195, 2007. DOI: 10.1002/mrm.21391 (cit. on p. 36).

[54] V. Caselles, A. Chambolle, and M. Novaga, "The discontinuity set of solutions of the tv denoising problem and some extensions", *Multiscale Modeling and Simulation*, vol. 6, no. 3, pp. 879–894, 2007. DOI: 10.1137/070683003 (cit. on p. 36).

[55] K. Bredies, K. Kunisch, and T. Pock, "Total generalized variation", *SIAM Journal on Imaging Sciences*, vol. 3, no. 3, pp. 492–526, 2010. DOI: 10.1137/090769521 (cit. on pp. 36, 38, 52).

[56] K. Bredies and M. Holler, "A tgv-based framework for variational image decompression, zooming, and reconstruction. part i: Analytics", *SIAM Journal on Imaging Sciences*, vol. 8, no. 4, pp. 2814–2850, 2015. DOI: 10.1137/15M1023865 (cit. on pp. 36, 44).

[57] ——, "A tgv-based framework for variational image decompression, zooming, and reconstruction. part ii: Numerics", *SIAM Journal on Imaging Sciences*, vol. 8, no. 4, pp. 2814–2850, 2015. DOI: 10.1137/15M1023865 (cit. on pp. 36, 52).

[58] K. Bredies, "Symmetric tensor fields of bounded deformation", *Annali di Matematica Pura ed Applicata*, vol. 192, no. 5, pp. 815–851, 2013. DOI: 10.1007/s10231-011-0248-4 (cit. on p. 37).

[59] K. Bredies and M. Holler, "Regularization of linear inverse problems with total generalized variation", *Journal of Inverse and Ill-Posed Problems*, vol. 22, no. 6, pp. 871–913, 2014. DOI: 10.1515/jip-2013-0068 (cit. on p. 37).

[60] F. Knoll, K. Bredies, T. Pock, and R. Stollberger, "Second order total generalized variation (tgv) for mri", *Magnetic Resonance in Medicine*, vol. 65, no. 2, pp. 480–491, 2011. DOI: 10.1002/mrm.22595 (cit. on p. 38).

[61] F. Knoll, C. Clason, K. Bredies, M. Uecker, and R. Stollberger, "Parallel imaging with nonlinear reconstruction using variational penalties", *Magnetic Resonance in Medicine*, vol. 67, no. 1, pp. 34–41, 2012. DOI: 10.1002/mrm.22964 (cit. on pp. 38, 59).

[62] T. Valkonen, K. Bredies, and F. Knoll, "Total generalized variation in diffusion tensor imaging", *SIAM Journal on Imaging Sciences*, vol. 6, no. 1, pp. 487–525, 2013. DOI: 10.1137/120867172 (cit. on p. 38).

[63] F. Knoll, G. Schultz, K. Bredies, D. Gallichan, M. Zaitsev, J. Hennig, and R. Stollberger, "Reconstruction of undersampled radial patloc imaging using total generalized variation", *Magnetic Resonance in Medicine*, vol. 70, no. 1, pp. 40–52, 2013. DOI: 10.1002/mrm.24426 (cit. on p. 38).

[64] C. Langkammer, K. Bredies, B. A. Poser, M. Barth, G. Reishofer, A. P. Fan, B. Bilgic, F. Fazekas, C. Mainero, and S. Ropele, "Fast quantitative susceptibility mapping using 3d epi and total generalized variation", *NeuroImage*, vol. 111, pp. 622–630, 2015. DOI: 10.1016/j.neuroimage.2015.02.041 (cit. on p. 38).

[65] D. Stäb, S. Bollmann, C. Langkammer, K. Bredies, and M. Barth, "Accelerated mapping of magnetic susceptibility using 3d planes-on-a-paddlewheel (pop) epi at ultra-high field strength", *NMR in Biomedicine*, vol. 30, no. 4, e3620, 2017. DOI: 10.1002/nbm.3620 (cit. on p. 38).

[66] S. M. Spann, K. S. Kazimierski, C. S. Aigner, M. Kraiger, K. Bredies, and R. Stollberger, "Spatio-temporal tgv denoising for asl perfusion imaging", *NeuroImage*, vol. 157, pp. 81–96, 2017. DOI: 10.1016/j.neuroimage.2017.05.054 (cit. on p. 38).

[67] K. Bredies, "Recovering piecewise smooth multichannel images by minimization of convex functionals with total generalized variation penalty", in *Lecture Notes in Computer Science*, ser. Lecture Notes in Computer Science, A. Bruhn, T. Pock, and X.-C. Tai, Eds., vol. 8293

LNCS, 2014, pp. 44–77. DOI: 10.1007/978-3-642-54774-4_3 (cit. on pp. 38, 124, 139).

[68] M. Holler and K. Kunisch, "On infimal convolution of tv type functionals and applications to video and image reconstruction", *SIAM Journal on Imaging Sciences*, vol. 7, no. 4, pp. 2258–2300, 2014 (cit. on pp. 39, 42, 144).

[69] G. Aubert and P. Kornprobst, *Mathematical Problems in Image Processing Partial Differential Equations and the Calculus of Variations*. 2000, vol. 147, p. 377. DOI: 10.1007/978-0-387-44588-5 (cit. on p. 39).

[70] P. Kornprobst, R. Deriche, and G. Aubert, "Image sequence analysis via partial differential equations", *Journal of Mathematical Imaging and Vision*, vol. 11, no. 1, pp. 5–26, 1999 (cit. on p. 39).

[71] H. Jung, K. Sung, K. S. Nayak, E. Y. p. Kim, and J. C. Ye, "K-t focuss: A general compressed sensing framework for high resolution dynamic mri", *Magnetic Resonance in Medicine*, vol. 61, no. 1, pp. 103–116, 2009. DOI: 10.1002/mrm.21757 (cit. on pp. 39, 70).

[72] R. Otazo, D. Kim, L. Axel, and D. K. Sodickson, "Combination of compressed sensing and parallel imaging for highly accelerated first-pass cardiac perfusion mri.", *Magnetic Resonance in Medicine*, vol. 64, no. 3, pp. 767–76, 2010. DOI: 10.1002/mrm.22463 (cit. on pp. 39, 91, 156).

[73] J. Liu, A. Lefebvre, M. O. Zenge, M. Schmidt, E. Mueller, and M. S. Nadar, "2d bssfp real-time cardiac cine-mri : Compressed sensing featuring weighted redundant haar wavelet regularization in space and time", *Journal of Cardiovascular Magnetic Resonance*, vol. 15, no. Suppl 1, p. 49, 2013. DOI: 10.1186/1532-429X-15-S1-P49 (cit. on p. 39).

[74] G. Adluru, S. P. Awate, T. Tasdizen, R. T. Whitaker, and E. V. R. DiBella, "Temporally constrained reconstruction of dynamic cardiac perfusion mri", *Magnetic Resonance in Medicine*, vol. 57, no. 6, pp. 1027–1036, 2007. DOI: 10.1002/mrm.21248 (cit. on p. 39).

[75] M. Lustig, J. M. Santos, D. Donoho, and J. M. Pauly, "K-t sparse: High frame rate dynamic mri exploiting spatio-temporal sparsity", in *Proc. Intl. Soc. Mag. Reson. Med. 14*, Seattle, 2006, p. 2420 (cit. on p. 40).

[76] L. Feng, M. B. Srichai, R. P. Lim, A. Harrison, W. King, G. Adluru, E. V. R. Dibella, D. K. Sodickson, R. Otazo, and D. Kim, "Highly accelerated real-time cardiac cine mri using k-t sparse-sense", *Magnetic Resonance in Medicine*, vol. 70, no. 1, pp. 64–74, 2013. DOI: 10.1002/mrm.24440 (cit. on p. 40).

[77] Z.-P. Liang, "Spatiotemporal imaging with partially separable functions", in *IEEE International Symposium on Biomedical Imaging*, vol. 2, Washington, DC, USA, 2007, pp. 988–991. DOI: 10.1109/ISBI.2007.357020 (cit. on p. 40).

[78] C. Brinegar, Y.-J. Wu, L. Fley, K. Hitchens, Q. Ye, C. Ho, and Z.-P. Liang, "Real-time cardiac mri without triggering, gating, or breath holding", in *Conf Proc IEEE Eng Med Biol Soc*, vol. 15, 2008, pp. 3381–3384. DOI: 10.1016/j.drugalcdep.2008.02.002.A (cit. on p. 40).

[79] H. Pedersen, S. Kozerke, S. Ringgaard, K. Nehrke, and W. Y. Kim, "K-t pca: Temporally constrained k-t blast reconstruction using principal component analysis.", *Magnetic resonance in medicine*, vol. 62, no. 3, pp. 706–16, 2009. DOI: 10.1002/mrm.22052 (cit. on p. 40).

[80] J. V. Velikina and A. A. Samsonov, "Reconstruction of dynamic image series from undersampled mri data using data-driven model consistency condition (mocco).", *Magnetic Resonance in Medicine*, vol. 00, no. 5, pp. 1–12, 2014. DOI: 10.1002/mrm.25513 (cit. on p. 40).

[81] H. Jung and J. C. Ye, "Motion estimated and compensated compressed sensing dynamic magnetic resonance imaging: What we can learn from video compression techniques", *International Journal of Imaging Systems and Technology*, vol. 20, no. 2, pp. 81–98, 2010. DOI: 10.1002/ima.20231 (cit. on p. 40).

[82] E. J. Candes and B. Recht, "Exact low-rank matrix completion via convex optimization", *2008 46th Annual Allerton Conference on Communication, Control, and Computing*, vol. 9, no. 6, pp. 806–812, 2008. DOI: 10.1109/ALLERTON.2008.4797640 (cit. on p. 40).

[83] J. P. Haldar and Z.-P. Liang, "Spatiotemporal imaging with partially separable functions: A matrix recovery approach.", in *IEEE International Symposium on Biomedical Imaging: From Nano to Macro*, Rotterdam, 2010, pp. 716–719. DOI: 10.1109/ISBI.2010.5490076 (cit. on p. 40).

[84] S. G. Lingala, Y. Hu, E. Dibella, and M. Jacob, "Accelerated dynamic mri exploiting sparsity and low-rank structure: K-t slr", *Transactions on Medical Imaging*, vol. 30, no. 5, pp. 1042–1054, 2011. DOI: 10.1109/TMI.2010.2100850 (cit. on pp. 40, 69, 70).

[85] B. Zhao, J. P. Haldar, A. G. Christodoulou, and Z.-P. Liang, "Image reconstruction from highly undersampled k-t-space data with joint partial separability and sparsity constraints", *Medical Imaging, IEEE Transactions on*, vol. 31, no. 9, pp. 1809–1820, 2012. DOI: 10.1109/TMI.2012.2203921 (cit. on p. 40).

[86] A. G. Christodoulou, H. Zhang, B. Zhao, T. K. Hitchens, C. Ho, and Z.-P. Liang, "High-resolution cardiovascular mri by integrating parallel imaging with low-rankand sparse modeling", *IEEE Transactions on Biomedical Engineering*, vol. 60, no. 11, pp. 3083–3092, 2013. DOI: 10.1109/TBME.2013.2266096 (cit. on p. 40).

[87] E. J. Candès, X. Li, Y. Ma, and J. Wright, "Robust principal component analysis?", *Journal of the ACM*, vol. 58, no. 3, pp. 1–37, 2011 (cit. on p. 41).

[88] H. Ji, S. Huang, Z. Shen, and Y. Xu, "Robust video restoration by joint sparse and low rank matrix approximation", *SIAM Journal on Imaging Sciences*, vol. 4, no. 4, pp. 1122–1142, 2011. DOI: 10.1137/100817206 (cit. on p. 41).

[89] H. Gao, S. Rapacchi, D. Wang, J. Moriarty, C. Meehan, J. Sayre, G. Laub, P. Finn, and P. Hu, "Compressed sensing using prior rank, intensity and sparsity model (prism): Applications in cardiac cine mri.", in *Proc. Intl. Soc. Mag. Reson. Med. 20*, 2012, p. 2242 (cit. on p. 41).

[90] R. Otazo, E. Candès, and D. K. Sodickson, "Low-rank plus sparse matrix decomposition for accelerated dynamic mri with separation of background and dynamic components", *Magnetic Resonance in Medicine*, vol. 73, no. 3, pp. 1125–1136, 2015. DOI: 10.1002/mrm.25240 (cit. on pp. 41, 69, 70, 91, 157).

[91] B. Trémoulhéac, N. Dikaios, D. Atkinson, and S. R. Arridge, "Dynamic mr image reconstruction-separation from undersampled k,t-space via low-rank plus sparse prior", *IEEE Transactions on Medical*

Imaging, vol. 33, no. 8, pp. 1689–1701, 2014. DOI: 10.1109/TMI.2014.2321190 (cit. on pp. 41, 69, 70, 80).

[92] M. Akçakaya, T. A. Basha, S. Pflugi, M. Foppa, K. V. Kissinger, T. H. Hauser, and R. Nezafat, "Localized spatio-temporal constraints for accelerated cmr perfusion", *Magnetic resonance in medicine*, vol. 72, no. 3, pp. 629–639, 2014. DOI: 10.1002/mrm.24963 (cit. on p. 41).

[93] F. Ong and M. Lustig, "Beyond low rank + sparse: Multi-scale low rank matrix decomposition.", *IEEE journal of selected topics in signal processing*, vol. 10, no. 4, pp. 672–687, 2016. DOI: 10.1109/JSTSP.2016.2545518 (cit. on p. 41).

[94] H. Yoon, K. S. Kim, D. Kim, Y. Bresler, and J. C. Ye, "Motion adaptive patch-based low-rank approach for compressed sensing cardiac cine mri", *IEEE Transactions on Medical Imaging*, vol. 33, no. 11, pp. 2069–2085, 2014. DOI: 10.1109/TMI.2014.2330426 (cit. on p. 41).

[95] M. Holler, "Higher order regularization for model based data decompression dissertation", PhD thesis, 2013 (cit. on p. 41).

[96] F. Knoll, C. Clason, C. Diwoky, and R. Stollberger, "Adapted random sampling patterns for accelerated mri", *Magnetic Resonance Materials in Physics, Biology and Medicine*, vol. 24, no. 1, pp. 43–50, 2011. DOI: 10.1007/s10334-010-0234-7 (cit. on p. 44).

[97] L. Wissmann, C. Santelli, W. P. Segars, and S. Kozerke, "Mrxcat: Realistic numerical phantoms for cardiovascular magnetic resonance", *Journal of Cardiovascular Magnetic Resonance*, vol. 16, no. 1, p. 63, 2014. DOI: 10.1186/s12968-014-0063-3 (cit. on pp. 46, 54, 56, 71).

[98] A. Beck and M. Teboulle, "A fast iterative shrinkage-thresholding algorithm for linear inverse problems", *SIAM Journal on Imaging Sciences*, vol. 2, no. 1, pp. 183–202, 2009. DOI: 10.1137/080716542 (cit. on p. 47).

[99] A. A. Chambolle and T. Pock, "A first-order primal-dual algorithm for convex problems with applications to imaging.", *Journal of Mathemtical Imaging and Vision*, vol. 40, no. 1, pp. 120–145, 2011. DOI: 10.1007/s10851-010-0251-1 (cit. on pp. 47, 52).

[100] Y. Malitsky and T. Pock, "A first-order primal-dual algorithm with linesearch", *SIAM Journal on Optimization*, vol. 28, no. 1, pp. 411–432, 2018. DOI: 10.1137/16M1092015 (cit. on p. 52).

[101] F. Liu, J. V. Velikina, W. F. Block, R. Kijowski, and A. A. Samsonov, "Fast realistic mri simulations based on generalized multi-pool exchange tissue model", *IEEE Transactions on Medical Imaging*, vol. 36, no. 2, pp. 527–537, 2017. DOI: 10.1109/TMI.2016.2620961 (cit. on pp. 54, 125).

[102] R. Grimm, J. Churt, A. Fieselmann, K. T. Block, B. Kiefer, and J. Hornegger, "A digital perfusion phantom for t1-weighted dce-mri", in *Proc. Intl. Soc. Mag. Reson. Med. 20*, vol. 20, Melbourne, 2012, p. 2559 (cit. on pp. 54, 91).

[103] M. Guerquin-Kern, L. Lejeune, K. P. Pruessmann, and M. Unser, "Realistic analytical phantoms for parallel magnetic resonance imaging", *IEEE Transactions on Medical Imaging*, vol. 31, no. 3, pp. 626–636, 2012. DOI: 10.1109/TMI.2011.2174158 (cit. on p. 54).

[104] Z. Wang, A. C. Bovik, H. R. Sheikh, and E. P. Simoncelli, "Image quality assessment: From error visibility to structural similarity", *IEEE Transactions on Image Processing*, vol. 13, no. 4, pp. 600–612, 2004. DOI: 10.1109/TIP.2003.819861 (cit. on p. 54).

[105] Z. Wang and A. C. Bovik, "Mean squarred error : Love it or leave it ?", *IEEE Signal Processing Magazine*, no. January, pp. 98–117, 2009 (cit. on p. 54).

[106] R. Dosselmann and X. Yang, "A comprehensive assessment of the structural similarity index", *Signal, Image and Video Processing*, vol. 5, no. 1, pp. 81–91, 2011. DOI: 10.1007/s11760-009-0144-1 (cit. on p. 55).

[107] O. N. Jaspan, R. Fleysher, and M. L. Lipton, "Compressed sensing mri: A review of the clinical literature", *British Journal of Radiology*, vol. 88, no. 1056, p. 20 150 487, 2015. DOI: 10.1259/bjr.20150487 (cit. on p. 55).

[108] P. M. Robson, A. K. Grant, A. J. Madhuranthakam, R. Lattanzi, D. K. Sodickson, and C. A. Mckenzie, "Comprehensive quantification of snr ratio and g-factor for image-based and k-space based parallel imaging reconstructions", *Magnetic Resonance in Medicine*, vol. 60, no. 4, pp. 895–907, 2010. DOI: 10.1002/mrm.21728.Comprehensive (cit. on p. 55).

[109] P. Kellman and E. R. McVeigh, "Image reconstruction in snr units: A general method for snr measurement", *Magnetic Resonance in Medicine*, vol. 54, no. 6, pp. 1439–1447, 2005. DOI: 10.1002/mrm.20713 (cit. on p. 55).

[110] M. S. Hansen, S. J. Inati, and P. Kellman, "Noise propagation in region of interest measurements", *Magnetic Resonance in Medicine*, vol. 73, no. 3, pp. 1300–1308, 2015. DOI: 10.1002/mrm.25194 (cit. on p. 55).

[111] K. Tobias Block and M. Uecker, "Simple method for adaptive gradient-delay compensation in radial mri", in *Proc. Intl. Soc. Mag. Reson. Med. 19*, vol. 19, 2011, p. 2816 (cit. on pp. 57, 94).

[112] K. T. Block, H. Chandarana, S. Milla, M. Bruno, T. Mulholland, G. Fatterpekar, M. Hagiwara, R. Grimm, C. Geppert, B. Kiefer, and D. K. Sodickson, "Towards routine clinical use of radial stack-of-stars 3d gradient-echo sequences for reducing motion sensitivity", *Journal of the Korean Society of Magnetic Resonance in Medicine*, vol. 18, no. 2, p. 87, 2014. DOI: 10.13104/jksmrm.2014.18.2.87 (cit. on pp. 57, 90, 94, 117, 122).

[113] P. J. Beatty, D. G. Nishimura, and J. M. Pauly, "Rapid gridding reconstruction with a minimal oversampling ratio", *IEEE Transactions on Medical Imaging*, vol. 24, no. 6, pp. 799–808, 2005. DOI: 10.1109/TMI.2005.848376 (cit. on p. 57).

[114] J. A. Fessler and B. P. Sutton, "Nonuniform fast fourier transforms using min-max interpolation", *IEEE Transactions on Signal Processing*, vol. 51, no. 2, pp. 560–574, 2003. DOI: 10.1109/TSP.2002.807005 (cit. on p. 57).

[115] F. Knoll, A. Schwarzl, C. Diwoky, and D. K. Sodickson, "Gpunufft - an open source gpu library for 3d regridding with direct matlab interface.", in *Proc. Intl. Soc. Mag. Reson. Med. 22*, vol. 34, 2014, p. 4292. DOI: 10.1002/mrm.24751 (cit. on pp. 57, 92).

[116] D. Potts, J. Prestin, and A. Vollrath, "A fast algorithm for nonequispaced fourier transforms on the rotation group", *Numerical Algorithms*, vol. 52, no. 3, pp. 355–384, 2009. DOI: 10.1007/s11075-009-9277-0 (cit. on p. 57).

[117] J. G. Pipe and P. Menon, "Sampling density compensation in mri: Rationale and an iterative numerical solution.", *Magnetic Resonance in Medicine*, vol. 41, no. 1, pp. 179–86, 1999. DOI: 10.1002/(SICI)1522-2594(199901)41:1<179::AID-MRM25>3.0.CO;2-V (cit. on p. 58).

[118] D. O. Walsh, A. F. Gmitro, and M. W. Marcellin, "Adaptive reconstruction of phased array mr imagery", *Magnetic Resonance in Medicine*, vol. 43, no. 5, pp. 682–690, 2000. DOI: 10.1002/(SICI)1522-2594(200005)43:5<682::AID-MRM10>3.0.CO;2-G (cit. on p. 58).

[119] M. Uecker, T. Hohage, K. T. Block, and J. Frahm, "Image reconstruction by regularized nonlinear inversion - joint estimation of coil sensitivities and image content", *Magnetic Resonance in Medicine*, vol. 60, no. 3, pp. 674–682, 2008. DOI: 10.1002/mrm.21691 (cit. on p. 59).

[120] M. Schloegl, M. Holler, and R. Stollberger, "A variational approach for coil-sensitivity estimation for undersampled phase-sensitive dynamic mri reconstruction", *Proc. Intl. Soc. Mag. Reson. Med*, vol. 23, p. 3692, 2015 (cit. on pp. 59, 71, 154).

[121] M. Buehrer, K. P. Pruessmann, P. Boesiger, and S. Kozerke, "Array compression for mri with large coil arrays", *Magnetic Resonance in Medicine*, vol. 57, no. 6, pp. 1131–1139, 2007. DOI: 10.1002/mrm.21237 (cit. on p. 60).

[122] T. Zhang, J. M. Pauly, S. S. Vasanawala, and M. Lustig, "Coil compression for accelerated imaging with cartesian sampling", *Magnetic Resonance in Medicine*, vol. 69, no. 2, pp. 571–582, 2013. DOI: 10.1002/mrm.24267 (cit. on p. 60).

[123] S. J. Inati, J. D. Naegele, N. R. Zwart, V. Roopchansingh, M. J. Lizak, D. C. Hansen, C. Y. Liu, D. Atkinson, P. Kellman, S. Kozerke, H. Xue, A. E. Campbell-Washburn, T. S. Sørensen, and M. S. Hansen, "Ismrm raw data format: A proposed standard for mri raw datasets", *Magnetic Resonance in Medicine*, vol. 77, no. 1, pp. 411–421, 2017. DOI: 10.1002/mrm.26089 (cit. on p. 61).

[124] M. S. Hansen and T. S. Sørensen, "Gadgetron: An open source framework for medical image reconstruction", *Magnetic Resonance in Medicine*, vol. 69, no. 6, pp. 1768–1776, 2013. DOI: 10.1002/mrm.24389 (cit. on p. 61).

[125] M. Uecker, F. Ong, J. Tamir, D. Bahari, P. Virtue, J. Y. Cheng, T. Zhang, and M. Lustig, "Robust 4d flow denoising using divergence-free wavelet transform", in *Proc. Intl. Soc. Mag. Reson. Med. 23*, 2015, p. 2486. DOI: 10.1002/mrm.25176 (cit. on p. 61).

[126] J. P. Finn, K. Nael, V. Deshpande, O. Ratib, and G. Laub, "Cardiac mr imaging: State of the technology.", *Radiology*, vol. 241, no. 2, pp. 338–54, 2006. DOI: 10.1148/radiol.2412041866 (cit. on p. 67).

[127] D. J. Atkinson and R. R. Edelman, "Cineangiography of the heart in a single breath hold with a segmented turboflash sequence.", *Radiology*, vol. 178, no. 2, pp. 357–360, 1991. DOI: 10.1148/radiology.178.2.1987592 (cit. on p. 67).

[128] D. T. Ginat, M. W. Fong, D. J. Tuttle, S. K. Hobbs, and R. C. Vyas, "Cardiac imaging: Part 1, mr pulse sequences, imaging planes, and basic anatomy", *American Journal of Roentgenology*, vol. 197, no. 4, pp. 808–815, 2011. DOI: 10.2214/AJR.10.7231 (cit. on p. 68).

[129] O. P. Simonetti, R. J. Kim, D. S. Fieno, H. B. Hillenbrand, E. Wu, J. M. Bundy, J. P. Finn, and R. M. Judd, "An improved mr imaging technique for the visualization of myocardial infarction.", *Radiology*, vol. 218, no. 1, pp. 215–23, 2001. DOI: 10.1148/radiology.218.1.r01ja50215 (cit. on p. 68).

[130] M. Schloegl, M. Holler, A. Schwarzl, K. Bredies, and R. Stollberger, "Infimal convolution of total generalized variation functionals for dynamic mri", *Magnetic Resonance in Medicine*, vol. 78, no. 1, pp. 142–155, 2017. DOI: 10.1002/mrm.26352 (cit. on p. 68).

[131] R. Ahmad, H. Xue, S. Giri, Y. Ding, J. Craft, and O. P. Simonetti, "Variable density incoherent spatiotemporal acquisition (vista) for highly accelerated cardiac mri", *Magnetic Resonance in Medicine*, vol. 74, no. 5, pp. 1266–1278, 2015. DOI: 10.1002/mrm.25507 (cit. on pp. 69–71).

[132] A. R. Padhani, "Dynamic contrast-enhanced mri in clinical oncology: Current status and future directions", *Journal of Magnetic Resonance Imaging*, vol. 16, no. 4, pp. 407–422, 2002. DOI: 10.1002/jmri.10176 (cit. on p. 89).

[133] P. S. Tofts, "Modeling tracer kinetics in dynamic gd-dtpa mr imaging", *Journal of Magnetic Resonance Imaging*, vol. 7, no. 1, pp. 91–101, 1997. DOI: 10.1002/jmri.1880070113 (cit. on p. 89).

[134] P. S. Tofts, G. Brix, D. L. Buckley, J. L. Evelhoch, E. Henderson, M. V. Knopp, H. B. Larsson, T. Y. Lee, N. A. Mayr, G. J. Parker, R. E. Port, J. Taylor, and R. M. Weisskoff, "Estimating kinetic parameters from dynamic contrast-enhanced t1- weighted mri of a diffusable tracer: Standardized quantities and symbols", *Journal of Magnetic Resonance Imaging*, vol. 10, no. 3, pp. 223–232, 1999. DOI: 10.1002/(SICI)1522-2586(199909)10:3<223::AID-JMRI2>3.0.CO;2-S (cit. on p. 89).

[135] E. K. Vos, G. J. S. Litjens, T. Kobus, T. Hambrock, C. A. H. V. D. Kaa, J. O. Barentsz, H. J. Huisman, and T. W. J. Scheenen, "Assessment of prostate cancer aggressiveness using dynamic contrast-enhanced magnetic resonance imaging at 3 t", *European Urology*, vol. 64, no. 3, pp. 448–455, 2013. DOI: 10.1016/j.eururo.2013.05.045 (cit. on p. 90).

[136] M. Rijpkema, J. H. Kaanders, F. B. Joosten, A. J. van der Kogel, and A. Heerschap, "Method for quantitative mapping of dynamic mri contrast agent uptake in human tumors", *Journal of Magnetic Resonance Imaging*, vol. 14, no. 4, pp. 457–463, 2001. DOI: 10.1002/jmri.1207 (cit. on p. 90).

[137] E. Henderson, B. K. Rutt, and T. Y. Lee, "Temporal sampling requirements for the tracer kinetics modeling of breast disease", *Magnetic Resonance Imaging*, vol. 16, no. 9, pp. 1057–1073, 1998. DOI: 10.1016/S0730-725X(98)00130-1 (cit. on pp. 90, 116).

[138] X. Barreau, G. Marnat, F. Gariel, and V. Dousset, "Intracranial arteriovenous malformations", *Diagnostic and Interventional Imaging*, vol. 95, no. 12, pp. 1175–1186, 2014. DOI: 10.1016/j.diii.2014.10.004 (cit. on p. 90).

[139] C. Eddleman, H. J. Jeong, and M. C. Hurley, "4d radial acquisition contrast-enhanced mr angiography and intracranial arteriovenous malformations", *Stroke*, vol. 40, no. 8, 2009 (cit. on p. 91).

[140] J. Hennig, K. Scheffler, J. Laubenberger, and R. Strecker, "Time-resolved projection angiography after bolus injection of contrast agent", *Magnetic Resonance in Medicine*, vol. 37, no. 3, pp. 341–345, 1997. DOI: 10.1002/mrm.1910370306 (cit. on p. 91).

[141] G. Laub and K. Randall, "Syngo twist for dynamic time-resolved mr angiography", *MAGNETOM Flash 2006*, pp. 92–95, 2006 (cit. on p. 91).

[142] L. Feng, R. Grimm, K. T. obias Block, H. Chandarana, S. Kim, J. Xu, L. Axel, D. K. Sodickson, and R. Otazo, "Golden-angle radial sparse parallel mri: Combination of compressed sensing, parallel imaging, and golden-angle radial sampling for fast and flexible dynamic volumetric mri", *Magnetic Resonance in Medicine*, vol. 72, no. 3, pp. 707–717, 2014. DOI: 10.1002/mrm.24980 (cit. on pp. 91, 92).

[143] S. G. Kim, L. Feng, R. Grimm, M. Freed, K. T. Block, D. K. Sodickson, L. Moy, and R. Otazo, "Influence of temporal regularization and radial undersampling factor on compressed sensing reconstruction in dynamic contrast enhanced mri of the breast", *Journal of Magnetic Resonance Imaging*, vol. 43, no. 1, pp. 261–269, 2016. DOI: 10.1002/jmri.24961 (cit. on pp. 91, 116).

[144] L. E. Kershaw and H. L. M. Cheng, "Temporal resolution and snr requirements for accurate dce-mri data analysis using the AATH model", *Magnetic Resonance in Medicine*, vol. 64, no. 6, pp. 1772–1780, 2010. DOI: 10.1002/mrm.22573 (cit. on p. 116).

[145] K. Bredies and H. Sun, "Preconditioned douglas-rachford algorithms for tv and tgv regularized variational imaging problems.", *Journal of Mathematical Imaging and Vision*, vol. 52, no. 3, pp. 317–344, 2015 (cit. on p. 117).

[146] J. Adler and O. Oktem, "Learned primal-dual reconstruction", *IEEE Transactions on Medical Imaging*, vol. 0062, no. 3, pp. 1–11, 2018. DOI: 10.1109/TMI.2018.2799231 (cit. on pp. 117, 145).

[147] H. Vrenken, J. J. G. Geurts, D. L. Knol, L. N. van Dijk, V. Dattola, B. Jasperse, R. A. van Schijndel, C. H. Polman, J. A. Castelijns, F. Barkhof, and P. J. W. Pouwels, "Whole-brain t1 mapping in multiple sclerosis: Global changes of normal-appearing gray and white matter.", *Radiology*, vol. 240, no. 3, pp. 811–20, 2006. DOI: 10.1148/radiol.2403050569 (cit. on p. 119).

[148] D. R. Messroghli, K. Walters, S. Plein, P. Sparrow, M. G. Friedrich, J. P. Ridgway, and M. U. Sivananthan, "Myocardial T1 mapping: Application to patients with acute and chronic myocardial infarction", *Magnetic Resonance in Medicine*, vol. 58, no. 1, pp. 34–40, 2007. DOI: 10.1002/mrm.21272 (cit. on p. 119).

[149] V. O. Puntmann, T. Voigt, Z. Chen, M. Mayr, R. Karim, K. Rhode, A. Pastor, G. Carr-White, R. Razavi, T. Schaeffter, and E. Nagel, "Native T1 mapping in differentiation of normal myocardium from diffuse disease in hypertrophic and dilated cardiomyopathy", *JACC: Cardiovascular Imaging*, vol. 6, no. 4, pp. 475–484, 2013. DOI: 10.1016/j.jcmg.2012.08.019. [Online]. Available: http://dx.doi.org/10.1016/j.jcmg.2012.08.019 (cit. on p. 119).

[150] M. Cheng, L. Hai-Ling, N. Stikov, N. R. Ghugre, and G. A. Wright, *Practical medical applications of quantitative mr relaxometry*, 2012. DOI: 10.1002/jmri.23718 (cit. on p. 119).

[151] E. Hahn, "An accurate nuclear magnetic resonance method for measuring spin-lattice relaxation times", *Physical Review*, vol. 76, no. 1, pp. 145–146, 1949. DOI: 10.1103/PhysRev.76.145 (cit. on p. 119).

[152] J. K. Barral, E. Gudmundson, N. Stikov, M. Etezadi-Amoli, P. Stoica, and D. G. Nishimura, "A robust methodology for in vivo t1 mapping", *Magnetic Resonance in Medicine*, vol. 64, no. 4, pp. 1057–1067, 2010. DOI: 10.1002/mrm.22497 (cit. on p. 119).

[153] D. C. Look and D. R. Locker, "Time saving in measurement of nmr and epr relaxation times", *Review of Scientific Instruments*, vol. 41, no. 2, pp. 250–251, 1970. DOI: 10.1063/1.1684482 (cit. on p. 120).

[154] E. K. Fram, R. J. Herfkens, G. A. Johnson, G. H. Glover, J. P. Karis, A. Shimakawa, T. G. Perkins, and N. J. Pelc, "Rapid calculation of t1 using variable flip angle gradient refocused imaging", *Magnetic Resonance Imaging*, vol. 5, no. 3, pp. 201–208, 1987. DOI: 10.1016/0730-725X(87)90021-X (cit. on p. 120).

[155] J. Homer and M. S. Beevers, "Driven-equilibrium single-pulse observation of t1 relaxation. a reevaluation of a rapid "new"method for determining nmr spin-lattice relaxation times", *Journal of Magnetic Resonance (1969)*, vol. 63, no. 2, pp. 287–297, 1985. DOI: 10.1016/0022-2364(85)90318-X (cit. on p. 120).

[156] S. C. Deoni, B. K. Rutt, and T. M. Peters, "Rapid combined t1 and t2 mapping using gradient recalled acquisition in the steady state", *Magnetic Resonance in Medicine*, vol. 49, no. 3, pp. 515–526, 2003. DOI: 10.1002/mrm.10407 (cit. on p. 120).

[157] S. C. Deoni, T. M. Peters, and B. K. Rutt, "High-resolution t1 and t2 mapping of the brain in a clinically acceptable time with despot1 and despot2", *Magnetic Resonance in Medicine*, vol. 53, no. 1, pp. 237–241, 2005. DOI: 10.1002/mrm.20314 (cit. on p. 120).

[158] ——, "Determination of optimal angles for variable nutation proton magnetic spin-lattice, t1, and spin-spin, t2, relaxation times measurement", *Magnetic Resonance in Medicine*, vol. 51, no. 1, pp. 194–199, 2004. DOI: 10.1002/mrm.10661 (cit. on p. 120).

[159] R. Venkatesan, W. Lin, and E. M. Haacke, "Accurate determination of spin-density and t1 in the presence of rf- field inhomogeneities and flip-angle miscalibration", *Magnetic Resonance in Medicine*, vol. 40, no. 4, pp. 592–602, 1998. DOI: 10.1002/mrm.1910400412 (cit. on p. 120).

[160] L. C. Chang, G. K. Cheng, P. J. Basser, and C. Pierpaoli, "Linear least-squares method for unbiased estimation of t1 from spgr signals", *Magnetic Resonance in Medicine*, vol. 60, no. 2, pp. 496–501, 2008. DOI: 10.1002/mrm.21669 (cit. on p. 120).

[161] R. Stollberger and P. Wach, "Imaging of the active b1 field in vivo.", *Magnetic Resonance in Medicine*, vol. 35, no. 2, pp. 246–51, 1996. DOI: 10.1002/mrm.1910350217 (cit. on p. 120).

[162] L. I. Sacolick, F. Wiesinger, I. Hancu, and M. W. Vogel, "B 1 mapping by bloch-siegert shift", *Magnetic Resonance in Medicine*, vol. 63, no. 5, pp. 1315–1322, 2010. DOI: 10.1002/mrm.22357 (cit. on p. 121).

[163] A. Lesch, M. Schloegl, M. Holler, and R. Stollberger, "Highly accelerated bloch-siegert b1+ mapping using variational modeling", in *Proc. Intl. Soc. Mag. Reson. Med. 24*, 2016, p. 1875 (cit. on p. 121).

[164] N. Stikov, M. Boudreau, I. R. Levesque, C. L. Tardif, J. K. Barral, and G. B. Pike, "On the accuracy of t1 mapping: Searching for common ground", *Magnetic Resonance in Medicine*, vol. 73, no. 2, pp. 514–522, 2015. DOI: 10.1002/mrm.25135 (cit. on p. 121).

[165] K. Keenan, K. Stupic, M. Boss, S. Russek, T. Chenevert, P. Prasad, W. Reddick, K. Cecil, J. Zheng, P. Hu, and E. Jackson, "Multi-site, multi-vendor comparison of t1 measurement using ismrm/nist system phantom", in *Proc. Intl. Soc. Mag. Reson. Med. 24*, 2016, p. 3290 (cit. on p. 121).

[166] M. Doneva, P. Börnert, H. Eggers, C. Stehning, J. Sénégas, A. Mertins, J. Senegas, and A. Mertins, "Compressed sensing reconstruction for magnetic resonance parameter mapping", *Magnetic Resonance in Medicine*, vol. 64, no. 4, pp. 1114–1120, 2010. DOI: 10.1002/mrm.22483 (cit. on pp. 122, 140).

[167] D. Ma, V. Gulani, N. Seiberlich, K. Liu, J. L. Sunshine, J. L. Duerk, and M. A. Griswold, "Magnetic resonance fingerprinting", *Nature*, vol. 495, no. 7440, pp. 187–192, 2013. DOI: 10.1038/nature11971 (cit. on p. 122).

[168] J. V. Velikina, A. L. Alexander, and A. Samsonov, "Accelerating mr parameter mapping using sparsity-promoting regularization in parametric dimension.", *Magnetic resonance in medicine*, vol. 70, no. 5, pp. 1263–73, 2013. DOI: 10.1002/mrm.24577 (cit. on pp. 122, 140).

[169] B. Zhao, W. Lu, T. K. Hitchens, F. Lam, C. Ho, and Z.-P. Liang, "Accelerated mr parameter mapping with low-rank and sparsity constraints.", *Magnetic resonance in medicine*, vol. 74, no. 2, pp. 489–98, 2015. DOI: 10.1002/mrm.25421 (cit. on p. 123).

[170] T. Zhang, J. M. Pauly, and I. R. Levesque, "Accelerating parameter mapping with a locally low rank constraint", *Magnetic Resonance in Medicine*, vol. 73, no. 2, pp. 655–661, 2015. DOI: 10.1002/mrm.25161 (cit. on p. 123).

[171] K. T. Block, M. Uecker, and J. Frahm, "Model-based iterative reconstruction for radial fast spin-echo mri", *IEEE Transactions on Medical Imaging*, vol. 28, no. 11, pp. 1759–1769, 2009. DOI: 10.1109/TMI.2009.2023119 (cit. on pp. 123, 141).

[172] T. J. Sumpf, M. Uecker, S. Boretius, and J. Frahm, "Model-based nonlinear inverse reconstruction for t2 mapping using highly undersampled spin-echo mri", *Journal of Magnetic Resonance Imaging*, vol. 34, no. 2, pp. 420–428, 2011. DOI: 10.1002/jmri.22634 (cit. on pp. 123, 141).

[173] T. J. Sumpf, A. Petrovic, M. Uecker, F. Knoll, and J. Frahm, "Fast t2 mapping with improved accuracy using undersampled spin-echo mri and model-based reconstructions with a generating function", *IEEE Transactions on Medical Imaging*, vol. 33, no. 12, pp. 2213–2222, 2014. DOI: 10.1109/TMI.2014.2333370 (cit. on p. 123).

[174] J. Tran-Gia, T. Wech, T. Bley, and H. Köstler, "Model-based acceleration of look-locker t1 mapping", *PLoS ONE*, vol. 10, no. 4, e0122611, 2015. DOI: 10.1371/journal.pone.0122611 (cit. on p. 123).

[175] V. Roeloffs, X. Wang, T. J. Sumpf, M. Untenberger, D. Voit, and J. Frahm, "Model-based reconstruction for t1 mapping using single-shot inversion-recovery radial flash", *International Journal of Imaging Systems and Technology*, vol. 26, no. 4, pp. 254–263, 2016. DOI: 10.1002/ima.22196 (cit. on p. 123).

[176] X. Wang, V. Roeloffs, J. Klosowski, Z. Tan, D. Voit, M. Uecker, and J. Frahm, "Model-based t1 mapping with sparsity constraints using single-shot inversion-recovery radial flash", *Magnetic Resonance in Medicine*, 2017. DOI: 10.1002/mrm.26726 (cit. on p. 123).

[177] F. Knoll, M. Holler, T. Koesters, R. Otazo, K. Bredies, and D. K. Sodickson, "Joint mr-pet reconstruction using a multi-channel image regularizer", *IEEE Transactions on Medical Imaging*, vol. 36, no. 1, pp. 1–16, 2017. DOI: 10.1109/TMI.2016.2564989 (cit. on pp. 124, 139).

[178] R. P. A. Teixeira, S. J. Malik, and J. V. Hajnal, "Joint system relaxometry (jsr) and crámer-rao lower bound optimization of sequence parameters: A framework for enhanced precision of despot t1 and t2 estimation", *Magnetic Resonance in Medicine*, vol. 79, no. 1, pp. 234–245, 2018. DOI: 10.1002/mrm.26670 (cit. on p. 140).

[179] O. Maier, M. Schloegl, A. Lesch, A. Petrovic, M. Holler, K. Bredies, T. Pock, and R. Stollberger, "Improved accelerated model-based parameter quantification with total-generalized-variation regularization.", in *Proc. Intl. Soc. Mag. Reson. Med. 25*, 2017, p. 3855 (cit. on p. 141).

[180] E. Springer, W. Bogner, P. Szomolanyi, and S. Trattnig, "Case study : Magnetic resonance fingerprinting (mrf) imaging of the brain", *MAGNETOM Flash*, no. 66, pp. 100–102, 2016 (cit. on p. 141).

[181] J. Assländer, M. A. Cloos, F. Knoll, D. K. Sodickson, J. Hennig, and R. Lattanzi, "Low rank alternating direction method of multipliers reconstruction for mr fingerprinting", *Magnetic Resonance in Medicine*, vol. 79, no. 1, pp. 83–96, 2018. DOI: 10.1002/mrm.26639 (cit. on p. 141).

[182] M. Holler, R. M. Huber, and F. Knoll, "Coupled regularization with multiple data discrepancies", *Inverse Problems*, 2018. DOI: 10.1088/1361-6420/aac539 (cit. on p. 145).

[183] K. Hammernik, T. Klatzer, E. Kobler, M. P. Recht, D. K. Sodickson, T. Pock, and F. Knoll, "Learning a variational network for reconstruction of accelerated mri data.", *Magnetic Resonance in Medicine*, vol. 79, no. 6, pp. 3055–3071, 2018. DOI: 10.1002/mrm.26977 (cit. on p. 145).

[184] E. Kobler, T. Klatzer, K. Hammernik, and T. Pock, "Variational networks: Connecting variational methods and deep learning", in *Lecture Notes in Computer Science*, vol. 10496 LNCS, 2017, pp. 281–293. DOI: 10.1007/978-3-319-66709-6_23 (cit. on p. 145).

List of Publications

Full Paper

Matthias Schloegl, Martin Holler, Andreas Schwarzl, Kristian Bredies and Rudolf Stollberger. *Infimal Convolution of Total Generalized Variation Functionals for dynamic MRI.* **Magnetic Resonance in Medicine, 78(1): 142-144 (2017)**, doi: 10.1002/mrm.26352

Bernhard Neumayer, Matthias Schloegl, Christian Payer, Thomas Widek, Sebastian Tschauner, Thomas Ehammer, Rudolf Stollberger and Martin Urschler. *Reducing acquisition time for MRI-based forensic age estimation.* **Scientific Reports, 8(1):2063 (2018)**, doi: 10.1038/s41598-018-20475

Andreas Lesch, Matthias Schloegl, Martin Holler, Kristian Bredies and Rudolf Stollberger. *Ultrafast 3D Bloch-Siegert B1+ Mapping using Variational Modeling.* **Magnetic Resonance in Medicine (2018)** (in press)

Oliver Maier, Jasper Schoormans, Matthias Schloegl, Gustav J Strijkers, Andreas Lesch, Thomas Benkert, Tobias Block, Bram F Coolen, Kristian Bredies and Rudolf Stollberger. *Rapid T1 quantification from high resolution 3D data with model-based reconstruction.* **Magnetic Resonance in Medicine (2018)**, doi: 10.1002/mrm.27502

Diego Salas-Gonzalez, J.M. Gorriz, Javier Ramirez, Matthias Schloegl, Elmar Wolfgang Lang, Andres Ortiz. Parameterization of the distribution of white and grey matter in MRI using the α-stable distribution. Comp. in Bio. and Med. 43(5): 559-567 (2013)

Conference Proceedings

Stefan Spann, Christoph Aigner, Matthias Schloegl, Andreas Lesch, Kristian Bredies, Stefan Ropele, D. Pinter, Lukas Pirpamer and Rudolf Stollberger. Acceleration of arterial spin labeling data using spatio-temporal total generalized variation (TGV) reconstruction. Proc. Intl. Soc. Mag. Reson. Med. 26 (2018), Paris, France

Stefan Spann, Matthias Schloegl, Christoph Aigner, Karl Koschutnig, Martin Holler, Kristian Bredies and Rudolf Stollberger. Denoising of functional Arterial Spin Labeling (fASL) perfusion data using infimal convolution of total generalized variation functionals (ICTGV). Proc. Intl. Soc. Mag. Reson. Med. 26 (2018), Paris, France

Oliver Maier, Matthias Schloegl, Jasper Schoormans, Bram Coolen, Tobias Block, Thomas Benkert, Gustav Strijkers, and Rudolf Stollberger. High Resolution T1 quantification from golden-angle radial 3D acquisitions. Proc. Intl. Soc. Mag. Reson. Med. 26 (2018), Paris, France

Matthias Schloegl,, Gernot Reishofer, Martin Holler, Thomas Benkert, Ulrike Wießpeiner, Kristian Bredies, Kai-Tobias Block, Rudolf Stollberger. Dynamic CE-MRA with high temporal resolution by combining radial acquisition and variational reconstruction. Proc. ESMRMB (2017): 344, Barcelona, Spain

Matthias Schloegl, Martin Holler, Oliver Maier, Thomas Benkert, Kristian Bredies, Kai Tobias Block, Rudolf Stollberger. Highly Accelerated Quantitative MRI with ICTGV Regularized Reconstruction. Proc. Intl. Soc. Mag. Reson. Med. 25 (2017), Hawaii, USA

Matthias Schloegl, Stefan Spann, Christoph Aigner, Martin Holler, Kristian Bredies, Rudolf Stollberger. Improved Denoising of Dynamic Arterial Spin Labeling with Infimal Convolution of Total Generalized Variation Functionals (ICTGV). Proc. Intl. Soc. Mag. Reson. Med. 25 (2017), Hawaii, USA

Oliver Maier, Matthias Schloegl, Andreas Lesch, Andreas Petrovic, Martin Holler, Kristian Bredies, Thomas Pock, Rudolf Stollberger. Improved Accelerated Model-based Parameter Quantification with Total-Generalized-Variation Regularization. Proc. Intl. Soc. Mag. Reson. Med. 25 (2017), Hawaii, USA

Andreas Lesch, Matthias Schloegl, Rudolf Stollberger. Robust Accelerated Reconstruction for Bloch-Siegert B1-mapping. Proc. Intl. Soc. Mag. Reson. Med. 25 (2017), Hawaii, USA

Bernhard Neumayer, Matthias Schloegl, Christian Payer, Thomas Widek, Thomas Ehammer, Rudolf Stollberger, M. Urschler. Accuracy of Age Esti-

mation based on Undersampled MR Images of the Hand. Proc. Intl. Soc. Mag. Reson. Med. 25 (2017), Hawaii, USA

Matthias Schloegl, Martin Holler, Kristian Bredies, Rudolf Stollberger Changing temporal resolution of DCE-MRI Radial VIBE data by ICTGV reconstruction. 102th Annual Meeting of The Radiological Society of North America (RSNA), (2016), Chicago, USA

Bernhard Neumayer, Matthias Schloegl, Christian Payer, Thomas Widek, Thomas Ehammer, Rudolf Stollberger, M. Urschler. Acceleration of MR Measurements for Age Estimation. Proc. ESMRMB (2016): 344, Vienna, Austria

Matthias Schloegl, Martin Holler, Andreas Schwarzl, Kristian Bredies, Rudolf Stollberger. ICTGV Reconstruction of DCE golden-angle radial VIBE data. Proc. ESMRMB (2016): 290, Vienna, Austria

Oliver Maier, Matthias Schloegl, Andreas Lesch , Andreas Petrovic, Rudolf Stollberger. Accelerated T1-Mapping with iteratively TV regularized Gauss-Newton Method. Proc. ESMRMB (2016): 205, Vienna, Austria

Matthias Schloegl, Bernhard Neumayer, Thommas Ehammer, Thomas Widek, Christian Payer, Martin Urschler, Rudolf Stollberger. Validation of TGV regularized accelerated MR reconstruction by age estimation. Proc. ESMRMB (2016): 111, Vienna, Austria

Andreas Lesch, Matthias Schloegl, Martin Holler and Rudolf Stollberger. Highly Accelerated Bloch-Siegert B1+ Mapping Using Variational Modeling. Proc. Intl. Soc. Mag. Reson. Med. 24 (2016), Singapur, Singapur

Matthias Schloegl, Martin Holler, Kristian Bredies, Karl Kunisch, and Rudolf Stollberger. ICTGV Regularization for Highly Accelerated Dynamic MRI. Proc. Intl. Soc. Mag. Reson. Med. 23, Toronto, Canada; (summa cum laude award)

Matthias Schloegl, Martin Holler, Kristian Bredies, and Rudolf Stollberger. A Variational Approach for Coil-Sensitivity Estimation for Undersampled Phase-Sensitive Dynamic MRI Reconstruction Proc. Intl. Soc. Mag. Reson. Med. 23, Toronto, Canada;

Matthias Schloegl, Clemens Diwoky, and Rudolf Stollberger. Motion detection for 3D radial balanced SSFP sequences. Proc. Intl. Soc. Mag. Reson. Med. 22, Milan, Italy;

Matthias Schloegl, Florian Knoll, Katharina Gruber, Franz Ebner, and Rudolf Stollberger. Quantitative Evaluation of Non-Linear Reconstruction Methods in MRI. Proc. Intl. Soc. Mag. Reson. Med. 21, Salt-Lake-City USA

Diego Salas-Gonzalez, J.M. Górriz, Javier Ramírez, Matthias Schloegl, Elmar Wolfgang Lang. Bayesian Segmentation of Magnetic Resonance Images Using the α-stable distribution. HAIS 2011, Wroclaw, Poland, May 23-25, 2011

Acronyms

ACL	Auto-Calibration-Lines 27
ADC	Analog-Digital-Converter 23
AIF	Arterial Input Function 90, 91, 95, 116
AVIONIC	Accelerated Variational Dynamic MRI Reconstruction 53
AVM	Arterio-Venous-Malformation 90, 93, 101, 117, 143
BSM	Bloch-Siegert-Method 121, 125, 126, 133
BV	Bounded Variation 33
CA	Contrast Agent 89, 90, 93, 94
CE	Contrast Enhanced 89
CE-MRA	Contrast-Enhanced Magnetic-Resonance-Angiography 90
CG	Conjugate Gradient 28, 47
CINE	Cinematographic cardiac MRI using ECG 16, 17, 67–71, 73–78, 82, 85
CS	Compressed Sensing 34–36, 39, 41, 47, 55, 68, 122
CSF	Cerebro-Spinal Fluid 125
DAM	Double-Angle-Method 120
DCE	Dynamic-Contrast-Enhanced 40, 89, 92–95, 101, 104, 116, 117, 119, 139, 143–145
DESPOT	Driven-equilibrium single-pulse observation of T_1 120
DICOM	Digital Imaging and Communications in Medicine 61

dMRI	Dynamic Magnetic Resonance Imaging iv, 1, 21, 31, 40–43, 47
DSC	Dynammic-Suszeptibility-Contrast 89
ECG	Electro-Cardiogram 15, 17, 67
EES	Extravascular Extracellular Space 89
FID	Free Induction Decay 12
FISTA	Fast Iterative Soft Thresholding 47
FLASH	Fast Low Angle Shot 12, 16, 18, 67
FOV	Field-of-View 22, 57
FSE	Fast Spin Echo 13
Gd	Gadolinium 89, 125, 139
GE	Gradient Echo 12, 13, 67, 68
GM	Gray Matter 119, 125, 126
GRAPPA	Generalized Autocalibrating Partially Parallel Acquisitions 27
GRASP	Arterial Input Function 91, 92, 94, 95, 101, 104, 116
HASTE	Half-fourier Acquisition Single-shot Turbo spin Echo 13
HVS	Human Visual System 54, 55
ICTGV	Infimal Convolution of Total Generalized Variation xii, 41, 46–48, 54, 56, 63, 64
iid	Independent and identically distributed 29
IR	Inversion Recovery 119, 120, 123, 125, 127, 139
IRGN	Iteratively-Regularized Gauss-Newton xviii, 122, 123, 125, 134–138
IRLL	Inversion-Recovery-Look-Locker 119, 121, 122
ISMRM	International Society for Magnetic Resonance in Medicine 61
ISMRMRD	ISMRM Raw Data 61
L+S	Low Rank Plus Sparse Decomposition xiii, 41, 46, 47, 51, 69, 70, 72–74, 76–78, 80, 91, 92, 94, 95, 101, 104, 116

LL	Lock-Locker 123
MAP	Maximum-A-Posteriori Estimator 29
MBR	Model-Based Reconstruction 121–123, 125, 135, 139–141
MESE	Multi-Echo-Spin-Echo 122
MIP	Maximum-Intensity-Projection 94, 104
MRA	Magnetic Resonance Angiography 17, 117
MRI	Magnetic Resonance Imaging iv, 1, 143–145
NMR	Nuclear Magnetic Resonance 119
NUFFT	Non-Uniform Fast Fourier Transform 57
PACS	Picture Archiving and Communication System 62
PCA	Principal Component Analysis 40, 41, 60
PI	Parallel Imaging 27, 30, 38, 47, 55, 58, 59, 67, 68, 75, 91
PSNR	Peak-Signal-to-Noise-Ratio 92, 95, 125, 149
qMRI	Quantitative MRI 119, 122, 123
RAVE	RAdial Volumetric Encoding xviii, 17, 90–93, 122, 125, 127, 134–141
RF	Radio Frequency 7–9, 12, 13
RIP	Restricted Isometry Property 35
RMSE	Root-Mean-Squared Error xii–xiv, 46, 54, 71, 73, 74, 84, 149
ROF	Rudin-Osher-Fatemi 33
SAR	Specific Absorption Rate 68
SE	Spin Echo 12
SENSE	Sensitivity Encoding 27
SER	Signal-to-Error-Ratio xiv, 69, 73, 75, 77–80, 148
SMASH	Simultaneous Acquisition of Spatial Harmonics 27
SNR	Signal-to-Noise Ratio, 23, 25, 28, 36, 44, 53, 55, 56, 120, 121, 125, 127, 133, 135, 140

SOS	Sum-Of-Squares reconstruction 70
SPIRiT	Iterative Self-consistent Parallel Imaging Reconstruction From Arbitrary k-Space 27
SSFP	Steady-State Free Precession 13, 16, 67, 69
SSIM	Structural Similarity Index xii–xiv, 54, 69, 71, 73–75, 77–79, 84
TE	Echo Time 12, 120
TGV	Total Generalized Variation 36, 59
TI	Inversion Time 125
TR	Repetition Time 67, 91, 120
TV	Total Variation 33, 59
TWIST	Time-resolved angiography With Interleaved Stochastic Trajectories 91, 93, 117
VFA	Variable-Flip-Angle xviii, 119–125, 127, 133–135, 139–141
VIBE	Volume-Interpolated-Breathhold Examination xviii, 122, 125, 127, 134, 139, 140
WM	White Matter 119, 125, 126

List of Symbols

BW Readout Bandwidth 24, 93
$K_{\mathbf{trans}}$ Exchange rate constant between plasma and leakage space 90, 91
N_c Number of receiver coils 23, 155
N_e Number of samples along encoding direction 23, 57
N_r Number of samples along readout direction 23, 57
N_t Number of samples along outer temporal direction 31
N_x Number of pixels in x-image dimension 23
N_y Number of pixels in y-image dimension 23
Δt Temporal resolution 31, 91–94, 104, 116
$\mathcal{H}$ Hamiltonian 4
Σ Noise-Covariance Matrix 24, 60, 61
η Vector with Noise Samples 24
$\hat{C}$ Coil Sensitivity Operator 23, 31
$\mathcal{DFT}$ Discrete Fourier transform 22, 23, 31
$\mathcal{K}$ MR forward operator 23
$\mathcal{U}$ image space 23, 31, 38, 39, 151, 152
$\mathcal{V}$ data space 31
v_e Fractional volume of contrast agent in leakage space 90
v_p Fractional volume of contrast agent in blood plasma 90
spf Number of spokes per dynamic frame for golden-angle radial acquisitions 92, 125, 141
c_p Tracer concentration in blood plasma 90
k_b Boltzmann's constant 24
r Reduction factor 44, 56